

---


Electronic Theses and Dissertations, 2004-2019

---

2005

## Liquid Crystal Optics For Communications, Signal Processing And 3-d Microscopic Imaging

Sajjad Khan  
*University of Central Florida*

 Part of the [Electromagnetics and Photonics Commons](#), and the [Optics Commons](#)  
Find similar works at: <https://stars.library.ucf.edu/etd>  
University of Central Florida Libraries <http://library.ucf.edu>

This Doctoral Dissertation (Open Access) is brought to you for free and open access by STARS. It has been accepted for inclusion in Electronic Theses and Dissertations, 2004-2019 by an authorized administrator of STARS. For more information, please contact [STARS@ucf.edu](mailto:STARS@ucf.edu).

---

### STARS Citation

Khan, Sajjad, "Liquid Crystal Optics For Communications, Signal Processing And 3-d Microscopic Imaging" (2005). *Electronic Theses and Dissertations, 2004-2019*. 581.  
<https://stars.library.ucf.edu/etd/581>

LIQUID CRYSTAL OPTICS FOR COMMUNICATIONS, SIGNAL PROCESSING AND 3-D  
MICROSCOPIC IMAGING

by

SAJJAD ALI KHAN

B.S. Pakistan Navy Engineering College, National University of Science & Technology,  
Karachi, Pakistan, 1998.

M.S. University of Central Florida, 2002

A dissertation submitted in partial fulfillment of the requirements  
for the degree of Doctor of Philosophy  
in the College of Optics & Photonics/CREOL  
at the University of Central Florida  
Orlando, Florida

Fall Term  
2005

Major Professor: Nabeel A. Riza

© 2005 Sajjad Ali Khan

## **ABSTRACT**

This dissertation proposes, studies and experimentally demonstrates novel liquid crystal (LC) optics to solve challenging problems in RF and photonic signal processing, freespace and fiber optic communications and microscopic imaging. These include free-space optical scanners for military and optical wireless applications, variable fiber-optic attenuators for optical communications, photonic control techniques for phased array antennas and radar, and 3-D microscopic imaging.

At the heart of the applications demonstrated in this thesis are LC devices that are non-pixelated and can be controlled either electrically or optically. Instead of the typical pixel-by-pixel control as is custom in LC devices, the phase profile across the aperture of these novel LC devices is varied through the use of high impedance layers. Due to the presence of the high impedance layer, there forms a voltage gradient across the aperture of such a device which results in a phase gradient across the LC layer which in turn is accumulated by the optical beam traversing through this LC device. The geometry of the electrical contacts that are used to apply the external voltage will define the nature of the phase gradient present across the optical beam. In order to steer a laser beam in one angular dimension, straight line electrical contacts are used to form a one dimensional phase gradient while an annular electrical contact results in a circularly symmetric phase profile across the optical beam making it suitable for focusing the optical beam. The geometry of the electrical contacts alone is not sufficient to form the linear and the quadratic phase profiles that are required to either deflect or focus an optical beam. Clever use of the phase response of a typical nematic liquid crystal (NLC) is made such that the

linear response region is used for the angular beam deflection while the high voltage quadratic response region is used for focusing the beam.

Employing an NLC deflector, a device that uses the linear angular deflection, laser beam steering is demonstrated in two orthogonal dimensions whereas an NLC lens is used to address the third dimension to complete a three dimensional (3-D) scanner. Such an NLC deflector was then used in a variable optical attenuator (VOA), whereby a laser beam coupled between two identical single mode fibers (SMF) was mis-aligned away from the output fiber causing the intensity of the output coupled light to decrease as a function of the angular deflection. Since the angular deflection is electrically controlled, hence the VOA operation is fairly simple and repeatable. An extension of this VOA for wavelength tunable operation is also shown in this dissertation.

A LC spatial light modulator (SLM) that uses a photo-sensitive high impedance electrode whose impedance can be varied by controlling the light intensity incident on it, is used in a control system for a phased array antenna. Phase is controlled on the Write side of the SLM by controlling the intensity of the Write laser beam which then is accessed by the Read beam from the opposite side of this reflective SLM. Thus the phase of the Read beam is varied by controlling the intensity of the Write beam.

A variable fiber-optic delay line is demonstrated in the thesis which uses wavelength sensitive and wavelength insensitive optics to get both analog as well as digital delays. It uses a chirped fiber Bragg grating (FBG), and a 1xN optical switch to achieve multiple time delays. The switch can be implemented using the 3-D optical scanner mentioned earlier.

A technique is presented for ultra-low loss laser communication that uses a combination of strong and weak thin lens optics. As opposed to conventional laser communication systems,

the Gaussian laser beam is prevented from diverging at the receiving station by using a weak thin lens that places the transmitted beam waist mid-way between a symmetrical transmitter-receiver link design thus saving prime optical power. LC device technology forms an excellent basis to realize such a large aperture weak lens.

Using a 1-D array of LC deflectors, a broadband optical add-drop filter (OADF) is proposed for dense wavelength division multiplexing (DWDM) applications. By binary control of the drive signal to the individual LC deflectors in the array, any optical channel can be selectively dropped and added. For demonstration purposes, microelectromechanical systems (MEMS) digital micromirrors have been used to implement the OADF. Several key systems issues such as insertion loss, polarization dependent loss, wavelength resolution and response time are analyzed in detail for comparison with the LC deflector approach.

A no-moving-parts axial scanning confocal microscope (ASCM) system is designed and demonstrated using a combination of a large diameter LC lens and a classical microscope objective lens. By electrically controlling the 5 mm diameter LC lens, the 633 nm wavelength focal spot is moved continuously over a 48  $\mu\text{m}$  range with measured 3-dB axial resolution of 3.1  $\mu\text{m}$  using a 0.65 numerical aperture (NA) micro-objective lens. The ASCM is successfully used to image an Indium Phosphide twin square optical waveguide sample with a 10.2  $\mu\text{m}$  waveguide pitch and 2.3  $\mu\text{m}$  height and width. Using fine analog electrical control of the LC lens, a super-fine sub-wavelength axial resolution of 270 nm is demonstrated. The proposed ASCM can be useful in various precision three dimensional imaging and profiling applications.

*To my parents, Murad Gul Khan Mohmand and Madina Murad,*

*and*

*Jani.*

## ACKNOWLEDGMENTS

*“Allah is the Light of the heavens and the earth. The Parable of His Light is as if there were a Niche and within it a Lamp: the Lamp enclosed in Glass: the glass as it were a brilliant star: Lit from a blessed Tree, an Olive, neither of the east nor of the west, whose oil is well-nigh luminous, though fire scarce touched it: Light upon Light! Allah doth guide whom He will to His Light: Allah doth set forth Parables for men: and Allah doth know all things.”*

*Translated by Yusuf Ali from Al-Quraan, Al-Noor (The Light) 024.035*

I am profoundly indebted to my parents, Murad Gul Khan Mohmand and Madina Murad, and my brothers Zahid, Amjad, Arshad, Imran and Luqman, for their constant unwavering support and encouragement throughout my life. No matter what calamity befell me, I could always bank on their support. Probably, it is the right time and place to acknowledge their personal sacrifices as well as my brothers' families' who donated their wedding jewelry for my graduate education here in CREOL. I believe there is no way I can thank them enough for what they have done for me throughout these years. I am deeply indebted to my absolutely lovely wife Shagufta for her understanding and patience during my graduate studies. Without her love and support, I would not have been able to complete this dissertation. I also want to sincerely thank my uncle Ziarat Gul and aunt Shahida for their unequivocal support and encouragement in my career.

I want to sincerely thank my PhD advisor Professor Nabeel Riza for his invaluable mentoring and continual guidance. I have learnt from him in a technical as well as in a personal sense, such as writing journal papers, giving technical talks, and becoming a team leader. No



doubt he has a great deal of contribution towards making me the gentleman that I am today. With his moral and financial support, I have been able to travel to several technical meetings and present our research at different forums. I am highly indebted to him for successfully nominating me for two prestigious student awards, namely, the 2005 Optical Society of America's (OSA) International New Focus/Bookham Student Award and the 2005 Institute of Electrical and Electronic Engineers (IEEE) Orlando Chapter's Outstanding Graduate Student Award.

I would also like to sincerely thank my dissertation committee members Dr. Shin-Tson Wu, Dr. James Harvey, Dr. Glenn Boreman and Dr. Michael Haralambous for evaluating my dissertation and for their invaluable technical suggestions. Special thanks are due to Dr. Wu's group who helped me on several occasions either with fabrication of LC cells or allowing me access to their laboratory equipment for my research, not to mention the technical insights on LCs that they have shared with me over the years. I would also like to thank Dr. Patrick LiKamWa and Dr. M. G. Jim Moharam for their useful discussions and guidance at several times during my research.

I would like to express my appreciation and indebtedness to PIPS laboratory group members including Dr. Sarun Sumriddetchkajorn, Dr. Zahid Yaqoob, Dr. Muzammil Arain, Farzan Ghauri, Mumtaz Sheikh, Martin Van Buren, Frederico Pereira, Douglas Jorgesen, Maarten Bakker, Jason Karp, and Tiffany Metzger. I would also like to thank my former roommates Ayman Faour, Syed Imran, and Dr. Muzammil Arain for their fantastic company. Especially I am thankful to Dr. Muzammil Arain for his friendship, entertainment and great food. I have benefited from his versatile culinary expertise for quite a while. Thanks are also due to the members and Officers of the UCF Pakistani Student Association for organizing and conducting

several picnics and fun events for entertainment as well as for increasing the awareness of the Pakistani culture on campus.

I would like to express my gratitude to CREOL faculty, students and staff for their support during my graduate studies. I would like to mention some friends who have made my stay more enjoyable. These include Waleed Mohamed, Mohamed Salem, Mohamed Sakami, Mohamed Abdur-Rehman 'Rami', Alok Mehta, Charles Middleton, Brian Monacelli, Dr. Cheolhwan Kim, Daniel May-Arriola, Zachary Roth, Yun-Hsing 'Claire' Fan, Chien-Hui 'Vicky' Wen, Yi-Hsin Lin, Dr. Sebastian Gauza and so many others who have helped me either in a personal or technical aspect.

I would also like to mention my appreciation for the CREOL students who elected me to be the Vice President for the IEEE/LEOS student chapter. I would like to say thank you to the IEEE LEOS Awards Committee for awarding me funds to travel to two of the LEOS Annual Meetings in Glasgow, Scotland, in 2002 and in Tucson, Arizona, in 2003. Finally, I would like to acknowledge major funding support from the DARPA STAB program and laboratory equipment support from Nuonics Inc.

# TABLE OF CONTENTS

LIST OF FIGURES .....	xii
LIST OF TABLES .....	xvii
LIST OF JOURNAL PUBLICATIONS .....	xviii
LIST OF CONFERENCE PUBLICATIONS .....	xix
CHAPTER 1: INTRODUCTION .....	1
Organization of Thesis .....	3
References .....	8
CHAPTER 2: LIQUID CRYSTALS BASED FLEXIBLE BEAMFORMING FOR OPTICALLY CONTROLLED PHASED ARRAY ANTENNAS .....	9
2.1 Introduction .....	9
2.2 Flexible Beamforming Architecture .....	10
2.3 Experimental Demonstration .....	17
2.4 System Issues .....	21
2.5 Conclusion .....	26
References .....	27
CHAPTER 3: HYBRID ANALOG-DIGITAL VARIABLE FIBER-OPTIC DELAY LINE .....	29
3.1 Introduction .....	30
3.2 Hybrid Variable Fiber-Optic Delay Line Design .....	31
3.3 Experimental Demonstration .....	38
3.4 Conclusion .....	44
References .....	45
CHAPTER 4: PROGRAMMABLE HIGH SPEED POLARIZATION MULTIPLEXED OPTICAL SCANNER .....	49
4.1 Introduction .....	50
4.2 Proposed Architecture .....	51
4.3 Experiment .....	55
4.4 Conclusion .....	57
References .....	59
CHAPTER 5: DEMONSTRATION OF 3-DIMENSIONAL WIDE ANGLE LASER BEAM SCANNER USING LIQUID CRYSTALS .....	62
5.1 Introduction .....	63
5.2 Hybrid Analog-Digital P-MOS Design .....	65
5.3 Experiments .....	74
5.4 Conclusion .....	85
References .....	87
CHAPTER 6: LIQUID CRYSTAL DEFLECTOR BASED VARIABLE FIBER-OPTIC ATTENUATOR .....	90
6.1 Introduction .....	91
6.2 Variable Optical Attenuator Theory .....	92
6.3 Experiment .....	99
6.4 Extended Applications .....	104

6.5 Conclusion .....	106
References .....	108
CHAPTER 7: WAVELENGTH TUNABLE VARIABLE FIBER-OPTIC ATTENUATOR USING LIQUID CRYSTAL-MIRROR HYBRID CONTROLS .....	111
7.1 Introduction .....	112
7.2 Wavelength Tunable VOA Architecture .....	113
7.3 Experiment .....	115
7.4 Conclusion .....	119
References .....	120
CHAPTER 8: NO-MOVING-PARTS AXIAL SCANNING CONFOCAL MICROSCOPY ...	122
8.1 Introduction .....	123
8.2 Proposed Axial Scanning Confocal Microscope Design .....	124
8.3 ASCM Experimental Demonstration .....	126
8.4 Conclusion .....	134
References .....	135
CHAPTER 9: ULTRA-LOW LOSS LASER COMMUNICATIONS TECHNIQUE USING SMART BEAMFORMING OPTICS .....	137
9.1 Introduction .....	138
9.2 Self-Imaging Technique for Low Loss Laser Communications .....	143
9.2.1 Gaussian Beam Propagation Theory .....	143
9.2.2 Self-Imaging Technique for Freespace Link Design .....	147
9.2.3 Symmetric Link Design Methodology .....	153
9.2.4 Asymmetric Lasercom Link Design .....	159
9.3 Discussion and Considerations .....	166
9.4 Conclusion .....	171
References .....	172
CHAPTER 10: BROADBAND RECONFIGURABLE OPTICAL ADD-DROP FILTER FOR DENSE WAVELENGTH-DIVISION-MULTIPLEXING SYSTEMS .....	177
10.1 Introduction .....	178
10.2 OADF Architecture .....	179
10.2.1 LC Deflector Array Approach .....	181
10.2.2 TI DMD™ Approach .....	183
10.3 DMD™-based OADF Experiment .....	184
10.4 Discussion .....	197
10.5 Conclusion .....	199
References .....	200
APPENDIX A: THE PARAXIAL APPROXIMATION FOR A THIN LENS .....	204
References .....	208
APPENDIX B: POWER CAPTURED BY A THIN LENS WITH A GAUSSIAN BEAM INPUT .....	209
References .....	212
APPENDIX C: CHARACTERISTICS OF MERCK BL006 NEMATIC LIQUID CRYSTAL MIXTURE .....	213
References .....	215

## LIST OF FIGURES

Figure 1.1 The measured phase response of a typical NLC material (Merck BL006 at 20°C) with a 50 $\mu\text{m}$ cell thickness at $\lambda=1550\text{ nm}$ .	3
Figure 2.1. Traditional interface between a pixelated beamformer and an antenna front-end showing the fixed 1:1 mapping between optical phase shifter array and antenna array. Example shows a transmissive LC pixelated array device. Any other type of pixelated device can also be accommodated in this interface. MMF: Multimode Fiber.	11
Figure 2.2. Block Diagram of the Proposed Flexible Photonic Beamforming Concept for PAAs. BS: Beam Splitter. The dot (.) represents the s polarized beam while the transversal arrow ( $\Downarrow$ ) represents the p polarized beam.	12
Figure 2.3. The non-pixelated Hamamatsu LC-SLM structure.	14
Figure 2.4. Configuration for a flip-chip bonded optical head for a 6x6 elements phased array.	17
Figure 2.5. Configuration for a fiber remoted antenna array for a 6x6 elements phased array.	18
Figure 2.6. Experimental setup of the proposed flexible beamforming concept implemented using acousto-optics and nematic LC technology. $\nu$ : Optical Frequency; $f$ : Focal Length of Lens L; AOD: Acousto-optic Deflector; M: Mirror.	18
Figure 2.7. 140 MHz oscilloscope traces from the Flexible Beamformer: (a) in-phase, (b) $\pi/2$ , (c) $\pi$ , (d) $3\pi/2$ and (e) $2\pi$ radians phase shifted signals from the detectors. The top trace is from the reference detector whereas the bottom trace is the desired.	20
Figure 2.8. The measured RF phase shift data from the flexible beamformer showing $2\pi$ phase shift control versus the write laser ( $\lambda = 632.8\text{nm}$ ) intensity on the write SLM of the Hamamatsu device.	21
Figure 2.9. The very high count of 230,400 pixels of the write amplitude-mode LC device in the Hamamatsu LC device module gives “Flexible Beamforming” additional powers such as high resolution phase averaging and overall system fault-tolerance via the macro-pixel per RF phase shifter concept.	22
Figure 2.10. Examples of remoting head flexibility, (a) within the antenna array remoting head and (b) across multiple independently steered antenna array remoting heads.	23
Figure 3.1. Schematic Diagram of the proposed hybrid analog-digital VFODL realized as a Parallel N-Bit Digital-Analog Time Delay Unit. TL: Tunable Laser; M: Modulator; PD: Photodiode Detector; ROFs: Reflective Optical Fibers.	32
Fig. 3.2: Schematic Diagram of another version of the proposed VFODL realized as a Serial N-bit Digital-Analog Time Delay Unit. BL: Broadband Laser; M: Modulator; PD: Photodiode Detector; TF: Tunable Filter.	33
Fig. 3.3: Analog-only mode demonstrated VFODL operation demonstrating high resolution near continuous time delay over a 800 ps range using wavelength tuning from 1536 nm to 1560 nm.	39
Fig. 3.4: Proposed VFODL operations using the hybrid analog-digital mode. Top trace is the reference signal from the RF signal generator that is time aligned with the VFODL reference output for a $\lambda = 1536\text{ nm}$ and switch set to port 1. The bottom traces are the time delayed VFODL outputs for VFODL setting of (a) $\lambda = 1560.00\text{ nm}$ and switch active for port 1 (b) $\lambda = 1547.20\text{ nm}$ and switch active for port 2 (c) $\lambda = 1553.00\text{ nm}$ and switch active	

for port 2 (d) $\lambda = 1536.00$ nm and switch active for port 3 (e) $\lambda = 1542.00$ nm and switch active for port 32.....	42
Fig. 4.1. P-MOS Architecture.....	52
Fig. 4.2. Basic single voxel scan hardware of the P-MOS module. ....	53
Fig. 4.3. Output scanned beams from the demonstrated 8 point voxel scanner. (a) Incident; (b) x-deflected by 0.66 mrad; (c) y-deflected by 0.75 mrad and (d) z-scan (1.84m P-MOS focal length), beams. ....	56
Fig. 4.4. The demonstration of the P-MOS as a 2-bit digital lens. The four photos show the four focal length states of (a) infinity, (b) 3m, (c) 2m, and (d) 1.2m, of the P-MOS exit beam. The distance between the two lenses is 6.7cm.....	57
Fig. 5.1. Design of the proposed hybrid analog-digital coarse-fine scan P-MOS module for continuous 1-D scanning. PS: 90° Polarization Switch, W: Passive Crystal Prism; WNLC; Nematic Liquid Crystal Electrically Programmable Prism set for a given drive voltage. Shown are four possible 1-D scan beams produced by digital only switching of the PSs. ..	66
Fig. 5.2. Top views of the NLC prism used for continuous scan in P-MOS. NLC molecule orientations are shown for (a) zero control signal applied, (b) when a control signal is present that reorients the NLC molecules to induce a spatial prism-like refractive index change and (c) the interferogram of the NLC prism using a 1550 nm source. p: horizontally polarized light component.....	69
Fig. 5.3. Experimentally obtained far-field spot pattern for a basic 2-stage 1-D coarse-fine P-MOS demonstration at 1550 nm. ....	75
Fig. 5.4. (a). Proposed Biasing Technique for the NLC prism. (b-d): The effective NLC cell shape and beam deflections for a two stage P-MOS where one NLC prism and one birefringent crystal prism have been used as shown in Fig. 4.1. Shown are NLC device states when (b): drive signal is OFF, (c): switch is set to state A (i.e., when $V_A > V_B$ ), and (d): switch is in state B (i.e., when $V_B > V_A$ ). Dark spots along the Y-axis represent the far-field spots as produced by the shown NLC device state while the white spots represent the total scan spots possible including those from the alternative NLC device states.....	76
Fig. 5.5. Experimentally obtained far-field spot pattern for 4-stage 1-D coarse digital P-MOS demonstration at 1550nm. $\alpha_1 = -9.95^\circ$ , $\alpha_2 = 19.95^\circ$ , $\alpha_3 = 4.95^\circ$ and $\alpha_4 = 9.95^\circ$ using Rutile prisms ( $n_e = 2.454$ , $n_o = 2.71$ @ $\lambda = 1550$ nm). $\alpha$ : apex angle of prism.....	78
Fig. 5.6. Simulated steering angles for a 4-stage coarse and one stage fine 1-D digital P-MOS at 1550 nm that can continuously access any spot within a $40.92^\circ$ wide scan domain. $\alpha_{LC} = \pm 0.35^\circ$ , $\alpha_1 = -9.95^\circ$ , $\alpha_2 = 19.95^\circ$ , $\alpha_3 = 4.95^\circ$ and $\alpha_4 = 9.95^\circ$ using Rutile prisms ( $n_e = 2.454$ , $n_o = 2.71$ @ $\lambda = 1550$ nm).....	79
Fig. 5.7. Demonstration of continuous steering using NLC prism in the 4-stage coarse 1-D P-MOS scanner of Fig. 5.5. $\alpha_{NLC} = \pm 0.35^\circ$ (NLC: Merck BL006, $\Delta n = 0.229$ at 1550 nm and $25^\circ \text{C}$ , see Appendix C).....	80
Fig. 5.8. Experimentally measured scanner optical throughput variation for the 4-stage 1-D coarse digital P-MOS demonstration at 1550 nm. ....	83
Fig. 5.9. Experimentally obtained 2-D far-field spot pattern for 2-stage coarse and 2-stage fine P-MOS demonstration at 1550 nm. ....	83
Fig. 5.10. Experimentally obtained 3-D spot pattern for 2-stage coarse and 3-stage fine P-MOS demonstration at 1550 nm.....	84

Fig. 5.11. Experimentally measured rise time for the FLC PS used in P-MOS demonstration at 1550 nm. ....	84
Fig. 6.1. Top views of proposed NLC beam-spoiling VOA designs using (a) two fiber collimators and two NLC deflectors with orthogonal NLC directors, (b) a dual collimator and a single NLC deflector with 45° Faraday rotator-mirror pair, and (c) an optical circulator, single fiber collimator with a single NLC deflector and 45° Faraday rotator-mirror pair. $\lambda/4$ : Quarter wave plate. ....	93
Fig. 6.2. Top views of the NLC deflector used to realize the VOAs. NLC molecule orientations are shown for (a) zero control signal applied and (b) when a control signal is present that reorients the NLC molecules to induce a spatial wedge-like refractive index change. p: horizontally polarized light component. ....	94
Fig. 6.3. Measured optical attenuation as a function of (a) drive frequency and (b) voltage. p: horizontally polarized light component parallel to cell nematic director. s: vertically polarized light component normal to the device NLC director.....	101
Fig. 6.4. Proposed NLC deflector based 1x2 switch designs using (a) a single fiber collimator, two parallel aligned NLC deflectors, a half wave plate and a dual fiber collimator, and (b) a triple fiber collimator and a single NLC deflector in a reflective mode. ....	105
Fig. 7.1. Proposed Wavelength Tunable Variable Fiber-Optic Attenuator Using Liquid Crystal-Mirror Hybrid Controls. C: Optical Circulator; VBG: Volume Bragg Grating; M: Mirror. ....	114
Fig. 7.2. Proposed Wavelength Tunable Variable Fiber-Optic Attenuator operating as VOA for mirror M selected wavelength of 1560 nm and attenuation plots for 0 and 20 dB settings using NLC deflector driven at two different operating voltages. (Inset) Module operating as a VOA for the mirror M direction selected 1550 nm wavelength. ....	117
Fig. 7.3. Proposed Wavelength Tunable Variable Fiber-Optic Attenuator operating with precise fine wavelength selection using NLC deflector driven at three different operating states giving a 1.44 nm liquid crystal tuned fine wavelength range. ....	118
Fig. 8.1. Proposed No-Moving-Parts Axial Scanning Confocal Microscope using a LC lens. S: Spherical lens, Pp: Linear polarizer along horizontal or p-axis, BS: Beam Splitter, MO1/ MO2/ MO3: Micro-Objective (MO) lenses.....	125
Fig. 8.2. Plots showing measured 3.1 $\mu\text{m}$ 3-dB axial resolution of the demonstrated ASCM with and without the LC lens inserted into the sample path. ....	128
Fig. 8.3. (a) Setup for measuring the ASCM imaging capability and (b) SEM image of the test sample. ....	129
Fig. 8.4. ASCM line-scanned optical intensity plots obtained for the InP waveguides sample. ....	130
Fig. 8.5. ASCM line-scanned analog optical intensity plots obtained for the InP waveguides sample corresponding to Fig. 8.4. ....	131
Fig. 8.6. Demonstrated LC lens-based ASCM classic 3-dB confocal resolution limited axial scanning transfer characteristics as a function of the LC lens drive frequency.....	132
Fig. 8.7. Super-fine axial scanning resolution transfer characteristics of the demonstrated LC lens-based ASCM. ....	133
Fig. 9.1: Gaussian beam propagation through a thin lens. S: Spherical thin lens.....	143
Fig. 9.2. Output beam waist location $x'$ from the thin lens and the output beam waist $w_2$ as functions of the thin lens focal length $f$ for an input beam waist $w_1$ of 0.25 mm, $\lambda=1.55 \mu\text{m}$ and $x=0$ . ....	145

Fig. 9.3. Configuration of a typical lasercom link. ....	147
Fig. 9.4. Gaussian beam through a pair of thin lenses in a self-imaging configuration. ....	148
Fig. 9.5. Beam waist location $x'$ from the thin lens S1 as a function of the S1 lens focal length $f$ for an input beam waist $w_1$ of 2 m, 3 m, 4 m and 5 m at $\lambda=1.55 \mu\text{m}$ and $x=0$ .....	149
Fig. 9.6. Beam waist location $x'$ from the thin lens as a function of the lens focal length $f$ for different wavelengths and an input beam waist of 4 m with $x$ being 0.....	150
Fig. 9.7. Proposed beamforming optic T for the TX implementing a low loss link using the self-imaging mechanism. The optic T consists of a strong thin lens S1 of a short focal length $f$ and a weak thin lens PL of a long focal length $x'$ . The PL can also be an ultra-thin electronically programmable thin lens. The distance between S1 and PL is $f$ , where $f$ is the focal length of S1. S1 is placed $f$ away from the laser source. ....	152
Fig. 9.8. Proposed low loss symmetric lasercom link design using strong (S1, S2) and weak (PL1, PL2) thin lens combinations for Gaussian beam propagation through freespace. $f_{S_1} = f_{S_2}$ and $f_{PL_1} = f_{PL_2}$ for the symmetric design. ....	153
Fig. 9.9. Flow chart for determining the various parameters of a low loss lasercom system given the Link length $L$ , the possible variation in link length $\Delta L$ , and operating wavelength $\lambda$ ..	155
Fig. 9.10. An approach to realize a large programmable optic. (a) Piston-type single pixels in an $N \times N$ array forming a large programmable optic. Gray-scale corresponds to phase: Black=Large phase, White=Small phase. (b) The corresponding staggered phase profile for a weak thin lens. Phase represented in Figure is not to scale. ....	159
Fig. 9.11. Proposed low loss asymmetric lasercom link design using strong (STX, SRX) and weak (PLTX, PLRX) thin lens combinations for Gaussian beam propagation through freespace. Note: $f_{STX} \neq f_{SRX}$ and $f_{PLTX} \neq f_{PLRX}$ due to the asymmetric design. ....	160
Fig. 9.12. Flow chart for determining the various parameters of an asymmetric low loss lasercom link given the Link length $L$ , the possible variation in link length $\Delta L$ , the TX or RX aperture and operating wavelength $\lambda$ . ....	163
Fig. 9.13. Proposed full-duplex transceiver structure for the low loss lasercom link using beam splitting optics. BS: Beam Splitter, PD: Photo-detector. ....	168
Fig. 10.1. Proposed OADF optical structure.....	181
Fig. 10.2. Proposed LC Deflector array design for the OADF. QWP: Quarter Wave Plate, LC: Liquid Crystal, ITO: Indium Tin Oxide, $\lambda$ : wavelength, AR: Anti-Reflection coating. ....	182
Fig. 10.3. Proposed OADF operation ray traces for (a) DMD <sup>TM</sup> set to $+\theta$ for Main-In to Main-Out setting and (b) DMD <sup>TM</sup> set to $-\theta$ for Add to Drop operations. (c) Modified OADF design using a fixed mirror that transforms the OADF to a multiwavelength $2 \times 2$ full reversible switch. ....	184
Fig. 10.4. Measured insertion loss for the OADF. (a) Insertion loss for the Main-In-to-Main-Out port configuration for the whole C-band and (b) a closer look at the insertion loss in a narrow wavelength band, and (c) Insertion loss for the Main-In-to-Drop/Add-to-Main-Out port in a narrow wavelength band.....	188
Fig. 10.5. (a) TI DMD <sup>TM</sup> geometry showing the active spectrum processing zone and (b) the micromirror pixel layout. A dark colored vertical micromirror array represents one column of micromirrors as controlled by the DMD <sup>TM</sup> software.....	189



Fig. 10.6. Measured resolutions of the OADF using a 5 mm diameter GRIN collimator. These resolution values for the 3-dB, 20-dB and 30-dB points are measured to be 1 nm, 1.6 nm and 1.8 nm, respectively. ....	190
Fig. 10.7. Measured resolutions of the OADF using a 1 cm diameter GRIN collimator. These resolution values for the 3-dB, 20-dB and 30-dB points are measured to be 0.41 nm, 0.55 nm and 0.7 nm, respectively. ....	191
Fig. 10.8. 0.8 nm (100 GHz) DWDM spacing C-Band operation of the OADF (a) The EDFA source input to the OADF and the retro-reflected spectrum on the Main-Out port. (b) The dropped channel on the Drop port, and (c) using a tunable laser diode, a new channel is added through the Add port demonstrating the ADD operation. ....	193
Fig. 10.9. A visible light photograph of the DMD™ chip showing the active spectrum processing zone. ....	194
Fig. 10.10. Measured wavelength resolution of the OADF by flipping a single micromirror column from + $\theta$ orientation to - $\theta$ orientation and then translating it by one micromirror location. ....	196
Fig. A.1: Geometry for the thin lens Paraxial approximation. ....	207
Fig. A.2: Plot of the thin lens expression obeying the Paraxial approximation and plot of the exact expression for a plano-convex lens. ....	208
Fig. B.1. Encircled Power in a Gaussian beam as a function of the normalized radius of the thin lens. The thin lens radius $r$ is normalized with respect to the incident beam $\frac{1}{e^2}$ radius $w$ . ....	211

## LIST OF TABLES

Table 2.1: Example of optical remoting head design. ....	25
Table 3.1: Demonstrated VFODL design and delays. ....	43
Table 6.1. VOA Design Parameters v/s Obtained Beam Spoiling Parameters. t: NLC deflector cell thickness; D: NLC deflector cell aperture; d: GRIN lens beam waist distance from GRIN lens exit aperture, $\theta_w$ : NLC deflector maximum deflection angle, $\theta_e$ : maximum freespace exit angle from the NLC deflector, and $x_0$ : maximum offset error due to angular deflection.....	106
Table 9.1. Key parameters for several types of symmetrical laser communication links. SMF: Single Mode Fiber.....	169
Table 10.1. Comparison of 1-D LC deflector array approach with the TI 2-D DMD <sup>TM</sup> approach. ....	199

## LIST OF JOURNAL PUBLICATIONS

1. N. A. Riza and S. A. Khan, "Programmable High-Speed Polarization Multiplexed Optical Scanner," *Optics Letters*, Vol. 28, No. 7, Page 561-563, April 1, 2003.
2. N. A. Riza, S. A. Khan, and M. A. Arain, "Flexible Beamforming for Optically Controlled Phased Array Antennas," *Optics Communications*, Vol. 227, Page 301-310, Nov. 2003.
3. N. A. Riza, M. A. Arain, and S. A. Khan, "Hybrid Analog-Digital Variable Fiber-Optic Delay Line," *Journal of Lightwave Technology*, Vol. 22, No. 2, Page 619-624, Feb. 2004.
4. S. A. Khan and N. A. Riza, "Demonstration of 3-Dimensional Wide Angle Laser Beam Scanner using Liquid Crystals," *Optics Express*, Vol. 12, Issue 5, Pages 868-882, March 2004.
5. N. A. Riza and S. A. Khan, "Liquid-Crystal-Deflector Based Variable Fiber-Optic Attenuator," *Applied Optics*, Vol. 43, Issue 17, Page 3449-3455, June 2004.
6. N. A. Riza and S. A. Khan, "Wavelength Tunable Variable Fiber-Optic Attenuator Using Liquid Crystal-Mirror Hybrid Controls," *IEEE Photonics Technology Letters*, Vol. 17, Issue 3, Page 621-623, March 2005.
7. N. A. Riza and S. A. Khan, "Ultra-Low Loss Laser Communications Technique using Smart Beamforming Optics," Available online 19 August 2005, *Optics Communications*.
8. S. A. Khan and N. A. Riza, "Demonstration of a Broadband Reconfigurable Optical Add-Drop Filter for Dense Wavelength-Division-Multiplexing Systems using MEMS Digital Micromirror Device," Accepted for publication in *Journal of Lightwave Technology*.
9. S. A. Khan and N. A. Riza, "No-Moving-Parts Axial Scanning Confocal Microscopy," Submitted for publication.

## **LIST OF CONFERENCE PUBLICATIONS**

1. Z. Yaqoob, S. A. Khan, and N. A. Riza, "Microwave and Optical Beam Control using JOP Devices," US – Japan Joint Optoelectronics Project (JOP) Participant's Workshop, Maui HI, USA, April 19-20, 2001.
2. N. A. Riza and S. A. Khan, "Photonic beamformer with flexible interface for phased array antennas," The 14th Annual Meeting of the IEEE Lasers and Electro-Optics Society, Vol. 2 , Page 816 -817, Nov. 12-13, 2001.
3. N. A. Riza, S. A. Khan, and M. A. Arain, "Flexible beamformer and remoting head for optically controlled phased array antennas," IEEE MTT-S International Microwave Symposium Digest, Vol. 3, Page 1941-1944, June 2-7, 2002.
4. N. A. Riza and S. A. Khan, "PMOS: Polarization Multiplexed Optical Scanner," The 86<sup>th</sup> Annual Meeting of the Optical Society of America, Orlando FL, USA, Sep. 29 - Oct. 3, 2002.
5. N. A. Riza and S. A. Khan, "Fully programmable high speed polarization multiplexed optical scanner," The 15th Annual Meeting of the IEEE Lasers and Electro-Optics Society, Vol. 2 , Page 453 -454, Glasgow, Scotland, Nov. 10-14, 2002.
6. S. A. Khan and N. A. Riza, "High Speed Polarization Multiplexed Optical Scanner for Three Dimensional Scanning Applications," SPIE Annual Meeting 2003, Vol. 5160, Page 204-207, Free-Space Laser Communication and Active Laser Illumination III; David G. Voelz, Jennifer C. Ricklin; Eds., Aug. 3–8, 2003, San Diego, CA.
7. S. A. Khan and N. A. Riza, "High Speed Coarse-Fine Laser Beam Steering Module for Polarization-Multiplexed Optical Scanner," The 16th Annual Meeting of the IEEE Lasers

and Electro-Optics Society, Vol. 1, Page 11-12, Oct. 27-28, 2003, Tucson, AZ. Digital Object Identifier 10.1109/LEOS.2003.1251576.

8. S. A. Khan and N. A. Riza, "High Resolution Broadband Variable Fiber-Optic Attenuator using Liquid Crystals," Optics in the Southeast (OISE), Organized by School of Optics/CREOL University of Central Florida, SPIE and Optical Society of America, Orlando, FL, Nov. 12–13, 2003.
9. S. A. Khan and N. A. Riza, "Confocal microscopy based agile optical endoscope using liquid crystals," Biophotonics/Optical Interconnects and VLSI Photonics/WBM Microcavities, 2004 Digest of the IEEE LEOS Summer Topical Meetings Page 10-11, June 28-30, 2004, San Diego, CA. Digital Object Identifier: 10.1109/LEOSST.2004.1338654.
10. S. A. Khan and N. A. Riza, "Demonstration of 3-Dimensional Wide Angle No-Moving Parts Laser Beam Steering," SPIE Annual Meeting 2004, Vol. 5550, Page 47-59, Free-Space Laser Communications IV; Jennifer C. Ricklin, David G. Voelz; Eds., August 2-6, 2004, Denver, CO.
11. S. A. Khan and N. A. Riza, "Wavelength Tunable and Broadband Variable Fiber-Optic Attenuators using Liquid Crystals," SPIE Defense & Security Symposium 2005, Orlando, FL, 28 March-1 April 2005.

## CHAPTER 1: INTRODUCTION

Liquid crystals (LCs) are materials in which there exists a certain order in the arrangement of molecules. As a result there is anisotropy in the electrical and optical properties.<sup>1</sup> LCs combine the properties of solids and isotropic liquids and exhibit electro-optical phenomenon, which has led to their use in a vast variety of applications including optical switching,<sup>2</sup> attenuators,<sup>3</sup> displays,<sup>4</sup> and spatial light modulators.<sup>5-7</sup> The basis of majority of these applications lies in the reorientation of the director (the axis of preferred orientation of the molecules) in the macroscopic volume of the material under the influence of an externally applied field. The extent of this reorientation is controlled by the anisotropy of the electrical and visco-elastic properties of the LC as well as on the initial orientation of the director. The optical properties of the medium, e.g., the LC material optical anisotropy is changed as a result of this reorientation meaning that light polarized along the initial molecular director orientation will see an index that can be controlled by varying the externally applied electric field. The extent of the electric field strength required to reorient the molecular director is small compared to that required in bulk crystals such as Lithium Niobate. This makes LCs suitable candidates for use in light modulation schemes, not to mention their compactness and low drive power requirement. In this dissertation, we propose and demonstrate novel applications of LCs such as for optically controlled phased array antennas, freespace optical scanners, variable optical attenuators, low loss freespace laser communication, 3-D and biomedical imaging. In the following chapters we touch upon each of these topics in detail.

At the heart of the applications demonstrated in this thesis are LC devices that are non-pixelated and can be controlled either electrically or optically. Instead of the typical pixel-by-

pixel control as is custom in LC devices, the phase profile across the aperture of these novel LC devices is varied through the use of high impedance layers. Due to the presence of the high impedance layer, there forms a voltage gradient across the aperture of such a device which results in a phase gradient across the LC layer which in turn is accumulated by the optical beam traversing through this LC device. The geometry of the electrical contacts that are used to apply the external voltage will define the nature of the phase gradient present across the optical beam. In order to steer a laser beam in one angular dimension, straight line electrical contacts are used to form a one dimensional phase gradient while an annular electrical contact results in a circularly symmetric phase profile across the optical beam making it suitable for focusing the optical beam. The geometry of the electrical contacts alone is not sufficient to form the linear and the quadratic phase profiles that are required to either deflect or focus an optical beam. Figure 1.1 shows the measured phase response in number of waves of a typical nematic liquid crystal (NLC) material (Merck BL006 at 20°C) with a 50  $\mu\text{m}$  cell thickness at  $\lambda=1550$  nm (see Appendix C). After the drive voltage has crossed a certain threshold, the phase response results in a linear phase change with respect to the drive voltage. The phase response changes into a quadratic curve as the voltage is further increased beyond the linear range. Clever use of the phase response of an NLC material is made in this thesis such that the low voltage linear response region is used for the angular beam deflection while the high voltage quadratic response region is used for focusing the beam.

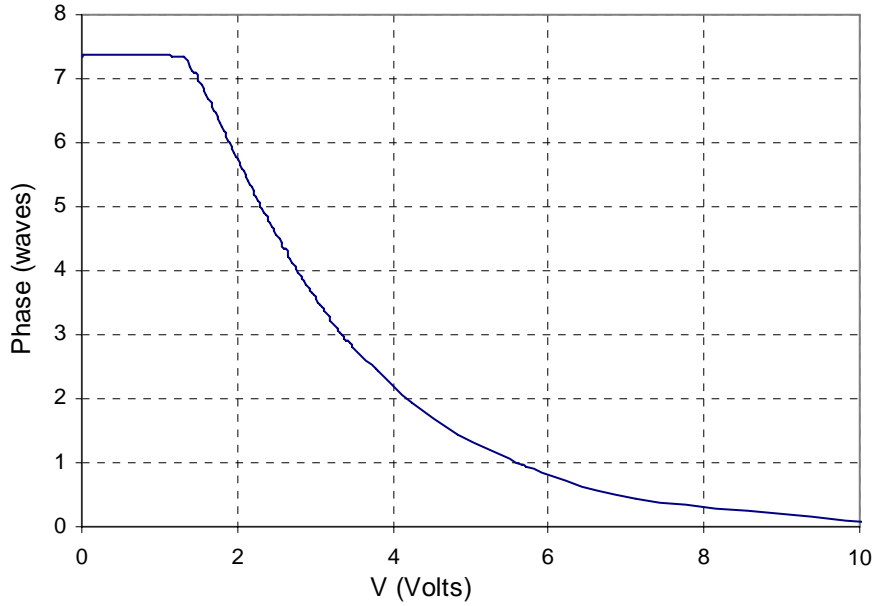


Figure 1.1 The measured phase response in number of waves of a typical NLC material (Merck BL006 at 20°C) with a 50  $\mu\text{m}$  cell thickness at  $\lambda=1550$  nm.

### Organization of Thesis

Chapter 2 proposes and demonstrates a unique photonic beamformer for phased array antennas in broadcast mode wireless communications. The system enables flexible antenna array upgrades via software and flexible front-head attachments. This array controller capability leads to user defined changes in number of antenna elements, antenna aperture shape, antenna aperture size and antenna carrier frequency. Experimental proof-of-concept flexible beamforming results are described that generate the desired set of phase shifted radio frequency signals. The flexible beamformer is particularly suited for generating multiple broadcast antenna beams.



In chapter 3 a variable fiber optic delay line (VFODL) is introduced that, to the best of our knowledge, is the first time that a hybrid analog-digital VFODL is proposed to solve the dilemma of efficiently enabling many settable and long duration time delays together with continuous and short time delays. In essence, this VFODL can provide near continuous high resolution time generation across an entire long time delay band. The VFODL is based on the concept of cascaded wavelength sensitive and wavelength insensitive time delays. A proof of concept VFODL built demonstrates near continuous 0.5 ps resolution time delay control across an entire 25.6 ns time delay band generating a total of 51,200 measurable time delay bins. The experimental VFODL also gives a 4.95 dB total optical loss and a 1ms time delay control setting speed. The proposed VFODL can be used in applications such as radio frequency (RF) photonic signal processing and radar testing.

In chapter 4, a Fast digital-analog control polarization-based optical scanner is presented with three-dimensional beamforming programmability. Features include low power consumption and large aperture liquid crystal-based optics, digital repeatability, and time multiplexed accurate analog beamforming. Analog frequency and amplitude control of the nematic liquid crystal beamformer cells allows continuous fine scan programmability over a 0.66 mrad horizontal-deflection, 0.75 mrad vertical deflection, and an infinity to 1.84 m focal length longitudinal scan. First time demonstrations include an 8-point volumetric scan and a 2-bit digital lens scan, both at 1310 nm, with a 35  $\mu$ s random-access time.

Chapter 5 presents an extension of our work on Polarization Multiplexed Optical Scanner. Design and demonstration of a versatile liquid crystal-based scanner is shown for steering a laser beam in three dimensions. The scanner consists of a unique combination of digital and analog control polarization-based beamforming optics resulting in both continuous

and random fashion beam steering. The design features a novel device biasing method, large aperture beamforming optics, low electrical power consumption, and ultra-fine as well as wide angle coarse beam steering. Demonstrations include one, two and three dimensional beam steering with a maximum of  $40.92^\circ$  continuous scan, all at 1550 nm. The minimum scanner aperture is 1 cm diameter and uses a combination of ferroelectric and nematic liquid crystals in addition to Rutile crystal birefringent prisms.

Chapter 6 demonstrates a compact, low component count, no-moving parts Variable Optical Attenuator (VOA) using beam spoiling implemented via an electrically reconfigurable non-pixelated Nematic Liquid Crystal (NLC) deflector. The VOA design features an in-line alignment polarization insensitive design without the use of bulky polarization splitting and combining optics. The proof-of-concept VOA at 1550 nm demonstrates 30 dB attenuation range, 2.5 dB insertion loss,  $\leq 0.8$  dB polarization dependent loss (PDL) and a 1 second maximum attenuation reset time. The VOA design can counter performance reducing environmental effects such as excess loss increase due to temperature variations.

Chapter 7 presents an extension of our VOA work described in chapter 6. A fiber optic module is proposed using a hybrid liquid crystal-mirror mechanics beam control mechanism that provides the dual functions of optical attenuation controls and wavelength selection with a high degree of sensitivity, all within one compact in-line module. Experimental module uses a liquid crystal deflector and a mechanically tuned bulk mirror as the hybrid optics. The module demonstrates a 1520-1570 nm coarse tuning range, a 1.44 nm fine tuning range, a  $>30$  dB attenuation range, a 3.7 dB optical insertion loss,  $< 0.1$  dB polarization dependent loss, and a Full Width Half-Maximum (FWHM) wavelength resolution of  $\leq 0.3$  nm. Module applications include tunable gain controlled optical transmitters and receivers.

In Chapter 8, for the first time, to the best of our knowledge, a no-moving-parts axial scanning confocal microscope (ASCM) system is designed and demonstrated using a combination of a large diameter liquid crystal (LC) lens and a classical microscope objective lens. By electrically controlling the 5 mm diameter LC lens, the 633 nm wavelength focal spot is moved continuously over a 48  $\mu\text{m}$  range with a measured 3-dB axial resolution of 3.1  $\mu\text{m}$  using a 0.65 numerical aperture (NA) micro-objective lens. The ASCM is successfully used to image an Indium Phosphide (InP) twin square optical waveguide sample with a 10.2  $\mu\text{m}$  waveguide pitch and 2.3  $\mu\text{m}$  height and width. Using fine analog electrical control of the LC lens, a super-fine sub-wavelength axial resolution of 270 nm is demonstrated. The proposed ASCM can be useful in various precision three dimensional (3-D) imaging and profiling applications.

In chapter 9 theory and design is presented for a technique for ultra-low loss laser communication that uses a combination of strong and weak thin lens optics, hence obeying the paraxial approximation. As opposed to conventional laser communication systems, the Gaussian laser beam is prevented from diverging at the receiving station by using a weak thin lens that places the transmitted beam waist mid-way between a symmetrical transmitter-receiver link design. The weak lens can be a fixed optic for static link distances or programmable for mobile scenarios. The programmable weak optic can be a single pixel or multi-pixel lens made by LC or mirror technologies. The proposed link design is appropriate for low air turbulence links such as short-range or indoor links and space based links.

For comparison with LC technology, in chapter, 10 we demonstrate an optimized optical add-drop filter (OADF) for dense wavelength-division-multiplexing (DWDM) systems using the Texas Instruments (TI) micro-electro-mechanical systems (MEMS) digital micromirror device (DMD)<sup>TM</sup>. This OADF features a polarization insensitive fault tolerant broadband operation, low

loss, and the ability to selectively add/drop with high wavelength resolution multiple channels in C telecommunications band. The proof-of-concept OADF designed for the C band demonstrates low insertion loss, 0.15 dB polarization dependent loss (PDL), 3-dB wavelength resolution of 0.4 nm and an average crosstalk of better than 30 dB. With the use of a reference mirror, the OADF becomes a multi-wavelength 2 x 2 routing switch. An analysis of the MEMS and LC approaches is conducted to summarize this chapter.

## References

1. L. M. Blinov, *Electro-optical and magneto-optical properties of liquid crystals*, (John Wiley & Sons Ltd., 1983).
2. R. A. Soref, "Liquid-crystal fiber-optic switch," *Optics Letters*, Vol. 4, Issue 5, Pages 155-157, May 1979.
3. E. G. Hanson, "Polarization-independent liquid-crystal optical attenuator for fiber-optics applications," *Applied Optics*, Vol. 21, Issue 7, Pages 1342-1344, April 1982.
4. E. Lueder, *Liquid Crystal Displays*, (John Wiley & Sons Ltd., 2001).
5. U. Efron, *Spatial Light Modulator Technology*, (Marcel Dekker, 1995).
6. I. C. Khoo and S. T. Wu, *Optics and nonlinear optics of liquid crystals*, (World Scientific, Singapore, 1993).
7. S. T. Wu and D. K. Yang, *Reflective liquid crystal displays*, (Wiley, New York, 2001).

## **CHAPTER 2: LIQUID CRYSTALS BASED FLEXIBLE BEAMFORMING FOR OPTICALLY CONTROLLED PHASED ARRAY ANTENNAS**

Unique photonic beamformer and remoting head for phased array antennas in broadcast mode wireless communications is proposed that enables flexible antenna array upgrades via software and flexible front-head attachments. This array controller capability leads to user defined changes in number of antenna elements, antenna aperture shape, antenna aperture size and antenna carrier frequency. Experimental proof-of-concept flexible beamforming results are described that generate the desired set of phase shifted radio frequency signals. The flexible beamformer is particularly suited for generating multiple broadcast antenna beams.

### 2.1 Introduction

With the growth in demand for high bandwidth communication services, phased array antennas (PAAs) are becoming an attractive choice for broadcasting multiple radio frequency (rf) beams such as in programmable satellite television distribution. Moreover, the alternative of a moving antenna in a spacecraft can result in vibrations and momentum due to movement that can produce an undesired change in the spacecraft speed and direction. In the last decade, research has been carried for PAA control using optical techniques.<sup>1</sup> In particular, liquid crystal (LC) technology has shown promise for phased array control.<sup>25</sup> Previously reported PAA optical control designs utilized pixelated, electrically addressed, LC devices to generate RF beam steering information. In such systems, number and size of individual LC pixels dictated the size of the optical head and in turn the number of elements in the antenna array. Such an approach

poses strict limitations on the antenna upgradeability in terms of number of elements in the antenna array. An effort to change the number of elements in the antenna array would require replacement of the existing LC devices in the beamformer with the ones having the proper number of pixels. This will require a new optical head, not to mention the changes to the beamformer controller system in order to match the new LC device size. Furthermore, pixelation causes diffraction with light from one pixel leaking into a detector or fiber collimator placed in front of an adjacent pixel, consequently sending wrong phase information to the corresponding antenna element.

It would be highly beneficial to develop a photonic beamforming approach where all aspects of the antenna control are flexible; namely, choice of antenna carrier frequency, number of RF phase/time delay shifters in the beamformer, and number and spatial distribution of the light sampling elements in the optical-to-RF interface remoting head. Recently we proposed such a unique flexible photonic beamforming concept.<sup>6,7</sup> In this work, the flexible beamforming concept is demonstrated using a compact system and experimental results are validated. With the proposed design, a PAA system will become upgradeable without requiring major hardware changes, thus expediting the use of smart PAAs in the wireless arena.

## 2.2 Flexible Beamforming Architecture

Fig. 2.1 shows the classic generalized 1:1 mapping between a pixelated spatial light modulator (SLM)-based beamformer and the antenna array front-end. This approach to

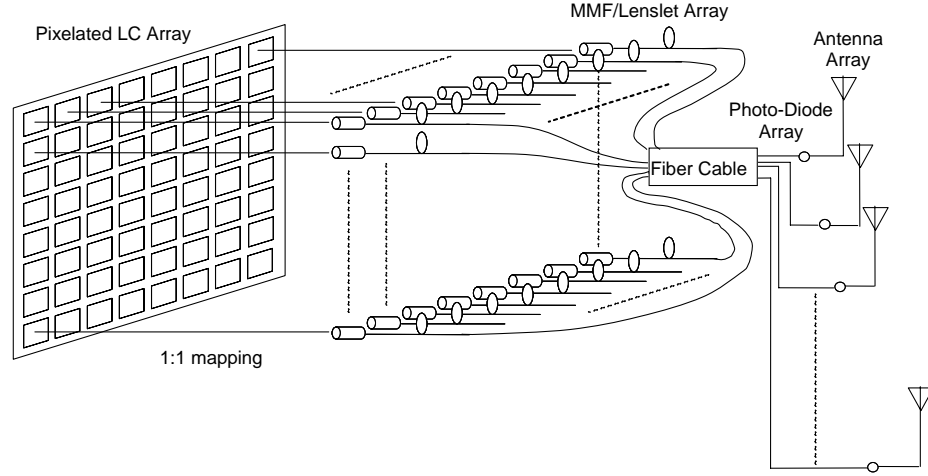


Figure 2.1. Traditional interface between a pixelated beamformer and an antenna front-end showing the fixed 1:1 mapping between optical phase shifter array and antenna array. Example shows a transmissive LC pixelated array device. Any other type of pixelated device can also be accommodated in this interface. MMF: Multimode Fiber.

beamforming causes several PAA system limitations that includes (a) fixing the number of antenna elements, (b) system loss and inter-fiber crosstalk due to pixel-based diffraction, (c) no system flexibility via fixed precision area mapping between pixel array and fiber-lens array, and (d) zero tolerance to fiber array fabrication errors and assembly misalignments. In addition, if direct interfacing of beamformer output light to the joint photodetector array-RF antenna array chip is used, the pixelated beamformer fixes the antenna aperture size, shape and number of antenna elements. In particular, this limitation is severe on multi-aperture antenna systems where no flexibility is left for system designers.



Fig. 2.2 shows a schematic of the proposed flexible beamforming approach involving three flexible sub-systems, namely:

- I. Flexible RF Carrier Generation,
- II. Flexible Beamformer, and
- III. Flexible Antenna Head

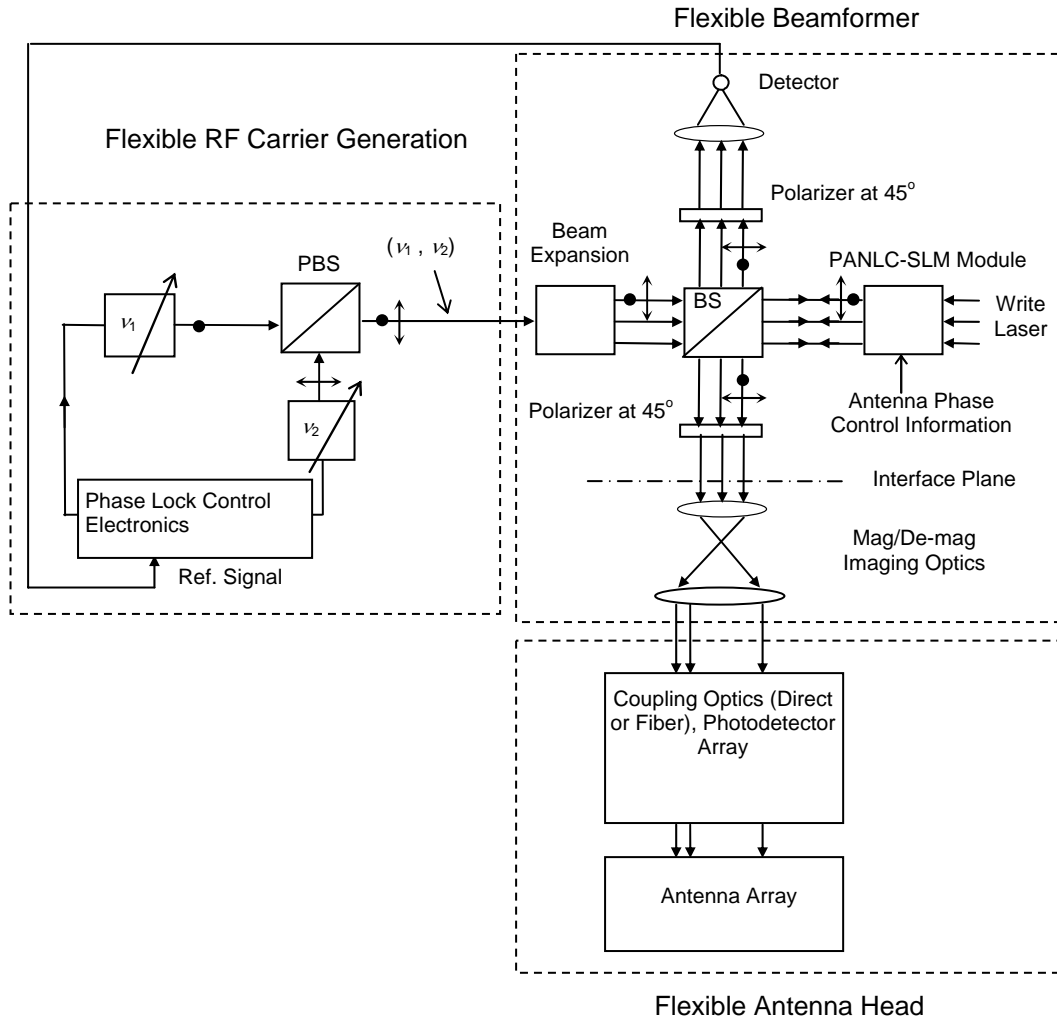


Figure 2.2. Block Diagram of the Proposed Flexible Photonic Beamforming Concept for PAAs.

BS: Beam Splitter. The dot (.) represents the s polarized beam while the transversal arrow ( $\uparrow$ ) represents the p polarized beam.

The carrier generation system is based on well known heterodyne mixing and is flexible as tuning of the phase-locked lasers can generate any desired RF from DC to 200 GHz.<sup>8</sup> As shown in Fig. 2.2, this design setup utilizes two laser sources with slightly different frequencies  $\nu_1$  and  $\nu_2$  (or angular frequencies of  $\omega_1$  and  $\omega_2$ ) that are phase locked with each other. Note that the dot (.) represents the  $s$  polarized beam while the transversal double arrow ( $\Updownarrow$ ) represents the  $p$  polarized beam. A beam splitter (BS) is used to split the incoming  $s$  and  $p$  polarized collinear light beams into two parts. Part of light from the BS is used to generate the reference signal (top) for phase-locking whereas the rest of light goes straight to the beamforming sub-system. For simplicity, the analog/digital data modulation optics in this subsystem is not shown in Fig. 2.2, although can be added via either optical phase modulation of one of the lasers or amplitude modulation of the beam pair.

As an example, the design in Fig. 2.2 utilizes LC technology for realizing the flexible beamformer sub-system. Specifically, an optically addressed, non-pixelated, reflective Parallel Aligned Nematic Liquid Crystal (PANLC) SLM module is used as the film-like non-pixelated flexible phase shifter array to realize the desired flexible photonic beamformer. The Hamamatsu PANLC-SLM device consists of two SLMs, one transmissive and the other reflective (see Fig. 2.3).<sup>9</sup> As the name, Parallel Aligned Nematic Liquid Crystal, suggests, both the SLMs are parallel rubbed nematic liquid crystal (NLC) devices. The transmissive SLM is pixelated while the reflective SLM is non-pixelated. The transmissive SLM is a high space-bandwidth product (e.g., half a million pixels) electrically addressed, amplitude mode device, or to put it simply, an optically generated phase based image former. A computer generated spatial intensity pattern (in grey-scale) that corresponds to the desired PAA phase map (e.g. black: 0 phase, white:  $2\pi$  phase) is written on this transmissive SLM via computer control. A HeNe laser beam at 632.8nm with a

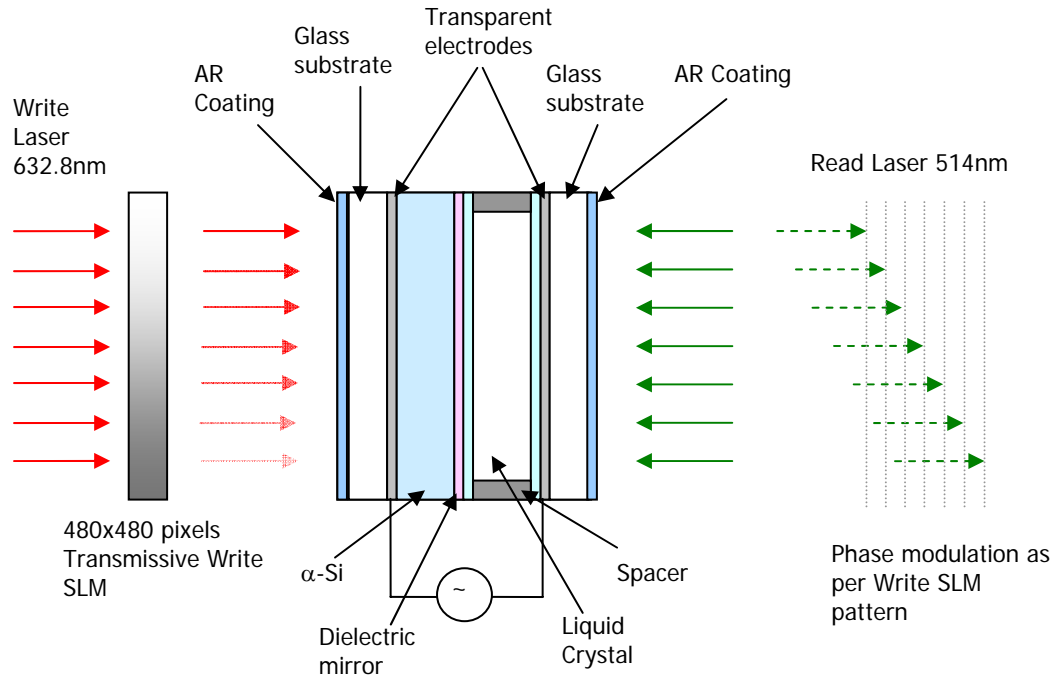


Figure 2.3. The non-pixelated Hamamatsu LC-SLM structure.

uniform irradiance is incident on this transmissive SLM. Hence, after traversing this SLM, the laser beam gets intensity modulated (hereafter called the Write beam) in the spatial domain. The two SLMs are coupled using a 1:1 imaging system (not shown in Fig. 2.3). The non-pixelated, reflective SLM is slightly different from an ordinary liquid crystal cell in that between one transparent electrode and the liquid crystal, there is sandwiched a layer of photo-sensitive amorphous silicon. As the intensity of the write beam is increased by controlling the transmissive SLM intensity pattern from the control computer, the impedance of the amorphous silicon layer decreases (and vice versa), causing a high electric field to be applied across the reflective SLM. A high E-field applied across a parallel rub NLC causes the molecules to lie along the E-field

direction. Thus, the NLC birefringence can be controlled by varying the grey-scale intensity pattern generated by the computer.

The SLM write light carries the required RF phase information image that is embedded via a high space bandwidth product (e.g., half a million pixels) electrically addressed, amplitude mode pixelated, transmissive LC SLM or an optically generated image former. The reflective non-pixelated SLM structure is critical to the approach in realizing a flexible interface between the RF front-end and the photonic beamformer. Because the SLM is film-like, essentially any desired spatial phase shifter structure can be generated via software leading to a truly flexible interface between the antenna elements and the beamformer. With reference to the known PANLC-SLM device, one of the two incident polarizations on the read side of the SLM picks up the desired phase information written from the write side of the SLM.<sup>9</sup>

The two orthogonally polarized beams incident on the pixel free reflective SLM can be expressed as

$$\begin{aligned} E_x(t) &= Ae^{j(2\pi\nu_1 t)} \\ E_y(t) &= Ae^{j(2\pi\nu_2 t + \alpha)} \end{aligned}$$

where A is the field amplitude,  $\nu_1$  and  $\nu_2$  are phase-locked optical frequencies,  $\alpha$  is the fixed relative phase shift, and x and y are the Cartesian coordinates of the two orthogonal polarization direction vectors. Based on the direction of the nematic director of the SLM (either x or y), the appropriate optical field (Either  $E_x$  or  $E_y$ ) acquires a SLM programmed phase shift  $\phi(x, y)$ . For instance, for a nematic director in the y-direction,

$E_x(t) = Ae^{j[2\pi\nu_1 t + \alpha + 2\frac{\pi}{\lambda_1} n_o 2d]}$  and  $E_y(x, y, t) = Ae^{j[2\pi\nu_2 t + \alpha + \phi(x, y)]}$ , where  $n_o$  is the ordinary index of refraction of the NLC material, d is the SLM NLC layer thickness, and  $\lambda_1$  and  $\lambda_2$  are the optical

wavelengths of the fields at frequencies  $\nu_1$  and  $\nu_2$  respectively. Also the SLM programmed optical phase shift at  $(x, y)$  SLM location is given as  $\phi(x, y) = \frac{2\pi}{\lambda_2} n_e[I(x, y)] \cdot 2d$  where  $n_e[I(x, y)]$  is the refractive index induced on the  $(x, y)$  SLM location via write light optical intensity  $I(x, y)$ . The combined optical field corresponding to the SLM phase modulation at the  $x, y$  coordinates after the 50:50 BS and the  $45^\circ$  combining polarizer is given by

$$E(x, y, t) = \frac{A}{2} [E_x + E_y]$$

The photo-current generated by the phase-detector that samples the SLM optical phase modulated location  $(x, y)$  is given by

$$\begin{aligned} i(x, y, t) &= |E(x, y, t)|^2 \\ &= \left| \frac{A}{2} \{ e^{j(2\pi\nu_1 t)} + e^{j[2\pi\nu_2 t + \alpha + \theta(x, y)]} \} \right|^2 \\ &= \frac{|A|^2}{4} [1 + 1 + 2 \cos[2\pi(\nu_1 - \nu_2)t + \alpha + \theta(x, y)]] \\ &= \frac{|A|^2}{4} [1 + 1 + 2 \cos[2\pi(\nu_1 - \nu_2)t + \alpha + \theta(x, y)]] \\ i(x, y, t) &= \frac{|A|^2}{2} [1 + \cos[2\pi(\nu_1 - \nu_2)t + \alpha + \theta(x, y)]] \end{aligned}$$

Hence the photocurrent produced contains the appropriate antenna carrier frequency  $\nu_1 - \nu_2$

and the PAA element phase shift  $\theta(x, y) = 4\pi \left[ \frac{n_o}{\lambda_1} - \frac{n_e[I(x, y)]}{\lambda_2} \right] d$  required for antenna control.

The third flexible subsystem is the antenna interface sub-system that is antenna dependent. This plug-in plug-out subsystem contains an optical interconnection system that matches and maps the antenna array to the read SLM face. This optical interconnection can be of

the direct type where a photodetector array chip is flip-chip bonded to the RF antenna array chip (see Fig. 2.4). Another interconnection is of the indirect kind where a multi-mode fiber (MMF) or lenslet array chip is interfaced via optical fibers to the given antenna array (see Fig. 2.5). In both cases, when a given antenna array requires photonic beamforming, this antenna's optical interface-head subsystem is plugged into the flexible beamformer sub-system, and via software control of the non-pixelated SLM phase shifter sites, antenna steering is achieved. In short, the proposed three sub-systems acting together form the overall flexible beamforming architecture.

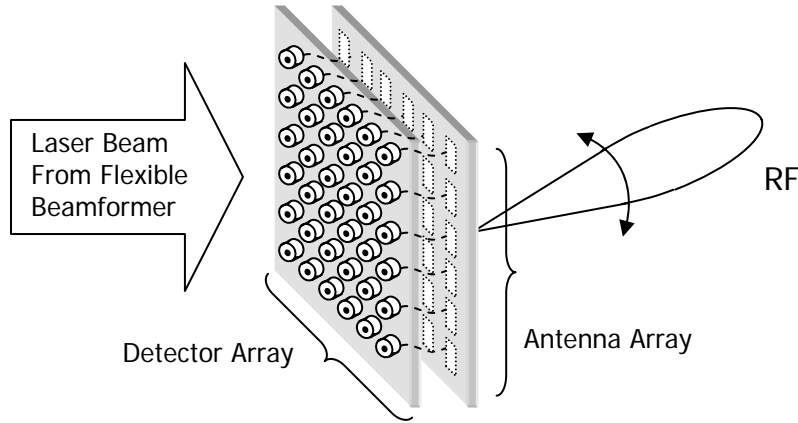


Figure 2.4. Configuration for a flip-chip bonded optical head for a 6x6 elements phased array.

### 2.3 Experimental Demonstration

Fig. 2.6 shows the experimental setup used to realize a proof-of-concept demonstration. The system uses a *p* or horizontally polarized 514.5 nm laser read beam with an irradiance of 4 mW/cm<sup>2</sup>, an Acousto-optic Deflector (AOD), a PANLC-SLM from Hamamatsu, and other beamforming optics. The AOD is fed with a 70 MHz RF signal and serves the purpose of splitting and recombining the optical beam(s) forming a coherent high stability heterodyne

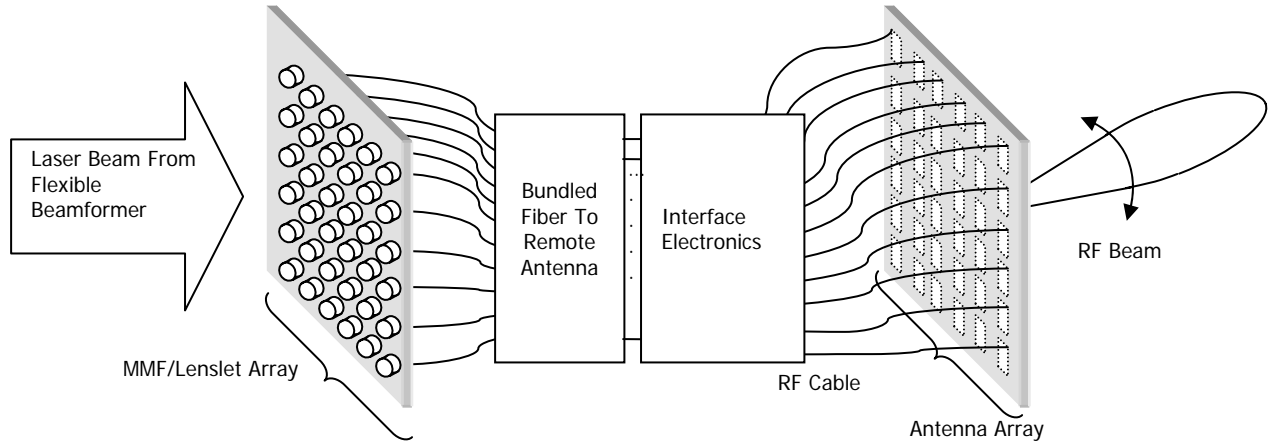


Figure 2.5. Configuration for a fiber remotored antenna array for a 6x6 elements phased array.

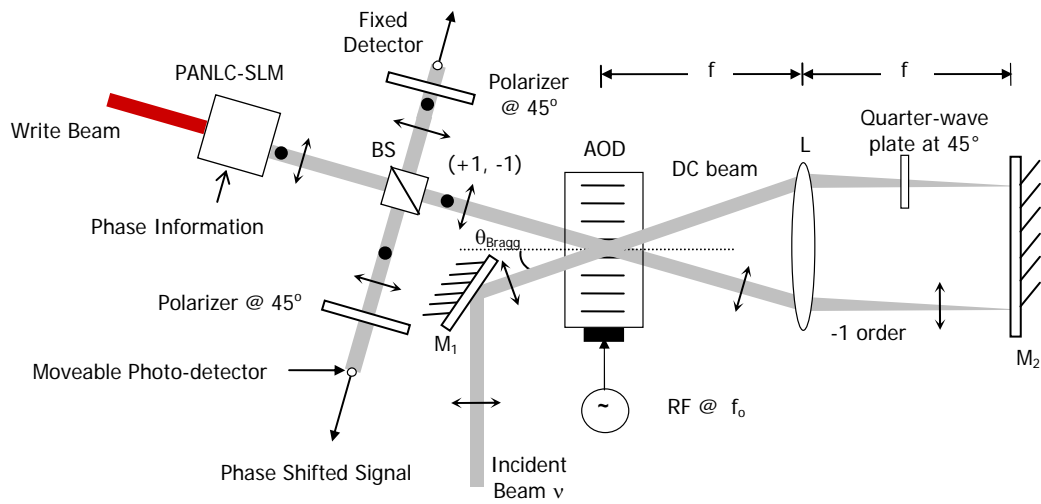
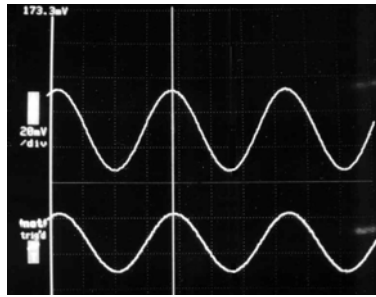


Figure 2.6. Experimental setup of the proposed flexible beamforming concept implemented using acousto-optics and nematic LC technology.  $v$ : Optical Frequency;  $f$ : Focal Length of Lens  $L$ ; AOD: Acousto-optic Deflector;  $M$ : Mirror.

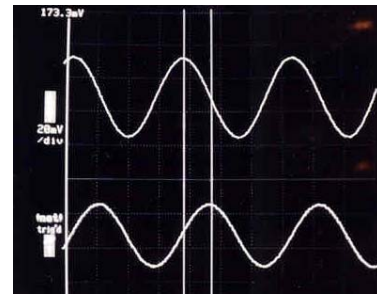
interferometer. This AOD-based system provides a setup to generate a tunable RF antenna carrier signal at the eventual photo-diode output where the heterodyne detected RF equals twice

the AOD drive frequency; in this case, 140 MHz. The AOD deflects the incident Bragg-matched laser beam into two parts; the undiffracted DC beam and the negative Doppler shifted -1 order diffracted beam. The DC beam passes through a Quarter wave plate (QWP) at  $45^\circ$  and reflects back from the mirror  $M_2$ . The effect of this QWP and mirror combination is that the polarization of the DC beam impinging on the AOD for the second time is orthogonal to that in the first through the AOD. The DC beam now undergoes a +1 diffraction. The two diffractions from the AOD are now collinear but orthogonally polarized. These collinear laser beams enter the beamforming sub-system where one polarized beam picks up the RF phase information from the PANLC-SLM. A photo-detector on a translational stage is used to simulate the flexible interface head or third sub-system in the overall PAA controller. This detector positioned in two dimensional space is tracked via software changes on the location of the RF phase map embedded on to the PANLC-SLM. Fig. 2.7 shows the RF signals generated from the fixed reference photo-detector and the movable output port detector for a given output port photo-detector location. These oscilloscope traces clearly indicate the ability of the proposed controller to provide desired phase shifts for PAAs with any antenna front-end interface. Figs. 2.7(a) shows the in-phase signals while (b)-(e) show the phase shifts of  $\pi/2$ ,  $\pi$ ,  $3\pi/2$  and  $2\pi$  with respect to the reference signal from the beamformer. Fig. 2.8 shows the measured RF phase shift data provided by the flexible beamformer, showing continuous  $2\pi$  phase shift control obtained using an SLM write beam of input intensity upto  $\sim 3\text{mW}$  at  $632.8\text{nm}$ .

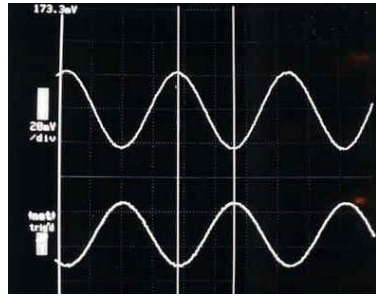




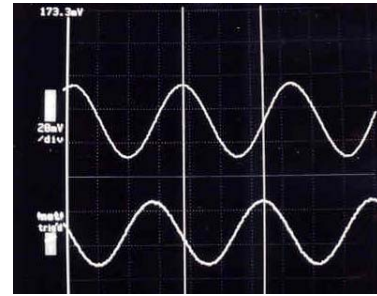
(a)



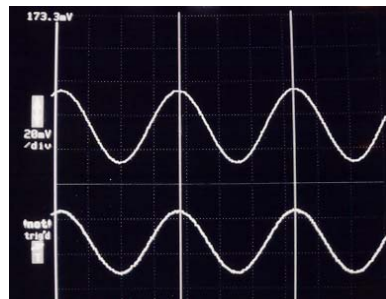
(b)



(c)



(d)



(e)

Figure 2.7. 140 MHz oscilloscope traces from the Flexible Beamformer: (a) in-phase, (b)  $\pi/2$ , (c)  $\pi$ , (d)  $3\pi/2$  and (e)  $2\pi$  radians phase shifted signals from the detectors. The top trace is from the reference detector whereas the bottom trace is the desired

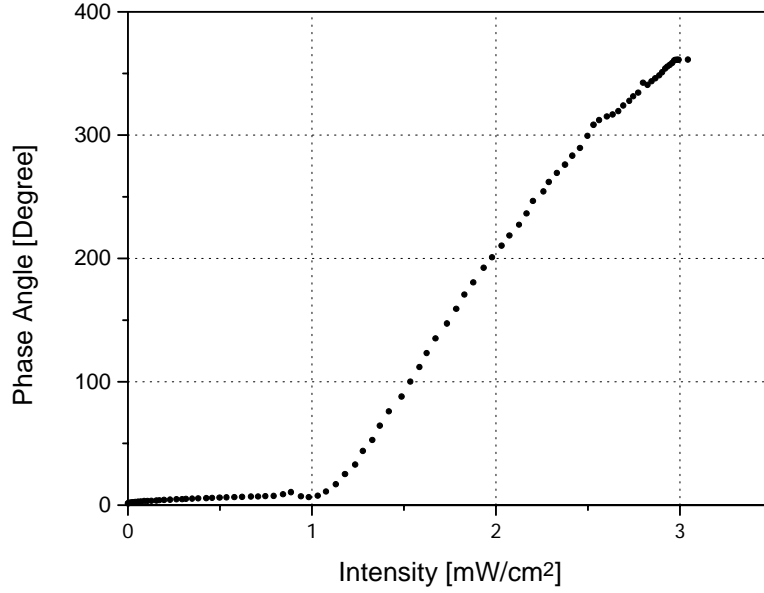


Figure 2.8. The measured RF phase shift data from the flexible beamformer showing  $2\pi$  phase shift control versus the write laser ( $\lambda = 632.8\text{nm}$ ) intensity on the write SLM of the Hamamatsu device.

## 2.4 System Issues

An important point shown in Fig. 2.9 is the high space bandwidth product (SBWP) benefits of the Hamamatsu device. Specifically, the image generation LC device has a very large number, i.e.,  $480 \times 480 = 230,400$  pixels, with each pixel being a small  $41.7 \text{ micron} \times 41.7 \text{ micron}$ . The active area of the optically addressed LC device is  $2 \text{ cm} \times 2 \text{ cm}$ . This area is used for generating the desired spatial distribution  $N$  RF phase shifters for the  $N$  elements of the PAA. Typically,  $N$  is from 50 to 5000. Since we have 230,400 pixels and much fewer antenna elements, as little as 46 pixels and as many as 4,608 LC pixels are required to create a phase

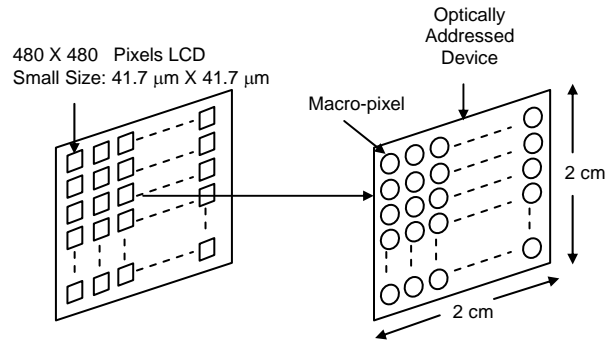


Figure 2.9. The very high count of 230,400 pixels of the write amplitude-mode LC device in the Hamamatsu LC device module gives “Flexible Beamforming” additional powers such as high resolution phase averaging and overall system fault-tolerance via the macro-pixel per RF phase shifter concept.

shifter site on the SLM for 50 to 5000 elements PAA, respectively. Hence, a macro-pixel effect is used to realize the RF phase shifters via optical means, giving greater flexibility to RF phase control versus previous single pixel phase control approaches. This high LC SLM SBWP adds to the overall phase control power of the proposed flexible beamforming approach by giving it a super-phase resolution capability. Phase resolution depends on the interferometric stability of the system and the phase control sensitivity of the SLM via its write-optics. A better than  $1.4^\circ$  phase accuracy using an 8-bit gray-scale LCD write-optics is demonstrated for our system. With such a large SBWP, an antenna designer can design the array and the optical head without worrying about the beamforming optics. The beamformer can then be programmed to match the designed optical head which can be any shape, as shown in Fig. 2.10. Moreover, signal processing for

multiple antenna arrays can be performed in a single beamformer due to the large available SBWP.

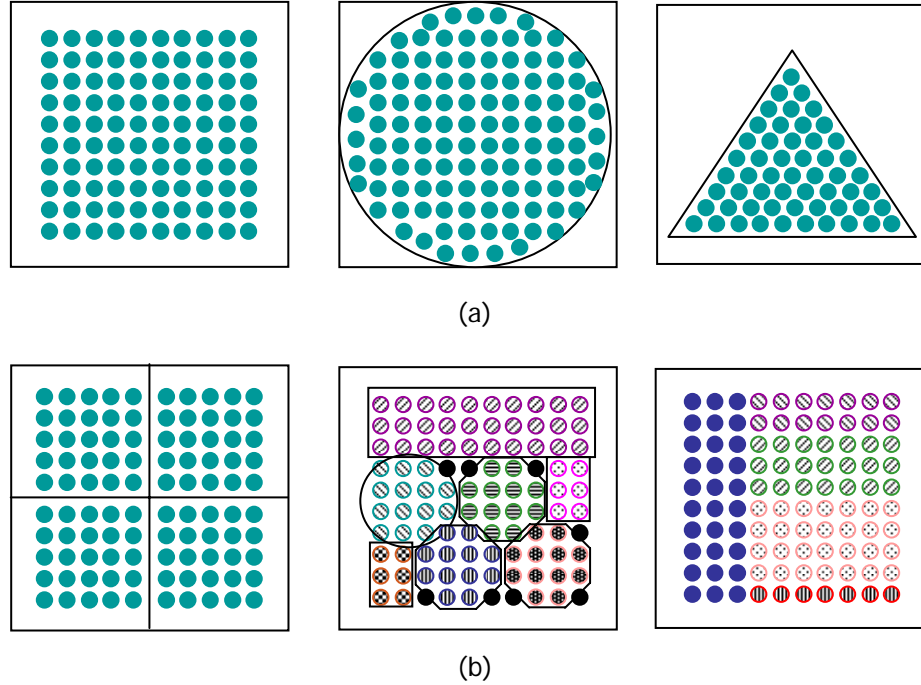


Figure 2.10. Examples of remoting head flexibility, (a) within the antenna array remoting head and (b) across multiple independently steered antenna array remoting heads.

Due to 480x480 pixels available on the write side of the PANLC-SLM, there is a large number of pixels available for phase control. The SLM pixel count does not need to match the antenna count as done in previous work in this field. What we propose is having a very large super pixel made up of many tiny pixels, thus giving the effect of a smooth pixel-free effect. More importantly, the output sampling plane is directly linked to the SLM surface that is indeed smooth and pixel free and hence we can sample the output plane without worrying about pixel effects like diffraction. In 1:1 mapped pixelated systems, a pixel failure will result in RF

wavefront distortion giving RF beam pointing error. In addition, the macro-pixel approach adds a unique fault-tolerance feature to the RF phase shifter, eliminating catastrophic RF phase shifter failure due to single LC pixel failure.

Another important parameter in a PAA is the time needed to reconfigure the antenna pattern. Since the Hamamatsu SLM device is controlled using software, the speed with which the antenna pattern can be reconfigured is the update rate of the SLM and corresponds to 25msec for the Hamamatsu device.<sup>9</sup> The software controlled nature of the Hamamatsu PANLC-SLM device also minimizes output port alignment sensitivity. In other words, the position of the photo-detector/ fiber array can be tracked by simply changing the computer generated spatial intensity pattern that corresponds to the PAA phase map. Currently, our system uses 514nm wavelength. It is expected that this system will finally be implemented in the near infrared region, such as 1.06 microns, 1.3 micron, or 1.55 microns as high speed microwave band modulators and photodetectors are readily available. The Hamamatsu SLM also works in this region, although some modifications need to be made to get full  $2\pi$  phase control.

The response time of the system is limited by the response time of the SLM. This in turn defines the time taken by the system to steer an RF beam from one destination to another. This is fundamentally limited by the strong inter-molecular forces in the NLC that is used in this SLM. A better material (e.g. NLC with lower viscosity) can reduce the response time. Note that the reflective nature of the SLM reduces the response time of this SLM by nearly half of what would be in a transmissive SLM with the same NLC material and same amount of phase modulation. Ferro-electric LC materials can also be employed to achieve analog optical phase modulation. These have a superior response time as compared to NLC's but are limited to small amount of

phase modulation. For example the BNS 512 X 512 SLM from Boulder Nonlinear Systems has a 1000Hz frame rate and can be used to achieve  $\pi/2$  phase modulation.

To get an idea of the current hardware capabilities, Table 2.1 presents an example of an optical remoting head design using a micro-lens array such as SELFOC® micro-lens from NSG America. Moreover, by optical magnification of the read SLM light, one can increase the number of micro-lenses/antenna elements in the optical head.

Table 2.1: Example of optical remoting head design.

Micro-lens diameter	1.0 mm
Micro-lens diameter tolerance	+5.0 mm / -10.0 mm
Hamamatsu LC-SLM clear aperture	2 cm x 2cm
Micro-lens pitch (micro-lens diameter + diameter tolerance)	(1+0.005) mm
Micro-lens-pitch for a 5% assembly tolerance	$1.005 \times (1+0.05) = 1.055$ mm
Number of micro-lenses in Optical Head along $x$ -direction	$2 \text{ cm} / 1.055 \text{ mm} \sim 19$
2-D array size in Optical Head (Number of Antenna Elements)	19 x19
Number of pixels available per phase shifter site in $x$ -direction	$480/19 \sim 25$
Total number of pixels available per phase shifter site	$25 \times 25 = 625$

Note: This design uses specifications from SELFOC® micro-lenses from NSG America.

## 2.5 Conclusion

In conclusion, we have proposed and experimentally demonstrated the basics of the concept of flexible photonic beamforming. The system proposed using a non-pixelated SLM is particularly appropriate for broadcast mode RF phase-steered PAAs. The demonstrated LC device-based beamformer has the capability to provide modulo- $2\pi$  RF phase shifts desired for narrowband beamforming with a response time of 25 msec. The experimental results attest to the functionality and applicability of the system in smart antennas for efficient wireless communication.<sup>10,11</sup> In addition, the proposed flexible beamformer can be directly interfaced with antenna apertures of various size, shapes and antenna sub-apertures, giving increased flexibility to the antenna designer. Future work relates to the optimization of the controller hardware. The flexible beamforming concept can be extended to photonic true time delay systems and other SLM device technologies.

## References

1. N. A. Riza, Editor, *Selected Papers On Photonic Control Systems For Phased Array Antennas*, SPIE Milestone Series, Vol. MS 136, 1997.
2. N. A. Riza, "Acousto-optic liquid-crystal analog beam former for phased-array antennas", *Applied Optics*, Vol. 33, Pages 3712-3724, 1994.
3. N. Madamopoulos and N. A. Riza, "Demonstration of an All-Digital 7-Bit 33-Channel Photonic Delay Line for Phased-Array Radars", *Applied Optics*, Vol. 39, Pages 4168-4181, 2000.
4. L. Pastur, S. T. Goldstein, D. Dolfi, J. P. Huignard, T. Merlet, O. Maas, J. Chazelas, "Two-Dimensional Optical Architectures for the Receive Mode of Phased-Array Antennas", *Applied Optics*, Vol. 38, Pages 3105-3111, 1999.
5. O. Kobayashi, H. Ogawa, "Amplitude and phase control of an RF signal using liquid-crystals by optoelectronic method", in *IEICE Transactions on Electronics*, Vol. E. 78-C(8), Pages 1082-1089, 1995.
6. N. A. Riza and S. A. Khan, "Photonic Beamformer with Flexible Interface for Phased Array Antennas", in *IEEE LEOS 14<sup>th</sup> Ann. Mtg.*, Vol. 2, Pages 816-817, San Diego, CA, USA, 2001.
7. N. A. Riza, S. A. Khan and M. A. Arain, "Flexible Beamformer and Remoting Head for Optically Controlled Phased Array Antennas", in *IEEE-MTTS International Microwave Symposium Digest*, Vol. 3, Pages 941-944, Seattle, WA, USA, 2002.



8. Lightwave Electronics, OMS-2010 Optical Microwave System, Sept. 2002, Product datasheet.
9. Hamamatsu Photonics K.K., Japan, PANLC-SLMM X7550, August 1998.
10. J. Stulemeijer, F.E. van Vliet, K. W. Benoist, D. H. P. Maat, M. K. Smit, "Compact photonic integrated phase and amplitude controller for phased-array antennas", IEEE Photonics Technology Letters, Vol. 11, Pages 122-124, 1999.
11. G. Grosskopf, R. Eggemann, S. Zinal, B. Kuhlow, G. Przyrembel, D. Rohde, A. Kortke and H. Ehlers, "Photonic 60-GHz maximum directivity beam former for smart antennas in mobile broad-band communications", IEEE Photon. Tech. Lett., Vol. 14, Pages 1169 - 1171, 2002.

### **CHAPTER 3: HYBRID ANALOG-DIGITAL VARIABLE FIBER-OPTIC DELAY LINE**

A variable fiber optic delay line (VFODL) is introduced that, to the best of our knowledge, is the first time that a hybrid analog-digital VFODL is proposed to solve the dilemma of efficiently enabling many settable and long duration time delays together with continuous and short time delays. In essence, this VFODL can provide near continuous high resolution time generation across an entire long time delay band. The VFODL is based on the concept of cascaded wavelength sensitive and wavelength insensitive time delays. A proof of concept VFODL built demonstrates near continuous 0.5 ps resolution time delay control across an entire 25.6 ns time delay band generating a total of 51,200 measurable time delay bins. The experimental VFODL also gives a 4.95 dB total optical loss and a 1ms time delay control setting speed. The proposed VFODL can be used in applications such as radio frequency (RF) photonic signal processing and radar testing.

### 3.1 Introduction

A variable fiber optic delay line (VFODL) is a highly sought after component with applications ranging from microwave/millimeter wave analog photonic signal processing to digital optical communication systems based on packet switching. The ideal VFODL is able to efficiently and continuously generate time delays with high temporal resolution over any given long time delay range. Over the years, efforts have been made to realize these VFODLs, particularly for microwave photonics applications where an RF signal riding on an optical carrier needs to be provided with a desirable delay. One way to efficiently generate many time delays over a long time delay range uses an N-bit switched binary architecture that employs  $2 \times 2$  digital switches to select given binary paths connected in a serial cascade (architecture).<sup>1</sup> Here, based on the delay range required, free-space, solid-optic, and fiber-based delay paths have been deployed in both serial and parallel switched architectures using a variety of switching technologies such as liquid crystals,<sup>2-3</sup> Lithium Niobate-integrated-optics,<sup>4-5</sup> micromechanics,<sup>6-7</sup> acousto-optics,<sup>8-9</sup> Gallium Arsenide-integrated-optics,<sup>10</sup> and Indium Phosphide and Silica-on-Silicon-integrated-optics.<sup>11</sup> Because of the digital switched nature of these VFODLs, time delay resolution is quantized to a discrete value and there is a tradeoff between resolution and number of binary switched stages. In effect, getting smaller resolutions across larger time delay ranges means adding more cascading, leading to higher losses and greater module complexity. Hence a dilemma exists to get both high resolution and long time delay range. Another approach for generating large delays is via resonant optical devices although this method has a tradeoff between delayed signal bandwidth and delay time.<sup>12</sup> A more recent and attractive technology for

generating time delays involves the use of wavelength tuning and Fiber Bragg Gratings (FBGs). Initially discrete FBGs positioned along specified fiber paths were used to produce discrete time delays based on the wavelength chosen.<sup>13-14</sup> Later the concept was extended to use a chirped FBG to generate near continuous time delay, but over short delay range due to the fabrication size limitations of FBGs and the laser tuning range.<sup>15-16</sup> To get more delay settings within an efficient structure, multi-wavelength fiber time delay processing was proposed using discrete FBGs delay segments within a serial optical switched structure.<sup>17-18</sup> In addition, wavelength tuning in combination with wavelength division multiplexer devices was also proposed to realize VFODLs.<sup>19-20</sup> So far, all these efforts, to the best of our knowledge, have not realized a VFODL that can deliver near continuous time delays over an arbitrary large time delay range. In this chapter, we describe such a desired VFODL that solves the prior resolution-range dilemma.

### 3.2 Hybrid Variable Fiber-Optic Delay Line Design

Fig. 3.1 shows one version of the proposed hybrid VFODL. The module has one electrical input port and one electrical output port from where emerges the given delayed electrical waveform riding on a delayed optical carrier. The module has two delay control ports; one to control the analog time delay while the other to control the digitally switched optical delay. Hence, the proposed structure is a cascade of an efficient digitally switched optical delay line in combination with an analog controlled optical delay line. This hybrid combination solves the earlier resolution-range dilemma as the digital delay is excellent for providing the long time delay range while the analog delay is excellent in providing the near continuous high resolution

delay between the discretized delays of the switched delay line. In effect, a near continuous time delay control can be generated across a large time delay range. Reflective Optical Fibers (ROFs) are used at the output ports of the optical switch that eliminates the need for alignment sensitive fiber-to-freespace coupling with bulk mirror optics. This reflective nature of the proposed ROF-based VFODL reduces optical loss, packaging cost, and size.

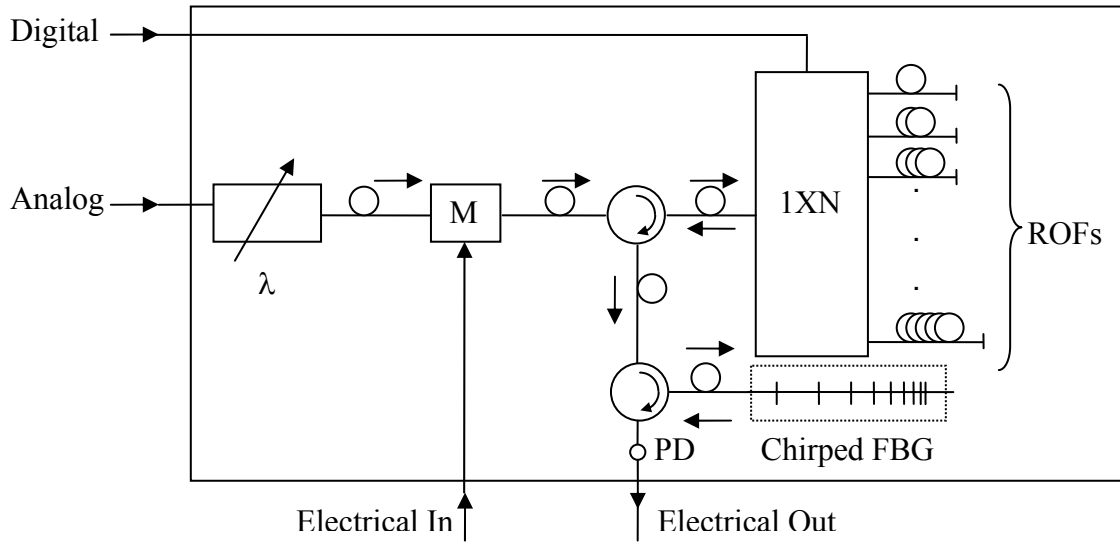


Figure 3.1. Schematic Diagram of the proposed hybrid analog-digital VFODL realized as a Parallel N-Bit Digital-Analog Time Delay Unit. TL: Tunable Laser; M: Modulator; PD: Photodiode Detector; ROFs: Reflective Optical Fibers.

Earlier, we proposed the use of a wavelength sensitive delay line in cascade with a wavelength insensitive delay line to realize a hardware efficient optical beamformer.<sup>17</sup> In Fig. 3.1, this same concept is extended, but with the use of a single input wavelength to realize the desired VFODL. Specifically, a wavelength sensitive chirped FBG is used in combination with

precisely cut  $N$  ROFs interconnected to a  $1 \times N$  polarization and wavelength independent switch. The maximum value of time delay obtained from the analog time delay unit sets the design value for the time delay  $T$  in the digital time delay unit obtained through ROFs. If desired, it is possible to use non-fiber delays such as integrated-optic, solid-optic, and free space delays to achieve the desired results. Also, the  $1 \times N$  switch can be assembled in any technology, as per requirements of the application. The digital switch operation picks a specific fiber delay to give the longer desired time delay from  $0$  to  $(N-1)T$ . The first fiber in the switch connections (the top one in Fig. 3.1) acts as a reference time delay fiber. The other fibers increase in length so as to increase the time delay by  $T$ . Hence the second fiber when engaged by the switch provides a  $T$  delay; similarly, the third fiber provides a  $2T$  delay; the fourth fiber a  $3T$  delay, and eventually the  $N$ th fiber provides a  $(N-1)T$  delay. Tuning the laser adjusts the analog time delay over a  $T$  time delay

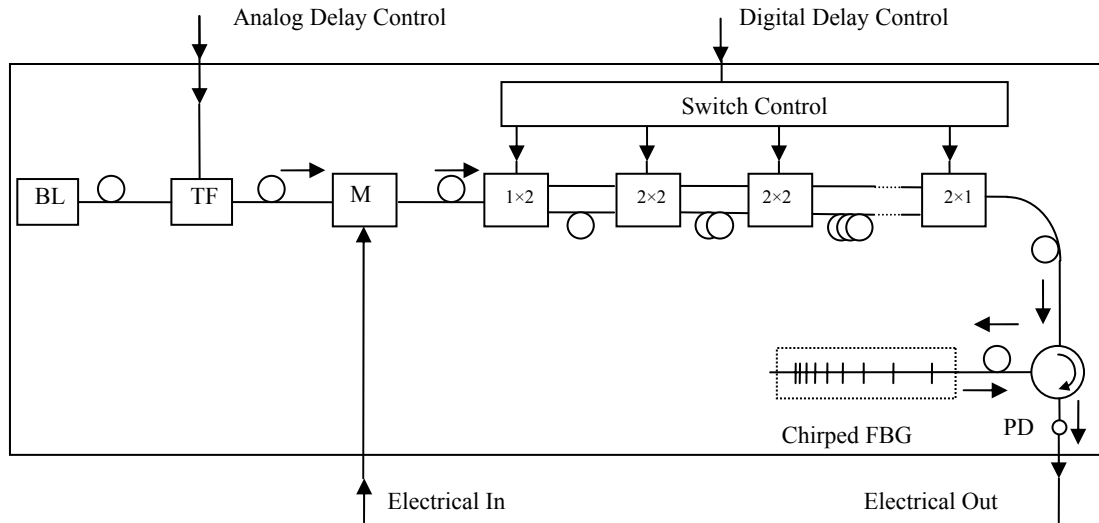


Fig. 3.2: Schematic Diagram of another version of the proposed VFODL realized as a Serial  $N$ -bit Digital-Analog Time Delay Unit. BL: Broadband Laser; M: Modulator; PD: Photodiode Detector; TF: Tunable Filter.

step across any of the discrete  $(N-1) T$  time delay regions picked by the digital optical switch and thus provides a near continuous time delay from 0 to  $NT$ . Hence, the desired goal of making a VFODL with near continuous analog time delay control over an arbitrary long time delay range is realized.

The procedure to generate any desired time delay requires the setting of the analog delay control signal and the digital delay control signal. Given a time delay  $T_1$  such that  $0 < T_1 < NT$ , the appropriate switching port is determined by calculating  $NT/T_1$ . When using the parallel architecture for the required digital delay, the integer part gives the port number to be used and the remainder gives the information about the specific wavelength to be used by the analog part of the VFODL. Note that the two control switching mechanisms are independent of each other and can be performed in parallel. Hence the VFODL random access switching speed is the greater of the two control switching values and not the sum of the two switching speeds. The operating speed of the VFODL depends upon the speed of the optical switch and the tunable laser. If we use analog tunable devices, the worst case scenario for the analog generated time delay will be the time required to switch from one end of the tuning range to the other end, while for the switch this will be the time required to go from port 1 to port  $N$ . This situation can be avoided by using all-digital parallel drive devices, leading to a fixed and short random access time delay setting time for the proposed VFODL.

Fig. 3.2 shows an alternate design of the proposed VFODL. Here, wavelength selection instead of wavelength tuning of a single source is used to generate analog time delay control. One advantage of this approach is that within a given analog  $T$  delay interval, multiple time delay signals can be generated for possible signal processing uses such as transversal filtering using array signal summation. Also note that this design uses an  $N$ -bit switched binary serial

delay structure versus a parallel 1xN switched structure; thus forming an efficient design when many switched delays are required. Specifically, parallel design gives N different digital delays while an N-bit serial design with N switching stages gives the more efficient  $2^N$  different digital delay settings.

It is well known that when light passes through some medium of non-uniform refractive index, it undergoes dispersion, i.e., different wavelength components travels with different speeds and hence there appears a time delay between propagating light signals of different wavelengths. This time delay, called the Group Delay (GD), depends upon the wavelength spread of the optical signal and the properties of the material in which light waves are propagating. If we consider a fiber of length L, then the GD is given by:<sup>21</sup>

$$\tau_g = \tau_m + \tau_w = \frac{L}{c} \frac{d\beta}{dk_0} + \frac{L}{c} \frac{d}{dk_0} [k_0 b(n_1 - n_2)] \quad (1)$$

where c is the velocity of light in vacuum,  $\lambda$  is the optical wavelength,  $n_1$  is the refractive index of fiber core,  $n_2$  is the refractive index of fiber cladding,  $k_0 = 2\pi/\lambda$ ,  $\beta = k_0 n$ , b is the material and geometry dependent constant, and n is the effective refractive index of the fiber.  $\tau_g$  consists of two components;  $\tau_m$ , the material dispersion delay and  $\tau_w$ , the waveguide dispersion delay. In single mode fibers,  $\tau_w$  is an order of magnitude lower than  $\tau_m$  and is usually neglected.<sup>21</sup> Hence we will consider only the material dispersion delay  $\tau_m$  that can be expressed as:

$$\tau_m = \frac{L}{c} \frac{d\beta}{dk_0} = \frac{L}{c} \left( n - \lambda_0 \frac{dn}{d\lambda_0} \right) \quad (2)$$

Here the term  $(n - \lambda_0 dn/d\lambda_0)$  is defined as the group index  $n_g$  of the optical fiber.<sup>22</sup> So (2) can be written as:



$$\tau_m = \frac{L}{c} n_g = \frac{L}{V_g}, \quad (3)$$

where  $V_g$  is called the group velocity. However, if we have a wavelength spread of  $\Delta\lambda$  in the input light signal, then according to (2), there will be a time delay between these components that can be calculated by taking the differential of  $\tau_m$  with respect to the wavelength. This wavelength spread dependent time delay is given by:

$$\Delta\tau_m = \frac{d\tau_m}{d\lambda_0} \Delta\lambda_0 = L\Delta\lambda_0 \left[ \frac{\lambda_0}{c} \frac{d^2 n}{d\lambda^2} \right] = L\Delta\lambda_0 D_m, \quad (4)$$

where  $D_m$  is called the material dispersion constant and is usually expressed in ps/nm/km.

Analog control of the time delay in the proposed VFODL relies upon the chirped FBG. As is well known, an FBG is a piece of optical fiber with a grating written inside it. This grating reflects a particular wavelength that satisfies the Bragg condition and is given by:<sup>23</sup>

$$\lambda_{Bragg} = 2n_{eff} \Lambda_g, \quad (5)$$

where  $\Lambda_g$  is the grating period and  $n_{eff}$  is the effective refractive index inside the FBG. In a continuously chirped grating,  $\Lambda_g$  is varied continuously throughout the length of the grating. This results in a different GD for each wavelength due to the fact that different wavelength components are reflected from different physical positions along the length of the grating. If we have a chirp of  $\Delta\Lambda_{chirp}$  in the grating period, then the corresponding chirped wavelength range is given by:

$$\Delta\lambda_{chirp} = 2n_{eff} \Delta\Lambda_{chirp}. \quad (6)$$

If we take a reference wavelength at the center of the chirped wavelength range of the grating, the time delay is expressed by:

$$\begin{aligned}\Delta\tau_{cg} &= \frac{(\lambda_0 - \lambda)}{\Delta\lambda_{chirp}} \frac{2L_g}{V_g} = \frac{(\lambda_0 - \lambda)}{\Delta\lambda_{chirp}} \frac{2L_g}{c} n_{eff} \\ &= \Delta\lambda \frac{2L_g}{\Delta\lambda_{chirp} c} n_{eff}\end{aligned}\quad (7)$$

where  $L_g$  is the length of the chirped grating and a factor of two appears due to the fact that the grating is traveled twice when light is reflected back in our proposed VFODL. Here we can define the grating dispersion constant as  $D_{cg} = \frac{2L_g}{\Delta\lambda_{chirp} c} n_{eff}$ . Note that in this expression, the length of the grating is also included and therefore  $D_{cg}$  is usually expressed in ps/nm. Combining (4) and (7), the total time delay due to the chirped grating can be expressed as:

$$\Delta\tau = \Delta\tau_m + \Delta\tau_{cg} \quad (8)$$

Usually  $\Delta\tau_{cg}$  is an order of magnitude higher than  $\Delta\tau_m$  because chirp gratings are designed to give high  $D_{cg}$  values, so the time delay is calculated using:

$$\Delta\tau = \Delta\lambda \frac{2L_g}{\Delta\lambda_{chirp} c} n_{eff} = \Delta\lambda D_{cg} \quad (9)$$

Equation 9 is the design equation for calculating time delays in the analog time delay unit of our VFODL. When light travel through a fiber of length  $L$  and effective refractive index  $n_{eff}$ , the absolute time delay is given by  $t = Ln/c$ . But we know that the light also suffers a time delay due to the dispersion in the medium. Hence the total time delay for an ROF such as used in the VFODL can be expressed by using (4) as:

$$\Delta T = \frac{2\Delta L n_{eff}}{c} + 2L\Delta\lambda_0 D_m, \quad (10)$$

where  $\Delta L$  is the incremental change in length of successive ROFs and  $\Delta T$  is the corresponding digital time delay step. Here the second term contributes to the timing jitter associated with the digital delay unit of the VFODL. It will be shown later that this timing jitter term is negligible compared to the first term in (10), and hence is neglected for designing the digital part of the demonstrated hybrid VFODL. Therefore,  $\Delta L$  can be approximated as:

$$\Delta L = \frac{\Delta T c}{2n_{eff}} \quad (11)$$

This equation is the design equation for the digital part of the VFODL.

### 3.3 Experimental Demonstration

The VFODL in Fig. 3.1 is designed and demonstrated in the laboratory. A mechanically tuned laser with a 1510-1600 nm tuning range is fiber-connected to a C-band (1530-1560 nm) Lithium Niobate Integrated-optic amplitude modulator. This modulator is fed by the RF signal that requires a given delay generated by the proposed hybrid VFODL. This delayed RF signal is produced by the high speed photo-diode connected to the fiber grating interconnected circulator.

The chirped grating used in our experiment has an average reflectivity of 92% (loss of 0.36 dB) with a bandwidth  $\Delta\lambda_{\text{chirp}}$  of 22.88 nm at center wavelength of 1548.682 nm. The value of  $D_{\text{cg}}$  supplied by the manufacturer is 35.2 ps/nm. Hence, using (9), the maximum time delay that can be achieved by this grating by tuning the wavelength is  $22.8 \times 35.2 = 805.37$  ps, which agrees closely with the experimentally measured value of 800 ps. Fig. 3.3 shows the VFODL

demonstrated time delay over a 800 ps range using wavelength tuning from 1536 nm to 1560 nm. The resolution of the VFODL is limited by the wavelength resolution of the tunable laser. The tunable laser with a 1ms tuning speed used in this experiment has a tuning resolution of 0.01 nm which using (9) corresponds to a time resolution of 0.35 ps. The measured value on oscilloscope is 0.5 ps that is limited by the bandwidth of the oscilloscope and agrees well within the limitations of oscilloscope. The design N is chosen to be 32 by employing a 1x32 optical-mechanical fiber-optic switch with a 1 ms switching speed and a measured 0.47 dB average optical loss and a  $\pm 0.3$  dB loss variation overall all 32 switch settings. The circulator connected to the switch has a three port optical loss of 1.29 dB while the circulator connected to the chirped grating has a 2.13 dB 3-port optical loss.

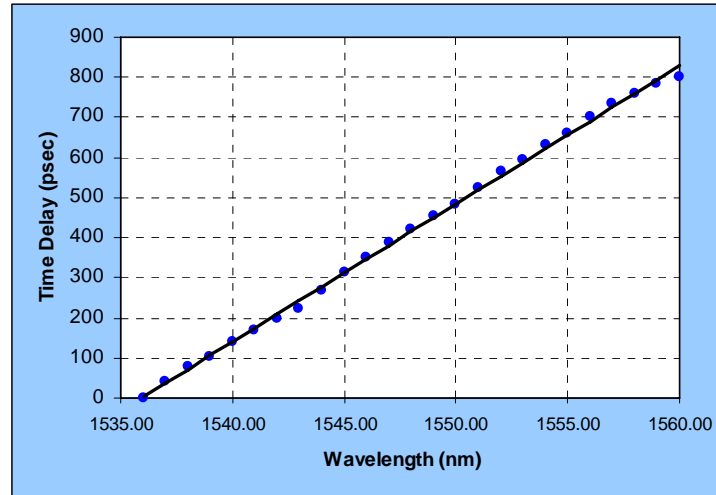


Fig. 3.3: Analog-only mode demonstrated VFODL operation demonstrating high resolution near continuous time delay over a 800 ps range using wavelength tuning from 1536 nm to 1560 nm.

As the tunable wavelength is offset from 1536 nm to 1560 nm, the delay from the chirped FBG kicks in, providing the 800 ps analog fill step between the 32 digital delay steps. A designed

basic step of 800 ps delay is required for the digital part of the VFODL; therefore using (11), we get  $\Delta L = 8$  cm. Here we have used a typical value of  $n_{\text{eff}} = 1.4682$  for Corning ® SMF-28™.<sup>24</sup> The switch port 1 is used as a reference time delay and an arbitrary fiber length of 40 cm is chosen for the VFODL design. The fibers connected to the consecutive ports are increased in length by 8 cm. This 8 cm fiber segment on double pass retroreflective delay is designed to give a 800 ps time delay. Hence, the lengths of ROFs are selected as 40 cm, 40+8=48 cm, 40+2×8=56 cm,..., 40+8×31= 288 cm, for the 32 state digital part of the VFODL. Note that each ROF is a specially fabricated fiber with a gold reflective tip at its end, making a highly effective and compact light reflector. The ROF coating is a broadband reflective coating with an average measured reflectivity of 87.5% (or optical loss of 0.7 dB). By switching through the 32 switch settings, the time delay goes from 0, 800 ps, 1600 ps,...to 24,800 ps, given that the wavelength is set for 1536 nm or alternatively from 800 to 25,600 ps when the wavelength is set to 1560 nm. The total optical loss of the demonstrated VFODL is 4.95 dB calculated as 1.29 dB (first circulator) + 2.13 dB (second circulator + 0.47 dB (optical switch) + 0.7 dB (ROF) + 0.35 dB (FBG) = 4.95 dB. In effect, this loss can be further reduced by 1-2 dB using lower loss and optimized components.

Table 1 shows the designed and demonstrated VFODL delays. Six switch ports, namely, port numbers 1, 2, 3, 30, 31, and 32 are engaged in the proof-of-concept measurements to demonstrate both short time delay control and long time delay control. As shown in Table 1, a combination of the digital switch setting and the laser wavelength can adjust the time delay across an entire 0 to 25.6 ns band, thus illustrating the power of the proposed VFODL. A mechanically tunable laser is used with a tuning speed of 1 ms over the 24 nm tuning range of the FBG while the random access switching speed of the optical switch is 1 ms. Hence, as

mentioned earlier, the worst case random access switching speed of the VFODL is 1 ms. Considering that the designed time delay step is 0.35 ps due to the tuning step of the laser, a total of  $\sim 73,142$  time delay bins can be generated across 25.6 ns via the designed VFODL. This in effect is a better than 16-bit VFODL realization. Because the deployed oscilloscope could measure upto a 0.5 ps resolution, the demonstrated time bins capacity of the VFODL is 51,200. Fig. 3.4 shows a sequence of time delay oscilloscope traces produced by analog plus digital mode operation of the designed VFODL. The top traces are the reference RF signal that feed the VFODL and are time aligned with the VFODL output at the wavelength of 1536 nm and ROF at port 1 of switch in operation. The lower traces indicate the optically delayed signal from the VFODL. In Fig. 3.4(a), the switch is set to engage the ROF at port 1, and the wavelength is set to 1560 nm. This setting should generate a relative delay of 800 ps, as indicated by the trace markers. In Fig. 3.4(b), the switch is set to port 2, with the wavelength set to 1547.2 nm. In this case, the relative delay is 800 ps from the ROF and 400 ps from the wavelength sensitive delay, giving a total of 1200 ps, as indicated in the traces. For the Fig. 3.4(c) situation, the switch is engaged for port 2 and wavelength of 1553 nm, generating a relative time delay of 1400 ps. In this case, 800 ps is from the ROF while 600 ps is from the chirp FBG. In Fig. 3.4(d), switch is set for port 3 with wavelength at 1536 nm, generating a time delay of 1600 ps, due only to the ROF. Finally in Fig. 3.4(e), the switch activates port 32 with a wavelength of 1542 nm, producing a total delay of 25,000 ps, where 24,800 ps is via the ROF and 200 ps is due to the chirp FBG. Hence, the data indicates that via hybrid analog-digital control of the proposed VFODL, a near continuous time delay can be generated efficiently and simply over a long time delay range.

In the analog time delay unit, the timing jitter is due to the finite line width of the laser. The spectral linewidth of the laser used in the experiment is 220 KHz that corresponds to a linewidth

of  $2 \times 10^{-6}$  nm. Using (4), the timing jitter associated with this line width is  $\pm 2 \times 10^{-6} \times 35.1 = \pm 0.07$  fs. This value is negligible in comparison to the tuning step-based resolution limit of 350 fs. In the digital time delay unit, the timing jitter is associated with the material dispersion delay of the fiber. The maximum length of the fibers used is  $< 3$  m and the bandwidth is 22.88 nm. Using typical values of  $D_m = 17.92$  ps/nm/km,<sup>24</sup> the timing jitter due to material dispersion is 1.23 ps for a maximum time delay of 25.6 ns. This corresponds to a 0.005% time jitter in the digital part of the demonstrated VFODL.

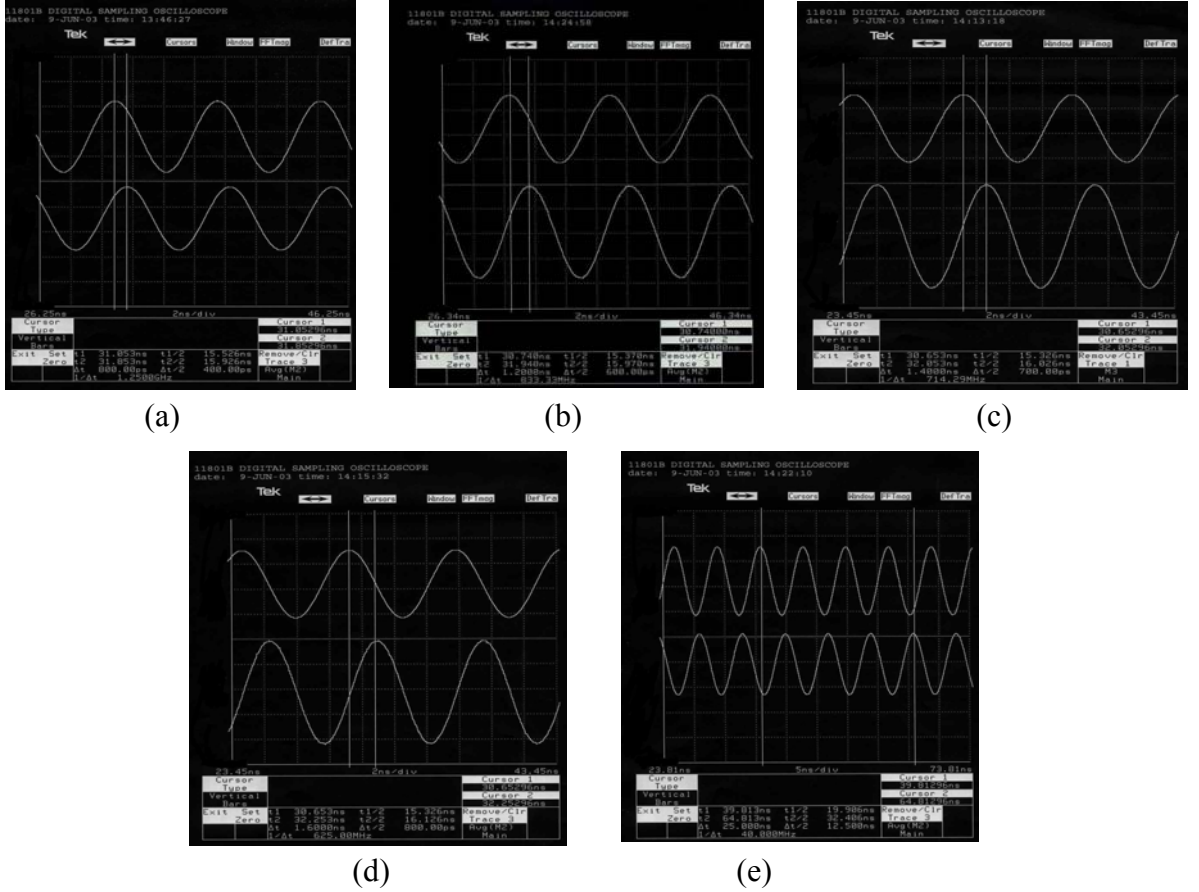


Fig. 3.4: Proposed VFODL operations using the hybrid analog-digital mode. Top trace is the reference signal from the RF signal generator that is time aligned with the VFODL reference output for a  $\lambda = 1536$  nm and switch set to port 1. The bottom traces are the time delayed

VFODL outputs for VFODL setting of (a)  $\lambda = 1560.00$  nm and switch active for port 1 (b)  $\lambda = 1547.20$  nm and switch active for port 2 (c)  $\lambda = 1553.00$  nm and switch active for port 2 (d)  $\lambda = 1536.00$  nm and switch active for port 3 (e)  $\lambda = 1542.00$  nm and switch active for port 32.

Table 3.1: Demonstrated VFODL design and delays.

Time Delay Range	Control Mechanism	Active Switch Port	Fiber Length at switch port
0-800 ps (0 to T)	Analog (1536-1560 nm)	1	40 cm
800-1600 ps T to 2T	Analog+Digital	2	48 cm
1.6-2.4 ns 2T to 3T	Analog+Digital	3	56 cm
23.2 – 24.0 ns 29T – 30T	Analog+Digital	30	272 cm
24.0 – 24.8 ns 30T – 31T	Analog+Digital	31	280 cm
24.8 – 25.6 ns 31T – 32T	Analog+Digital	32	288 cm



### 3.4 Conclusion

In this chapter, we have demonstrated, to the best of our knowledge, the first analog-digital variable optical delay line that provides the highly desirable features of near continuous high resolution time delays with a large number of time delay settings, all with the capability of producing long time delays. The design scheme is simple and uses cascading of a wavelength insensitive digitally switched optical delay line with a wavelength sensitive analog tuned optical delay line. The proposed VFODL parameters can be adapted for specific applications by selecting the chirped FBG and optical switch specifications. For instance, engaging high speed optical switches<sup>25</sup> and high speed tunable lasers<sup>26</sup> can provide nanosecond regime high speed VFODL operations. More recently, digitally switched optical delay lines have become commercially available,<sup>27</sup> and can help transition the proposed VFODL approach. The demonstrated VFODL has successfully shown a  $< 0.5$  ps resolution over a 25.6 ns time delay range with a 1 ms time delay setting speed and a average 4.95 dB optical loss. The proposed VFODL can greatly impact applications such as phased array antenna controls, RF signal processing in the optical domain, biomedical optics, and radar testing.

## References

1. P. Goutzoulis, D. K. Davies, and J. M. Zomp, "Prototype binary fiber optic delay line", in *Optical Engineering*, Vol. 28(11), pp. 1193-1202, (1989).
2. L. Pastur, S. Tonda-Goldstein, D. Dolfi, J. Huignard, T. Merlet, O. Maas, J. Chazelas, "Two-Dimensional Optical Architectures for the Receive Mode of Phased-Array Antennas", in *Applied Optics-IP*, Vol. 38 (14), pp. 3105-3111 (1999).
3. N. Madamopoulos and N. A. Riza, "Demonstration of an All-Digital 7-Bit 33-Channel Photonic Delay Line for Phased-Array Radars", *Applied Optics-IP*, Vol. 39 (23) pp. 4168-4181 (2000).
4. R. A. Soref, "Programmable time-delay devices", in *Applied Optics*, Vol. 23(21), pp. 3736-3737 (1984).
5. E. Ackerman, S. Wanuga, D. Kasemset, W. Minford, N. Thorsten, and J. Watson, "Integrated 6-Bit photonic true-time-delay unit for lightweight 3-6 GHz radar beamformer", in *IEEE International Microwave Symposium Digest, Part II*, pp. 681-684 (1992).
6. G. A. Magel, T.-H. Lin, L. Y. Pang, and W. -R. Wy, "Integrated optic switches for phased-array applications based on electrostatic actuation of metallic membranes", in *Optoelectronic Signal Processing for Phased Array Antennas IV*, B. M. Hendrickson, eds., *Proc. SPIE* Vol. 2155, 107-113 (1994).
7. N. A. Riza and Dennis L. Polla, "Micromechanical fiber optic switches for optical networks", in *Integrated Optics and Microstructures*, M. Tabib-Azar and D. L. Polla, eds, *Proc. SPIE* 1793, 108-126 (1992).

8. N. A. Riza, "Acousto-optic device-based high-speed high-isolation photonic switching fabric for signal processing", in *Optics Letters*, Vol. 22 (13), pp. 1003-1005 (July 1997).
9. N. A. Riza, "Acousto-optically switched optical delay lines", in *Optics Communication*, Vol. 145, pp. 15-20 (1998).
10. C. T. Sullivan, S. D. Mukherjee, M. K. H.- Brenner, A. Gopinath, E. Kalweit, T. Marta, W. Goldberg, and R. Walterson, "Switched time-delay elements based on ALGaAs/GaAs optical waveguide technology at 1.32  $\mu$ m for optically controlled phased array antennas", in *Optical technology for Microwave Applications IV and Optoelectronic Signal Processing for Phased –Array Antennas III*, S.-K. Yao, B. M. Hendrickson, eds, Proc. SPIE 1703, 264-271 (1992).
11. J. Stulemeijer, "Integrated Optics for Microwave Phased-Array Antennas", Chapter 4, Ph. D. Thesis, supervised under Prof. M. K. Smit, Technical University of Delft, Netherlands, February 2002.
12. G. Lenz, B. J. Eggleton, C. K. Madsen, and R. E. Slusher, "Optical delay lines based on optical fibers", in *IEEE Journal of Quantum Electronics*, Vol. 37 (4) , pp. 525-532, (2001).
13. G. A. Ball, W. H. Glenn, and W. W. Morey, "Programmable fiber optic delay line", in *Photonics Technology Letters*, Vol. 6 (6), pp.741-743 (1994).
14. R. A. Soref, "Fiber grating prism for true time delay beam steering", in *Fiber and Integrated Optics*, Vol. 15, pp. 325-333 (1996).
15. J. L. Corral, J. Marti, S. Regidor, J. M. Fuster, R. Laming, and M. J. Cole, "Continuously variable true time-delay optical feeder for phased-array antenna employing chirped fiber gratings", in *IEEE Transactions on Microwave theory and techniques*, Vol. 45 (8), pp. 1531-(1997).

16. A. Molony, L. Zhang, J. A. R. Williams, I. Bennion, C. Edge, and J. Fells, "Fiber bragg-grating true time-delay systems: discrete-grating array 3-b delay lines and chirped-grating 6-b delay lines", in IEEE Transactions on Microwave theory and techniques, Vol. 45 (8), pp. 1527-1530 (1997).
17. N. A. Riza and N. Madamopoulos, "Phased-array antenna, maximum-compression, reversible photonic beam former with ternary designs and multiple wavelengths", in Applied Optics-IP, Vol. 36 (5), pp. 983-996(1997).
18. D. T. K. Tong and M. C. Wu, "Multiwavelength optically controlled phased-array antennas", in IEEE Transactions on Microwave theory and techniques, Vol. 46 (1), pp. 108-115 (1998).
19. S. Yegnanarayanan, P. D. Trinh, and B. Jalali, "Recirculating photonic filter: a wavelength-selective time delay for phased-array antennas and wavelength code-division multiple access", in Optics Letters, Vol. 21 (10), pp. 740-742, (1996).
20. N. A. Riza and S. Sumriddetchkajorn, "Micromechanics-based wavelength-sensitive photonic beam control architectures and applications," in Applied Optics, Vol. 39, No. 6, pp. 919-932, 20 Feb. 2000.
21. G. Lachs, Fiber Optic Communications, (McGraw-Hill, USA 1998).
22. A. Yariv and P. Yeh, Optical Waves in Crystals, (Addison-Wesley, San Francisco, CA 1984).
23. R. Kashyap, Fiber Bragg Gratings, Academic Press, London, UK 1999).
24. Notes on Corning ® SMF-28™ <http://www.corning.com/opticalfiber/pdf/CO9562.pdf>
25. G. Alibert, F. Delorme, P. Boulet, J. Landdreau, and H. Nakajima, "Subnanosecond tunable laser using a single electroabsorption tuning super structure grating", in Photonics Technology Letters, Vol. 9, pp. 895-897,(1997).

26. R. Krahenbuhl, M. M. Howerton, J. Dubinger, A. S. Greenblatt, "Performance and modeling of advanced Ti:LiNbO<sub>3</sub> digital optical switches", in J. of Lightwave Tech., Vol. 20, pp. 92 - 99, (2002).
27. Preliminary data sheet on Programmable Delay Line, [www.littleoptics.com](http://www.littleoptics.com).

## **CHAPTER 4: PROGRAMMABLE HIGH SPEED POLARIZATION MULTIPLEXED OPTICAL SCANNER**

Fast digital-analog control polarization-based optical scanner with complete three-dimensional beamforming programmability is presented. Features include low power consumption and large aperture liquid crystal-based optics, digital repeatability, and time multiplexed accurate analog beamforming. Analog frequency and amplitude control of the nematic liquid crystal beamformer cells allows continuous fine scan programmability over a 0.66 mrad horizontal-deflection, 0.75 mrad vertical deflection, and an infinity to 1.84 m focal length longitudinal scan. First time demonstrations include an 8-point volumetric scan and a 2-bit digital lens scan, both at 1310 nm, with a 35  $\mu$ s random-access time.

#### 4.1 Introduction

Several technologies have been used to make devices for one dimensional (1-D) and two dimensional (2-D) laser beam steering, including nematic liquid crystals (NLCs) <sup>1</sup>, ferroelectric liquid crystals (FLCs) <sup>2</sup>, optical microelectromechanical systems (MEMS) technology <sup>3</sup>, and ferroelectric electrooptic materials such as lead zirconate titanate <sup>4,5</sup>. Certain applications can benefit from three dimensional (3-D) beam steering where a point of light can be both translated and focused/defocused. Following phased array radar 3-D beamforming methods, researchers have devised optical phased array devices where the 2-D planar structure of the optical device is populated with individually controllable optical phase shifter sites <sup>6,7</sup>. Optical devices have been built using 1-D or 2-D pixel layout geometries with various electrode and driving electronic structures. Although 3-D steering has been achieved, it is accompanied by key system limitations. First, pixelation or discrete sampled spatial phase control across the scan aperture has been used because of finite size of the device electrodes or pixels. Due to pixelation, optical diffraction orders are formed that cause unwanted insertion loss and crosstalk for the scanned beam. Also, the discrete phase map nature leads to quantization noise in the beam map, resulting in a non-smooth beam profile. Finally limitations in throughput and beam quality over the scan range occur due to device fill factor and electric field fringing effects, respectively. All pixel sites on the device 2-D electrode map require accurate and repeatable analog phase control. Typically, a device may have a million pixels to effectively produce high fidelity scan beams in 3-D. These requirements in-turn imply complex and costly drive electronics for what is supposed to be a highly compact 3-D optical scanner. A further drive circuitry complication arises if fast

(sub-milliseconds) speed is required to form the agile beam. Hence, a challenge exists to realize a simple to control, fast, high beam fidelity, 3-D optical beam scanner. Such a 3-D scanner is described in this work.

Specifically, a digital-analog, pixel-free, fast random-access beam scan time, fully programmable, high beam fidelity, ease in scalability, 3-D optical scanner is proposed and demonstrated <sup>8,9</sup>. Specifically demonstrated is a near infrared band (e.g., 1310 nm) 3-D scanner suitable for fine beam controls as required in long range laser communications <sup>10</sup>. Previously, digital cascaded polarization switched scanners have been proposed with visible band operations, but these scanners have been limited to 1-D and 2-D scans with other issues such as high drive voltages and bulky optics, pixelation, non-stackable (i.e., non-parallel glass cells) and non-programmable birefringent plate designs <sup>11-13</sup>. We begin with a description of a versatile digital-analog polarization-based scanner architecture that can provide programmable coarse and fine scan controls. Specifically, the power of the fully programmable 3-D fine scan Polarization Multiplexed Optical Scanner (P-MOS) is demonstrated via experiments of voxel (volumetric picture element) scans and digital lens scans. The description concludes with the expected features possible using the proposed P-MOS.

## 4.2 Proposed Architecture

Applications such as inter-satellite laser links require both fine and coarse beam pointing. Long range (up to 40,000 km) links require one micro radian fine angle scan controls in order to maintain link with a typical satellite operating at a 7 km/s relative velocity <sup>14</sup>. On the other hand,



several milli radians of coarse scan control enables agile reconfigurability with other satellite terminals. Fig. 4.1 introduces a 3-D scanner architecture called polarization multiplexed optical scanner or P-MOS that provides the best of both worlds of highly repeatable fast random-access digital scans with the fine tweaking and programmability of analog scans. The first stage of the P-MOS is a digital and analog controlled module consisting of  $N$  fast response digitally controlled  $90^\circ$  polarization rotators (PRs) and the  $N$  analog controlled slower response fine beamforming power optical cells. The second stage of the P-MOS consists of  $M-N$  PRs sandwiched between passive coarse beamforming power birefringent optical cells. Previously, the use of passive non-programmable birefringent crystal optics for coarse 2-D scans has been shown using the digital polarization switching method <sup>11</sup>. Hence, the focus of this work is to demonstrate the first part of the P-MOS stage; namely, the fine beamforming controls fully programmable 3-D P-MOS module.

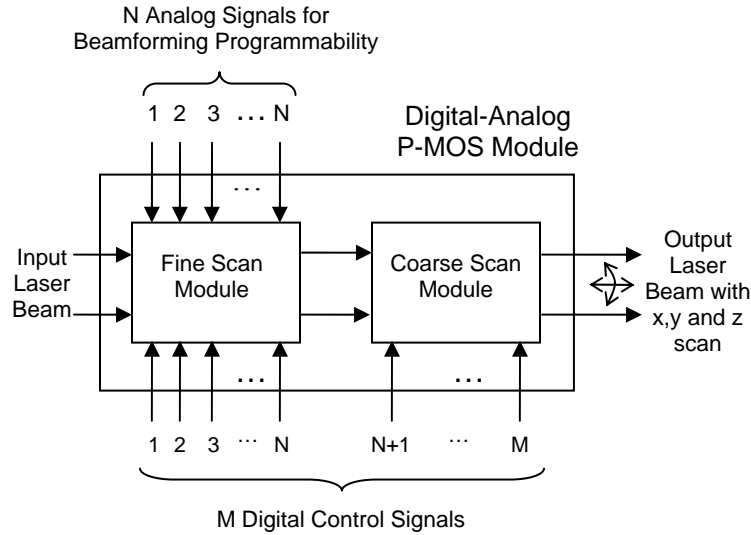


Fig. 4.1. P-MOS Architecture.

Fig. 4.2 shows the basic 3-D single voxel scan hardware of the Digital-Analog Mode P-MOS. Here a 3-D fully programmable optical beamformer is made by cascading three fast

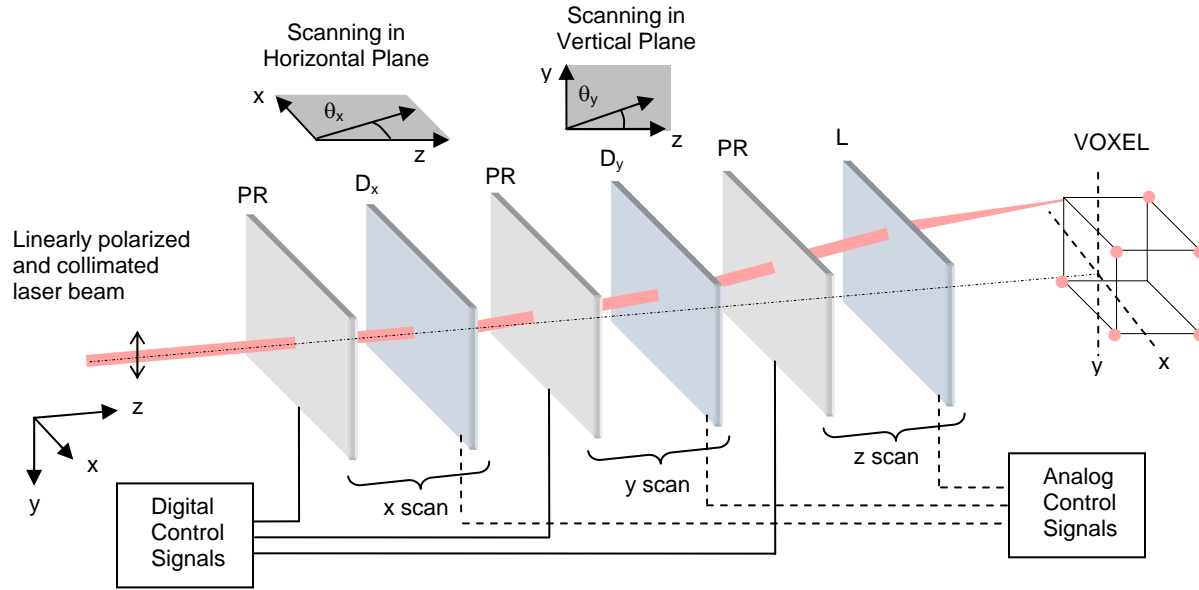


Fig. 4.2. Basic single voxel scan hardware of the P-MOS module.

electrically driven pixel-free  $90^\circ$  PRs with inter-dispersed three electrically controlled slower speed analog mode non-pixelated birefringent plates acting as variable deflectors D's and a variable focal length lens L. This 3-D voxel module can be cascaded with other 3-D voxel modules to generate  $2^K$  beams in space if  $K/3$  3-D voxel modules are used where  $K$  is the total number of PRs in the entire P-MOS architecture. Because thin film planar liquid crystals optics is used to form the hardware, large ( $>$  centimeter diameter) scanner apertures using low (e.g., mW) level total powers is expected. Beam scanning is accomplished by two methods in the P-MOS. First, only digital control of the PRs is implemented with the Ds and Ls preprogrammed for a given fixed setting. In this case, the scanner random-access time is the switching time of the PR. In the second case, all PRs are set such that only a given voxel P-MOS module is observed by the input linearly polarized beam with the other modules undergoing analog reprogramming of their Ds and Ls. In effect, any analog beamforming scanner state within the power of the

specific D and L can be generated using time multiplexed addressing of these birefringent plates. In this case, the scanner beam switching speed is given by  $T/P$ , where T is the time it takes to reprogram the analog mode D or L, and P is the number of 3-D voxel modules that make the P-MOS. In this case, apriori scan information for the optical scanner is required. As shown later, birefringent-mode NLC can be used for making the D and L, with response time in the several milliseconds. Hence, the time multiplexed P-MOS can further reduce the scanner time to near a millisecond.

Earlier, the use of a high resistance layer with two parallel electrodes was proposed to generate a smooth voltage ramp between electrodes to form a pixel-free deflector<sup>15</sup>. Later, others proposed and demonstrated the use of a high impedance thin film layer intermeshed with the array electrode structure of an NLC beamformer device to produce smooth optical phase modulation between electrodes<sup>16-18</sup>. As NLC molecules are much smaller than pixel feature size, a near smooth phase map is formed between electrodes. This design concept was extended using fewer specially designed electrodes (e.g., two) around the optical aperture of the NLC device, leading to a pixel free NLC device design<sup>10,19</sup>. For the proposed fine P-MOS module, using the earlier principles of electrode meshing with high impedance substrates, electrically programmable NLC birefringent phase plates D and L (from OKO Tech. Holland) are realized and used in the P-MOS experiment. The liquid crystal cell is filled with Merck BL006 (see Appendix C) that has a birefringence ( $\Delta n = n_e - n_o$ ) of 0.286 at 20°C and  $\lambda = 589.3\text{nm}$ . The LC layer has a uniform thickness of 50 $\mu\text{m}$ . The clear aperture of the devices is 5mm. The substrates are deposited with two different electrodes. One substrate is deposited with a low impedance layer such as Indium Tin Oxide (ITO) for use as the ground electrode while the other substrate is

deposited with a uniform layer of high impedance material for use as the control electrode. To use these NLC cells as angular deflectors, voltage is applied between two parallel linear metallic contacts that are deposited at the edges of the control electrode which results in a linearly varying electric field between the front (control) and back (ground) electrodes causing the index to vary linearly across the clear aperture of the device. This index modulation can only be seen by that component of the input polarization that is along the director of the liquid crystal. Thus the PR half-wave plate can be used to control the input polarization for a desired deflection angle of the output beam. For using these NLC cells as reconfigurable lenses, an annular electrical contact is deposited on the periphery of the device aperture. When the control signal is applied, the voltage drops as we move from the edge to the center of the clear aperture in a quadratic fashion. The consequence of this is a lens-like index distribution between the front and back electrode that can be seen by only one polarization of the input laser beam.

### 4.3 Experiment

For the proof-of-concept experiment, the incident laser beam ( $\lambda=1.31\mu\text{m}$ ) was expanded to 5 mm diameter, collimated, and linearly polarized. FLC PRs are used that show a fast 35 $\mu\text{sec}$  switching speed for the scanner at  $\lambda=1.31\mu\text{m}$ . For the voxel scan experiment, two NLC deflectors (D's) and an NLC lens (L), both 5 mm in diameter are used, and each having its own FLC PR. The FLC PRs were antireflection (AR) coated and have a measured average insertion loss of 0.7 dB. This is mainly due to absorption. The non-AR coated NLC deflectors and lenses have an average insertion loss of 0.73 dB, half of which is due to Fresnel reflections. The proof-

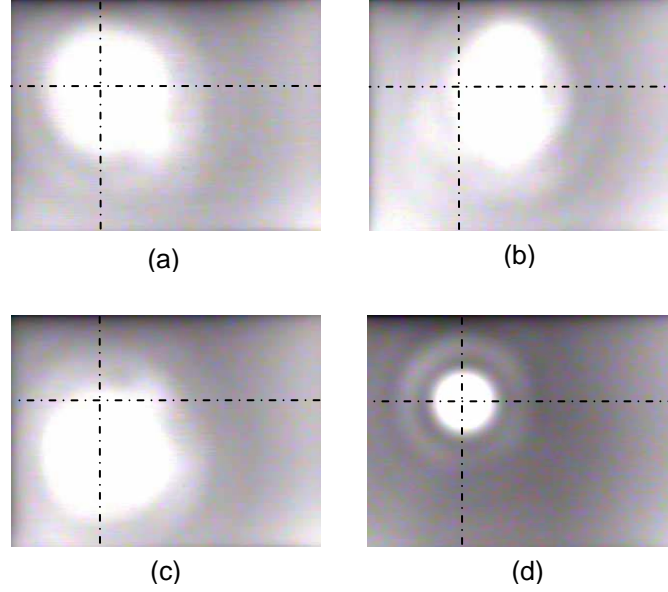


Fig. 4.3. Output scanned beams from the demonstrated 8 point voxel scanner. (a) Incident; (b) x-deflected by 0.66 mrad; (c) y-deflected by 0.75 mrad and (d) z-scan (1.84m P-MOS focal length), beams.

of-concept results for 3-D scanning are shown in Fig. 4.3. Photos are taken at 1.84m distance from the P-MOS end face where the input 5 mm diameter beam focuses when the L is turned on for the focusing effect. Demonstrated are maximum 0.66 mrad and 0.75 mrad deflections in x and y directions, respectively. The Fig. 4.3 photos show slight beam shifts on the infrared (IR) camera due to the short distance between the P-MOS and camera. Slight blooming of the IR camera is observed while near circular scan beam quality is preserved. The demonstrated voxel scanner insertion loss is 4.3 dB and is estimated to be 2 dB given optimal cell designs. Fine continuous analog beamforming reconfiguration of the pixel-free deflectors and lens is also achieved by simply applying a different set of voltages and frequencies in the range of 2 to 10 V and 500Hz to 25 KHz, respectively. Fig. 4.4 shows the demonstration of the P-MOS module as a 2-bit digital lens with four independent focus settings. In this case, two FLC cells and two NLC

lenses were used where the two NLC lenses were preprogrammed for given fixed focal lengths of 3m and 2m with a separation of 6.7 cm between them. These experiments indicate the basic programmability and ease of beamforming controls for the proposed P-MOS, with scanned beams observed via an IR camera showing essentially preserved beam profiles, a feature possible with the non-pixelated scanner design.

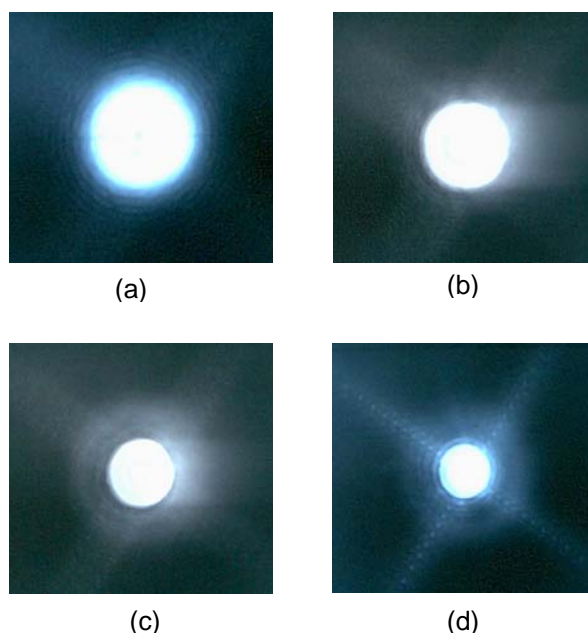


Fig. 4.4. The demonstration of the P-MOS as a 2-bit digital lens. The four photos show the four focal length states of (a) infinity, (b) 3m, (c) 2m, and (d) 1.2m, of the P-MOS exit beam. The distance between the two lenses is 6.7cm.

#### 4.4 Conclusion

In summary, a versatile high speed 3-D scanner design is proposed and demonstrated for optical beamforming applications such as laser communications, 3-D displays, scanning 3-D optical microscopy, data retrieval, and vision applications. The joint digital-analog controls

aspect of the fine P-MOS module is demonstrated via an eight point voxel scan and a 2-bit digital lens scan experiment. To the best of our knowledge, this is the first time such a scanner has been demonstrated. Note that because of the cascaded nature of the P-MOS, care must be taken to reduce voxel scan stages (e.g., ten) to keep losses minimal.

## References

1. A. F. Fray and D. Jones, "Liquid crystal light deflector", U.S. Patent 4066334, 1978.
2. B. Lofving and S. Hard, "Beam steering with two ferroelectric liquid-crystal spatial light modulators", Opt. Lett., Vol. 23, Issue 19, 1541, 1998.
3. M. H. Kiang, O. Solgaard, K. Y. Lau and R. S. Muller, "Electrostatic combdrive-actuated micromirrors for laser-beam steering and positioning", J. of Microelectromechanical Systems, Vol. 7, Issue 1, 27, 1998.
4. R. A. Meyer, "Optical beam steering using a multichannel Lithium Tantalate crystal", Appl. Opt., Vol. 11, Issue 3, 613, 1972.
5. Q. W. Song, X. M. Wang, R. Bussjager and J. Osman, "Electro-optic beam steering device based on a Lanthanum-modified Lead Zirconate Titanate ceramic wafer", Appl. Opt., Vol. 35, Issue 17, 3155, 1996.
6. J. P. Huignard, M. Malard and G. de Corlieu, "Static deflector device for an infrared beam", U.S. Patent 4639091, 1987.
7. P. F. McManamon, E. A. Watson, T. A. Dorschner and L. J. Barnes, "Applications look at the use of liquid crystal writable gratings for steering passive radiation", Opt. Engg., Vol. 32, Issue 11, 2657, 1993.
8. N. A. Riza, "BOPSCAN Technology: A methodology and implementation of the billion point optical scanner", OSA Top. Mtg., Proc. SPIE, Vol. 3482, 572, 1998.



9. N. A. Riza, "Digital control polarization based optical scanner", US Patent 6031658, 2000.
10. W. Klaus, "Development of LC optics for free-space laser communications", Intl. J. Electron. Comm., Vol. 56, Issue 4, 243, 2002.
11. H. Meyer, D. Riekman, K. P. Schmidt, U. J. Schmidt, M. Rahlff, E. Schroder and W. Thust, "Design and performance of a 20-stage digital light beam deflector", Appl. Opt., Vol. 11, Issue 8, 1972.
12. R. McRuer, L. R. McAdams and J. W. Goodman, "Ferroelectric liquid-crystal digital scanner", Opt. Lett., Vol. 15, Issue 23, 1990.
13. C. M. Titus, P. J. Bos and O. D. Lavrentovich, "Efficient, accurate liquid crystal digital light deflector", Proc. SPIE, Vol. 3633, 244, 1999.
14. J. B. Hawthorn, A. Harwit, and M. Harwit, "Laser telemetry from space", Science, Vol. 297, July 26, 2002.
15. A. Purvis, G. Williams, N. J. Powell, M. G. Clark and M. C. K. Wiltshire, "Liquid-crystal phase modulators for active micro-optic devices", Proc. SPIE, Vol. 1455, 145, 1991.
16. R. M. Matic, "Blazed phase liquid crystal beam steering", Proc. SPIE, Vol. 2120, 1994.
17. N. A. Riza and M. C. DeJule, "Three-terminal adaptive nematic liquid-crystal lens device", Opt. Lett., Vol. 19, Issue 14, 1013, 1994.
18. G. Love, J. V. Major and A. Purvis, "Liquid-crystal prisms for tip-tilt adaptive optics", Opt. Lett., Vol. 19, Issue 15, 1170, 1994.

19. G. Vdovin, A. Naumov, M. Loktev, V. Belopukhov, F. Vladimirov, and G. Love, "Wave front control systems based on modal liquid crystal lenses", Rev. Sci. Instrum., Vol. 71, Issue 9, 2000.

## **CHAPTER 5: DEMONSTRATION OF 3-DIMENSIONAL WIDE ANGLE LASER BEAM SCANNER USING LIQUID CRYSTALS**

Design and demonstration of a versatile liquid crystal-based scanner is shown for steering a laser beam in three dimensions. The scanner consists of a unique combination of digital and analog control polarization-based beamforming optics resulting in both continuous and random fashion beam steering. The design features a novel device biasing method, large aperture beamforming optics, low electrical power consumption, and ultra-fine as well as wide angle coarse beam steering. Demonstrations include one, two and three dimensional beam steering with a maximum of  $40.92^\circ$  continuous scan, all at 1550 nm. The minimum scanner aperture is 1 cm diameter and uses a combination of ferroelectric and nematic liquid crystals in addition to Rutile crystal birefringent prisms.

## 5.1 Introduction

An optical scanner is a device that can control the position of a light beam in one or more orthogonal spatial dimensions. As early as the 1960s, researchers have proposed and demonstrated several techniques with varying success that can be used to scan a laser beam. These include scanners based on birefringent crystals,<sup>1-9</sup> nematic liquid crystals (NLCs),<sup>10</sup> ferroelectric liquid crystals (FLCs),<sup>11</sup> optical microelectromechanical systems (MEMS),<sup>12</sup> and ferroelectric electrooptic materials such as lead zirconate titanate.<sup>13,14</sup> Several applications can benefit from 3-D beam steering where a beam of light can be translated in two orthogonal spatial directions transverse to the beam propagation direction as well as be focused/defocused along the propagation direction. The focusing ability is highly desirable in applications where the received information-carrying beam is to be focused on a small detector area, as it will improve the signal-to-noise ratio and hence decrease the probability of error in the received signal. A number of polarization based scanners have been demonstrated which use the property of birefringent media to steer the optical beam in two different directions based upon the state of polarization of the incident light.<sup>15-20</sup> A polarization switch is used to control the state of polarization of the light while a passive birefringent material prism is used to steer the beam into one of the two scanning destinations. By cascading several polarization switch-prism pairs, multiple scan spots can be obtained. The birefringent material prisms used so far have been passive devices whereby the linearly polarized beam incident upon them will generate one of the two fixed spots based upon the state of linear polarization of the incident beam. Apart from birefringent crystals,<sup>1-9,15</sup> these passive birefringent devices have included liquid crystal (LC) filled prisms (i.e., the LC cell

enclosure is shaped like a glass prism).<sup>16,17</sup> This fixed LC prism approach is effective for small (e.g., a few degrees) angular deflections as the preferred molecular orientation of the LC molecules can not be preserved in thicker high birefringence LC cells, leading to increased scattering losses. These previously demonstrated polarization based scanners (Refs. [1-9,15-17]) have been limited to 1-D and 2-D scans with discrete scan beam spots. Other limitations of these scanners have included high drive voltages, pixelation, and non-programmable birefringent plate designs.

In certain applications it is desirable to have the ability to quickly reconfigure the scan directions to cover for errors in the overall scanning system. Such example applications are free-space optical wireless, inter-satellites links, optical microscopy, mobile military platforms, and 3-D displays. For example in free-space optical wireless links, reconfigurability is needed to counter for building sways or temperature and weather fluctuations that cause a variation in the index of the air medium and hence a change in the direction of the outgoing optical beam from the scanning device. In another case, inter-satellite links need fine angular scanning tunability of the order of  $1 \mu\text{rad}$  at high speeds (e.g., 1 KHz)<sup>21</sup> to keep track of the fast moving destination satellite.<sup>22</sup> Yet another case of mobile military platforms needs a scan dynamic range of  $\pm 45^\circ$ .<sup>23</sup> Hence, demand exists for a no moving parts, 3-D scanner that can provide both random and continuously addressable scanning over a large angular scan dynamic range with high resolution beam control.

Recently, such a 3-D scanner was proposed that can continuously scan a large angular dynamic range and has the capability to address the third dimension; i.e., the ability to focus or defocus a beam of light along its direction of propagation.<sup>18</sup> The demonstration showed how large aperture, non-pixelated liquid crystal devices can be used to form a fully programmable high speed

polarization based scanner.<sup>19</sup> In this paper, the ref. 19 concept is extended to demonstrate a 3-D Polarization-Multiplexed Optical Scanner (P-MOS) for random as well as continuous optical scanning over a wide angular dynamic range while maintaining high resolution beam pointing control.<sup>20</sup> Specifically, multiple proof-of-concept experiments at the telecommunications band wavelength of 1550 nm are carried out and results are presented. Video demonstrations of these experiments (Figs. 3,5,7,9 and 10) can be found in ref#20 and the Optics Express website.

<http://www.opticsexpress.org/abstract.cfm?URI=OPEX-12-5-868>

## 5.2 Hybrid Analog-Digital P-MOS Design

In the proposed hybrid analog-digital P-MOS, the state-of-polarization of a linearly polarized incident laser beam is controlled in orthogonal states to achieve beam scanning. As shown in Fig. 5.1, key elements of the proposed P-MOS are a polarization control element and a polarization dependent beam steering element. For polarization control, fast response digitally controlled 90° polarization switches (PSs) are used. For angular scanning, birefringent material prisms (Ws) are used to steer the beam into a desired spot. Using N polarization switch-prism pairs  $2^N$  scan spots can be obtained. For coarse angular scanning, passive birefringent crystal prisms are used. Multiple coarse stages are cascaded to achieve a large angular dynamic range with discrete scan spots. To fill the uncovered spaces between these discrete scan spots, analog-mode electrically controlled NLC prisms are incorporated into the scanner design to realize a true analog-digital hybrid controls scanner. The Fig. 5.1 design shows a P-MOS capable of continuous 1-D scanning where the NLC device acts as an analog control programmable varying

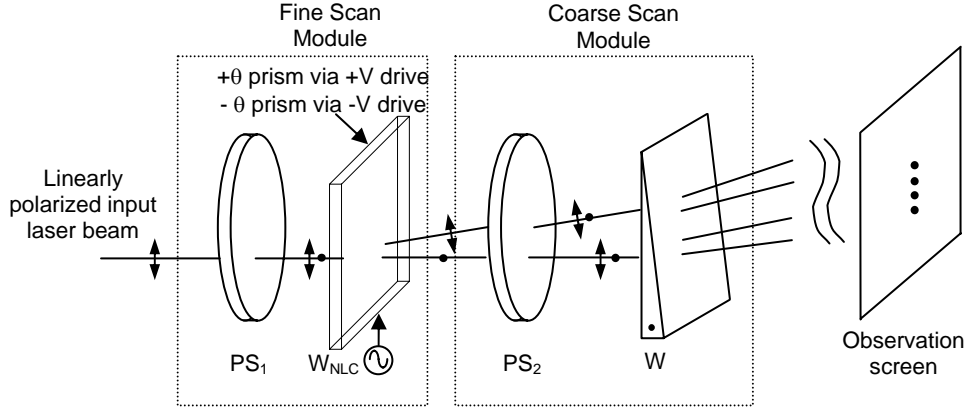


Fig. 5.1. Design of the proposed hybrid analog-digital coarse-fine scan P-MOS module for continuous 1-D scanning. PS:  $90^\circ$  Polarization Switch, W: Passive Crystal Prism; WNLC; Nematic Liquid Crystal Electrically Programmable Prism set for a given drive voltage. Shown are four possible 1-D scan beams produced by digital only switching of the PSs.

tilt prism. Specifically, by switching the electrode drive signal of the NLC device, the tilt direction can be flipped, thus leading to an effective doubling of the NLC prism effect by using just one NLC tilt prism. As later explained in detail, this idea is key to the design of the proposed P-MOS that can allow a high resolution beam scan between the discrete states of the P-MOS.

Recall that in the P-MOS, one PS and one prism combine to form one deflection stage. Moreover, two such 1-D stages can be cascaded in the orthogonal orientation to achieve a 2-D scanner. As opposed to scanners that use pixelated elements for beam scanning where some power is coupled into higher diffraction orders resulting in lower throughput efficiency, the proposed P-MOS design utilizes large-aperture pixel-free devices resulting in diffraction order free beam steering.

LC based devices have also been used to demonstrate focusing/defocusing of laser beams.<sup>18-21,26-27</sup> Due to their birefringent nature, these devices work for only one polarization. If the input light polarization is parallel to the LC molecular director, the light gets focused/defocused; otherwise it passes through the LC cell un-perturbed. Hence, these LC based lenses can be effectively used in 3-D P-MOS scanning.

In order to manipulate the laser beam position at a desired point in space, the linear polarization of the incident beam is controlled using for example, electrically switchable FLC half-wave plates. FLC polarization switches are used because of their fast switching speed (several microseconds), low voltage (e.g.,  $\pm 5$  V) digital operation, and thin cell design. Specifically,  $90^\circ$  polarization rotation is achieved by re-orientation of the FLC director due to Clarke-Lagerwall effect induced by the application of a bipolar electric field across the cell.<sup>24</sup> The retardation for an FLC birefringent phase plate can be expressed by the relation:

$$\Gamma = 2\pi \Delta n \cdot d/\lambda \quad (1)$$

where  $\Delta n$  is the birefringence of the FLC material and  $d$  is the FLC cell thickness. For a given wavelength and FLC material, the thickness of the half wave plate is given as:

$$d = (\lambda \cdot \Delta n) / 2 \quad (2)$$

For  $\lambda = 1550$  nm, the FLC material has a birefringence of 0.14 ( $\Delta n = n_e - n_o = 1.62 - 1.48$ ), giving a half-wave plate thickness of  $5.54 \mu\text{m}$ .<sup>25</sup> Thus a thin FLC cell is formed for effective cascading with the P-MOS design.

For the P-MOS, the NLC prism device is a homogeneously aligned NLC cell with uniform thickness.<sup>26-27</sup> The design is slightly different from an ordinary NLC cell in that the glass substrates are deposited with two different electrodes. One substrate is deposited with a low



impedance layer such as Indium Tin Oxide (ITO) for use as the ground electrode while the other substrate is deposited with a uniform layer of high impedance material for use as the control electrode. To use these NLC cells as angular deflectors, voltage is applied between two parallel linear metallic contacts that are deposited at the edges of the control electrode. This results in a linearly varying electric field between the front (control) and back (ground) electrodes causing the index to vary in a near linear fashion across the clear aperture of the device. This index modulation can only be seen by that component of the input polarization which is along the director of the liquid crystal. As shown in Fig. 5.2, a ray polarized along the molecular NLC director passing through the NLC prism acquires a phase shift at the device position  $x$  that can be expressed as:

$$\phi(V, f, x) = [2\pi/\lambda] n(V, f, x) \cdot d \quad (3)$$

where  $\lambda$  is the optical wavelength,  $d$  is the NLC layer thickness,  $n(V, f, x)$  is the electrically controlled NLC refractive index the light sees, and  $V$  is the amplitude in Volts and  $f$  is the frequency in Hertz of the NLC device drive signal. Looking at the two extreme ray positions of  $x=0$  and  $x=D$ , the beam deflection of the entire wavefront incident on the NLC prism can be studied. Specifically, the  $x=0$  position ray suffers a phase shift given by:

$$\phi(V, f, x=0) = \phi_o = [2\pi/\lambda] n(V, f, 0) \cdot d, \quad (4)$$

while the extreme ray at  $x=D$  suffers a phase shift given by:

$$\phi(V, f, x=D) = \phi_D = [2\pi/\lambda] n(V, f, D) \cdot d. \quad (5)$$

Hence the phase shift between the edges of refracted plane wave exiting the NLC prism is given by:

$$\Delta\phi_A = \phi_D - \phi_0, \quad (6)$$

where between the  $x=0$  and  $x=D$  points, the incident plane wave acquires a linearly increasing phase shift. For state A of the NLC deflector, at  $x=D$ , the applied voltage is below a certain threshold level, so the index seen by the incoming ray of  $p$ -polarization is essentially  $n_e$ , the NLC

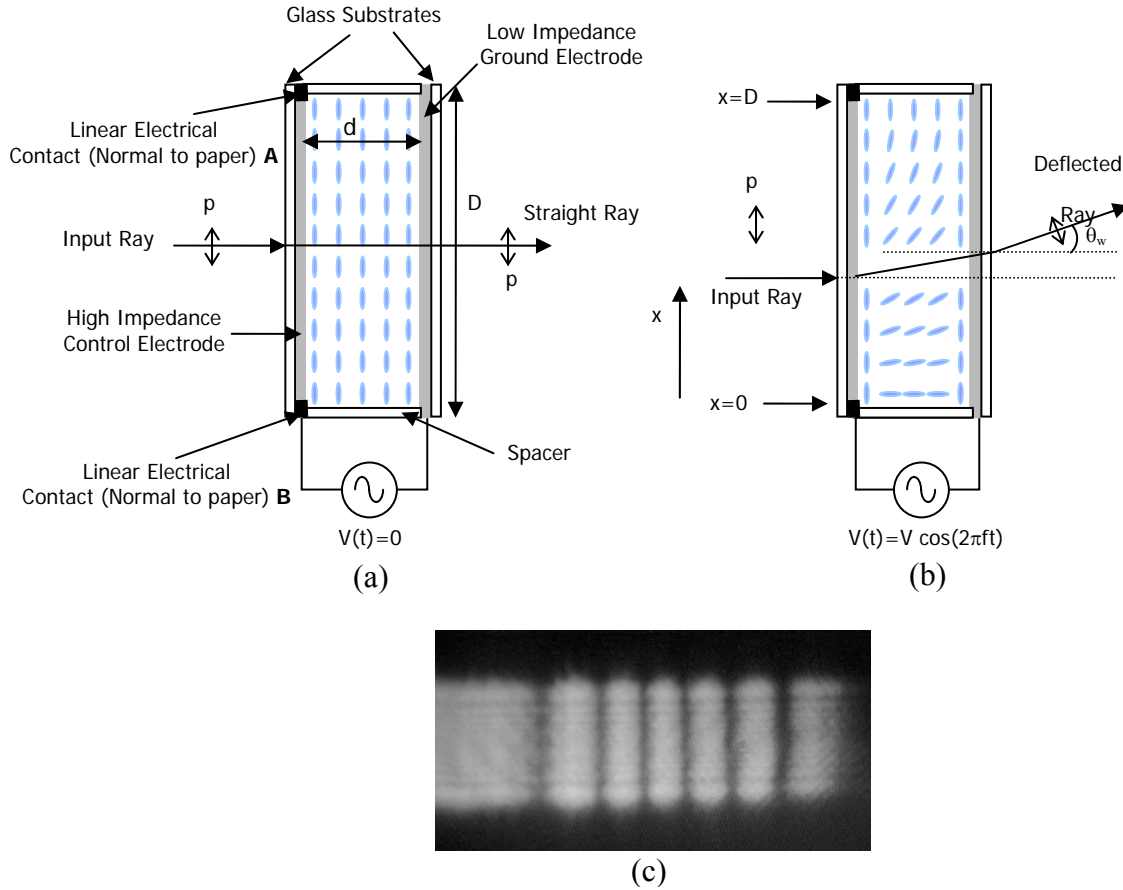


Fig. 5.2. Top views of the NLC prism used for continuous scan in P-MOS. NLC molecule orientations are shown for (a) zero control signal applied, (b) when a control signal is present that reorients the NLC molecules to induce a spatial prism-like refractive index change and (c) the interferogram of the NLC prism using a 1550 nm source. p: horizontally polarized light component.

material extraordinary index of refraction. Therefore  $\phi_D = 2\pi/\lambda \cdot (n_e \cdot d)$  and  $\Delta\phi_A$  becomes:

$$\Delta\phi_A = (2\pi/\lambda) [n_e - n(V, f, 0)] d. \quad (7)$$

Similarly, note that at the  $x=0$  location where the other device electrode is present in state A,  $V$  and  $f$  can be controlled to set  $n(V, f, x=0) = n_o$ , where  $n_o$  is the ordinary refractive index of the NLC material. In this case, the prism is generating its maximum birefringence  $\Delta n = n_e - n_o$  and hence also produces the largest phase shift between rays across the device aperture  $D$ . This in turn leads to the maximum beam deflection angle  $\theta_m$  for the programmable NLC prism. From phased array theory, the beam steered angle  $\theta_{w_i}$  due to an inter-element phase shift  $\Delta\phi_A$  is given by:

$$(2\pi D/\lambda) \sin \theta_{w_i} = \Delta\phi_A, \quad (8)$$

where  $D$  is the phased array inter-element distance or in this case the NLC prism aperture. By equating equations (7) and (8), the electrically controlled prism angle  $\theta_{w_i}$  as seen by a wave polarized along the molecular director is written as:

$$(2\pi D/\lambda) \sin \theta_{w_i} = (2\pi/\lambda) [n_e - n(V, f)] \cdot d \quad (9)$$

This in turn leads to:

$$\theta_{w_i}(V, f) = \sin^{-1} \left\{ \frac{d}{D} [n_e - n(V, f)] \right\}, \quad (10)$$

Since  $\theta_{w_i}$  is a function of the control signal amplitude and frequency, the output can be steered in different directions by controlling the drive signal. This results in an actively reconfigurable prism where the prism apex angle and hence the steering beam direction can be programmed as per demand.

A critical aspect of this NLC deflector device is exploited in the design of the proposed P-MOS; namely, the switching of the drive signals to the two control electrodes on the high impedance substrate of the cell. In effect, for state B of the NLC device,

$$\Delta\phi_B = \phi_D - \phi_0, \quad (11)$$

$$\Delta\phi_B = (2\pi/\lambda) [n(V, f, D) - n_e] \cdot d \quad (12)$$

$$\Delta\phi_B = -\Delta\phi_A \quad (13)$$

Hence, equation (13) implies that in state B of the NLC deflector, the tilt direction is reversed and the tilt angle  $\theta_{w_2} = -\theta_{w_1} = \theta_w$ . In short, an input laser beam can be made to sweep a symmetric positive and negative angle  $\theta_w$  about the laser beam input axis. Using electrical drive switching, thus, the given single NLC deflector device with a fixed maximum birefringence  $n_e - n_o$  can be used to produce double the tilt control as compared to the non-switched NLC deflector device. This specific benefit is exploited in the proposed P-MOS to enable a near continuous beam scan field.

In order to get scanning in the longitudinal direction (along the beam propagation direction), any NLC based lens can be used. The structure of the used NLC lens is very similar to that of the NLC deflector, except for an annular electrical contact that is deposited on the periphery of the device aperture instead of the linear contacts for the deflector. When the control signal is applied across the NLC lens cell using this annular contact, the voltage drops from the edge to the center of the clear aperture in a quadratic fashion. The consequence of this voltage variation is a lens-like index distribution between the front and back electrode of the device that can be seen only by the input light polarization which is parallel to the NLC molecular director.

For an NLC lens with a clear aperture of diameter  $D$  and a cell thickness of  $d$ , the focal length  $F$  using the Fresnel's approximation is given by:<sup>26</sup>

$$F = \frac{D^2}{8d(\Delta n_c - \Delta n_p)} , \quad (14)$$

where  $\Delta n_c$  and  $\Delta n_p$  are the birefringences at the center of the NLC lens cell and the periphery of the annular contact, respectively. Since,  $\Delta n_c$  and  $\Delta n_p$  are a function of the drive voltage and frequency, therefore the focal length  $F$  can be varied by varying the control signal. Moreover, the difference of these two can be made equal to the intrinsic birefringence  $\Delta n$  by controlling the drive signal. So, for an NLC lens cell with 50  $\mu\text{m}$  cell thickness and 5 mm clear aperture diameter, the focal length  $F$  using Merck BL006 ( $\Delta n=0.229$ , see Appendix C) is 27.3 cm at  $\lambda=1550$  nm. Notice that  $F$  will be different for different wavelengths following the birefringence dispersion of the NLC material used. By changing the amplitude and frequency of the applied signal, the lens power can be varied in a desired fashion to focus the laser beam at a desired spot along the propagation direction. Use of these NLC lenses with the earlier described deflectors can result in realizing 3-D beam scanning.

As mentioned earlier, in order to get large angular deflections, the P-MOS also uses fixed birefringent crystal prisms. The optic axis (c-axis) of the birefringent crystal prism can be oriented such that the  $s$  and  $p$  polarizations each experience a different index of refraction. At the entrance face the following relation holds true:

$$n_{\text{inc}} \sin \theta_{\text{inc}} = n_o \sin \theta_o = n_e \sin \theta_e , \quad (15)$$

where  $n_{\text{inc}}$  is the index of refraction of the material surrounding the birefringent crystal prism,  $\theta_{\text{inc}}$  is the angle of incidence with respect to the normal to the prism entrance surface, and  $\theta_o$  and  $\theta_e$

are the refracted angles inside the birefringent material as seen by the ordinary  $n_o$  and extra-ordinary  $n_e$  indices, respectively. At the exit face we have:

$$\theta_{\text{exit}[o]} = \sin^{-1}[n_o \sin (\theta_o + \alpha)/n_{\text{inc}}] - (\alpha + \theta_{\text{inc}}) \quad (16)$$

$$\theta_{\text{exit}[e]} = \sin^{-1}[n_e \sin (\theta_e + \alpha)/n_{\text{inc}}] - (\alpha + \theta_{\text{inc}}) , \quad (17)$$

where  $\alpha$  is the apex angle of the prism and  $\theta_{\text{exit}}$  is measured from the incident beam direction. In the case when  $n_{\text{inc}} = 1$  and the first prism (in a cascade of such birefringent crystal prisms) interface is normal to the incident light propagation direction,  $\theta_{\text{inc}} = 0$ , equations (16) and (17) reduce to:

$$\theta_{\text{exit}[o]} = \sin^{-1}[n_o \sin (\alpha)] - \alpha \quad (18)$$

$$\theta_{\text{exit}[e]} = \sin^{-1}[n_e \sin (\alpha)] - \alpha \quad (19)$$

$$\Delta\theta = \theta_{\text{exit}[e]} - \theta_{\text{exit}[o]} . \quad (20)$$

Successive application of the boundary conditions gives the exit angles from a birefringent crystal prism. As seen from equations (16-20), the angular separation,  $\Delta\theta$ , between the ordinary and the extra-ordinary components of the light emerging from the prism depends upon the angle of incidence, the two indices and the apex angle of the prism. For large index or large apex angle the angular separation is larger. Also, higher birefringence will result in larger separation. Another important point to note is that two different materials with the same value for birefringence  $\Delta n$  but with different average index will result in different values for angular separation where we assume the same apex and incidence angles. Although large index of refraction is desirable as it results in thinner angular prisms, these prisms must be carefully coated with anti-reflection layers to reduce Fresnel reflections from the prism surfaces. Fresnel

reflections are an important aspect to consider in a cascaded design as they can cause high insertion losses for the proposed scanner. Moreover, one needs to make sure that the absorption coefficient of the material is small in the wavelength band of operation of the P-MOS.

### 5.3 Experiments

The goals of the P-MOS experiment are to demonstrate large angular scans as well as 3-D scans in both random and continuous fashion. Multiple experiments were conducted to demonstrate beam deflection in one, two and three dimensions. All the experiments were conducted at the telecommunications band wavelength of 1550 nm using a 0.5 mm  $1/e^2$  diameter collimated beam from a fiber coupled semiconductor laser. In the first experiment, 1-D beam deflection is demonstrated in digital (random access) fashion where a single birefringent crystal prism made of Rutile ( $n_e=2.454$ ,  $n_o=2.71$  @  $\lambda=1550$  nm) and an NLC (Merck BL006,  $\Delta n=0.229$  at 1550 nm and 25° C, see Appendix C) prism are used to scan the beam into  $2^2=4$  spots. The Rutile prisms have a clear aperture of 2 cm x 2 cm and are anti-reflection (AR) coated. The non-AR coated NLC cell used has a 5 mm aperture and a 50  $\mu$ m thickness. The configuration used is exactly that of Fig. 5.1. Two FLC polarization switches are used to control the polarization of the 1550 nm laser beam in digital fashion in order to address these 4 spots. Figure 5.3 shows the resulting experimentally measured far-field spot pattern for this experimental configuration. The two yellow spots show the birefringent crystal prism deflection spots whereas the white spots are from the NLC prism deflection. Notice that in this demonstration the NLC prism is always

turned on with a given fixed voltage/frequency drive and only the beam polarization is controlled to produce the scanning far field spot pattern.

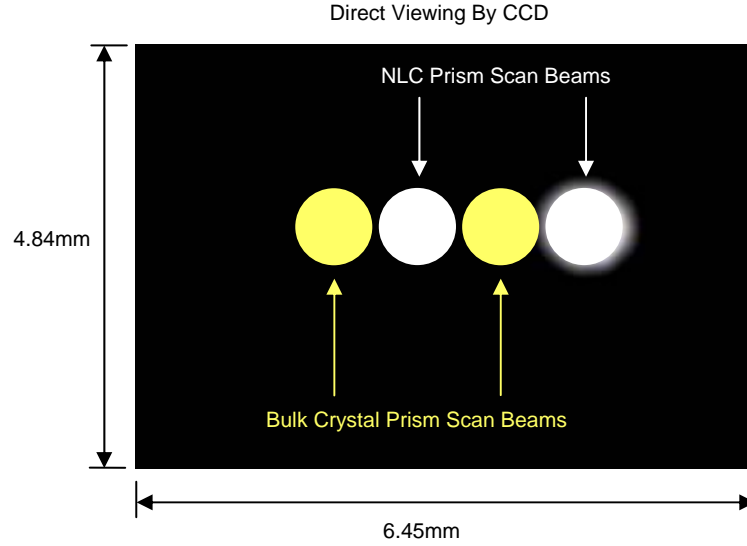


Fig. 5.3. Experimentally obtained far-field spot pattern for a basic 2-stage 1-D coarse-fine P-MOS demonstration at 1550 nm.

An important aspect of the NLC prism cell is highlighted in Fig. 5.4(a); namely the bias switching controls for the NLC prism as discussed earlier in Eq. (13). In Fig. 5.4(b-d), effective NLC cell shape and beam deflections for a two stage P-MOS are shown where one NLC prism and one birefringent crystal prism have been used as outlined in the design of Fig. 5.1. In Fig. 5.4 (b), when the drive signal is in the OFF state, the NLC cell acts as an ordinary birefringent material cell, causing a uniform phase retardation throughout the NLC cell aperture. The birefringent crystal prism in Fig. 5.4(b) causes the beam to be steered into two different spots K and L depending upon the polarization of the incoming laser beam. For simplicity, the FLC PSs have not been shown in Fig. 5.4. In Fig. 5.4(c), when the switch is thrown to state A (i.e., when



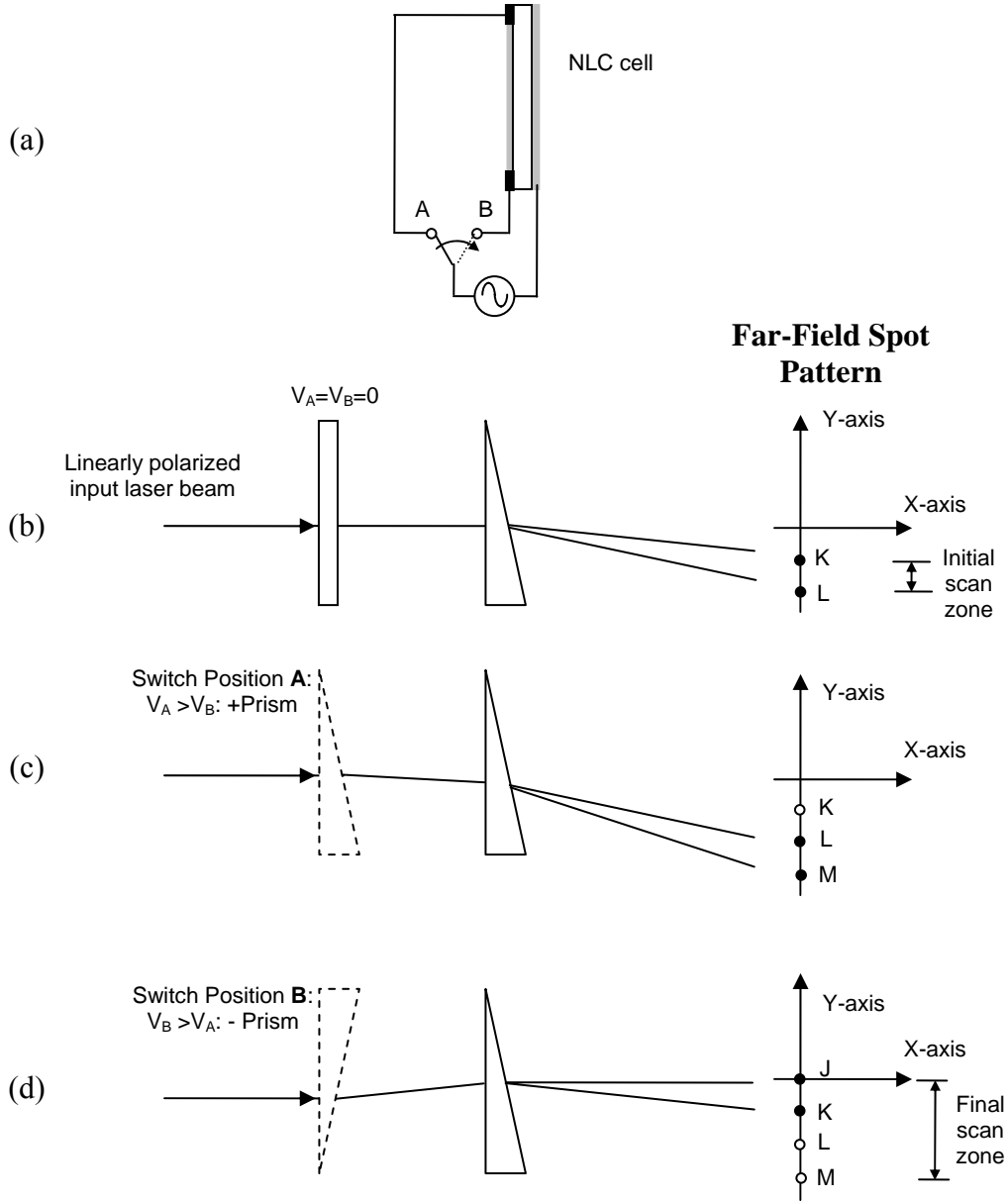


Fig. 5.4. (a). Proposed Biasing Technique for the NLC prism. (b-d): The effective NLC cell shape and beam deflections for a two stage P-MOS where one NLC prism and one birefringent crystal prism have been used as shown in Fig. 4.1. Shown are NLC device states when (b): drive signal is OFF, (c): switch is set to state A (i.e., when  $V_A > V_B$ ), and (d): switch is in state B (i.e., when  $V_B > V_A$ ). Dark spots along the Y-axis represent the far-field spots as produced by the

shown NLC device state while the white spots represent the total scan spots possible including those from the alternative NLC device states.

$V_A > V_B$ ), an index ramp is formed across the NLC cell aperture converting it into an effective prism that will deflect the light polarized along the NLC molecular director. This process in-turn causes the two deflections from the birefringent crystal prism to be shifted to the L and M positions and the angular scan to be doubled in the small angle approximation regime (i.e.,  $\sin \theta \cong \theta$ ) as compared to the case when only a single birefringent crystal prism is used. Figure 5.4 (d) shows the case when the switch is set to state B (i.e., when  $V_B > V_A$ ) causing an index ramp in the direction opposite to the previous case, resulting in the output beam from the two stage P-MOS to be steered into positions J and K. These corresponding far-field spots are shown at the right of Figs. 5.4(b-d). As can be seen from the far-field spot pattern in Fig. 5.4(d), the scan zone is three times the scan zone when the NLC prism was not used. If instead of the NLC prism device, another birefringent crystal prism is used with the same apex angle, the total scan zone is only doubled and not tripled. In addition, when using the fixed apex angle prisms (such as birefringent crystal prisms or LC filled passive prisms), there is no mechanism for covering the intermediate space between the spots from these prisms. Hence, the unique electrode bias switching not only increases the scan zone, but via NLC device drive signal amplitude and frequency control actively covers the intermediate space between the birefringent crystal prism scan spots (as demonstrated in a later video, Fig. 5.7).

In the second experiment, 1-D large angular beam deflection is demonstrated where four birefringent crystal prisms and four FLC polarization switches are used to scan the beam into  $2^4 = 16$  spots. The angular scan dynamic range is  $33.11^\circ$  as shown by the red star \* data-set in Fig.

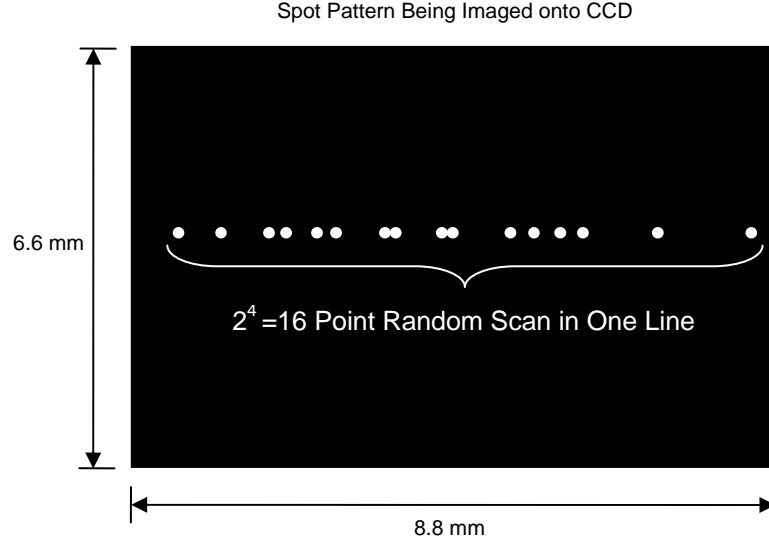


Fig. 5.5. Experimentally obtained far-field spot pattern for 4-stage 1-D coarse digital P-MOS demonstration at 1550nm.  $\alpha_1 = -9.95^\circ$ ,  $\alpha_2 = 19.95^\circ$ ,  $\alpha_3 = 4.95^\circ$  and  $\alpha_4 = 9.95^\circ$  using Rutile prisms ( $n_e = 2.454$ ,  $n_o = 2.71$  @  $\lambda = 1550\text{nm}$ ).  $\alpha$ : apex angle of prism.

5.6 and the video image in Fig. 5.5. The maximum angular separation between any two spots in this experiment is  $7.12^\circ$  as shown by the difference between polarization states#15 and 16 (see Fig. 5.6). As noted from equations (16-20), the linear approximation to Snell's law can not be applied for large angles and hence as the deflection angle increases, so does the non-linearity in the angular separation between scan points. In order to cover for such non uniform angular separation of the far field spot pattern, an NLC prism is introduced at the input to the first stage in the P-MOS setup. The NLC device molecular director is oriented along the incident laser beam polarization direction ( $p$  in this case). Computer based simulation are carried out in order to determine the desired electrically controlled angle of the NLC prism device to completely fill

the gaps between the spot pattern. As shown in Fig. 5.2, since the NLC prism has two linear contacts at the edges of the control electrode marked A and B, one of the contacts is set at the threshold voltage for the NLC cell. At the other contact, a higher voltage is applied such that an index ramp is formed in the NLC cell along, say, +x-dimension which results in a thin optical prism that can be seen by only one polarization component ( $p$  in this case). Controlling the

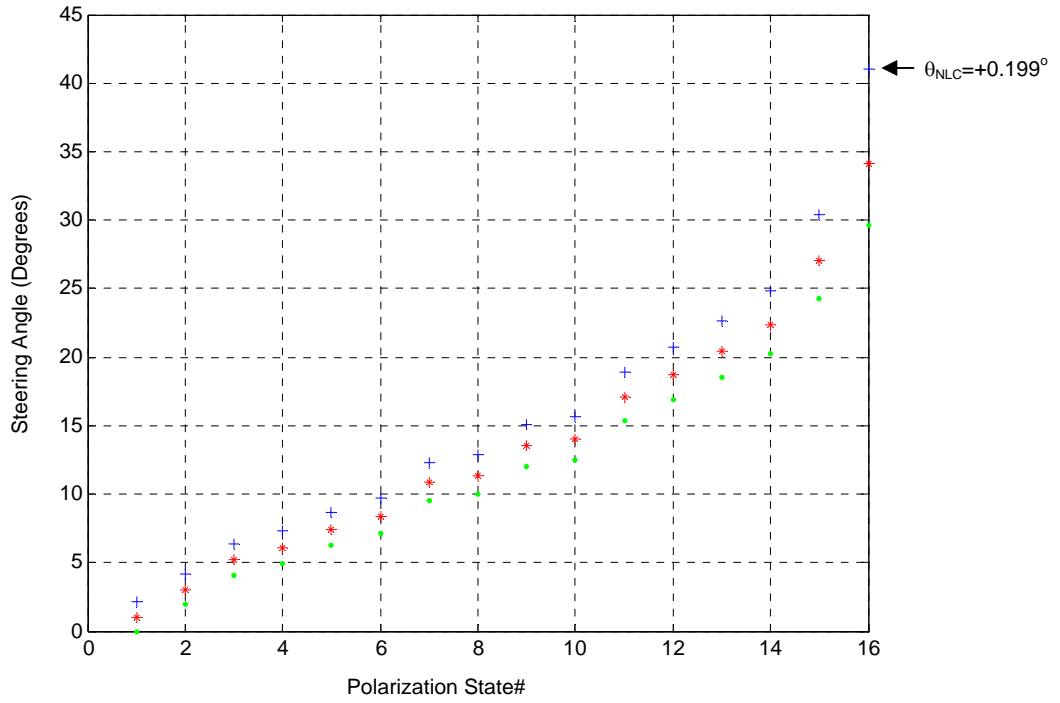


Fig. 5.6. Simulated steering angles for a 4-stage coarse and one stage fine 1-D digital P-MOS at 1550 nm that can continuously access any spot within a  $40.92^\circ$  wide scan domain.  $\alpha_{LC} = \pm 0.35^\circ$ ,  $\alpha_1 = -9.95^\circ$ ,  $\alpha_2 = 19.95^\circ$ ,  $\alpha_3 = 4.95^\circ$  and  $\alpha_4 = 9.95^\circ$  using Rutile prisms ( $n_e = 2.454$ ,  $n_o = 2.71$  @  $\lambda = 1550$  nm).

potential difference between these two metallic contacts results in varying the optical prism apex angle. As mentioned earlier, by swapping the voltage levels between these two contacts, the index ramp and hence the prism angle can be formed along the -x-dimension. The simulation was carried out keeping in mind this dual nature of the given NLC device prism angle. From the conducted simulation, the NLC prism angle  $\pm\theta_w$  needed for completely filling this experimental design spot pattern is found out to be  $\pm 0.35^\circ$ . The resulting range of angles that can be accessed by this experimental P-MOS scanner are shown in Fig. 5.6 by the dataset labeled green star \* and blue cross + for  $-\theta_w$  and  $+\theta_w$ , respectively. The NLC prisms used had a cell thickness of 50  $\mu\text{m}$  and a clear aperture of 5 mm. The maximum prism angle  $\theta_w$  that was obtained from these

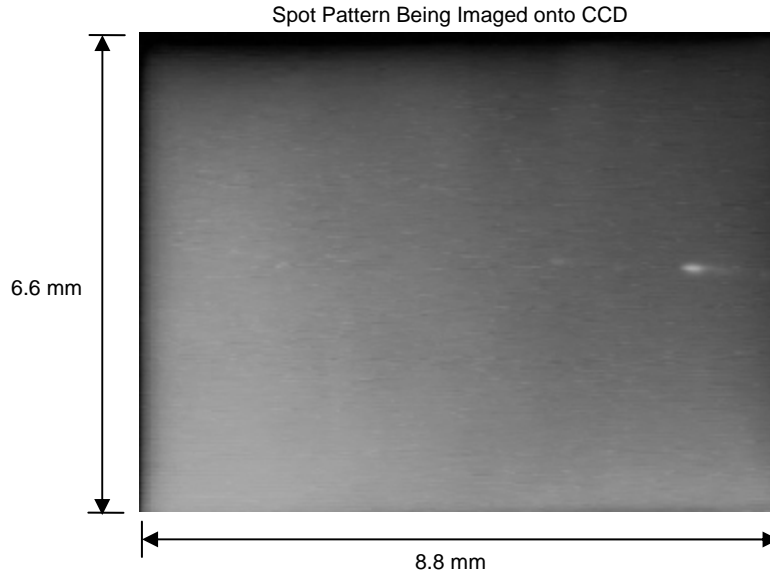


Fig. 5.7. Demonstration of continuous steering using NLC prism in the 4-stage coarse 1-D P-MOS scanner of Fig. 5.5.  $\alpha_{\text{NLC}} = \pm 0.35^\circ$  (NLC: Merck BL006,  $\Delta n = 0.229$  at 1550 nm and  $25^\circ \tilde{C}$ , see Appendix C).

devices was  $0.131^\circ$ , so three of the NLC prism devices were cascaded to form an equivalent NLC wedge in order to achieve a continuously tunable scan of  $0.35^\circ$ . The experimental scanning demonstration works as follows: All the PSs are controlled such that the scanner output beam corresponds to a certain polarization state#, say, for example 1. The NLC wedge module is driven with voltages that result in  $\theta_w = -0.35^\circ$ . The output beam from the scanner corresponds to the initial or starting point for the scan domain. The polarization switches are kept in the same state and the NLC drive signal is varied such that  $\theta_w$  decreases gradually from  $-0.35^\circ$  to  $0^\circ$  which is also the state corresponding to the spot generated by the bulk crystal prisms in the absence of the NLC prism in polarization state#1. Then the voltage levels between the two metallic contacts A and B are inter-changed so that the NLC index ramp corresponds to a positive angle  $+\theta_w$  and the drive signal is varied such that  $\theta_w$  increases from  $0^\circ$  to  $+0.35^\circ$ . Once, the maximum  $0.35^\circ$  has been reached, the control state of the PSs is varied such that they correspond to polarization states#2. Again, the NLC prism angle  $\theta_w$  is varied, following the same sequence as in polarization state#1, i.e., from  $-0.35^\circ$  to  $+0.35^\circ$ . Once the maximum  $\theta_w$  is reached, the polarization state can be switched to the next higher level and the same sequence of steps is followed until the whole scan domain is accessed in this manner. It can be noticed from Fig. 5.6 that in some of the polarization states, the steering angle values overlap with the adjacent polarization states. This means that in order to scan the angular zone corresponding to such a polarization state, scanning will start with an intermediate value of  $\theta_w$ . A look-up table for NLC drive specifications versus steering angle can be followed in this regard to avoid overlapped scanning zones. Similarly, in the final polarization state#16, the maximum steering angle ( $40.92^\circ$ ) is achieved with a value of  $\theta_w=0.199^\circ$  which is less than the maximum value of  $\theta_w$  as in

this configuration of the scanner, any value of  $\theta_w$  higher than  $0.199^\circ$  results in total internal reflection inside the last birefringent crystal prism. Hence, by controlling the polarization state and the NLC prism drive signals, a total steering angle of  $40.92^\circ$  can be obtained in the current configuration. For demonstration purposes, in Fig. 5.7, continuous scanning is shown between the final two polarization states (i.e., #15 & #16) since they constitute the worst case scenario where  $7.12^\circ$  of angular separation lies between these two spots.

Throughput efficiency was measured for the far field spot pattern for the 16-point random scan (dataset \* of Fig. 5.5) as shown in Fig. 5.8. It is observed that the throughput efficiency remains more or less constant in a broad angular range and decreases gradually as the steering angle reaches the maximum. The insertion loss for the experimental non-AR coated NLC prism was measured to be 0.73 dB which includes 0.35 dB loss from Fresnel reflections. The average insertion loss for the 1" diameter FLC PS's was measured to be 0.7 dB at 1550 nm while their average optical polarization extinction ratio was 28 dB. The Rutile prisms had a 2 cm x 2 cm face area, were AR coated and had an average insertion loss of 0.04 dB. The insertion loss for these prisms varies as the angles of incidence and exit vary as shown by experimental data in Fig. 5.8. For the demonstrated 4-stage hybrid analog-digital P-MOS, the total average insertion loss is  $\sim 5$  dB ( $= 3 \times 0.73$  (For 3 NLCs) +  $4 \times 0.7$  (For 4 FLC PSs)). This number is reduced to  $\sim 3.93$  dB when a single AR coated NLC device is used instead of three NLC devices.

Experiments were also carried out to demonstrate the capability of the P-MOS to steer the beam in two and three dimensions. Fig. 5.9 shows a 4-stage P-MOS, where two birefringent crystal prisms and two NLC prisms are used to digitally access 16-spot pattern (4-bit) in a two dimensional grid in the far-field. Recall that each stage has its own polarization switch. One birefringent crystal prism and an NLC prism are used to address each dimension. In the Fig. 5.10

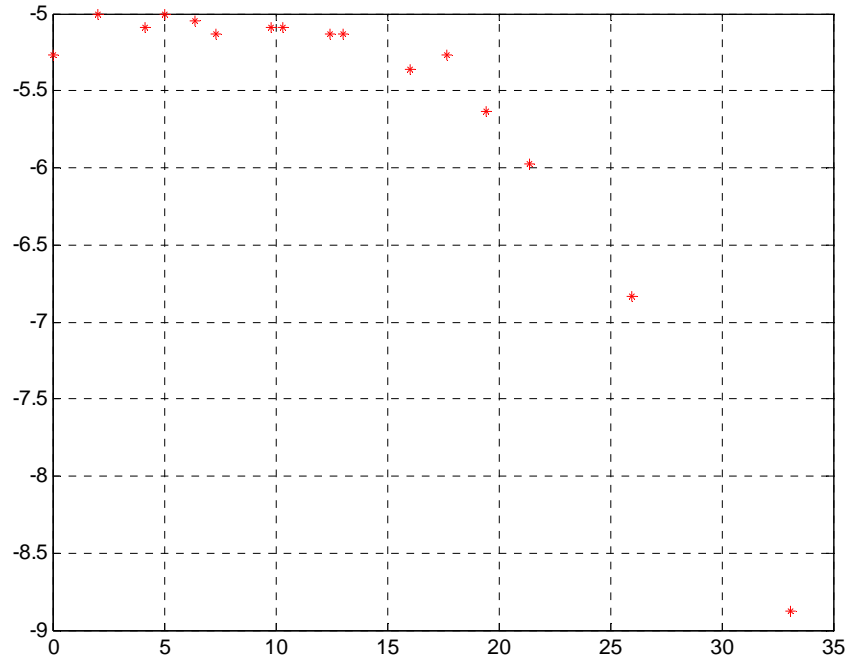


Fig. 5.8. Experimentally measured scanner optical throughput variation for the 4-stage 1-D coarse digital P-MOS demonstration at 1550 nm.

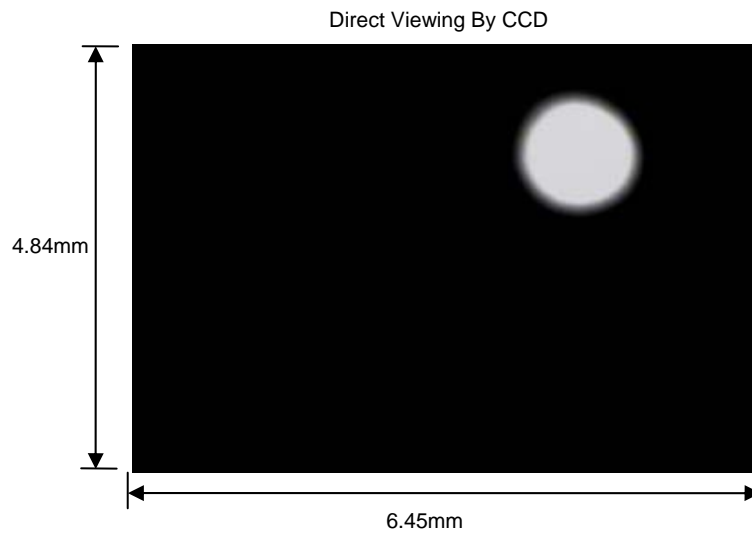


Fig. 5.9. Experimentally obtained 2-D far-field spot pattern for 2-stage coarse and 2-stage fine P-MOS demonstration at 1550 nm.



demonstration, a 2-stage coarse and 3-stage fine P-MOS is used to address all three dimensions in a single scanner. The two coarse stages consist of birefringent crystal prisms while the three fine stages consist of two NLC prisms and a single NLC lens device.<sup>19</sup> The NLC lens is used to scan the third dimension; i.e., to focus or defocus the beam along its direction of propagation. The goal of this experiment was to demonstrate the capability of the P-MOS to scan all three dimensions in a desired fashion.

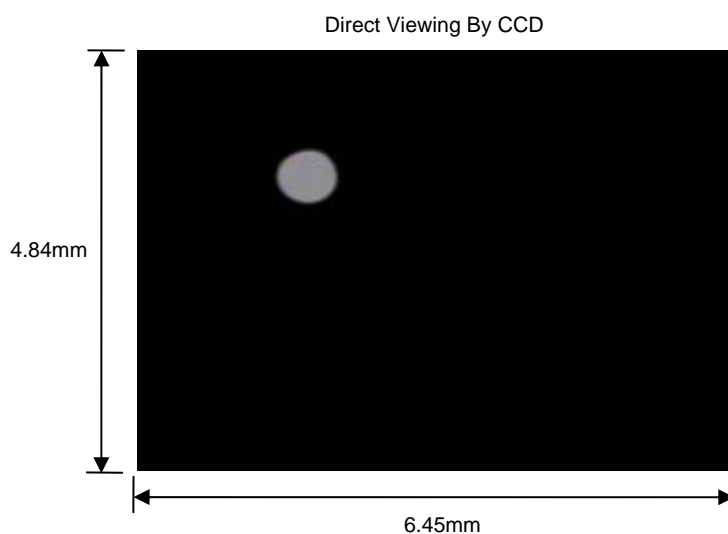


Fig. 5.10. Experimentally obtained 3-D spot pattern for 2-stage coarse and 3-stage fine P-MOS demonstration at 1550 nm.

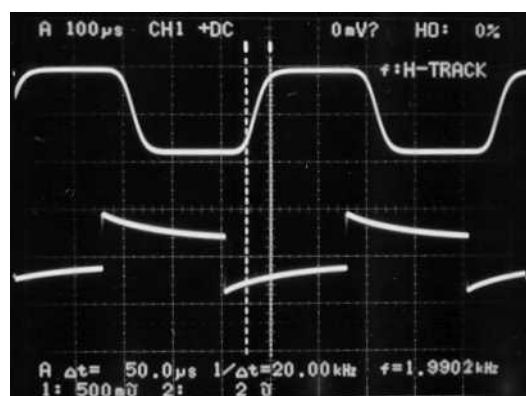


Fig. 5.11. Experimentally measured rise time for the FLC PS used in P-MOS demonstration at 1550 nm.

In the parallel drive P-MOS architecture, the scanner response time will depend upon the slowest device in the system. In a P-MOS where only birefringent crystal and fixed drive voltage LC prisms are used for scanning with actively driven FLC PSs, the scanner response time will be equal to a single FLC PS's response time. Figure 5.11 shows the measured 50  $\mu$ sec fast response of the demonstrated FLC half wave plate at  $\lambda=1550$  nm, alongwith the corresponding drive signal. Hence in the hybrid P-MOS where both birefringent crystal prisms and actively driven NLC prisms are used for scanning, the limiting factor for the response time is the NLC prism.

In order to get the relatively large NLC prism angles such as  $0.35^\circ$  with a fast response time, multiple thin NLC cells can be cascaded in order to achieve the total angle of  $0.35^\circ$ . In this way, a scanning speed of the order of a few milliseconds can be achieved with the NLC device although at the expense of throughput efficiency. Today, research is being conducted in the area of high birefringence materials that have low viscosity.<sup>28</sup> Use of such materials will further reduce the response time of the NLC prism down into the sub-millisecond regime.

#### 5.4 Conclusion

In summary, we have demonstrated a versatile polarization based scanner design that is well suited for optical beamforming applications such as freespace laser communications, 3-D displays, scanning 3-D optical microscopy, and data retrieval applications. Specifically, for the first time, 1550 nm band random as well as continuous mode large  $40.92^\circ$  angle beam steering is experimentally demonstrated using a unique hybrid analog-digital mode P-MOS architecture that possesses high beam quality and minimal pixel-based high order diffractive effects. In particular,

a unique electrical biasing control of the active NLC prism devices is used to provide a near continuous and high resolution beam scan over a wide angular dynamic range. Video demonstrations include one, two and three dimensional beam steering experiments.

## References

1. U. J. Schmidt, "Optical processing of information," 1962 Proc. Washington Symposium, Eds. D. Pollock, C. Koester and J. Tippet, pages 98-103, Spartan, Washington, D.C, 1963.
2. W. Kulcke, T. Harris, K. Kosanke, E. Max, IBM J. Res. And Develop., Vol. 8, Pages 64-67, 1964.
3. T. Nelson, Bell Sys. Tech. J., Vol. 43, Pages 821-845, 1964.
4. W. Tabor, Bell Sys. Tech. J., Vol. 43, Pages 1153-1154, 1964.
5. U. J. Schmidt, "A high speed digital light beam deflector," Physics Letters, Vol. 12, Issue 3, Pages 205-206, (Oct. 1964).
6. R. A. Soref, D. H. McMahon, "Optical design of Wollaston-prism digital light deflectors," Applied Optics, Vol. 5, Issue 3, Pages 425-434, (Mar. 1966).
7. W. Kulcke, K. Kosanke, E. Max, M. A. Habegger, T. J. Harris, H. Fleisher, "Digital light deflectors," Applied Optics, Vol. 5, Issue 10, Pages 1657-1667, (Oct. 1966).
8. V. J. Fowler, J. Schlafer, "A survey of laser beam deflection techniques," Applied Optics, Vol. 5, Issue 10, Pages 1675-1682, (Oct. 1966).
9. T. C. Lee and J. D. Zook, "Light beam deflection with electrooptic prisms," IEEE Journal of Quantum Electronics, Vol. 4, Issue 7, Pages 442-454, (Jul. 1968).
10. A. F. Fray and D. Jones, "Liquid crystal light deflector," U.S. Patent 4066334, (1978).
11. B. Lofving and S. Hard, "Beam steering with two ferroelectric liquid-crystal spatial light modulators," Opt. Lett., Vol. 23, Issue 19, Pages 1541-1543, (1998).

12. M. H. Kiang, O. Solgaard, K. Y. Lau and R. S. Muller, "Electrostatic combdrive-actuated micromirrors for laser-beam scanning and positioning," *Journal of Microelectromechanical Systems*, Vol. 7, Issue 1, Pages 27-37, (1998).
13. R. A. Meyer, "Optical beam steering using a multichannel lithium tantalate crystal," *Appl. Opt.*, Vol. 11, Issue 3, Pages 613-616, (1972).
14. Q. W. Song, X. M. Wang, R. Bussjager and J. Osman, "Electro-optic beam-steering device based on a lanthanum-modified lead zirconate titanate ceramic wafer," *Appl. Opt.* Vol. 35, Issue 17, Pages 3155-3162, (1996).
15. H. Meyer, D. Riekman, K.P. Schmidt, U. J. Schmidt, M. Rahlff, E. Schroder and W. Thust, "Design and performance of a 20-stage digital light beam deflector," *Appl. Opt.*, Vol. 11, Issue 8, Pages 1732-1736, (1972).
16. R. McRuer, L. R. McAdams and J. W. Goodman, "Ferroelectric liquid-crystal digital scanner," *Opt. Lett.*, Vol. 15, Issue 23, Pages 1415-1417, (1990).
17. C. M. Titus, P. J. Bos and O. D. Lavrentovich, "Efficient, accurate liquid crystal digital light deflector," *Proc. SPIE*, Vol. 3633, Page 244, (1999).
18. N. A. Riza, "Digital control polarization based optical scanner," US Patent 6031658, (2000).
19. N. A. Riza and S. A. Khan, "Programmable High Speed Polarization Multiplexed Optical Scanner," *Opt. Lett.*, Vol. 28, Issue 7, Pages 561-563, (2003).
20. S. A. Khan and N. A. Riza, "Demonstration of 3-dimensional wide angle laser beam scanner using liquid crystals," *Optics Express*, Vol. 12, Issue 5, Pages 868-882, (March 2004).

21. W. Klaus, "Development of LC optics for free-space laser communications," International Journal of Electronic Communications, Vol. 56, Issue 4, Pages 243-253, (2002).
22. J. B. Hawthorn, A. Harwit, and M. Harwit, "Laser telemetry from space," Science, Vol. 297, July 26, (2002).
23. B. W. Matkin, "Steered agile beams program support for Army requirements," Proc. SPIE, Vol. 4489, 1-12, Free-Space Laser Communication and Laser Imaging; David G. Voelz, Jennifer C. Ricklin; Eds, 46th Annual Meeting of SPIE, 29 July - 3 August (2001).
24. P. Yeh and C. Gu, *Optics of Liquid Crystal Displays*, (John Wiley & Sons Inc., New York, 1999).
25. FLC Liquid Crystal Light Valves User Manual, Displaytech Inc., Longmont, CO, USA, (1996).
26. M. Yu. Loktev, V. N. Belopukhov, F. L. Vladimirov, G. V. Vdovin, G. D. Love and A. F. Naumov, "Wave front control systems based on modal liquid crystal lenses," Review of Scientific Instruments, Vol. 71, Issue 9, Pages 3290-3297, September (2000).
27. N. A. Riza and M. C. DeJule, "Three-terminal adaptive nematic liquid-crystal lens device," Opt. Lett., Vol. 19, Issue 14, Pages 1013-1015, (1994).
28. S. Gauza, H. Wang, C. H. Wen, S. T. Wu, A. Seed, and R. Dabrowski, "High Birefringence Isothiocyanato Tolane Liquid Crystals," Japanese Journal of Applied Physics Part I, Vol. 42, Pages 3463-3466, (2003).

## **CHAPTER 6: LIQUID CRYSTAL DEFLECTOR BASED VARIABLE FIBER-OPTIC ATTENUATOR**

A compact, low component count, no-moving parts Variable Optical Attenuator (VOA) is demonstrated for the first time using beam spoiling implemented via an electrically reconfigurable non-pixelated Nematic Liquid Crystal (NLC) deflector. The VOA design features an in-line alignment polarization insensitive design without the use of bulky polarization splitting and combining optics. The proof-of-concept VOA at 1550 nm demonstrates 30 dB attenuation range, 2.5 dB insertion loss,  $\leq 0.8$  dB polarization dependent loss (PDL) and a 1 second maximum attenuation reset time. The VOA design can counter performance reducing environmental effects such as excess loss increase due to temperature variations.

## 6.1 Introduction

As the demand for high data rate telecommunication networks increases, optical devices are sought that are low in cost, utilize little drive power, and have broadband robust operation. The Variable Optical Attenuator (VOA) is one such component that is needed in wavelength division multiplexed (WDM) systems to dynamically control the channel power per wavelength. A variety of technologies have been proposed to realize single channel VOAs such as micro-mirrors<sup>1</sup>, acousto-optics<sup>2</sup>, and thermo-optics<sup>3,4</sup>. Liquid crystals (LCs), because of their no moving parts, low loss, and low power consumption nature have long been considered an excellent alternative for making optical components.<sup>5</sup> Specifically analog operation<sup>6-8</sup> and all-digital operation LC VOAs<sup>9,10</sup> have also been proposed. An issue with polarization controlled LC VOAs is their need to use bulky polarization beam displacement and combining optics such as crystal beam displacement prisms (BDPs) to enable polarization independent designs. In addition, these VOAs are extremely sensitive to polarization extinction changes such as due to temperature swings in the LC cells that in-turn lead to unwanted VOA light throughput fluctuations. In effect, any deterioration in LC cell polarization extinction ratios causes useful signal light to be rejected via the combining BDP. Thus, an LC VOA that can counter this excess loss variation problem would be highly desirable.

Recently, a simple LC VOA structure was proposed that forms a compact VOA that does not use BDPs and moreover can eliminate the extinction ratio-based loss throughput problem.<sup>11</sup> Specifically, this VOA design implements attenuation via the use of LC-based optical beam



spoiling. The rest of the work for the first time describes the design and demonstration of this fiber-optic VOA using a non-pixelated NLC deflector device to implement beam spoiling.

## 6.2 Variable Optical Attenuator Theory

Figure 6.1(a) shows one in-line design of the proposed Nematic Liquid Crystal (NLC) deflector-based VOA using self-imaged identical fiber Gradient Index (GRIN) rod lenses.<sup>12</sup> The two GRIN lenses are separated by  $2d$ , where  $d$  is the beam waist location distance leading to a low loss design. Two NLC deflectors with orthogonal NLC directors are placed between the GRIN lenses. Figure 6.1(b) shows the second approach to realize the VOA using a dual fiber collimator, a single NLC deflector, and a  $45^\circ$  power Faraday rotator-mirror pair. This reflective design results in a compacter architecture as compared to that of Figure 6.1(a). Finally, Figure 6.1(c) shows the third proposed in-line VOA design that takes advantage of today's highly low loss (e.g.,  $<1$  dB) compact optical circulator devices. In the absence of any NLC device control signal, all input light is directed to the desired VOA output port. For VOA control, the amplitude and frequency of the NLC deflector electrical drive signals are varied to implement beam deflections leading to the desired VOA attenuation level.

The NLC deflector is different from an ordinary parallel rub NLC cell in that instead of having the NLC layer sandwiched between two Indium Tin Oxide (ITO) electrodes, the NLC material is sandwiched between an ITO electrode which acts as the ground electrode, and a high impedance control electrode (see Fig. 6.2(a)). Earlier, the use of a high resistance layer with two parallel electrical contacts was proposed to generate a smooth voltage ramp between these

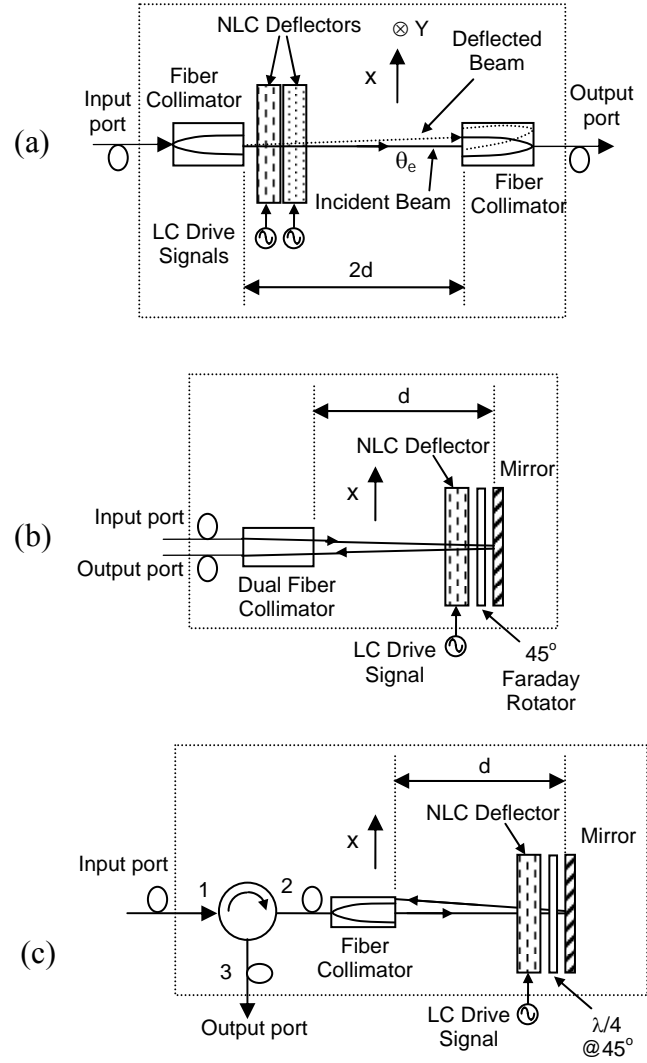


Fig. 6.1. Top views of proposed NLC beam-spoiling VOA designs using (a) two fiber collimators and two NLC deflectors with orthogonal NLC directors, (b) a dual collimator and a single NLC deflector with 45° Faraday rotator-mirror pair, and (c) an optical circulator, single fiber collimator with a single NLC deflector and 45° Faraday rotator-mirror pair.  $\lambda/4$ : Quarter wave plate.

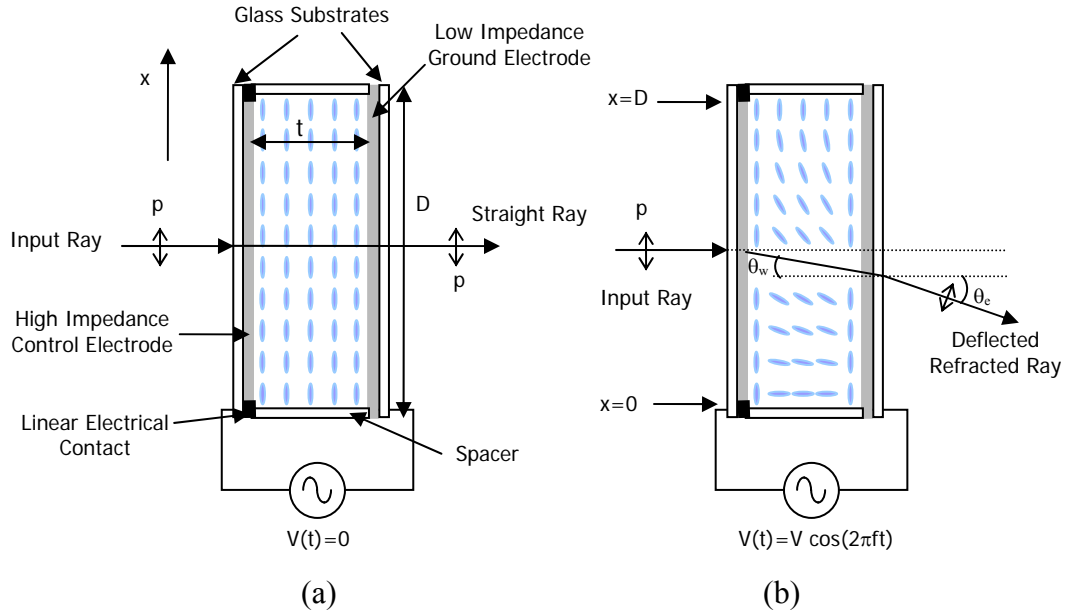


Fig. 6.2. Top views of the NLC deflector used to realize the VOAs. NLC molecule orientations are shown for (a) zero control signal applied and (b) when a control signal is present that reorients the NLC molecules to induce a spatial wedge-like refractive index change.  $p$ : horizontally polarized light component.

contacts to form a pixel-free deflector.<sup>13-14</sup> At the edges of the control electrode, linear electrical contacts are deposited which are used to apply the drive signal. When a signal is applied to one of these linear electrical contacts, the voltage drops linearly across the high impedance layer. The resulting E-field present across the NLC layer varies linearly across the aperture of the device leading to an index modulation that varies across the aperture of the device in a near-linear fashion (see Figure 6.2(b)). Notice that this index modulation is along the NLC director and thus can be seen only by that component of the input polarized light which is along the NLC director.

As a consequence, a scheme is needed to cater for both orthogonal polarization components of the input light entering via the VOA fiber-optics. In Figure 6.1(b, c), the  $45^\circ$  power Faraday rotator (or a quarter wave plate) with a mirror makes the reflective VOA design polarization insensitive. For the transmissive Figure 6.1(a) design, two orthogonal director NLC deflectors cater for both the components of the input polarization, making a polarization independent VOA. Thus a thin optical wedge formed in the NLC layer results in the refraction of the laser beam away from its original path, causing it to deflect along one dimension and hence un-optimize light coupling with the receiving GRIN lens.

Specifically in Figure 6.1(a), one orthogonal polarization component deflects in the x-direction while the other orthogonal polarization component deflects in the y-direction. This is because the NLC deflectors used are identical design devices, except being physically flipped by  $90^\circ$  with respect to each other for alignment purposes. This can be overcome by having two NLC cells with orthogonal directors but with the linear metallic electrical contacts parallel in both the cells such that the resulting phase ramp and hence the beam deflection for both the polarizations is in the same direction. Because of the symmetry of the VOA design, attenuation levels due to beam spoiling of both polarizations is the same, leading to a polarization insensitive design. Nevertheless, note that since two NLC deflectors are used with possible independent drive signals, any non-uniformity due to fabrication of the two cells can be cancelled by using two calibrated and independent drive signals for the two cells. For the Figure 6.1(b, c) designs, both polarizations undergo 1-D deflections in the x direction and so using a single NLC deflector is sufficient to deliver the polarization independent VOA operation. Next, the theoretical foundations are laid for the proposed NLC deflector-based VOA.

With reference to Figure 6.2, a ray polarized along the molecular NLC director passing through the NLC deflector device acquires a phase shift at the device position  $x$  that can be expressed as:

$$\phi(V, f, x) = [2\pi/\lambda] n(V, f, x) t \quad (1)$$

where  $\lambda$  is the optical wavelength,  $t$  is the NLC layer thickness,  $n(V, f, x)$  is the electrically controlled NLC refractive index the light sees, and  $V$  is the amplitude in Volts and  $f$  is the frequency in Hertz of the NLC device drive signal. Looking at the two extreme ray positions of  $x=0$  and  $x=D$ , the beam deflection of the entire wavefront incident on the NLC deflector can be studied. Specifically, the  $x=0$  position ray suffers a phase shift given by:

$$\phi(V, f, x=0) = \phi_o = [2\pi/\lambda] n(V, f, 0) t, \quad (2)$$

while the extreme ray at  $x=D$  suffers a phase shift given by:

$$\phi(V, f, x=D) = \phi_D = [2\pi/\lambda] n(V, f, D) t. \quad (3)$$

Hence the phase shift between the edges of refracted plane wave exiting the NLC deflector is given by:

$$\Delta\phi = \phi_D - \phi_o,$$

where between the  $x=0$  and  $x=D$  points, the incident plane wave acquires a linearly increasing phase shift. At  $x=D$ , the applied voltage is designed via the electrode structure to be zero, so the index seen by the incoming ray of p-polarization is essentially  $n_e$ , the NLC material extraordinary index of refraction. Therefore  $\phi_D = 2\pi/\lambda (n_e t)$  and  $\Delta\phi$  becomes:

$$\Delta\phi = (2\pi/\lambda) [n_e - n(V, f, 0)] t. \quad (5)$$

Similarly, note that at the  $x=0$  location where the other device electrode is present,  $V$  and  $f$  can be controlled to set  $n(V, f, x=0) = n_o$ , where  $n_o$  is the ordinary refractive index of the NLC material. In this case, the NLC deflector is generating its maximum birefringence  $\Delta n = n_e - n_o$  and hence also produces the largest phase shift between rays across the device aperture  $D$ . This in turn leads to the maximum beam deflection angle  $\theta_m$  for the programmable NLC deflector. From phased array theory, the beam steered angle  $\theta_w$  due to an inter-element phase shift  $\Delta\phi$  is given by:

$$(2\pi D/\lambda) \sin\theta_w = \Delta\phi, \quad (6)$$

where  $D$  is the phased array inter-element distance or in this case the NLC device aperture. By equating equations (5) and (6), the electrically controlled deflector angle  $\theta_w$  as seen by a wave polarized along the molecular director is written as:

$$(2\pi D/\lambda) \sin\theta_w = (2\pi/\lambda) [n_e - n(V, f)] t \quad (7)$$

This in turn leads to:

$$\theta_w(V, f) = \sin^{-1} \left\{ \frac{t}{D} [n_e - n(V, f)] \right\}, \quad (8)$$

A laser beam passing through the described thin NLC deflector (see Figure 6.2) is refracted at the freespace output of the deflector by an angle  $\theta_e$  that depends upon the average index  $\langle n \rangle$  of the NLC material, and the electrically set deflector angle  $\theta_w$ , and the index of the output media (in this case, air), leading to the expression:

$$\langle n \rangle \sin\theta_w = \sin\theta_e. \quad (9)$$

For a parallel rub NLC cell,  $\langle n \rangle$  is given as:<sup>15</sup>

$$\langle n^2 \rangle = (n_e^2 + 2n_o^2)/3. \quad (10)$$

Hence  $\theta_e$  can be written as:

$$97 \quad (11)$$

$$\theta_e = \sin^{-1}(\langle n \rangle \sin \theta_w).$$

It is because of the adjustable deflection angle  $\theta_e$  in the air that the laser beam going back into the fiber collimator is displaced from its perfectly aligned self-imaging state, leading to the controlled attenuation of light passing through the VOA. In addition, the output power coupled back into the fiber depends upon the separation distance between the NLC deflector and the fiber collimator. The deflected beam causes angular tilt and offset mis-alignments for the GRIN lens which result in a fiber-optic coupling loss.<sup>12,16</sup> For example, in the case of Figure 6.1(b) and (c) VOA designs, the attenuation offset misalignment  $x_o$  via beam deflection is given as:

$$x_o = d \tan \theta_e \quad (12)$$

Therefore,  $x_o$  becomes:

$$x_o = d \tan \{ \sin^{-1}(\langle n \rangle \sin \theta_w) \}, \quad (13)$$

and using the expression for  $\theta_w$  from (8) gives:

$$x_o = d \tan \left[ \sin^{-1} \left[ \langle n \rangle \left\{ \frac{t}{D} [n_e - n(V, f)] \right\} \right] \right]. \quad (14)$$

As the NLC deflector angles are designed to be small (e.g.,  $<0.21^\circ$ ), the small angle approximation of  $\sin \theta \cong \tan \theta \cong \theta$  can be applied giving:

$$x_o \cong d \langle n \rangle \left\{ \frac{t}{D} [n_e - n(V, f)] \right\} = d \langle n \rangle \theta_w. \quad (15)$$

In conclusion, the proposed VOA attenuation is controlled by producing a given beam offset misalignment  $x_o$  induced by an NLC deflector produced beam tilt misalignment angle  $\theta_w$ . More specifically, it can be seen from equation (15) that the VOA attenuation depends upon the beam waist position  $d$  from the GRIN lens, the average NLC refractive index  $\langle n \rangle$ , the NLC cell

thickness  $t$ , device aperture  $D$ , device programmable birefringence  $n_e - n(V, f)$ , and the drive signal voltage  $V$  and frequency  $f$ .

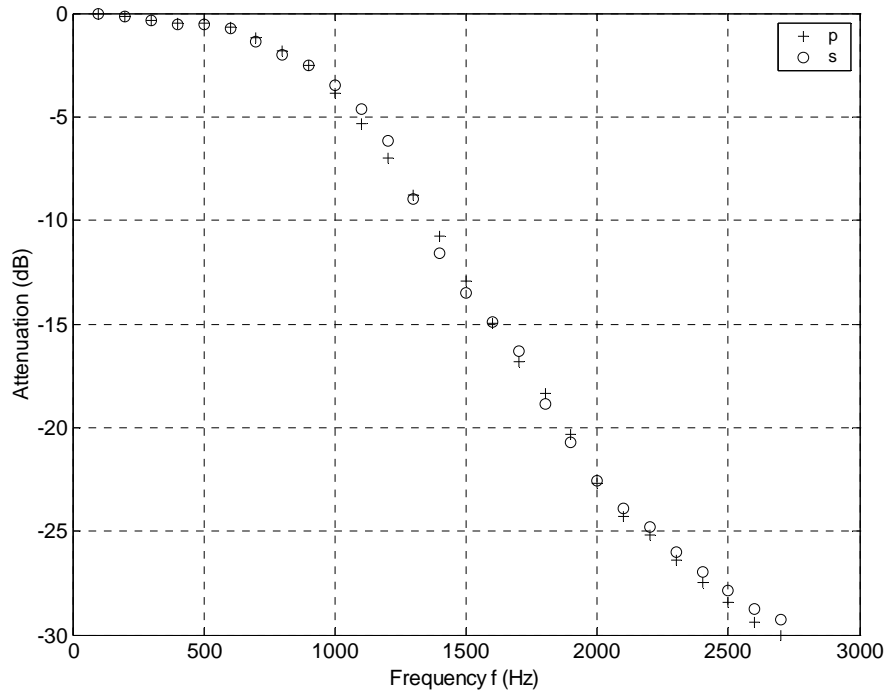
### 6.3 Experiment

The Figure 6.1(c) design is used as the proof-of-concept experimental setup at  $\lambda=1550\text{nm}$  for the proposed VOA. This design uses a  $9\text{ }\mu\text{m}$  core single mode fiber (SMF) coupled collimator, an NLC deflector, a quarter wave plate (QWP) for  $1550\text{nm}$ , a mirror and a circulator. The circulator and the single fiber collimator emulate the presence of a dual fiber collimator, as in Figure 6.1(b). First, the GRIN lens is characterized using the self-imaging technique.<sup>12</sup> The GRIN lens has a  $5\text{ mm}$  physical diameter with a  $2.5\text{ mm}$  exit beam  $1/e^2$  diameter. Insertion loss for the GRIN lens using freespace-to-fiber coupling via the self-imaging mechanism is measured to be  $0.4\text{ dB}$ . The beam waist location distance  $d$  of the chosen GRIN lens is  $25\text{ cm}$  and the  $1/e^2$  beam diameter is  $2.49\text{ mm}$ . The QWP positioned within  $1\text{ mm}$  of the mirror is oriented at  $45^\circ$  with respect to the NLC director. The distance between the NLC deflector and the QWP is  $13\text{ mm}$ . The insertion loss measured in this arrangement is  $2.5\text{ dB}$  which includes a  $0.7\text{ dB}$  loss per pass through the non-AR coated NLC deflector, a  $0.4\text{ dB}$  free-space to GRIN lens coupling loss and  $0.7\text{ dB}$  circulator loss. The NLC deflector used in the experiment has a clear aperture diameter  $D$  of  $5\text{ mm}$  and a NLC layer with a uniform thickness  $t$  of  $50\text{ }\mu\text{m}$ . The NLC used is Merck BL006 that has a manufacturer specified birefringence ( $\Delta n = n_e - n_o = 1.816 - 1.53$ ) of  $0.286$  at  $25^\circ\text{C}$  room temperature and  $\lambda=589.3\text{ nm}$  (see Appendix C). The NLC birefringence  $\Delta n$  depends upon the operating wavelength. Typically for NLCs with large birefringence (e.g.

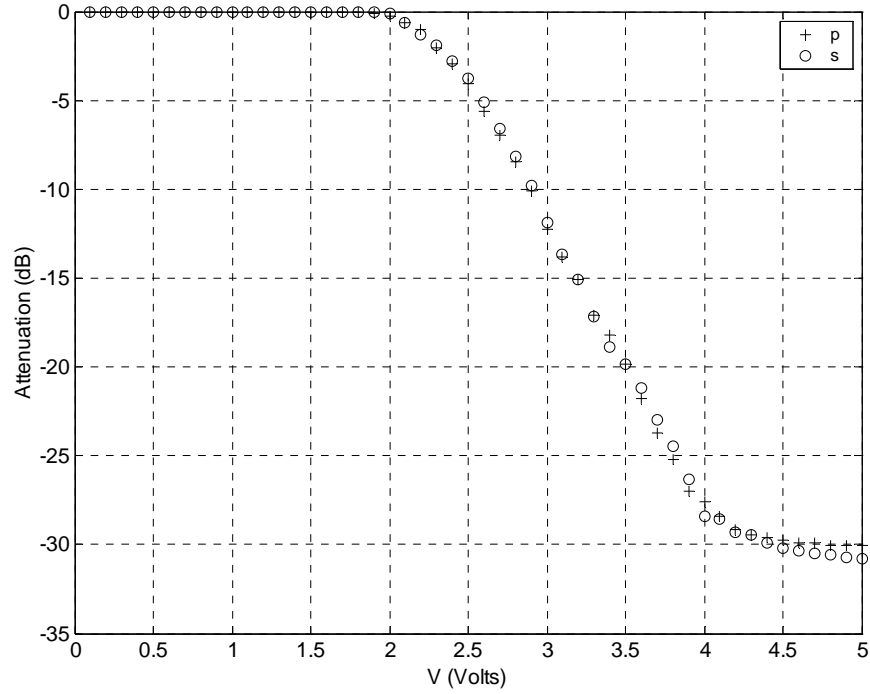


$\Delta n \sim 0.2$ ) in the visible band such as the Merck BL006, the birefringence decreases by  $\sim 15\text{-}20\%$  going from visible to near infrared band.<sup>17</sup> The birefringence was also measured at 1550 nm and 25°C to be 0.229, which is within the 15-20% approximation range. Hence, for a given device drive signal, the VOA attenuation will decrease for longer wavelengths as compared to that for the shorter wavelengths. For example, VOA operation in the 35 nm bandwidth C telecommunications band centered at 1545 nm is relatively constant due to small expected birefringence variation (typically  $<1\%$ ) within this infrared wavelength region<sup>15</sup>. Using equation (10), the average refractive index  $\langle n \rangle$  is then calculated to be 1.63. Using the mentioned NLC deflector specifications and equation (8), the deflector angle  $\theta_w$  maximum obtained using this device at 1550 nm is 2.29 mradian ( $0.131^\circ$ ). As listed in Table 6.1, the maximum angle  $\theta_e$  at which the laser beam emerges from the NLC deflector is calculated using equation (11) to be 3.73 mradian ( $0.21^\circ$ ). Table 1 also gives the expected VOA beam angular and lateral misalignments for a variety of design specifications including the present experimental design. It can be concluded from Table 6.1 that using a given NLC device with a smaller aperture and hence larger beam deflection angle will result in a compact VOA design.

Figure 6.3(a) shows the measured VOA optical attenuation for the Figure 6.1(c) VOA as a function of the drive signal frequency  $f$  using a  $V=5$  Volt square wave signal. Figure 6.3(b) shows the measured optical attenuation as a function of the applied square-wave voltage for an  $f=2.7$  kHz signal drive. The VOA attenuation dynamic range in both these cases is  $\sim 30$  dB, generated by the combined tilt and offset beam spoiling effects. The PDL is measured to be  $<0.8$  dB whereas the VOA resolution based on the resolution of present drive electronics is measured to be  $\pm 0.1$  dB. Due to the large 5 mm aperture and large 50  $\mu\text{m}$  thickness of the NLC layer, the response time of the current VOA is of the order of 1 second. The insertion loss and the response



(a)



(b)

Fig. 6.3. Measured optical attenuation as a function of (a) drive frequency and (b) voltage. p: horizontally polarized light component parallel to cell nematic director. s: vertically polarized light component normal to the device NLC director.

time can further be reduced by varying the parameters of the NLC deflector such as the thickness of the cell and its clear aperture. Note that because of the large "d" GRIN lens used in the experiment for ease of implementation, the NLC deflector and related retro-reflecting polarization independence creating optics are not in close proximity, thereby not negating PDL to the desired <0.2 dB. For a custom design, where the NLC deflector, QWP, and mirror are all stacked together with a short "d" dual collimator GRIN lens, both lower PDL and insertion loss can be achieved.

A key VOA parameter is its longest reset time.  $t_s = t_1 + t_2$  where  $t_1$  is the NLC response time to set the NLC deflector to a given required beam steering voltage  $V$ .  $t_2$  is the NLC deflector response time when  $V=0$  and the device is reset to its zero beam steering angle state. For a homogeneous NLC cell the response time is given by:<sup>18</sup>

$$\tau_r = \frac{\tau_o}{\left| \left( \frac{V}{V_{th}} \right)^2 - 1 \right|}, \quad (16)$$

where  $\tau_o$  is the LC director's relaxation time and is given as:<sup>18</sup>

$$\tau_o = \frac{\gamma_1 t^2}{\pi^2 K_{11}}, \quad (17)$$

and  $V_{th}$  is the NLC threshold voltage and is given by:<sup>18</sup>

$$V_{th} = \pi \sqrt{\frac{K_{11}}{\epsilon_o \Delta \epsilon}}, \quad (18)$$

where  $K_{11}$  is the splay elastic constant,  $\epsilon_o$  is the free-space dielectric permittivity,  $\Delta \epsilon$  is the dielectric anisotropy, and  $\gamma_1$  is the visco-elastic coefficient. As can be noted from the equations (16-18),  $V_{th}$  is more or less constant for a certain NLC and  $\tau_o$  depends on the cell thickness  $t$ . For

a given cell size and NLC material,  $\tau_o$  will be fixed and hence the response time  $\tau_r$  depends only on the ratio  $V/V_{th}$ . The response time decreases as the ratio  $V/V_{th}$  is increased. For the present VOA, its longest reset time  $t_s$  can be approximated by using  $t_1=\tau_r$  and  $t_2=\tau_o$ . Hence the VOA maximum reset time is

$$t_s = \tau_r + \tau_o . \quad (19)$$

Since  $\tau_o$  is generally fixed, it can be concluded from equation (19) that the VOA reset time is not the same for the different attenuation levels. For example, to reset the VOA for maximum attenuation, the reset time is the shortest as  $V \gg V_{th}$ .

Notice from equation (17) that the NLC deflector device response time  $\tau_o$  has a square law relation with the NLC cell thickness  $t$ ; hence a reduction in the cell thickness will result in a shorter overall reset time for the VOA. For example, reducing the thickness by half will result in a 4 times faster VOA response. Recall that the NLC deflector used is a non-pixelated NLC cell making the device refractive in nature as opposed to a diffractive device that would otherwise give unwanted diffraction orders and hence excess loss.

The NLC used has a large nematic temperature range from  $-15^\circ\text{C}$  to  $113^\circ\text{C}$ .<sup>19</sup> In a typical NLC material, birefringence decreases as a function of temperature. In an NLC based VOA where BDPs are used to separate and recollect the orthogonal polarized light components, temperature change causes birefringence change leading to polarization extinction ratio changes. This causes the light throughput fluctuations in the VOA that can cause irrecoverable light loss. Due to the beam steering nature of the proposed NLC-based VOA, a temperature change causes a birefringence change in the NLC deflector leading to a change in deflection angle and hence attenuation level. More importantly, the desired VOA attenuator level can be recovered by electrically controlling the NLC deflector to recover the original deflection angle. Unlike the

BDP-based LC VOAs, the NLC deflector based VOA does not suffer from irrecoverable VOA excess loss. Specifically, the proposed VOA when used with a feedback loop can operate properly even in an environment with temperature swings and no temperature stabilization hardware.

#### 6.4 Extended Applications

The VOA architectures shown in Figure 6.1 can be extended to other useful devices. Specifically, a 1x2 switch is formed by replacing the output port single fiber collimator in Figure 6.1(a) by a dual fiber collimator and inserting a half wave plate in-between the two NLC deflectors that have their directors parallel to each other (see Figure 6.4(a)). The half wave plate is present so that both the polarization components are steered into the same direction. For such a 1x2 switch, the insertion loss is estimated to be  $<0.67$  dB using AR coated devices. This 0.67 dB mainly comes from the absorption in the NLC material and can be reduced by having a thinner NLC layer and smaller device aperture. Also notice that the two NLC deflectors can be driven individually so as to cancel the effects of thickness variation in different cells or to get an even finer control over the device operation. Figure 6.4(b) shows an alternate structure for the 1x2 switch using a triple fiber collimator in a reflective design. Such a programmable compact 1x2 switch can be useful in photonic applications where on-demand programmable signal taps are needed for in line spectral analysis and power monitoring.

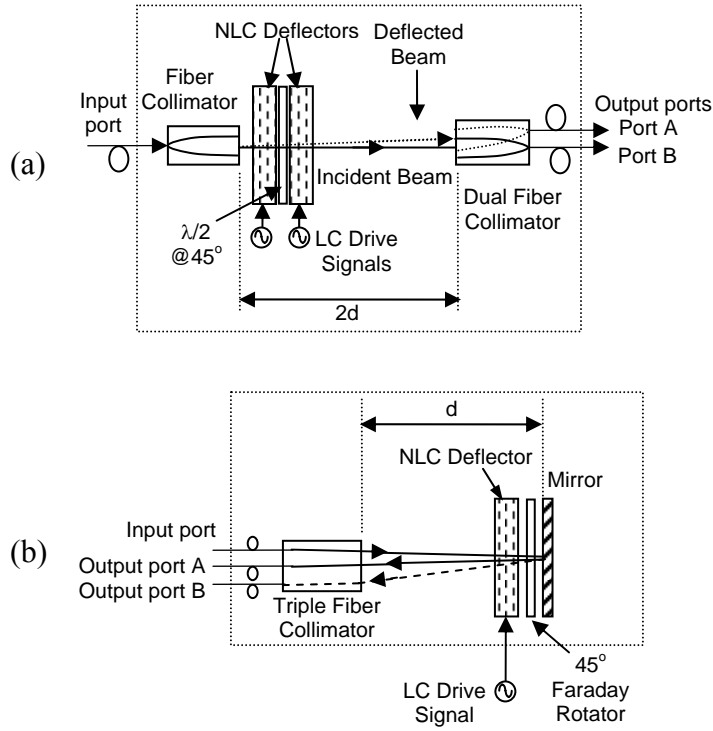


Fig. 6.4. Proposed NLC deflector based 1x2 switch designs using (a) a single fiber collimator, two parallel aligned NLC deflectors, a half wave plate and a dual fiber collimator, and (b) a triple fiber collimator and a single NLC deflector in a reflective mode.

Table 6.1. VOA Design Parameters v/s Obtained Beam Spoiling Parameters.  $t$ : NLC deflector cell thickness;  $D$ : NLC deflector cell aperture;  $d$ : GRIN lens beam waist distance from GRIN lens exit aperture,  $\theta_w$ : NLC deflector maximum deflection angle,  $\theta_e$ : maximum freespace exit angle from the NLC deflector, and  $x_o$ : maximum offset error due to angular deflection.

\*Demonstrated experimental design.

VOA Design Parameters			Fiber-optic Coupling Beam Spoiling Parameters		
$t$ ( $\mu\text{m}$ )	$D$ (mm)	$d$ (cm)	$\theta_w$ (mrad)	$\theta_e$ (mrad)	$x_o$ (mm)
10	0.42	2	23.81	38.82	0.78
10	0.4	4	25	40.76	1.63
20	0.42	2	47.64	77.7	1.56
20	0.4	4	50	81.59	3.27
50	0.42	2	119.33	195.29	3.96
50 *	5 *	25 *	2.29	3.73	0.93

## 6.5 Conclusion

In summary, a novel fiber-optic VOA is demonstrated using an electrically controlled NLC deflector that implements optical power attenuation via beam spoiling-based single-mode fiber coupling loss. The proposed VOA can be electrically compensated to deliver a fixed excess loss with changing environmental conditions. The VOA features a compact no moving parts

design with high attenuation dynamic range, low loss, low PDL potential, and broadband capability. Experiments at 1550 nm demonstrate fiber-optic component specifications useful for many applications, such as for test instrumentation and fiber-optic communications. The basic VOA design can also be extended to realize a small 1x2 switch.



## References

1. C. Marxer, P. Griss, N. F. de Rooij, "A variable optical attenuator based on silicon micromechanics," IEEE Photonics Technology Letters, Vol. 11, Issue 2 , Pages 233-235, February 1999.
2. M.J. Mughal and N. A. Riza, "Compact acoustooptic high-speed variable attenuator for high-power applications," IEEE Photonics Technology Letters, Vol. 14, Issue 4, Pages 510-512, April 2002.
3. X. Orignac, "First ion-exchanged dual thermo-optic variable optical attenuator," International Conference on Transparent Optical Networks, Pages 89-92, 9-11 June 1999.
4. J. L. Jackel, J. J. Veselka, and S. P. Lyman, "Thermally tuned glass Mach-Zehnder interferometer used as a polarization insensitive attenuator," Applied Optics, Vol. 24, No. 5, Pages 612-614, March 1985.
5. R. A. Soref, "Liquid-crystal fiber-optic switch," Optics Letters, Vol. 4, Issue 5, Pages 155-157, May 1979.
6. E. G. Hanson, "Polarization-independent liquid-crystal optical attenuator for fiber-optics applications," Applied Optics, Vol. 21, Issue 7, Pages 1342-1344, April 1982.
7. K. Hirabayashi, M. Wada and C. Amano, "Compact Optical-Fiber Variable Attenuator Arrays with Polymer-Network Liquid Crystals," Applied Optics-LP, Vol. 40, Issue 21 Pages 3509-3517, July 2001.

8. J. J. Pan, H. Wu, W. Wang, X. Qiu and J. Jiang, "Temperature independent, accurate LC VOA through electric feedback control," Proceedings of National Fiber Optics Engineers Conference (NFOEC), Pages 943-949, Orlando, Florida, USA, September 2003.
9. N. A. Riza, "Fault-tolerant fiber-optical beam control modules," US Patent No. 6,222,954, April 24, 2001.
10. N. A. Riza and Y. Huang, "Digital fault-tolerant variable fiber optic attenuator using liquid crystals," Advances in Optical Information Processing IX, Proc. SPIE Vol. 4046, Pages 101-106, Dennis R. Pape; Ed., July 2000.
11. N. A. Riza, "Multi-technology multi-beam-former platform for robust fiber-optical beam control modules," US Patent No. 6,525,863, February 25, 2003.
12. M. van Buren and N. A. Riza, "Foundations for Low-Loss Fiber Gradient-Index Lens Pair Coupling with the Self-Imaging Mechanism," Applied Optics-LP, Vol. 42, Issue 3, Pages 550-565, January 2003.
13. G. D. Love, J. V. Major and A. Purvis, "Liquid-crystal prisms for tip-tilt adaptive optics," Optics Letters, Vol. 19, Issue 15, Pages 1170-1172, August 1994.
14. A. F. Naumov, M. Yu. Loktev, I. R. Guralnik, and G. Vdovin, "Liquid-crystal adaptive lenses with modal control," Optics Letters, Vol. 23, Issue 13, Pages 992-994, July 1998.
15. L. M. Blinov, *Electro-optical and magneto-optical properties of liquid crystals* (John Wiley & Sons Ltd., Chichester, U.K., 1983).
16. S. Yuan, and N. A. Riza, "General Formula for Coupling-Loss Characterization of Single-Mode Fiber Collimators by use of Gradient-Index Rod Lenses," Applied Optics-LP, Vol. 38, Issue 15, Pages 3214-3222, May 1999.

17. S. T. Wu, School of Optics and the Center for Research and Education in Optics and Lasers, University of Central Florida, 4000 Central Florida Blvd., Orlando, FL 32816-2700 (Personal communication, 2003).
18. I. C. Khoo and S. T. Wu, *Optics and nonlinear optics of liquid crystals* (World Scientific, Singapore, 1993).
19. Merck Liquid Crystals Catalog, Darmstadt, Germany, 2003.

## **CHAPTER 7: WAVELENGTH TUNABLE VARIABLE FIBER-OPTIC ATTENUATOR USING LIQUID CRYSTAL-MIRROR HYBRID CONTROLS**

In this chapter, a Fiber optic module is proposed using a hybrid liquid crystal-mirror mechanics beam control mechanism that provides the dual functions of optical attenuation controls and wavelength selection with a high degree of sensitivity, all within one compact in-line module. Experimental module uses a liquid crystal deflector and a mechanically tuned bulk mirror as the hybrid optics. The module demonstrates a 1520-1570 nm coarse tuning range, a 1.44 nm fine tuning range, a >30 dB attenuation range, a 3.7 dB optical insertion loss, < 0.1 dB polarization dependent loss, and a Full Width Half-Maximum (FWHM) wavelength resolution of  $\leq 0.3$  nm. Module applications include tunable gain controlled optical transmitters and receivers.

## 7.1 Introduction

The fiber-optic variable optical attenuator (VOA) is a basic processing element in many optical systems. It is desirable that such a VOA is controlled with minimal electrical power and operates over broad optical bands. With their compact no moving parts, low loss, and low power consumption attributes, liquid crystals (LCs) have been considered attractive for realizing these VOAs within pure digital<sup>1-2</sup> and analog manifestations.<sup>3-5</sup> Nevertheless, these LC VOA designs use bulky beam displacement prisms (BDPs) for splitting and combining the two orthogonal polarization components in order to realize a polarization independent fiber-optic VOA. Recently, a compact LC VOA structure was proposed that does away with the use of BDPs making one compact VOA unit.<sup>6</sup> Specifically, the ref.6 VOA can operate over a broad optical band making it an essentially wavelength insensitive module. There are some applications where it is desirable to have a wavelength tunable VOA. Such applications include an optical receiver that requires the ability to tune to a chosen wavelength in a broad optical band and simultaneously has the feature of controlling optical light flow or attenuation in the photo-detection optoelectronics. In other words, an electronically tunable wavelength sensitive VOA is required. Another possible application is a gain controlled tunable optical transmitter.

This chapter shows how the ref.6 VOA can be simply modified to realize the desired wavelength agile VOA. Earlier proposed was a hybrid LC plus mirror optics approach to free-space beam controls within fiber-optic structures where the excellent fine pointing ability of LC optics is exploited for super-fine free-space beamforming and the much better (compared to LCs) larger angular range of mirror optics is engaged to implement the high angular dynamic range

beam pointing.<sup>7</sup> Shown in this chapter is how the hybrid LC-mirror beam controls approach is combined with wavelength sensitive optics within the ref.6 VOA design to realize the desired wavelength agile VOA. Independently, micro-electromechanical systems (MEMS) mirror optics alone has been engaged to realize single wavelength selection modules for applications such as wavelength scanned optical spectrum analysis<sup>8</sup> and agile wavelength selection for an optical receiver.<sup>9</sup> The focus of the proposed work is realization of an all-in-one compact module using hybrid LC-mirror controls that enables both wavelength selection operations and VOA operations, all with high dynamic range and accuracy. The rest of the chapter describes the proposed module design and related experiments.

## 7.2 Wavelength Tunable VOA Architecture

Figure 7.1 shows the proposed hybrid design wavelength agile fiber-optic VOA. The basic design uses a fiber-optic circulator (C), a transmissive volume Bragg grating (VBG), one LC deflector, a quarter wave plate (QWP), and a mirror M. The design is similar to the ref.6 VOA design, except for the insertion of the grating optic and the active use of both the LC and mirror optics. The circulator is used to direct input and output light to and from the module. The input light is coupled to the freespace optics using a self-imaging type single mode fiber (SMF) gradient index (GRIN) rod lens. A QWP is placed between the LC deflector and M to minimize polarization dependent loss (PDL) in the overall module. In addition, the QWP produces the desired linear polarization flipping operations so that the polarization dependent LC deflectors operate as polarization independent devices. The distance  $d$  between M and the GRIN lens is

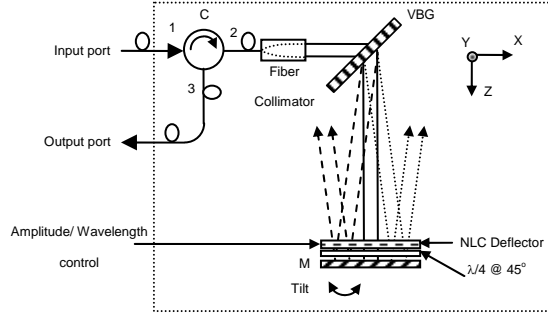


Fig. 7.1. Proposed Wavelength Tunable Variable Fiber-Optic Attenuator Using Liquid Crystal-Mirror Hybrid Controls. C: Optical Circulator; VBG: Volume Bragg Grating; M: Mirror.

such that the Gaussian beam emerging from the GRIN lens forms its minimum beam waist at the mirror location leading to a low loss self-imaging design.<sup>10</sup> The VBG is placed at the Bragg angle orientation  $\theta_{\text{Bragg}}$  for the band central wavelength so that the input broadband source spectrum in the first order spreads by an angle of  $2\Delta\theta = \theta_{\text{max}} - \theta_{\text{min}}$  along x-axis (see Fig. 7.1), all with the minimal insertion loss, where  $\theta_{\text{max}} = \sin^{-1}[(\lambda_{\text{max}}/L) - \sin\theta_{\text{Bragg}}]$  and  $\theta_{\text{min}} = \sin^{-1}[(\lambda_{\text{min}}/L) - \sin\theta_{\text{Bragg}}]$ , and  $L$  is the grating period. For the designed VOA operating spectrum,  $\lambda_{\text{max}}$  and  $\lambda_{\text{min}}$  correspond to the maximum and minimum wavelength values, respectively. An anti-parallel rub nematic LC (NLC) deflector is placed adjacent to M. Mirror M is a one dimensional tilt mirror used for selection of wavelength. If mirror based two dimensional x-y steering is deployed for both coarse wavelength selection and attenuation, two independent mirrors should be used to avoid crosstalk. The output of the module is always the chosen narrow band of the input light that is Bragg coupled back via the VBG into the GRIN lens. The extent of this narrow band  $\Delta\lambda$  is

defined by the VBG resolution and is expressed as  $\Delta\lambda = \frac{L\lambda}{|m|W}$ , where  $m$  is the grating order

number,  $\lambda$  is the hybrid LC-mirror optics selected Bragg wavelength, and  $W$  is the  $1/e^2$  beam diameter incident on the grating.<sup>11</sup> Due to the divergent nature of the beam produced by the VBG, only the Bragg matched component of the light is coupled back into the GRIN lens and hence enters the SMF. The rest of the off-axis unselected input light after double pass through the VBG does not enter the SMF. For selecting the desired wavelength to be coupled back into the GRIN lens, first the mirror  $M$  is tilted about the  $y$ -axis in order to select the correct Bragg angle for the chosen wavelength within the source spectrum.  $M$  can provide a wide tilt angle range needed to cover a broad spectral/angular band of the input light signal, although with limited mirror fine positioning repeatability. This fine tilt tuning need can be handled by using another NLC deflector in the module that is driven by a given voltage signal that accurately fine tweaks the beam deflection angle about  $y$ -axis to match the desired Bragg angle for the chosen wavelength. Once the wavelength is chosen, the next step is the VOA implementation for this given wavelength. This is achieved via the NLC deflector based beam deflection about  $x$ -axis. Fundamentally here, attenuation is realized via returning beam misalignment along the  $y$ -direction (not the grating vector direction) into the GRIN lens.<sup>10</sup> Thus, the hybrid LC-mirror controls give both high dynamic range and high resolution for controls of the proposed module.

### 7.3 Experiment

For the proof-of-concept experiment, the Fig. 7.1 design is implemented in the laboratory. The SMF GRIN lens used has a 5 mm physical diameter with a 2.5 mm exit beam  $1/e^2$  diameter. The beam waist location distance  $d$  of the chosen GRIN lens is 25 cm and the  $1/e^2$  beam diameter



at beam waist location is 2.49 mm. The QWP positioned within 2 mm of the mirror is oriented at  $45^\circ$  with respect to the NLC director. The distance between the NLC deflector and the QWP is 9.5 mm. The total fiber-to-fiber module insertion loss measured is 3.7 dB which includes a 0.7 dB loss per pass through the non-AR coated NLC deflector, a 0.1 dB insertion loss for the freespace-to-fiber coupling via the self-imaging mechanism, a 1.4 dB circulator loss, and 0.4 dB loss per pass through the VBG. Insertion loss variation for the module was measured to be  $\pm 0.2$  dB in the entire 1520-1570 nm band.

Amplified spontaneous emission (ASE) from an erbium doped fiber amplifier was used as the broadband input source for the wavelength agile VOA. The VBG placed 4 cm away from the GRIN lens is a 980 lines/mm Dickson grating that spreads the 50 nm source spectrum by  $4.55^\circ$  which corresponds to a linear spread of 1.67 cm at the mirror M. The grating Bragg center wavelength  $\lambda_{\text{Bragg}}$  chosen is 1550 nm and  $\theta_{\text{Bragg}}$  is  $46.76^\circ$ . Figure 7.2 (dashed line) shows Optical Spectrum Analyzer (OSA) traces of the input source spectrum from 1520 nm to 1570 nm wavelength range. The VBG resolution  $\Delta\lambda$  is calculated to be 0.27 nm which is verified by the measured FWHM bandwidth of the module output light spectra as seen in Fig. 7.2. The NLC deflector used has a diameter of 5 mm and a NLC layer with a uniform thickness of 50  $\mu\text{m}$ .<sup>6</sup> The NLC deflector is oriented to perform fine VOA operations by deflecting the beam about x-axis with M set initially for the 1550 nm test wavelength that enables retro-reflection via the entire optics. To demonstrate the broadband operation of the module as a wavelength selective VOA, the mirror M is tilted about the y-axis to set the reflection at 1560 nm as shown in Fig. 7.2, with attenuation controlled via NLC deflector drive controls. The selected spectrum shows two attenuation settings of 0 dB and 20 dB. Note that the present wavelength tuning performance depends upon the characteristics of the mechanical mirror stage used, in this case a standard

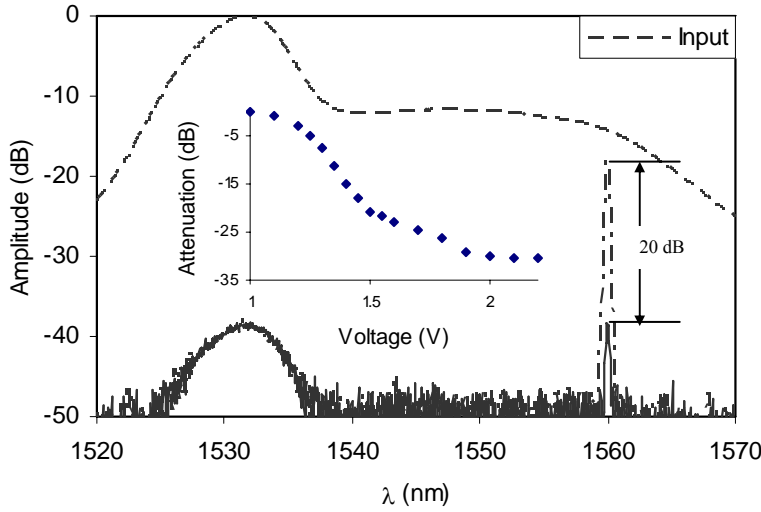


Fig. 7.2. Proposed Wavelength Tunable Variable Fiber-Optic Attenuator operating as VOA for mirror M selected wavelength of 1560 nm and attenuation plots for 0 and 20 dB settings using NLC deflector driven at two different operating voltages. (Inset) Module operating as a VOA for the mirror M direction selected 1550 nm wavelength.

commercial Newport stage. In general, note that any small variation of this or any other stage over a long period of time can be compensated for using the NLC deflector based wavelength tuning, an additional feature of the proposed module. Module PDL is measured to be  $< 0.1$  dB over the entire 1520-1570 nm wavelength band. The fine attenuation control resolution of the NLC deflector is measured to be 0.05 dB for a chosen 1550 nm wavelength with an attenuation dynamic range of 30.6 dB by changing the drive voltage to the NLC deflector as also shown in the Fig. 7.2 inset.

To demonstrate fine precision no moving parts wavelength selection in the module, the Fig. 7.1 NLC deflector is engaged. To perform this experiment, the NLC deflector in the previous setup is rotated by  $90^\circ$  in order to produce the needed fine beam deflection about y-axis.

Since the NLC deflector has a metallic contact on each edge, the electric field gradient formed is either in +x direction or in -x direction.<sup>6</sup> This leads to the capability of tuning the wavelength twice that of a deflector with a single electrical contact. When the drive signal is applied in order to cause a voltage gradient in the +x direction the optical beam gets deflected in the +x direction and as a result a slightly different wavelength is coupled back to the GRIN lens. The total wavelength fine tunability that was experimentally achieved by using the two aforementioned electrical contacts in order to get deflection in both +x and -x direction was measured to be 1.44 nm with a drive signal of 2.2 V<sub>pp</sub> as shown in Fig. 7.3. Assuming that the VBG resolution is not a limiting factor, the optical spectrum analyzer measured NLC deflector wavelength tuning resolution is 10±2 pm. The solid curve in Fig. 7.3 corresponds to no applied signal while the two dashed curves correspond to 2.2 V<sub>pp</sub> applied signal at 1 KHz square waveform to the two opposing linear metallic contacts, resulting in a FWHM spectral width of 0.29 nm, 0.27 nm and 0.29 nm (viewing Fig.7.3 from left to right).

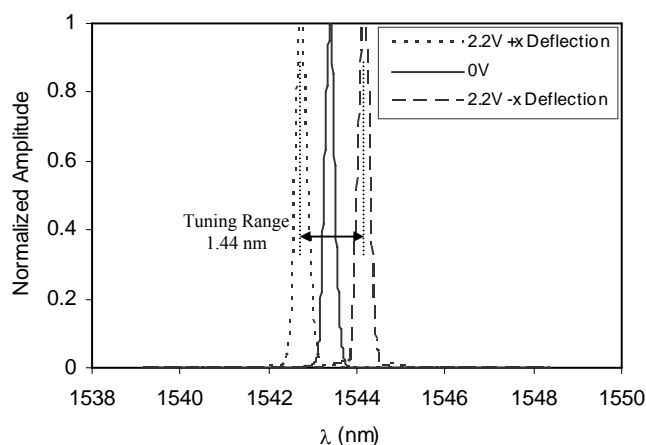


Fig. 7.3. Proposed Wavelength Tunable Variable Fiber-Optic Attenuator operating with precise fine wavelength selection using NLC deflector driven at three different operating states giving a 1.44 nm liquid crystal tuned fine wavelength range.

## 7.4 Conclusion

The power of combined LC-mirror optics approach is shown for enabling a wavelength selective VOA module. The LC optics are used for fine beam steering while the mirror optic is engaged for larger angle beam steering within the fiber-optic module, thus playing into the strengths of the two steering technologies. A proof-of-concept module is designed and indeed demonstrates the wide dynamic range as well as high resolution capabilities for both wavelength selection and light attenuation controls. Improvements in the attenuation coarse dynamic range of the module is possible using a non-circulator based two fiber module design. Reset speed of the module is linked to the speed of mirror-control and NLCs that have typical response times of the order of a few milliseconds. Response time of the NLC cell used is  $\sim 1$  second due to its relatively large thickness compared to ordinary NLC devices. Multiple thin NLC cells each giving an incremental value of the total deflection angle and a typical low 0.04 dB loss, can be cascaded in order to achieve the desired attenuation and wavelength control resolution and dynamic range with a relatively faster response time. Research is underway to synthesize NLC materials for larger birefringence and smaller viscosity in order to obtain faster response times.<sup>12</sup> Faster response times can also be achieved for NLCs using either the dual frequency effect or the transient-nematic effect.

## References

1. N. A. Riza, "Fault-tolerant fiber-optical beam control modules," US Patent No. 6,222,954, April 24, 2001.
2. N. A. Riza and Y. Huang, "Digital fault-tolerant variable fiber optic attenuator using liquid crystals," Advances in Optical Information Processing IX, Proc. SPIE Vol. 4046, Pages 101-106, Dennis R. Pape; Ed., July 2000.
3. E. Hanson, "Polarization-independent liquid-crystal optical attenuator for fiber-optics applications," Applied Optics, Vol. 21, Issue 7, Pages 1342-1344, April 1982.
4. K. Hirabayashi, M. Wada and C. Amano, "Compact Optical-Fiber Variable Attenuator Arrays with Polymer-Network Liquid Crystals," Applied Optics-LP, Vol. 40, Issue 21 Pages 3509-3517, July 2001.
5. J. Pan, H. Wu, W. Wang, X. Qiu and J. Jiang, "Temperature independent, accurate LC VOA through electric feedback control," Proceedings of National Fiber Optics Engineers Conference (NFOEC), Pages 943-949, Orlando, Florida, USA, September 2003.
6. N. A. Riza and S. Khan, "Liquid-Crystal-Deflector Based Variable Fiber-Optic Attenuator," Applied Optics, Vol. 43, Issue 17, Page 3449-3455, June 2004.
7. N. A. Riza, "Multi-technology multi-beam-former platform for robust fiber-optical beam control modules," US Patent No. 6,525,863, February 25, 2003.
8. K. Nakamura, T. Saitoh and Y. Takahashi, "High-speed optical performance monitor for WDM network using MEMS scanning mirror," IEEE/LEOS International Conference on Optical MEMS, Pages 97-98, Waikoloa, Hawaii, August 2003.

9. J. Berger, F. Ilkov, D. King, A. Tselikov, D. Anthon, "Widely tunable, narrow optical bandpass Gaussian filter using a silicon microactuator," Optical Fiber Communication Conference, 252-253, Atlanta, GA, 23-28 March 2003.
10. M. van Buren and N. A. Riza, "Foundations for Low-Loss Fiber Gradient-Index Lens Pair Coupling with the Self-Imaging Mechanism," Applied Optics-LP, Vol. 42, Issue 3, Pages 550-565, January 2003.
11. Z. Yaqoob and N. Riza, "Low-loss wavelength-multiplexed optical scanners using volume Bragg gratings for transmit-receive lasercom systems," Optical Engineering, Vol. 43, Issue 5, Pages 1128-1135, May 2004.
12. S. Gauza, H. Wang, C. H. Wen, S. T. Wu, A. Seed, and R. Dabrowski, "High Birefringence Isothiocyanato Tolane Liquid Crystals," Japanese Journal of Applied Physics Part I, 42, 3463-3466, 2003.

## **CHAPTER 8: NO-MOVING-PARTS AXIAL SCANNING CONFOCAL MICROSCOPY**

For the first time, to the best of our knowledge, a no-moving-parts axial scanning confocal microscope (ASCM) system is designed and demonstrated using a combination of a large diameter liquid crystal (LC) lens and a classical microscope objective lens. By electrically controlling the 5 mm diameter LC lens, the 633 nm wavelength focal spot is moved continuously over a 48  $\mu\text{m}$  range with a measured 3-dB axial resolution of 3.1  $\mu\text{m}$  using a 0.65 numerical aperture (NA) micro-objective lens. The ASCM is successfully used to image an Indium Phosphide (InP) twin square optical waveguide sample with a 10.2  $\mu\text{m}$  waveguide pitch and 2.3  $\mu\text{m}$  height and width. Using fine analog electrical control of the LC lens, a super-fine sub-wavelength axial resolution of 270 nm is demonstrated. The proposed ASCM can be useful in various precision three dimensional (3-D) imaging and profiling applications.

## 8.1 Introduction

Over the years, the confocal microscope has been effectively used to optically image three dimensional (3-D) structures of microscopic objects.<sup>1-4</sup> The basic confocal microscope instrument consists of a sampling arm and a detection arm. A beam splitter (BS) directs the light to the sampling arm and the detection arm. A high NA micro-objective lens is employed in the sampling arm to illuminate the sample under observation. In the reflective geometry of the confocal microscope, light focused onto the sample is reflected and directed to the detection arm by the BS. In the detection arm, a spherical lens focuses this reflected light at a tiny pinhole. The diameter of the pinhole is chosen such that only the main lobe of the Airy pattern passes through it to the photo-detector. Hence, only light reflected from the focal spot of the micro-objective lens reaches the detector. The pinhole rejects the out-of-focus light as well as the reflections from points on the focal plane adjacent to the focused spot. Since one point of the object is imaged at a time, the 3-D image is formed by transverse dimension raster scanning using scanning mirrors and sequential mechanical motion of the sample in the depth dimension using a motorized translation stage. The NA of the micro-objective defines the transverse resolution as well as the depth resolution, also called the optical section thickness. The rejection of out-of-focus light is the most important feature of a confocal microscope as it reduces the blur from adjacent optical sections due to its confocal nature resulting in significant contrast improvement as compared to conventional optical microscopes. The number of optical sections that can be imaged depends upon the instrument optical quality and opacity and turbidity of the sample. As one opts for finer optical sectioning, a more precise and consequently costlier motion controller is required to



move the sample in the depth direction. Depending on the size of the motion controller and the sample, axial data acquisition can become a slow process due to inertia and associated momentum. This leads to limitations in particular when the sample contains fast temporal effects such as flow patterns, neuronal and cellular activity. Ideally, a no-moving-parts fast and agile axial scanning confocal microscope system would be very helpful in producing true real-time 3-D scans with precision and repeatability. Previously, non-mechanical means for axial scanning have been suggested such as using a broadband source and a highly chromatic objective lens.<sup>5-8</sup> In addition, the use of a multi-element adaptive deformable mirror in a confocal microscope has been used to create multiple focal spots via a genetic algorithm.<sup>9</sup> Earlier, a no-moving-parts 3-D freespace laser beam scanning technique<sup>10-11</sup> was demonstrated using LCs.<sup>12</sup> In particular, the use of agile focus tunable optics using LCs and optical Micro-Electro-Mechanical Systems (MEMS) technology was proposed to realize various axial scanning confocal microscopy architectures.<sup>13-</sup>  
<sup>14</sup> This chapter for the first time shows the design and proof-of-concept experimental demonstration of one of these LC-based no-moving-parts ASCMs.

## 8.2 Proposed Axial Scanning Confocal Microscope Design

The proposed no-moving-parts ASCM design is shown in Fig. 8.1. This design is similar to that of a classical confocal microscope, except that the sample arm is built with the objective lens being a combination of a micro-objective lens and a tunable focus LC lens. Together, the two lenses form an electronically controlled agile axial scanning system that can rapidly focus the laser spot at different depth locations along the sample thickness. An important point to

notice is the difference in the scanning approach between the classical confocal microscope and the proposed no-moving-parts ASCM. In the classical approach the sample is scanned in the axial direction by translating it mechanically in the axial direction using a motorized precision translation stage while the axial location of the focused laser spot is fixed. On the other hand, in the proposed no-moving-parts ASCM, the sample is fixed in its axial location while the focused laser spot is moved in the axial direction to a desired location along the sample thickness where imaging is required. This operation is achieved by simply varying the drive signal to the LC lens.

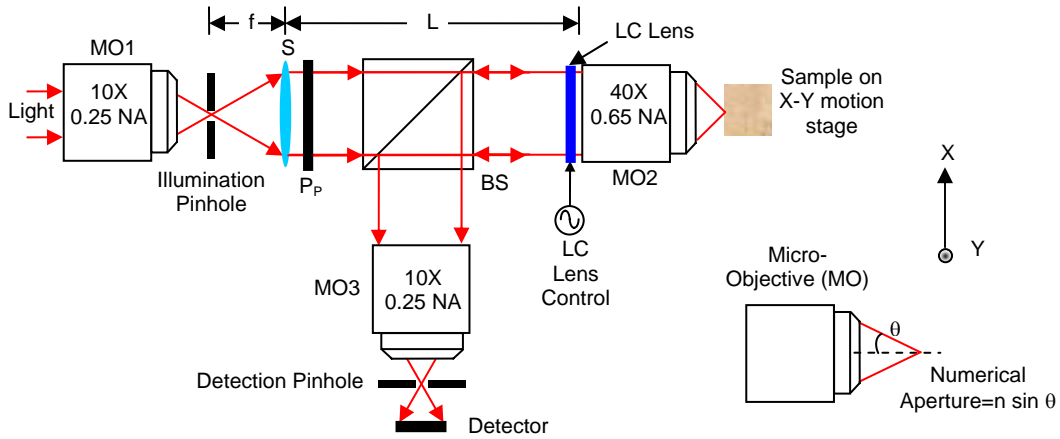


Fig. 8.1. Proposed No-Moving-Parts Axial Scanning Confocal Microscope using a LC lens. S: Spherical lens, Pp: Linear polarizer along horizontal or p-axis, BS: Beam Splitter, MO1/ MO2/ MO3: Micro-Objective (MO) lenses.

The deployed LC lens consists of a homogeneously aligned nematic LC material sandwiched between two glass substrates. On one of the glass substrates, there is a transparent low impedance electrode while the other one has a high impedance electrode.<sup>15</sup> An annular metallic contact is deposited on top of the high impedance electrode. The low impedance electrode works as a ground electrode. As the voltage is applied to the annular metallic contact, a circularly symmetric voltage gradient results which causes a circularly symmetric index gradient

for the light polarization that is oriented along the initial LC molecular director. This index variation results in focusing of the incident laser beam, the LC device focal length being  $F=D^2/(8d\Delta n)$ , where  $\Delta n$  is the birefringence of the LC material,  $d$  is the LC layer thickness, and  $D$  is its clear aperture. Since birefringence can be controlled through the electrical drive signal, the focal length can be varied in a desired fashion and hence the laser beam can be scanned in the axial direction. In an upright microscope configuration, as the index gradient increases, the focal length decreases and hence the focal spot moves upwards and closer to the objective lens itself.

For a confocal microscope, an important aspect is its 3-dB transverse resolution  $d_{Tr}$  and the 3-dB axial directions resolution  $d_{Ax}$  that are given by:<sup>4</sup>

$$d_{Tr} = \frac{0.46\lambda}{NA}, \quad (1a)$$

$$d_{Ax} = \frac{1.4n\lambda}{NA^2}, \quad (1b)$$

respectively.  $NA=n \sin\theta$  where  $\theta$  is the half angle of the focusing beam as shown in Fig. 8.1.<sup>4</sup>  $n$  is the index of the medium that is present between the micro-objective and the sample. As can be seen from the equation (1) relations, the transverse and axial resolutions can be improved by employing shorter wavelength lasers, choosing a higher NA micro-objective lens, and immersing the sample in a high refractive index liquid such as water or oil.

### 8.3 ASCM Experimental Demonstration

For the proof-of-concept experiment, the Fig. 8.1 reflective ASCM is designed and assembled in the laboratory. A 15 mW He-Ne laser at 633 nm wavelength is used as the

illumination source. The laser beam is spatially filtered using a 10  $\mu\text{m}$  pinhole and a Micro-Objective (MO) labeled MO1 which is a 10X 0.25 NA lens assembly. The beam is then collimated using a 5 cm focal length spherical lens S, producing a  $1/e^2$  Gaussian beam waist diameter of 5 mm at the S lens plane. A linear polarizer  $P_p$  is placed after S so that light is horizontally or p-polarized. The LC lens used is a 5 mm diameter device with an LC layer thickness of 50  $\mu\text{m}$ . The LC material employed is Merck BL006 with a birefringence  $\Delta n$  of 0.286 at  $\lambda=589\text{ nm}$  and  $20^\circ\text{C}$  (see Appendix C). The LC device nematic director is aligned along the horizontal or p-direction. The sampling 40X microscope objective MO2 used has a NA of 0.65 and a 5 mm clear aperture. Using the equation (1) relations for MO2,  $d_{Tr} = 0.45\text{ }\mu\text{m}$  and  $d_{Ax} = 2.1\text{ }\mu\text{m}$  with  $n=1$  and  $\theta=41^\circ$ . The distance between the LC lens and MO2 is 4 mm. The distance L is 60 cm to accommodate the mechanical translation stages used to mount the optical components. The distance from the BS to the MO2 and MO3 is 40 cm where MO3 is the 10X detection arm objective with 0.25 NA. The optical detector and power meter used are Newport Model 818-SL and 1830-C, respectively. The detection pinhole has a diameter of 10  $\mu\text{m}$ . Notice that MO2 and MO3 have different magnifications; hence the spot size at the detection pinhole is four times larger than that formed by MO2. All the MOs and pinholes used are low-end off-the-shelf components from Newport Corp.

In order to characterize the ASCM, a flat aluminum mirror is used as an axially moving sample on a precision  $\pm 30\text{ nm}$  positional accuracy Aerotech Model FiberAlign 130 motion controller stage with the mirror being moved with a height increment of 100 nm for determining the ASCM axial resolution  $d_{Ax}$ . Figure 8.2 shows this data, indicating that  $d_{Ax}=3.1\text{ }\mu\text{m}$  with the LC lens in the sample path and without the LC device in the path. Hence the inserted LC lens

indeed acts as a thin optic placed in the instrument and therefore does not optically degrade the basic resolution of the microscope. To compare, equation (1) indicates a MO2 theoretical resolution  $d_{Ax}=2.1\text{ }\mu\text{m}$ . In our case, we expect this degradation from the theoretical ideal to be due to aberrations in our specific low-end objective lenses used in combination with a tunable focus weak lens.

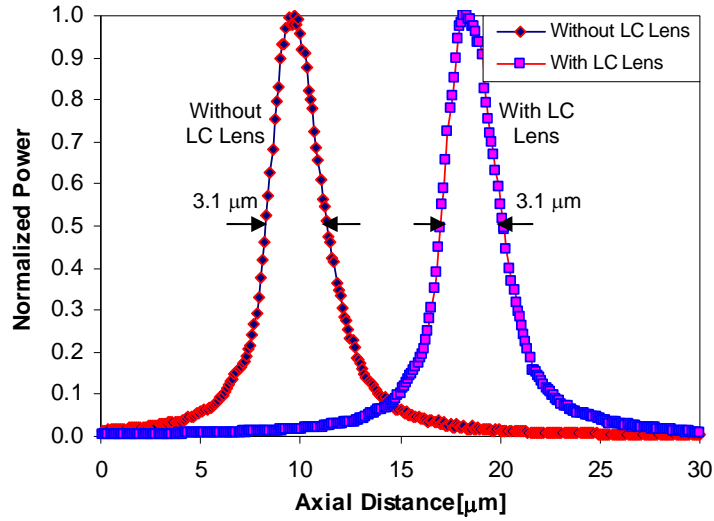


Fig. 8.2. Plots showing measured  $3.1\text{ }\mu\text{m}$  3-dB axial resolution of the demonstrated ASCM with and without the LC lens inserted into the sample path.

To determine the imaging capability of the ASCM, a semiconductor sample with dual InP square waveguides is deployed. Each waveguide has a  $2.3\text{ }\mu\text{m}$  width and a  $2.3\text{ }\mu\text{m}$  height with a  $7.9\text{ }\mu\text{m}$  inter-waveguide gap as measured by a Scanning Electron Microscope (SEM); see line-scanned SEM image of sample in Fig. 8.3(b). Three different planes in the waveguide chip were imaged. Plane SS' is the *substrate* plane. Plane TT' is the *top* surface of the rectangular waveguides. Plane BB' is *below* the substrate plane by an amount equal to the height of the rectangular waveguides. First, the laser beam is focused at the SS' plane by employing the high

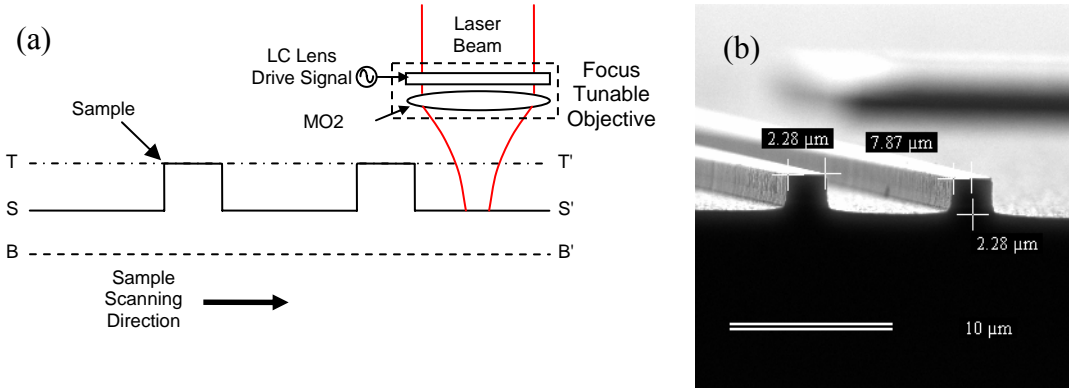


Fig. 8.3. (a) Setup for measuring the ASCM imaging capability and (b) SEM image of the test sample.

precision Aerotech 3-D motion controller previously used for measuring the ASCM  $d_{Ax}$  value. Line scan images are taken and plotted in Fig. 8.4. Plane SS' is mechanically placed in the focal plane of the micro-objective and a mechanically implemented line scan is taken and plotted as the top intensity plot in Fig. 8.4(a) marked SS'. Next, the sample is moved up by  $2.3 \mu\text{m}$  mechanically such that the laser beam is now focused inside the sample at plane BB'. The corresponding mechanically line-scanned intensity plot is shown in Fig. 8.4(b) marked BB'. This plot is the scaled version of the first plot of Fig. 8.4(a) of plane SS', as the beam is now defocused at the SS' plane. The LC lens is then turned on to electronically move the focal plane up to SS' plane. The drive signal is tweaked to get a maximum optical signal on the photo-detector. Again a line scan is taken as shown in Fig. 8.4(c) marked SS'. As can be seen by comparing the intensity plots of Fig. 8.4(a) and Fig. 8.4(c), the LC lens is capable of bringing the sample back into focus by simple control of the drive signal. Next, the LC lens is turned off and the sample is mechanically moved into plane TT' with the corresponding line scan intensity plot shown in Fig. 8.4(d). The sample stage is then moved up by  $2.3 \mu\text{m}$  such that the plane SS' is

now in focus. The corresponding intensity plot is shown in Fig. 8.4(e). Finally, the LC lens is turned on again to electronically bring the focal plane to the TT' plane, with the corresponding intensity plot shown in Fig. 8.4(f). As observed in Fig. 8.4 and expected, the intensity plot of Fig. 8.4(f) is the same as that of Fig. 8.4(d). Figure 8.5 shows an alternate representation of the Fig. 8.4 data by using analog intensity plots. In short, the plots of Fig. 8.4 and Fig. 8.5 clearly show that the demonstrated ASCM is capable of resolving transverse features of at least  $2.3\ \mu\text{m}$  width and axial features of  $2.3\ \mu\text{m}$  height. As shown in Fig. 8.5, the measured 3-dB width of the InP waveguides using the demonstrated LC lens-based ASCM is  $2.1\ \mu\text{m}$  and the measured waveguide pitch is  $10.3\ \mu\text{m}$ . It is important to note that the micro-objective used in the current demonstration is not a high NA top quality lens. Hence the proposed ASCM transverse and axial resolutions can be greatly improved such as by using a higher NA high quality objective and by decreasing the wavelength of illumination.

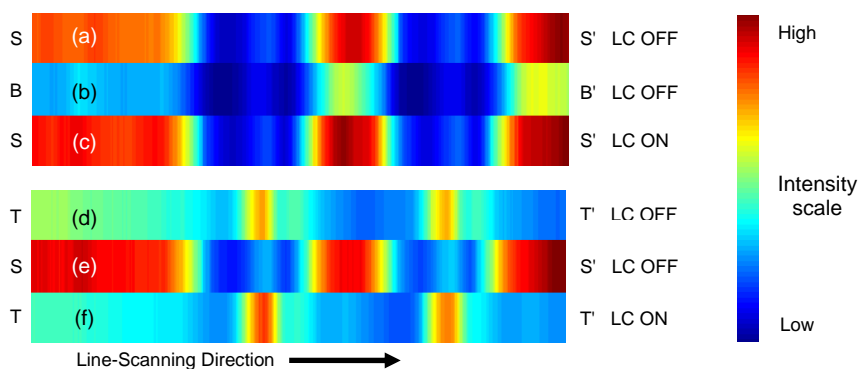


Fig. 8.4. ASCM line-scanned optical intensity plots obtained for the InP waveguides sample.

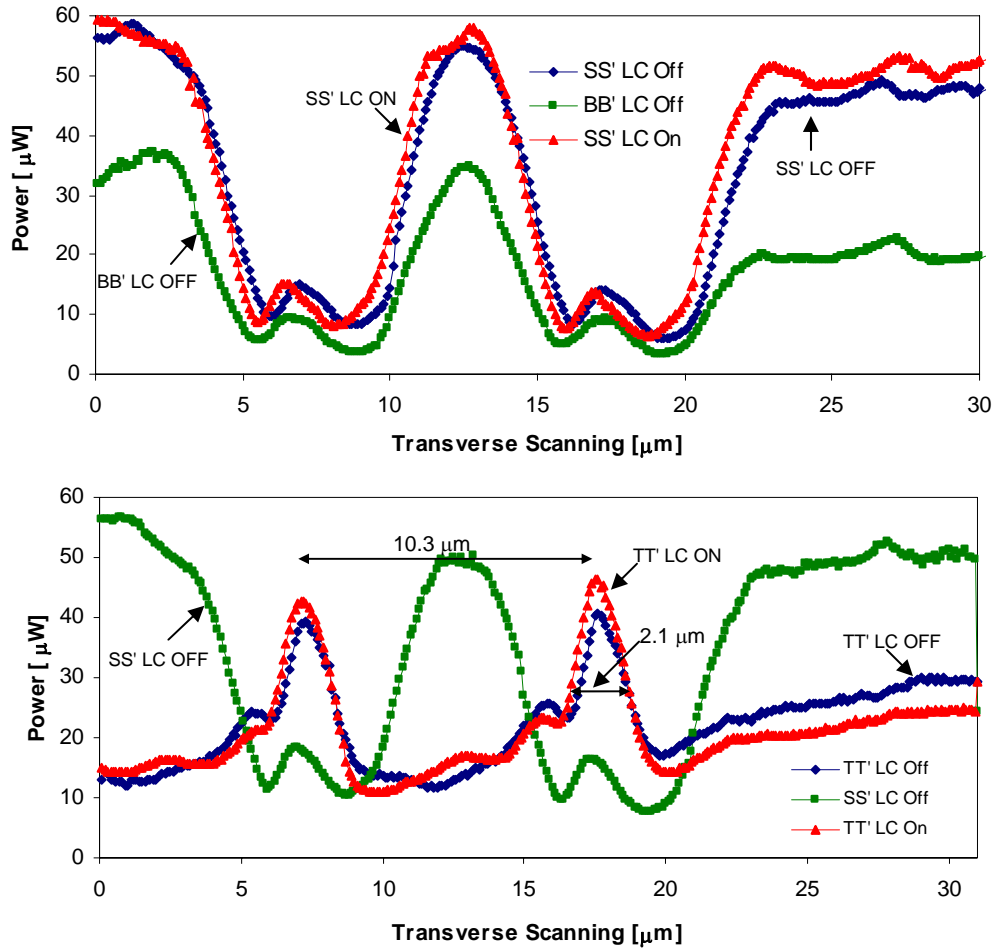


Fig. 8.5. ASCM line-scanned analog optical intensity plots obtained for the InP waveguides sample corresponding to Fig. 8.4.

Figure 8.6 shows the measured 48  $\mu\text{m}$  axial scanning range of the LC lens-based ASCM with the drive signal being a square wave with fixed amplitude of 5.4 Volts. To determine the finest focal plane shift possible using the present LC lens, a flat aluminum mirror is placed in the sample arm. The drive signal to the LC lens is finely varied and the shift of focal plane in the axial direction is measured by mechanically translating the sample in sub-micron sized steps using the precision motion controller while tracing the optical power maxima on the photo-detector. The resulting plot in Fig. 8.7 shows that the LC lens is capable of scanning in sub-



depth-of-focus steps as shown by the 270 nm resolution achieved in this case. Note that this is an important achievement showing that the LC lens with precise electronic drive control is capable of achieving a much higher axial resolution/optical section thickness if employed next to a high NA micro-objective lens. In such a way, the proposed LC-based ASCM forms a super-precision sub-wavelength axial depth profiler. Do note that this result is possible because the LC lens is an analog device controlled by an analog electrical drive signal that controls the smooth analog molecular rotation of the LC molecules. Notice that including the LC lens, all optics used were non- Anti-Reflection (AR) coated resulting in reduction in optical throughput. For 633 nm, the single pass optical loss due to the LC lens is 0.9 dB. This is a relatively high loss due to the fact that the current LC device was optimized for use in the 1550 nm wavelength range.

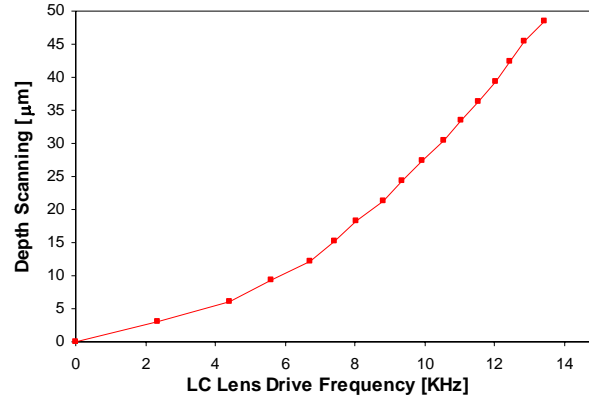


Fig. 8.6. Demonstrated LC lens-based ASCM classic 3-dB confocal resolution limited axial scanning transfer characteristics as a function of the LC lens drive frequency.

Assuming a 100% reflective sample, the total loss from source to detector for the built ASCM is 15 dB. This includes a 6.7 dB loss from the BS, a 3.6 dB loss from the LC-lens-MO2 combination, a 1 dB loss from MO3, and 3.7 dB loss due to the process of laser beam spatial filtering and collimation. Loss can be reduced by using AR coated components including the

lower loss (e.g. 0.35 dB) LC lens. Furthermore, by replacing the BS with a polarization BS, a more efficient microscope can be realized. In this case, a quarter wave plate will be needed in the reflective geometry to direct the returning light from the sample into the detection arm. Since the beam emerging from the wave-plate will have both p and s (or vertical) polarization components, two LC lenses with orthogonal nematic directors will be needed to cater for both polarization components. The present reset speed of the used analog LC lens is 1 second. To enable much faster axial scan reset times (e.g., 10  $\mu$ sec), the earlier demonstrated digital LC lens can be deployed.<sup>12</sup> Furthermore, a no-moving-parts full 3-D scanning ASCM can be realized using all LC devices that form both angular beam deflectors for scanning in the transverse dimension and variable lenses for axial scanning.<sup>12</sup>

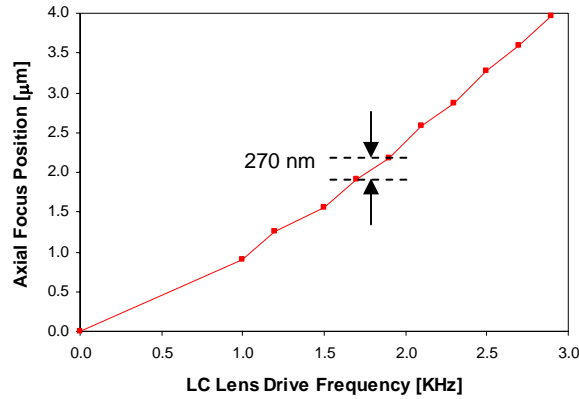


Fig. 8.7. Super-fine axial scanning resolution transfer characteristics of the demonstrated LC lens-based ASCM.

The LC lens-based ASCM presented here can be extended to enable fluorescence imaging of biological samples. This is done by incorporating a dichroic beam splitter instead of the BS in Fig. 8.1 and adding a photo-multiplier tube in the detection arm. Hence, the modified

ASCM can provide in vivo imaging of biological samples to help detect cellular activity without the motion artifacts associated with motion controller based image acquisition.

#### 8.4 Conclusion

The proposed no-moving-parts ASCM is inherently free from the deleterious motion artifacts that are typically associated with fine axial motion control mechanics. In short, an improvement is expected in the instrument long-term reliability and repeatability. Hence the proposed ASCM has the potential to become a useful tool for investigating the 3-D structure of microscopic and potentially nano-scopic objects in biomedicine, electronics, and photonics. The demonstrated visible band ASCM allowed the imaging of two InP waveguides with 2.3  $\mu\text{m}$  width and height dimensions. Using the digital LC lens, a fast 3-D image acquisition confocal microscope is possible for real-time monitoring of cellular activity.<sup>12</sup> Future work relates to fluorescence imaging of biological samples and full 3-D imaging using all LC or hybrid LC-MEMS scanning approaches.

## References

1. M. Minsky, "Microscopy Apparatus," US Patent 3013467, 1961.
2. T. Wilson, "Confocal Microscopy," Academic Press, San Diego, 1990.
3. T. Corle and G. Kino, "Confocal Scanning Optical Microscopy and Related Imaging Systems," Academic Press, San Diego, 1996.
4. M. Rajadhyaksha, R. Anderson, R. Webb, "Video-Rate Confocal Scanning Laser Microscope for Imaging Human Tissues In Vivo," Applied Optics, Vol. 38, Issue 10, Pages 2105-2115, April 1999.
5. G. Molesini, G. Pedrini, P. Poggi, F. Quercioli, "Focus wavelength encoded optical profilometer," Opt. Comm., Vol. 49, Issue 4, Pages 229-233, 1984.
6. B. Picard, "Method for the scanning confocal light optical microscopic & indepth examination of an Extended field & devices for implementing said method," US Patent 4965441, Oct.23, 1990.
7. M. A. Browne, O. Akinyemi, A. Boyde, "Confocal surface profiling using chromatic aberration," Scanning, 14, 145-153, 1992.
8. H. J. Tiziani and H. M. Uhde, "Three dimensional image sensing by chromatic confocal microscopy," Appl. Optics, 33, 1838-1843, 1994.
9. Y. Yasuno, S. Makita, T. Yatagai, T. Wiesendanger, A. Ruprecht, and H. Tiziani, "Non-mechanically-axial-scanning confocal microscope using adaptive mirror switching," Optics Express, Vol. 11, Issue 1, Pages 54-60, 2003.

10. N. A. Riza, "BOPSCAN Technology: A methodology and implementation of the billion point optical scanner", OSA Top. Mtg., Proc. SPIE, 3482, 572, 1998.
11. N. A. Riza, "Digital control polarization based optical scanner", US Patent 6031658, 2000.
12. N. A. Riza and S. A. Khan, "Polarization multiplexed optical scanner," Optics Letters, Vol.28, Issue 7, pp.561, 2003.
13. N. A. Riza and A. Bokhari, "Agile Optical Confocal Microscopy Instrument Architectures For High Flexibility Imaging," Proc. SPIE Vol. 5324, p. 77-88, Three-Dimensional and Multidimensional Microscopy: Image Acquisition and Processing XI; Jose-Angel Conchello, Carol J. Cogswell, Tony Wilson; Eds. SPIE Biomedical Optics, Jan. 24-29, 2004, San Jose, CA.
14. S. A. Khan and N. A. Riza, "Confocal microscopy based agile optical endoscope using liquid crystals," Biophotonics/Optical Interconnects and VLSI Photonics/WBM Microcavities, 2004 Digest of the IEEE LEOS Summer Topical Meeting, Pages 10-11, June 28-30, 2004, San Diego, CA.
15. G. Vdovin, A. Naumov, M. Loktev, V. Belopukhov, F. Vladimirov, and G. Love, "Wave front control systems based on modal liquid crystal lenses", Rev. Sci. Instrum., 71, 9, 2000.

## **CHAPTER 9: ULTRA-LOW LOSS LASER COMMUNICATIONS TECHNIQUE USING SMART BEAMFORMING OPTICS**

Theory and design is presented for a technique for ultra-low loss laser communication that uses a combination of strong and weak thin lens optics, hence obeying the paraxial approximation. As opposed to conventional laser communication systems, the Gaussian laser beam is prevented from diverging at the receiving station by using a weak thin lens that places the transmitted beam waist mid-way between a symmetrical transmitter-receiver link design. The weak lens can be a fixed optic for static link distances or programmable for mobile scenarios. The programmable weak optic can be a single pixel or multi-pixel lens made by liquid crystal or mirror technologies. The proposed link design is appropriate for low air turbulence links such as short-range or indoor links and space based links.

## 9.1 Introduction

Laser communications has been around since the advent of the laser itself.<sup>1</sup> Laser communications scenarios include but are not limited to: short-range (indoor/a few meters) links,<sup>2</sup> terrestrial short-hop building-to-building links (1-5 km), terrestrial (line of sight ~100 km) links,<sup>3,4</sup> submarine-to-aircraft links,<sup>5</sup> submarine-to-satellite links,<sup>6</sup> airborne links (~50 km to 500 km),<sup>7</sup> mobile platform-to-airborne links, mobile platform-to-satellite links, ground-to-Low Earth Orbit (LEO) satellite links which range from several hundred km to a few thousand km,<sup>8,9</sup> aircraft-to-satellite links,<sup>10</sup> ground-to-Geostationary Earth Orbit (GEO) satellite links which range from 35,000 km to ~42,000 km, LEO-to-LEO satellite cross-links (~3,000 km), LEO-to-GEO satellite cross-links (~40,000 km),<sup>11-14</sup> GEO-to-GEO satellite cross-links (~80,000 km),<sup>13</sup> and ground-to-planetary probe links (> 100,000 km to several millions of km).<sup>15</sup>

Of importance in these links is the communication medium which can sometimes degrade the communication link performance. In short range or indoor links only physical obstruction in the line of sight link can disrupt the communication. In contrast, propagation effects on laser communications in the atmosphere need to be considered carefully.<sup>16</sup> The atmosphere is roughly a 20 km thick air blanket surrounding the earth. Due to temperature changes and wind flow, the index of refraction of the air randomly varies temporally. This causes the laser beam to both wander around the desired propagation direction and be spread as well along the propagation path in an indeterministic fashion, thus causing the loss of useful signal power.

The effect of the atmosphere is severe in links which involve a ground based station as the transmitter (TX) in a satellite uplink configuration because of the fact that the laser beam undergoes the atmospheric turbulence in the beginning of the communication link. This is true for example in a ground-to-LEO or a ground-to-GEO uplink where the ground terminal acts as the TX. Typical distances are in the range of  $\sim 400$  km to a few thousand km for a ground-to-LEO link while those for a ground-to-GEO link are  $\sim 40,000$  km. For example, in a ground-to-GEO uplink, the laser beam will encounter the atmospheric turbulence in the first 1 % of the communication medium, resulting in large unwanted beam divergence and intensity variations (scintillation) at the satellite receiver (RX) terminal. Alternately, when the GEO satellite station acts as the TX in a satellite-to-ground link, the laser beam first travels for the 99 % of the link length in space and in the last 1 % comes across the atmosphere. Hence at the ground RX, the received beam properties are governed predominantly by the TX beam divergence. Moreover due to their limitations of prime-power, weight and volume, large size telescopes are not feasible in satellites resulting in a laser beam that diverges rapidly compared to a larger size transmit beam. As a result the ground terminal has to have a larger telescope in order to receive the TX beam from the satellite terminal resulting in an asymmetric laser communication link configuration. This configuration is feasible as the ground terminals can afford to incorporate the large telescope sizes required in asymmetric links. Ground terminals can also afford to use high power lasers and complex wavefront correction adaptive techniques in order to overcome undesirable beam spread and scintillation caused by the atmospheric turbulence. In effect, this makes the lasercom solution a better choice for satellite-to-ground links.

Since the satellite itself in most of the configurations such as imagery and reconnaissance is the data transmitting terminal, a high speed downlink is required as compared to a moderate



speed uplink that is needed for satellite control and feedback purposes. Intersatellite cross-links involve space as the communication link medium, and hence atmospheric effects do not come into play making lasercom a preferred choice in these links. For example, the SILEX demonstration in Nov. 2001 used a link between LEO satellite SPOT4 (832 km orbit, 25 cm TX telescope, 25 cm RX telescope, 60 mW GaAlAs laser diode @ 847 nm and 50 Mbits/s NRZ modulation) and GEO satellite ARTEMIS (31000 km orbit, 12.5 cm TX telescope, 25 cm RX telescope, 37 mW GaAlAs laser diode @ 819 nm and 2 Mbits/s PPM).<sup>12</sup> Image data was transferred from SPOT4 to ARTEMIS at a 50 Mbits/s rate for the first time using solely an optical link. The optical communication terminal onboard ARTEMIS was also tested before the actual inter-satellite link establishment using an earth based ground station as a mock-up LEO satellite.<sup>9</sup> The ground station had a 1 m Zeiss RX telescope and a  $847\pm 5$  nm Titanium-Sapphire laser with a peak power of 6 W that was pumped by an Argon ion laser. The ground station used four mutually incoherent TX beams with 4 cm diameters to counter far-field divergence caused by the atmospheric turbulence and scintillation. Due to the fast velocity relative to earth ( $\sim 7$  km/s),<sup>14</sup> high speed tracking and pointing is required for the LEO-to-ground links making it difficult to establish and maintain the link as compared to LEO-to-GEO and GEO-to-ground links. The relatively "fixed" position of the GEO-satellites as viewed from earth makes lasercom a viable option due to the relatively slow pointing and tracking speed requirements.

In a communication system it is highly desirable to collect the largest amount of signal power by the receiver in order to get the maximum detection signal-to-noise ratio (SNR). In the laser communications arena, this means collecting the maximum amount of laser light at the RX with the given RX telescope. A higher SNR also enables a high information throughput in a shorter period of time as well as low TX drive power and lower bit error rate (BER). Acquisition,

pointing and tracking in the laser communications system are very important aspects to consider in order to establish a reliable communication link. Wavelength is directly related to the amount of angular spread that a laser beam undergoes in a free-space communication link. For example, a 775 nm laser wavelength as compared to the telecom eye safe 1550 nm wavelength source results in a beam that diverges half as much as the 1550 nm beam and requires as a result a RX telescope of only half the diameter of that of the 1550 nm telescope. In general, a laser beam has a Gaussian profile meaning that the beam diverges as it emerges out of the laser cavity.<sup>17</sup> Typically a diverging beam would result in the RX collecting only a small portion of this beam resulting in loss of useful optical signal power. In a laser communication system where it is not possible to extract more power out of the laser cavity, collecting as much photon flux as possible at the RX becomes critical.

Another more recent application for a low loss freespace optical link is quantum communications where information is coded by the quantum nature of light.<sup>18,19</sup> Keeping link loss down is even more important for quantum optical communications as optical amplifiers cannot be used in the link design to boost power.<sup>20</sup> Thus for quantum coding based links, lost photons must be greatly minimized to achieve significant link propagation distance. In short, the proposed low loss link concept is critical for achieving a significant bit rate-link distance product when using super-secure quantum coding for laser communications.

In this chapter, we propose a novel technique to implement low loss laser communication. Specifically, the use of programmable beamforming optics is introduced to control the divergence angle of the laser beam in the medium and prevent it from diverging unwantedly in the communication link. This proposal is focused on a methodology for collecting the largest amount of the optical signal using programmable beamforming optics. In particular,

the beamforming optics in the TX and RX are optimized to implement a self-imaging configuration previously demonstrated for ultra-short distance fiber-freespace-fiber coupling.<sup>22</sup> First, the Gaussian beam propagation metrics are formulated and then example link designs are presented to show how the proposed technique can be implemented in real world scenarios. Programmable beamforming optics can also be used to establish the link as the laser beam divergence can be increased in order for the RX to be able to first "see" the TX beam, and then the TX beam can be gradually narrowed in order to increase the SNR and start the information transfer. These and other design issues are next described in this chapter.

## 9.2 Self-Imaging Technique for Low Loss Laser Communications

### 9.2.1 Gaussian Beam Propagation Theory

A thin lens of focal length  $f$  transforms a  $\frac{1}{e^2}$  input beam waist  $w_1$  at a distance of  $x$  from the lens to a  $\frac{1}{e^2}$  output beam waist  $w_2$  at a distance  $x'$  (see Fig. 9.1) within the Paraxial approximation regime that requires the plano-convex thin lens  $F\#$  to be  $\geq 1.67$  (see Appendix A). Using Gaussian beam propagation and ABCD matrices, the distance  $x'$  at which the new beam waist  $w_2$  is located is given by:<sup>17</sup>

$$x' = f \frac{x(x-f) + z_l^2}{(x-f)^2 + z_l^2}, \quad (1)$$

and the beam waists  $w_1$  and  $w_2$  are related by:

$$\frac{w_2^2}{w_1^2} = \frac{f^2}{(x-f)^2 + z_l^2}, \quad (2)$$

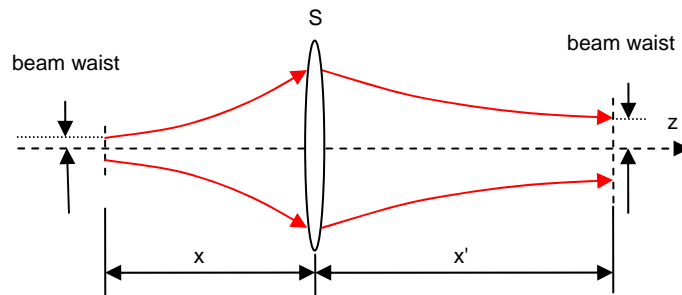


Fig. 9.1: Gaussian beam propagation through a thin lens. S: Spherical thin lens.

where  $z_I = \frac{\pi w_I^2}{\lambda}$  is called the confocal beam parameter and  $n$  is the index of the medium in which the wave is traveling. As can be seen, the location of the output beam waist depends upon the input beam waist, the distance  $x$ , the focal length  $f$  of the thin lens used and the wavelength  $\lambda$ . Notice from equation (1) that in the case when the input beam waist  $w_1$  is located at a distance of  $f$  from the thin lens (i.e.,  $x=f$ ), then the output beam waist  $w_2$  will also be a distance of  $f$  away from the thin lens. Moreover, in the case when the input beam waist  $w_1$  is located at the thin lens itself (i.e.:  $x=0$ ), the expression in equation (1) reduces to:

$$x' = \frac{f z_I^2}{f^2 + z_I^2}, \quad (3)$$

and the beam waists  $w_1$  and  $w_2$  are related by:

$$\frac{w_2^2}{w_1^2} = \frac{f^2}{f^2 + z_I^2}. \quad (4)$$

If equation (3) is plotted as a function of the thin lens focal length  $f$ , it can be seen that there is an upper limit on  $x'$ , i.e., how far the output beam waist  $w_2$  can be located from  $S$  for a given  $\lambda$  and  $w_1$ . Fig. 9.2 shows the equation (3) case when  $w_1=0.25$  mm and  $\lambda=1.55$   $\mu\text{m}$  and the corresponding output beam waist  $w_2$  as a function of the thin lens focal length  $f$  given by equation (4). In order to get the maximum  $x'$ , equation (3) is differentiated with respect to  $f$  and the differential is then equated to zero, i.e.:

$$\frac{d}{df}(x') = \frac{d}{df} \left( \frac{f z_I^2}{f^2 + z_I^2} \right). \quad (5)$$

$$\frac{d}{df}(x') = z_I^2 \frac{(z_I^2 - f^2)}{(f^2 + z_I^2)^2}. \quad (6)$$

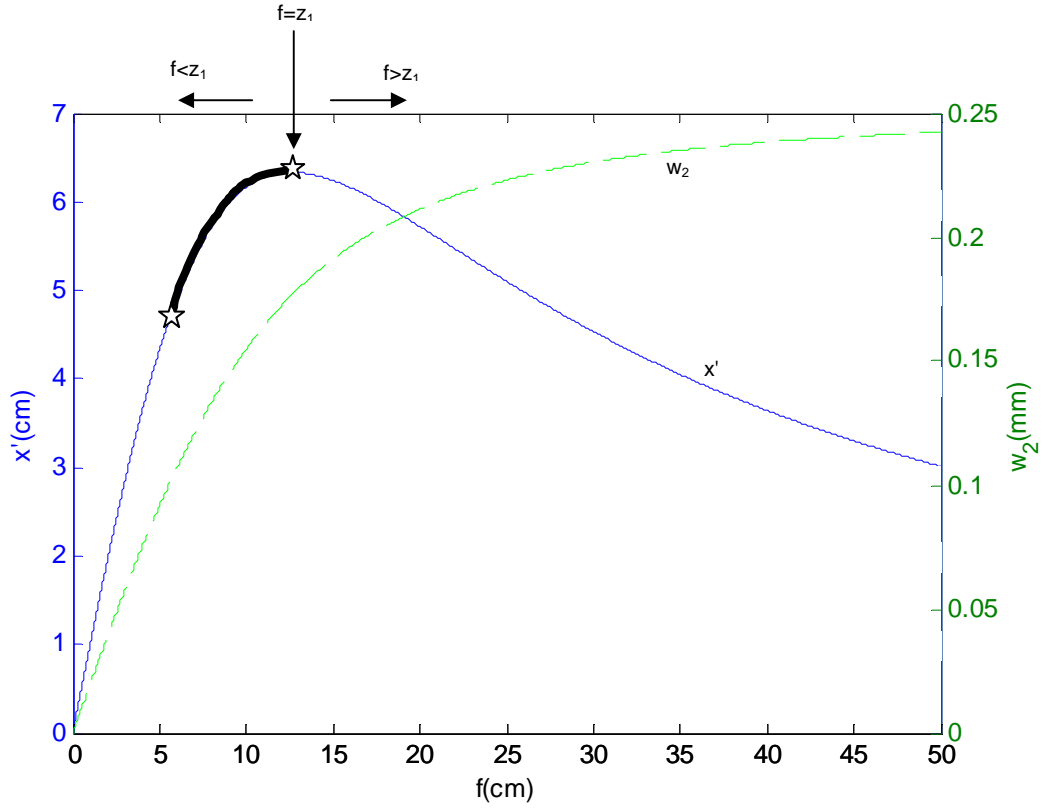


Fig. 9.2. Output beam waist location  $x'$  from the thin lens and the output beam waist  $w_2$  as functions of the thin lens focal length  $f$  for an input beam waist  $w_1$  of 0.25 mm,  $\lambda=1.55 \mu\text{m}$  and  $x=0$ .

By equating equation (6) to zero, it can be seen that  $x'_{\text{max}}$  is obtained when  $f=z_1$ , the confocal beam parameter. Using equation (3) gives:

$$x'_{\text{max}} = \frac{f}{2} = \frac{z_1}{2} = \frac{\pi w_1^2}{2\lambda}. \quad (7)$$

Using  $f=z_1$  in equation (4) gives the output beam waist  $w_2$  at  $x'_{\text{max}}$  to be:

$$w_2 = \frac{w_1}{\sqrt{2}}. \quad (8)$$

Since  $z_1$  is dependent upon both the beam waist  $w_1$  and wavelength  $\lambda$ , a different input beam waist  $w_1$  and a wavelength  $\lambda$  will result in a different  $x'_{\max}$  and related  $w_2$ . In short,  $x'_{\max}$  implies that given a certain input beam waist  $w_1$  incident at the thin lens with  $x=0$  and wavelength  $\lambda$ , an output beam waist  $w_2$  is formed at a distance of  $x'_{\max}$  only with a thin lens focal length  $f$  that is equal to  $z_1 = \frac{\pi n w_1^2}{\lambda}$ .

In a typical laser communication link, the configuration used is as shown in Fig. 9.3.<sup>10,21</sup> At the TX the laser beam diverges as it emerges out of the TX enclosure. The RX consists of a capturing thin lens which collects only a fraction of the actual TX laser beam power and focuses it onto a detector placed in the focal plane of this thin lens. The divergence of a Gaussian beam leads to enlargement of the beam diameter at the RX. The beam waist follows the relation:<sup>17</sup>

$$w^2(z) = w_1^2 \left( 1 + \frac{z^2}{z_1^2} \right), \quad (9)$$

where  $z$  is the longitudinal propagation dimension. This divergence results in loss of useful optical power and hence degradation of the SNR at the RX. In earlier work, it was demonstrated that if the separation distance  $Z_0$  between two identical fiber GRIN rod lenses is exactly equal to twice the GRIN lens beam waist location distance  $d_1$ , then zero loss is obtainable.<sup>22</sup> The ref. 22 theory is extended in this chapter to lasercom links such as freespace optical wireless and laser satellite links. The divergence causes a drastic loss of power due to improper separation distance between the TX and the RX. For example, when  $\lambda=1550$  nm, beam waist  $w_1$  at the TX is 1 mm, the separation distance  $z$  between TX and RX is 1 km, and the receiving thin lens has a diameter  $D$  of 10 cm, only about 2 % of the transmitted power is collected by the capturing lens (see Appendix B). This calculation also assumes ideal conditions, i.e., the received beam is centered

on the capturing lens and there is no absorption/scattering/turbulence in the communication medium. Furthermore, there can also be other factors that will result in further loss of optical power, namely, angular tilt and offset misalignments between the TX and RX terminals as well as Fresnel reflections.<sup>22</sup> Fresnel losses can be reduced by having all the optical components in the system coated with anti-reflection films.

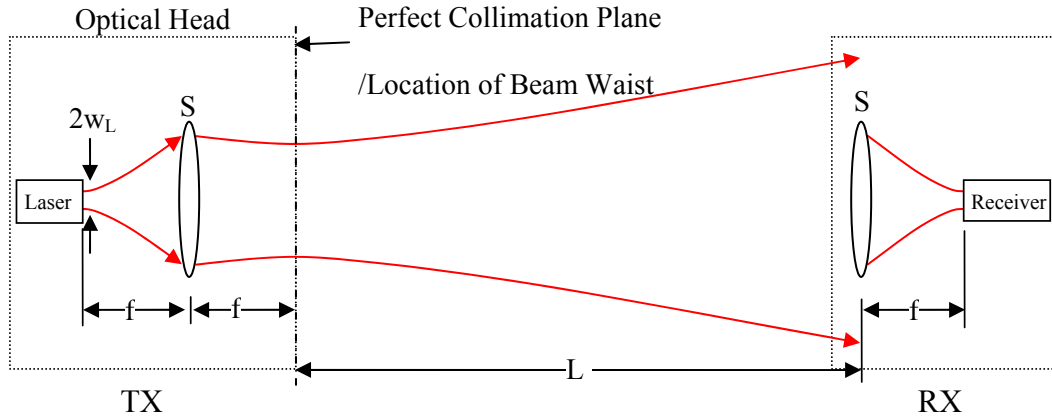


Fig. 9.3. Configuration of a typical lasercom link.

### 9.2.2 Self-Imaging Technique for Freespace Link Design

In order to get the maximum power at the RX, this work proposes the use of a programmable self-imaging configuration between the freespace link TX and RX.<sup>22</sup> To begin an introduction to this approach for Gaussian beam based freespace links, Fig. 9.4 shows that if the thin lenses  $S_1$  and  $S_2$  are chosen to have the same focal length and the distance  $P$  is equal to  $f$ , then  $Q$  is equal to  $f$ . On the other hand if the distance  $R$  is equal to  $f$ , then the distance  $Y$  at which the output beam waist is located at the RX is also  $f$  away from the thin lens  $S_2$ . Due to symmetry, the output beam waist  $w_3$  at the RX becomes equal to  $w_1$ . This is a symmetric configuration in which the two thin lenses  $S_1$  and  $S_2$  have the same focal length resulting in distances,  $P$ ,  $Q$ ,  $R$  and



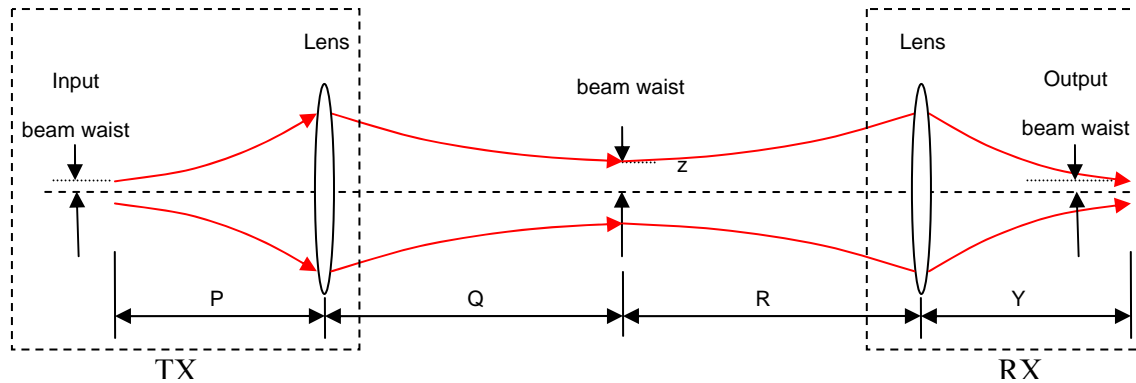


Fig. 9.4. Gaussian beam through a pair of thin lenses in a self-imaging configuration.

$Y$  each being equal to  $f$ . As shown in Fig. 9.5 using equation (3), for large distances such as in satellite communication, the distance between the TX and the RX is very large rendering this 4- $f$  link design impractical for low loss laser communications. This is due to the fact that such long focal lengths will require the lenses  $S_1$  and  $S_2$  to be placed at distances which are not feasible in practice even if the assumed large input beam waists  $w_1$  of several meters were attainable.

Figure 9.6 shows using equation (3), that for a fixed input beam waist  $w_1$ , a change in wavelength means a different output beam waist location. For example, choosing the lower blue wavelength compared to a near IR wavelength greatly increases the possible communication link length  $L$ . Moreover, in some links such as inter-satellite links where atmospheric turbulence is not present in the communication medium, a choice of wavelengths is available to the designer in order to optimize the link performance. But the limitation here is that such large focal lengths (i.e., weak optical lens powers) can not be fabricated with current day technology and a TX telescope can not afford to incorporate such a long focal length in the classical 4- $f$  configuration. To overcome the TX size limitation, the use of another thin lens, designated by PL in Fig. 9.7, is

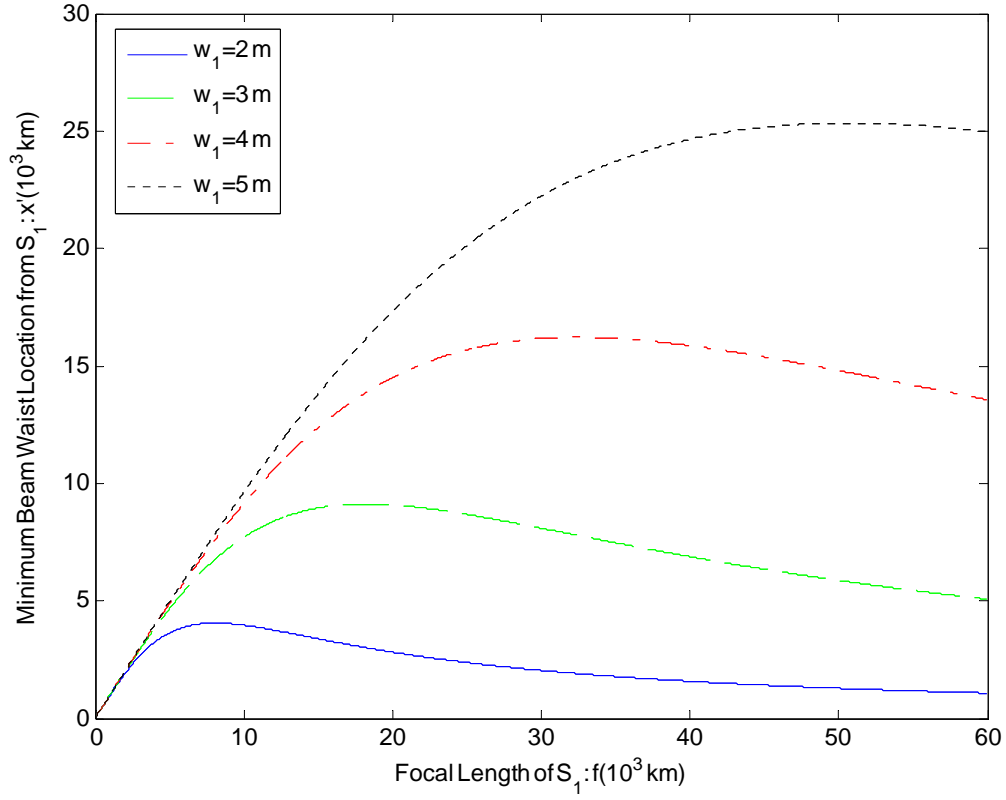


Fig. 9.5. Beam waist location  $x'$  from the thin lens  $S_1$  as a function of the  $S_1$  lens focal length  $f$  for an input beam waist  $w_1$  of 2 m, 3 m, 4 m and 5 m at  $\lambda=1.55 \mu\text{m}$  and  $x=0$ .

proposed in this chapter that can be placed after the thin lens  $S_1$  in the TX such that PL is located in the output beam waist position of  $S_1$ . The fact that the output beam waist location  $x'$  of the thin lens PL is dependent only on its focal length and the beam waist  $w_2$  at its input, the self-imaging condition is realized that can be used to meet any desired link length  $2x'=L$ . Using this configuration serves two purposes; first it allows the minimum possible diameter of the telescope exit aperture enabling compact TX size and secondly it allows the output beam waist to be independent of the input beam waist location  $x$ . Figure 9.7 shows the proposed beamforming

optic T for the TX implementing a low loss link using the self-imaging mechanism. The optic T consists of a strong thin lens  $S_1$  of a short focal length  $f$  and a weak thin lens PL of a long focal length  $x'$ . The PL can be either a fixed or an ultra-thin electronically programmable thin lens. The distance between  $S_1$  and PL is  $f$ , where  $f$  is the focal length of  $S_1$ .  $S_1$  is placed  $f$  away from the laser source.

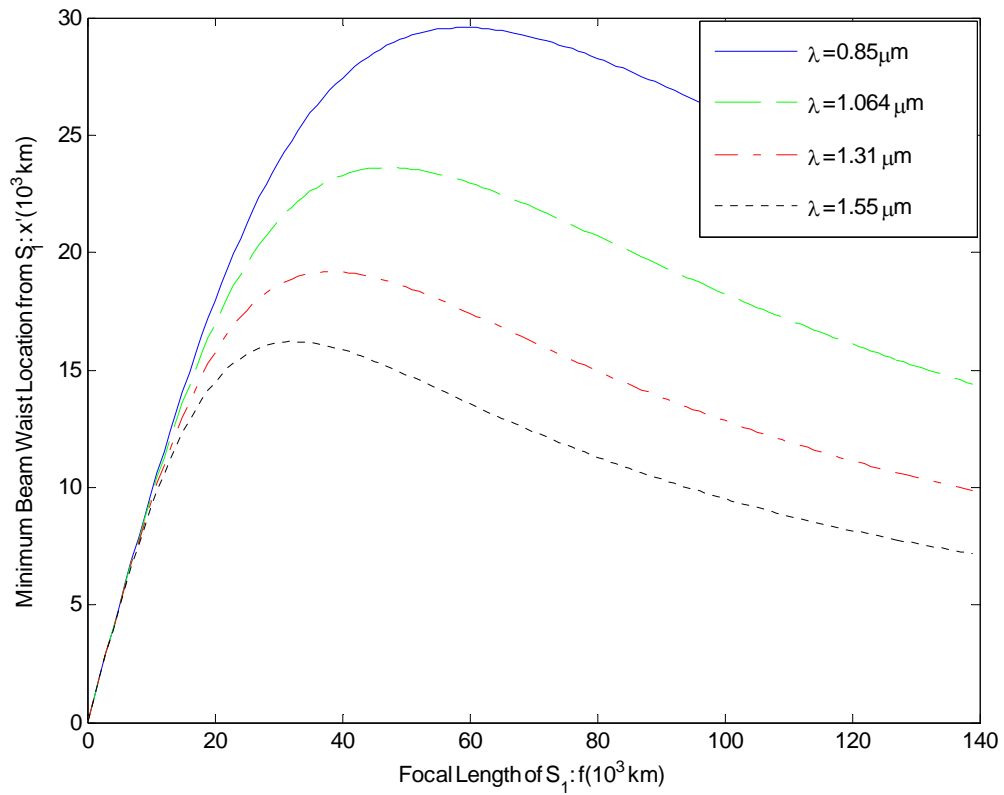


Fig. 9.6. Beam waist location  $x'$  from the thin lens as a function of the lens focal length  $f$  for different wavelengths and an input beam waist of 4 m with  $x$  being 0.

Given a symmetric communication link with a separation distance  $L$  between the TX and RX, the thin PL lens needs to form a beam waist  $w_3$  in the middle of the link, i.e., at  $L/2$  in order

to transmit all the energy to the receiving terminal. For short distances, such as upto a few meters, such PL lenses can be fabricated with ordinary glass. Using a fixed focal length thin lens will fix the allowed communication link length  $L$  and thus will not provide the same total power at the RX terminal for any variations in the link distance  $L$  such as in mobile platform links. The solution to this problem is to make the thin PL lens programmable such as an ultra-thin electronically programmable Liquid Crystal (LC) spherical lens or a deformable membrane mirror with a focal length that is suitable for the application under consideration, e.g.,  $L > 20,000$  km for inter-satellite links. This combination of  $S_1$  and PL resides inside the TX enclosure. The smart PL lens can cater for the changes in the link distance variation which is a highly sought after feature in some applications such as mobile and inter-satellite links where link distances slowly yet continuously change due to platform movement.

For a LC lens, the focal length is given as:<sup>24</sup>

$$f_{PL} = \frac{D^2}{8d\Delta n_E}, \quad (10)$$

where  $D$  is the diameter of the lens,  $d$  is the LC cell thickness and  $\Delta n_E$  is the electrically controlled birefringence of the lens LC material. Since birefringence can be electrically varied in an LC device, the focal length of the LC lens increases by decreasing  $\Delta n_E$ . In the absence of the applied E-field, the  $\Delta n_E$  is 0 and the focal length is infinity. Hence, in this case, the PL acts as a planar slab of transparent optical material. A higher applied E-field corresponds to a higher  $\Delta n_E$ . Hence, an increase in the communication link length, for example by an amount of  $\Delta L$ , is easier to cater for as the applied E-field can be reduced in order to form the beam waist at the new location  $\frac{L + \Delta L}{2}$ . In the case that the link length  $L$  decreases by an amount of  $\Delta L$ , the lens PL



lens combination  $S_2$ ,  $PL_2$  represented by  $R_P$  in the RX. The key innovation of this link design versus the 4-f link is that the distance  $P$  can be made much smaller than the distance  $Q$  (see Fig. 9.4) leading to small size TX and RX optics.

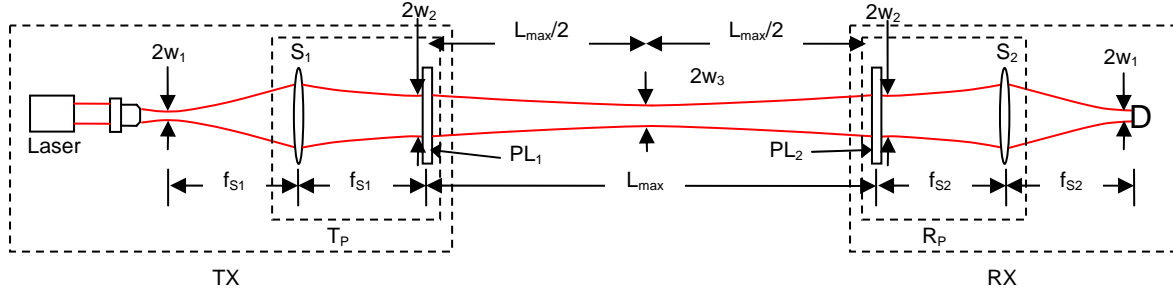


Fig. 9.8. Proposed low loss symmetric lasercom link design using strong ( $S_1$ ,  $S_2$ ) and weak ( $PL_1$ ,  $PL_2$ ) thin lens combinations for Gaussian beam propagation through freespace.  $f_{S_1} = f_{S_2}$  and  $f_{PL_1} = f_{PL_2}$  for the symmetric design.

### 9.2.3 Symmetric Link Design Methodology

For a certain symmetrical lasercom system, knowing the distance  $L \pm \Delta L$  between the TX and the RX, where  $\pm \Delta L$  is the possible link length variation, and  $\lambda$  being the wavelength of operation, the remaining link design parameters can be determined by following the flow chart shown in Fig. 9.9. First, the goal is to find the largest input beam waist  $w_2$  required for  $L_{\max}$ , where  $L_{\max} = L + \Delta L$ . This beam waist  $w_2$  is half the transmit optical aperture. Given  $L_{\max}$ , and the fact that the beam waist  $w_3$  has to be located at the half-way distance between TX and RX, the required input beam waist  $w_2$  is determined using equation (7) as:

$$2x'_{\max} = L_{\max} = f_{PL_1} = z_2 = \frac{\pi w_2^2}{\lambda}, \quad (11)$$

giving the beam waist  $w_2$ :

$$w_2 = \sqrt{\frac{\lambda L_{max}}{\pi}}. \quad (12)$$

Now what remain to be determined are the beam waist  $w_1$  of the laser source and the focal length  $f_{s_1}$  of the fixed spherical thin lens  $S_1$ . Ideally, this focal length  $f_{s_1}$  is desired to be as small as possible in order to reduce the TX optics length. Since  $S_1$  is placed at a distance of  $f_{s_1}$  from the  $PL_1$ , by using equation (2), where  $x=f_{s_1}$ , the relationship between the beam waist  $w_1$  and the focal length of thin lens  $S_1$  required can be determined as:

$$w_1 = \frac{f_{s_1} \lambda}{\pi w_2}, \quad (13)$$

where the index  $n$  of the propagation medium was chosen to be 1 in the above relation. Inserting the expression for  $w_2$  from equation (12) into equation (13):

$$w_1 = f_{s_1} \sqrt{\frac{\lambda}{\pi L_{max}}}. \quad (14)$$

Notice that equation (14) implies that the laser spot size  $w_1$  will define the focal length  $f_{s_1}$  of the fixed thin lens  $S_1$  required to form the output beam waist  $w_2$ . By either choosing a laser source with a certain beam waist of  $w_1$  or by choosing a reasonable focal length  $f_{s_1}$  for  $S_1$  (such that  $F/\# \geq 1.67$  for thin lens  $S_1$ , see appendix A), the unknown parameter can be determined from equation (14). Since a symmetric link case is considered, therefore the beam waist at the RX side, i.e.,  $w_5$  on the detector will be the same as  $w_1$ , and  $w_4$  is equal to  $w_2$ . For a minimum link separation distance  $L_{min}=L-\Delta L$ , the new focal length of  $PL_1$ , i.e.:  $f_{PL_1 min}$  needs to be determined. Having chosen a laser with a certain beam waist  $w_1$ , and the fixed thin lens  $S_1$  with focal length  $f_{s_1}$ , the

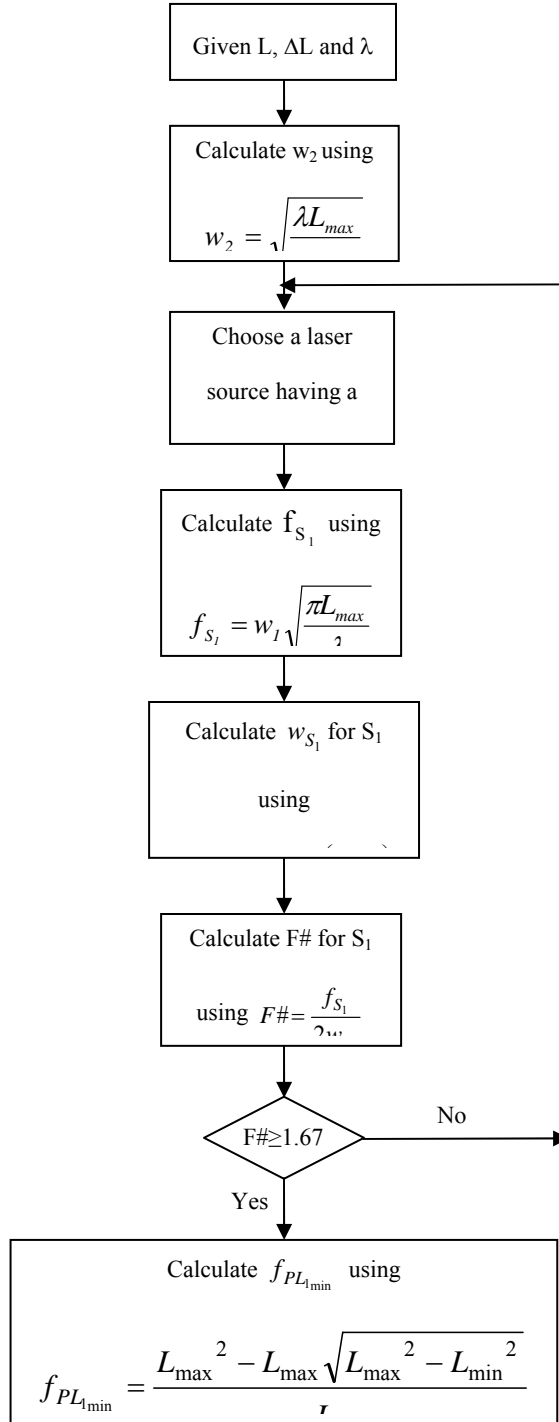


Fig. 9.9. Flow chart for determining the various parameters of a low loss lasercom system given the Link length  $L$ , the possible variation in link length  $\Delta L$ , and operating wavelength  $\lambda$ .



beam waist at the output  $w_2$  is now fixed. Equations (7) or (11) can no longer be used to determine  $f_{PL_1 \min}$ , instead equation (3) will be used. Hence, the focal length of  $PL_1$  can be calculated using equation (3) as:

$$x'_{\min} = \frac{f_{PL_1 \min} z_2^2}{f_{PL_1 \min}^2 + z_2^2}. \quad (15)$$

where  $z_2 = \frac{\pi w_2^2}{\lambda}$ . Since the above equation is a quadratic one. i.e., we can rewrite it as:

$$f_{PL_1 \min}^2 x'_{\min} - f_{PL_1 \min} z_2^2 + z_2^2 x'_{\min} = 0 \quad (16)$$

Replacing  $z_2$  by  $L_{\max}$  (from equation (11)),  $2x'_{\min}$  by  $L_{\min}$  and solving equation (16) for  $f_{PL_1 \min}$ :

$$f_{PL_1 \min} = \frac{L_{\max}^2 \pm L_{\max} \sqrt{L_{\max}^2 - L_{\min}^2}}{L_{\min}}. \quad (17)$$

Note that equation (17) has two solutions that are both valid as can be seen in Fig. 9.2 that plots the values of the thin lens focal length that gives a desired  $L_{\max}=2x'_{\max}$  value. As  $f$  changes away from  $z_1$  (where  $z_1$  corresponds to the maximum in the  $x'$  curve) the beam waist location  $x'$  becomes closer to the lens itself. Also one can notice in Fig. 9.2 that as the focal length  $f$  is increased, the output beam waist  $w_2$  increases in size and tends towards the input beam waist size  $w_1$  as  $f$  approaches infinity while on the other side where  $f < z_1$ , the output beam waist  $w_2$  decreases as we decrease the focal length  $f$  below the  $f=z_1$  point for maximum  $x'$ . This is an important point to note as the diameters of the optics required will be defined by the chosen focal lengths. Although it might be desirable to increase the output beam waist  $w_2$  in some applications, here we choose the case where  $f_{PL_1 \min}$  is less than  $z_1$  (as pointed in Fig. 9.2 by a dark line on the left side of the  $x'$  curve maximum) hence resulting in a smaller output beam waist  $w_2$  compared to  $w_1$ . Nevertheless, one can always use the other solution of equation (17)

which means longer focal length and larger output beam waist  $w_2$ , yet the same beam waist location  $x'$  as in the first solution. Hence, by looking at Fig. 9.2, one can choose the solution of equation (17) in the region where  $x'$  lies to the left side of the maxima causing the output beam waist  $w_2$  to decrease. Therefore, for a decrease in the link length to  $L-\Delta L$ , the required focal length  $f_{PL_{min}}$  to form the new beam waist half-way between the TX and RX will also decrease.

The focal length  $f_{PL_{min}}$  is then given as:

$$f_{PL_{min}} = \frac{L_{max}^2 - L_{max}\sqrt{L_{max}^2 - L_{min}^2}}{L_{min}}. \quad (18)$$

Equation (18) gives the shortest focal length required for the  $PL_1$ . Table 1 gives example design parameters for several proposed symmetrical low loss laser communication links.

The  $f_{PL_{min}}$  and  $f_{PL_{max}}$  correspond to two values along the curve as seen in Fig. 9.2 highlighted with a star each. The PL lens needs to be able to vary the focal length between these two values (the dark curve between these two stars) so that the Gaussian beam waist is located in the middle of the communication link to be able to capture atleast 86% of the power in the incident beam (see Appendix B). The two values for  $f_{PL_{min}}$  and  $f_{PL_{max}}$  can also be chosen on the left side of the maximum of  $x'$  curve in Fig. 9.2 if desired, with the chosen PL lens capable of varying the focal length between these two values to cater to the link length variation between  $L_{min}$  and  $L_{max}$ .

Note that in the symmetric link case discussed,  $PL_1$  and  $PL_2$  are identical and so are  $S_1$  and  $S_2$ . A key parameter to note is the PL lens minimum aperture of  $2w_2$  that ranges from a small 3 mm to a rather large 9.42 m (see Table I). Notice that the last two cases for Ground-to-GEO satellite links do not meet the  $F\# \geq 1.67$  criterion set in Appendix A. The fixed thin lens  $S1$  has an

$F\# < 1.67$ . Hence for these two cases the design will need to be modified so that the  $F\# \geq 1.67$  criterion is met. We recalculate the parameters by changing the input beam waist  $w_1$  to new values which are shown in the same row such that the new  $F\#$  is larger than 1.67.

So far, typical single pixel liquid crystal lenses have up to about 1 cm apertures.<sup>24-26</sup> Figure 9.10 shows an approach to realize a larger size thin PL lens by combining many single pixel piston-type elements. Do note that as the PL aperture sizes increase, the required PL minimum focal length also increases; thus requiring many low power pixels to complete the larger aperture PL lens. It is clear that as link distances increase, the control complexity of the multi-pixel PL lens will also increase in addition to adding diffraction effects due to a multi-pixel lens structure. An alternate technology to use for making a large PL lens is adaptive membrane mirrors driven by piezo-actuators such as used for adaptive optics in large telescopes such as the Keck telescope.<sup>27</sup> For example, the Subaru optical telescope has an 8.2 m diameter primary mirror and uses 261 robotic fingers which fit into holes that are drilled in this 20 cm thick primary mirror in order to correct mirror shape for optimal wavefront quality as well as a 36-actuator based bi-morph deformable mirror along with a wavefront sensor to form an adaptive optics system resulting in diffraction limited images in the infra-red wavelength band.<sup>28</sup>

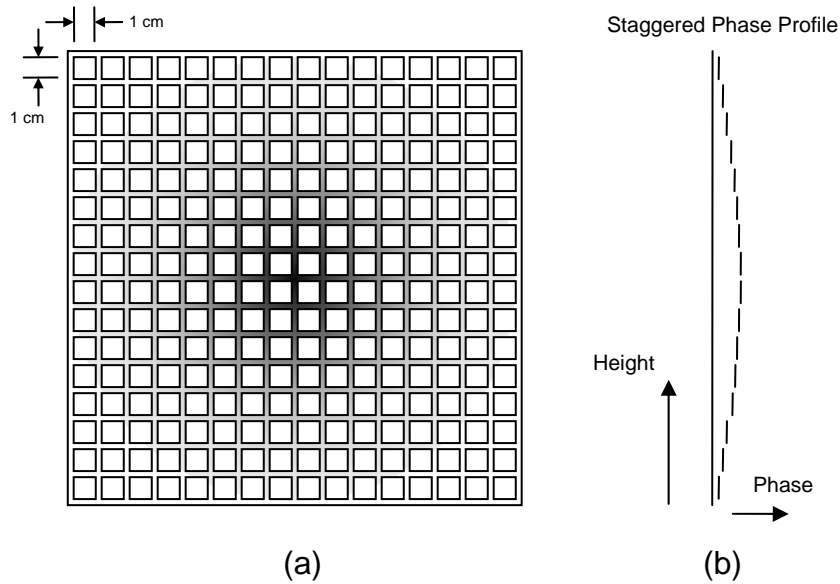


Fig. 9.10. An approach to realize a large programmable optic. (a) Piston-type single pixels in an  $N \times N$  array forming a large programmable optic. Gray-scale corresponds to phase: Black=Large phase, White=Small phase. (b) The corresponding staggered phase profile for a weak thin lens. Phase represented in Figure is not to scale.

#### 9.2.4 Asymmetric Lasercom Link Design

In some applications the communication link configuration can be asymmetric implying that the TX and RX optics are not a one to one match. For example in ground-to-satellite links due to weight and volume limitations the satellite can carry only a limited size telescope while the ground station can afford to have a larger heavy and bulky optic. In a satellite-to-ground

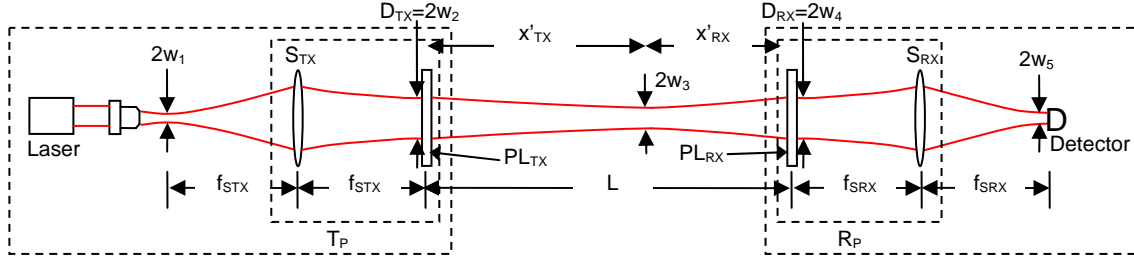


Fig. 9.11. Proposed low loss asymmetric lasercom link design using Strong (STX, SRX) and weak (PLTX, PLRX) thin lens combinations for Gaussian beam propagation through freespace.

Note:  $f_{STX} \neq f_{SRX}$  and  $f_{PLTX} \neq f_{PLRX}$  due to the asymmetric design.

link, if the allowed telescope aperture is  $D$  and the link distance  $L$  and its variation  $\pm\Delta L$  and the design wavelength  $\lambda$  are given, the remaining low loss link design parameters can be determined as follows. Assuming the satellite to be in the TX mode, first the satellite terminal parameters can be determined. Referring to Fig. 9.11, since the system is asymmetrical, therefore let us say the beam waist in the communication medium is a distance of  $x'_{TX}$  away from the TX. This implies that the  $PL_{RX}$  at the RX has to form a beam waist at a distance of  $x'_{RX}$  ( $=L-x'_{TX}$ ) away from the RX. To incorporate for the link length variation of  $\pm\Delta L$ , these quantities can be modified as:

$$L_{\max} = L + \Delta L = x'_{TX \max} + x'_{RX \max} \quad (19)$$

Using the expression derived earlier in equation (7), one can also say:

$$x'_{TX \max} = \frac{f_{PLTX \max}}{2} = \frac{z_2}{2} = \frac{\pi w_2^2}{2\lambda} \quad \text{and} \quad x'_{RX \max} = \frac{f_{PLRX \max}}{2} = \frac{z_4}{2} = \frac{\pi w_4^2}{2\lambda} \quad (20)$$

Since,  $w_2$  (or  $w_4$ ) is known i.e.,  $w_2 = D_{TX}/2$  (or  $w_4 = D_{RX}/2$ ) where  $D_{TX}$  ( $D_{RX}$ ) is the diameter of the TX (RX)  $f_{PLTX \max}$  and  $x'_{TX \max}$  can be determined. Since  $L_{\max}$  and  $x'_{TX \max}$  are now both

known, they give  $x'_{RX \max}$  from equation (19). Having  $x'_{RX \max}$  known,  $f_{PL_{RX \max}}$  as well as  $w_4$  can be found using equation (20).

Given the  $w_2$  ( $w_4$ ) and using equation (2), where  $x=f$ , the value of the focal length for the thin lens  $S_{TX}$  ( $S_{RX}$ ) at the satellite TX (ground RX) that will transform a beam of waist  $w_2$  ( $w_4$ ) into a waist of  $w_1$  ( $w_5$ ) can be determined as:

$$f_{S_{TX}} = \frac{\pi w_1 w_2}{\lambda}, \quad f_{S_{RX}} = \frac{\pi w_4 w_5}{\lambda}, \quad (21)$$

where the index  $n$  of the propagation medium was chosen to be 1 in the above relation. Assuming a value for  $f_{S_{TX}}$  ( $f_{S_{RX}}$ ) in equation (21),  $w_1$  ( $w_5$ ) can be determined or vice versa. Since key parameters such as  $w_2$ ,  $w_4$ ,  $f_{S_{TX}}$  and  $f_{S_{RX}}$  are known, one can proceed to calculate the focal lengths  $f_{PL_{TX \min}}$  and  $f_{PL_{RX \min}}$  that are needed to form the beam waist  $w_3$  at a distance of  $x'_{TX \min}$  away from the TX in the case when the link distance decreases to  $L_{\min}$ . Recall, that:

$$L_{\min} = L - \Delta L = x'_{TX \min} + x'_{RX \min}. \quad (22)$$

Since,

$$\frac{x'_{TX \max}}{L_{\max}} = \frac{x'_{TX \min}}{L_{\min}}, \quad (23)$$

$x'_{TX \min}$  can be determined from this relation as all the other quantities are known. Using equation (3) gives:

$$x'_{TX \min} = \frac{f_{PL_{TX \min}} z_2^2}{f_{PL_{TX \min}}^2 + z_2^2}. \quad (24)$$

Equation (24) is a quadratic relation in which the only unknown quantity is  $f_{PL_{TX \min}}$ . Solving for  $f_{PL_{TX \min}}$ , results in:

$$f_{PL_{TX_{min}}} = \frac{z_2^2 \pm z_2 \sqrt{z_2^2 - 4x'^2_{TX_{min}}}}{2x'_{TX_{min}}} . \quad (25)$$

Replacing  $z_2$  in the above equation with  $2x'_{TX_{max}}$  from equation (20) gives:

$$f_{PL_{TX_{min}}} = \frac{4x'^2_{TX_{max}} \pm 2x'_{TX_{max}} \sqrt{4x'^2_{TX_{max}} - 4x'^2_{TX_{min}}}}{2x'_{TX_{min}}} . \quad (26)$$

Once again, for a decrease in link distance  $L$ , using the earlier mentioned argument regarding the possibility of a smaller beam waist  $w_2$  by choosing a solution on the left hand side of the  $x'$  curve in Fig. 9.2, the focal length of the PL lens  $f_{PL_{TX}}$  is chosen to decrease in order to form the beam waist at the new position which is closer to the TX as compared to that in the case of  $L_{max}$ . Therefore,

$$f_{PL_{TX_{min}}} = 2 \frac{x'^2_{TX_{max}} - x'_{TX_{max}} \sqrt{x'^2_{TX_{max}} - x'^2_{TX_{min}}}}{x'_{TX_{min}}} . \quad (27)$$

In a similar fashion the  $f_{PL_{RX_{min}}}$  can be determined as:

$$f_{PL_{RX_{min}}} = 2 \frac{x'^2_{RX_{max}} - x'_{RX_{max}} \sqrt{x'^2_{RX_{max}} - x'^2_{RX_{min}}}}{x'_{RX_{min}}} \quad (28)$$

The flow chart in Fig. 9.12 summarizes the described procedure for determining the key link parameters for designing an asymmetric lasercom link using the proposed low loss self-imaging technique.

As an example, let us consider the SPOT4 LEO satellite used in the SILEX experiment where  $L=832$  km orbit,  $\Delta L=\pm 100$  km,  $D_{TX}=25$  cm TX telescope, and  $\lambda=847$  nm is trying to establish a direct link to a ground station. Here the SPOT4 satellite needs to form a beam waist at a distance of 28.97 km (from equation (20)) away from its exit aperture for the case of  $L_{max}$ , the  $f_{PL_{TX_{max}}}$  required is 57.95 km (from equation (20)),  $f_{PL_{RX_{max}}}$  is  $1.806 \times 10^6$  m (from equation (19))

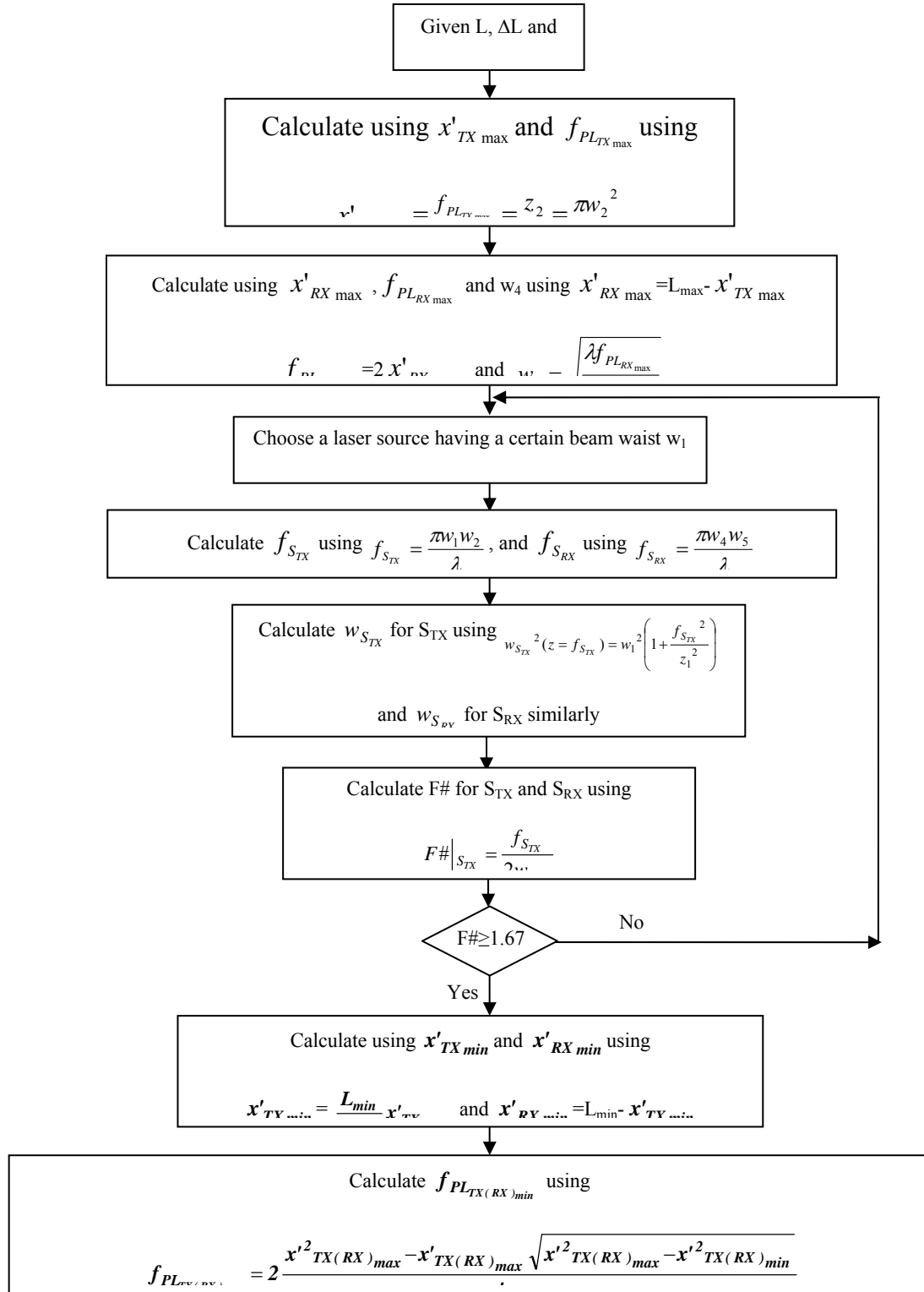


Fig. 9.12. Flow chart for determining the various parameters of an asymmetric low loss lasercom link given the Link length  $L$ , the possible variation in link length  $\Delta L$ , the TX or RX aperture and operating wavelength  $\lambda$ .



and (20)) and a RX aperture ( $2w_4$ ) on the ground station required is 1.4 m (from equation (20)). Assuming a 2  $\mu\text{m}$  laser spot size for  $2w_1$  and a detector size of 16  $\mu\text{m}$  (for  $2w_5$ ) for high bit rate operation, the corresponding  $f_{S_{TX}}$  and  $f_{S_{RX}}$  are calculated using equation (21) to be  $f_{S_{TX}}=46.36$  cm and  $f_{S_{RX}}=20.7$  m. Now, in the case when the link distance decreases to  $L_{\min}$ , using equation (23),  $x'_{TX\min}=22.76$  km and  $x'_{RX\min}=709.24$  km and using equations (27) and (28), the  $f_{PL_{TX\min}}=28.12$  km and  $f_{PL_{RX\min}}=876.16$  km. It is also important to calculate the F# for each of the thin lenses that result from this calculation. Since each of the PL lenses has a very long focal length, e.g.:  $f_{PL_{TX\min}}=28.12$  km, their F#s are very large, e.g.:  $F\#_{PL_{TX}}=\frac{f_{PL_{TX\min}}}{2w_2}=224960$  so one should be more careful about the fixed lenses  $S_{TX}$  and  $S_{RX}$ . The F# for these fixed thin lenses can be calculated using  $F\#_{S_{TX}}=\frac{f_{S_{TX}}}{2w_{S_{TX}}}$  where  $w_{S_{TX}}$  is calculated using equation (9). Hence we calculate F#s for the fixed lenses  $S_{TX}$  and  $S_{RX}$  to be 1.85 and 14.83, respectively.

If this low loss self-imaging approach were used in the SILEX experiment to download data directly from the SPOT4 LEO satellite terminal to the ground terminal, the unnecessary time latency of 204 msec will not have accrued in the downloading of data that was present in the 61,168 km LEO-to-GEO-to-ground link used. The large telescope aperture ( $2w_4$ ) of 1.4 m on the ground terminal can reasonably be achieved and the laser source beam spot size of 2  $\mu\text{m}$  assumed here can easily be obtained using commercially available micro-objective lenses.

Another very suitable application is the communication link between the International Space Station (ISS) and its ground control. The Mission Control Center, Houston, Texas, sends commands to the ISS via an  $\sim 18$  m diameter high gain microwave ground terminal at NASA's

White Sands test Facility near Las Cruces in southern New Mexico using S-band (2-3 GHz) and UHF frequencies (800 MHz) along with Ku-band (10-17 GHz).<sup>29</sup> The S-band is used for voice communication and file transmission. The UHF band is used during spacewalks and other relatively short-distance communication while the high-bandwidth Ku-band is used for video transmission as well as for the two-way transfer of files. The Ku-band also carries data from experiments and other payloads to Mission Control, the Payload Operations Integration Center, and scientists on the ground. As an example scenario, consider the communication between the ISS and its ground control to be via a lasercom link which uses the self-imaging technique as proposed in this chapter. Assume the ISS has an exit telescope with a diameter  $D_{TX}$  of 0.25 m, the link distances are  $L_{min}=278$  km,  $L_{max}=460$  km,<sup>30</sup> and  $\lambda=1.55$   $\mu\text{m}$ . Using the very same procedure that we followed for the SILEX link earlier, we determine that the ISS satellite needs to form a beam waist at a distance of 15.84 km (from equation (20)) away from its exit aperture for the case of  $L_{max}$ , the  $f_{PL_{TX_{max}}}$  required is 31.67 km (from equation (20)),  $f_{PL_{RX_{max}}}$  is 888.3 km (from equation (19) and (20)) and a RX aperture ( $2w_4$ ) on the ground station required is 1.32 m (from equation (20)). Assuming a single mode fiber with a spot size  $2w_1$  of 9  $\mu\text{m}$  and a detector size of 16  $\mu\text{m}$  (for  $2w_5$ ) for high bit rate operation, the corresponding  $f_{S_{TX}}$  and  $f_{S_{RX}}$  are calculated using equation (21) to be  $f_{S_{TX}}=1.14$  m and  $f_{S_{RX}}=10.73$  m. Now, in the case when the link distance decreases to  $L_{min}$ , using equation (23),  $x'_{TX_{min}}=9.57$  km and  $x'_{RX_{min}}=268.43$  km and using equations (27) and (28), the  $f_{PL_{TX_{min}}}=10.65$  km and  $f_{PL_{RX_{min}}}=298.8$  km. The Rx aperture  $D_{RX}$  on the ground station needs to be 1.32 m in order to collect the TX laser beam. The F# for each of the thin lenses  $S_{TX}$  and  $S_{RX}$  are calculated to be 4.56 and 8.11, respectively. This approach can allow the transfer of data from the ISS to ground with more than four times the

speed of the current communication technique as about 40 Gbps of data transfer rate is possible using off-the-shelf commercially available components. It can also be seen that the use of lasercom permits the incorporation of small telescopes for communication purposes which are significantly cost-effective both in the design and in the maintenance phases of the link.

### 9.3 Discussion and Considerations

The design and analysis carried out here assumes the laser beam profile to be Gaussian and the beam waists  $w$  to be the  $\frac{1}{e^2}$  radius. Since only 86% of power is contained in the beam diameter of  $2w_n$ , the system still loses 0.65 dB of the input source power provided the detector diameter is equal to  $2w_5$ . In order to prevent this loss, the diameters of the optics' used including the detector can be increased, if possible, up to a maximum of  $4w$  so that all (i.e., >99.96%) of the incident laser power can be transported to the receiver (see Appendix B), assuming ideal conditions.

An important issue is whether the self-imaging approach is practical for large focal lengths as will be required for long range links such as satellite links. Since, the lower limit on the variation of the link length  $L-\Delta L$  will define the shortest focal length  $f_{PL}$  of the PL lens required in a certain communication link, the three parameters in equation (10), i.e.,  $D$ ,  $d$  and  $\Delta n_E$  can be varied in the design process in order to control the focal length. For long focal lengths, as can be noticed in equation (10), the diameter of the lens  $D$  can be increased, as the focal length  $f_{PL}$  increases quadratically with increasing  $D$ . Alternatively, the thickness  $d$  of the LC layer used in the PL can be decreased as it is inversely related to the focal length  $f_{PL}$  or such an LC material

can be selected which has a weak birefringence  $\Delta n_E$  so that the focal length  $f_{PL}$  can be appropriately controlled between  $f_{PL_{min}}$  and  $f_{PL_{max}}$ . Choosing a short thickness  $d$  is a more attractive option as it will have a favorable effect on the response time of the PL as it has quadratic relation with the response time  $\tau$ .

LCs are known for having weak birefringences and are typically several microns in thickness, hence they result in realizing weak power thin lenses. The LC based PL lenses can in effect be called the closest possible realization of an ideal thin lens as these typically have several micrometers thicknesses. Another important issue is the characterization of such a long focal length lens. For this purpose, interferometric techniques can be employed to obtain the transfer characteristics of the PL lens focal length  $f_{PL}$  as a function of the drive voltage  $V$ . The PL lens can reasonably be considered a thin lens as the typical thickness  $d$  required will be negligibly small compared to a conventional lens thickness. In addition, LC molecular motion can be accurately controlled by high resolution (e.g., >10 bits) voltage drive signals, leading to the precision of optical phase control required to synthesize a LC lens.

The generalized diagram of Fig. 9.8 consists of a TX on one end of the communication link and a RX on the other end. This diagram can be extended to include both a TX and a RX on each end using a beam splitter (BS) in the beam path converting it into a full-duplex lasercom transceiver as shown in Fig. 9.13. This design will result in a 3-dB optical loss to both the TX and the RX beams. Since liquid crystal devices have polarization dependent operation, hence their use means incorporation of techniques to cater for both the orthogonal components of the incident light polarization. This can be done by the use of two LC thin lenses with orthogonally oriented LC director configurations. If in case polarization independent operation is not required, the two communicating terminals can each choose a different orthogonal linear polarization

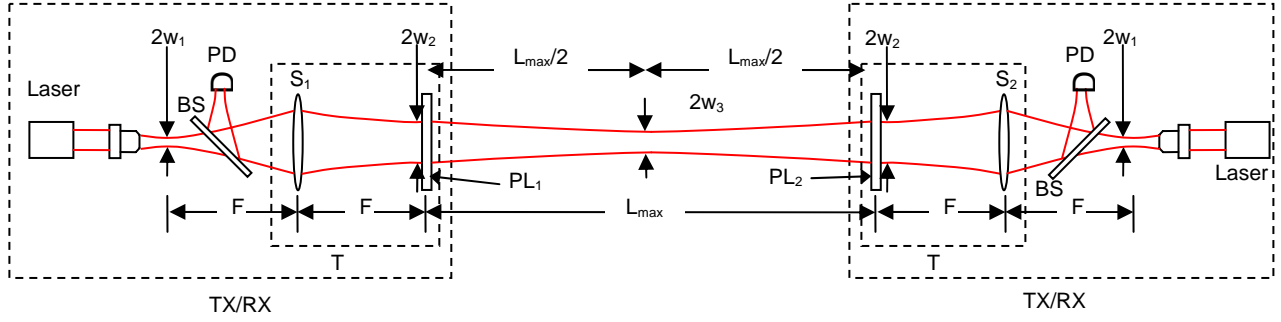


Fig. 9.13. Proposed full-duplex transceiver structure for the low loss lasercom link using beam splitting optics. BS: Beam Splitter, PD: Photo-detector.

component for transmission and the BS can be replaced by a polarizing beam splitter (PBS) to properly direct incoming and outgoing light to the appropriate optics. As a result the 6-dB loss will not accrue as in the case of using BSs for polarization independent operation. Nevertheless, the two orthogonal LC thin lenses will remain. Employing dichroic mirrors instead of the BSs and using laser sources with the same linear polarization but different wavelengths for each transmitter will result in a system with a single LC thin lens per transceiver.

The links considered in Table 1 show design for common lasercom applications. All the example designs here were carried out for two different wavelengths to point out the difference in size of the telescope apertures as well as the focal lengths required for the thin lenses  $S_1$  ( $S_2$ ) and  $PL_1$  ( $PL_2$ ). The telescope aperture should be atleast twice the beam waist at  $PL_1$  (or  $PL_2$ ), i.e.,  $2w_2$ . In the indoor-short range example, the link distance range is chosen to be 1 to 9 meters. The focal length of  $PL_1$  ( $PL_2$ ) required in order to self-image the TX beam waist at the RX is 50.2 cm.  $PL_1$  ( $PL_2$ ) can be designed to have an even shorter focal length in order to first have a highly diverging beam, so that the RX can first acquire the TX beam due to possibly large field of

Table 9.1. Key parameters for several types of symmetrical laser communication links. SMF: Single Mode Fiber.

Application Environment	Link Distance $L \pm \Delta L$	Operating Wavelength $\lambda$ ( $\mu\text{m}$ )	Laser Beam Diameter $2w_1$ (assumed)	Required PL Aperture or Beam Diameter $2w_2$ at PL	Focal Length of $S_1$ ( $S_2$ ), $f_{S_1}$ ( $f_{S_2}$ )	Minimum Focal Length of $PL_1$ ( $PL_2$ ) $f_{PL_1 \min}$ ( $f_{PL_2 \min}$ )	$S_1$ lens $F\# = f_{S_1} / 2 w_{S_1}$
Indoor-very short range (Home, Office)	5 $\pm$ 4 m	1.55	9 $\mu\text{m}$ (Using SMF)	4.2 mm	1.92 cm	50.2 cm	4.56
Indoor-very short range (Home, Office)	5 $\pm$ 4 m	0.8	5 $\mu\text{m}$ (Using SMF)	3.02 mm	1.49 cm	50.2 cm	4.91
Indoor-Long range (Stadiums, Subway, Auditorium)	5-200 m	1.55	9 $\mu\text{m}$ (Using SMF)	19.86 mm	9.06 cm	2.5 m	4.56
Indoor-Long range (Stadiums, Subway, Auditorium)	5-200 m	0.8	5 $\mu\text{m}$ (Using SMF)	14.2 mm	7 cm	2.5 m	4.91
Terrestrial-Short range (Freespace Campus/Corporate/Inter-office)	1000 $\pm$ 200 m	1.55	9 $\mu\text{m}$ (Using SMF)	4.86 cm	22.19 cm	458.4 m	4.56
Terrestrial-Short range (Freespace Campus/Corporate/Inter-office)	1000 $\pm$ 200 m	0.8	5 $\mu\text{m}$ (Using SMF)	3.48 cm	17.16 cm	458.4 m	4.91
Terrestrial-Long range (Remote/isolated rural areas, Observatories)	100 $\pm$ 5 km	1.55	9 $\mu\text{m}$ (Using SMF)	45.52 cm	2.08 m	66.62 km	4.56
Terrestrial-Long range (Remote/isolated rural areas, Observatories)	100 $\pm$ 5 km	0.8	5 $\mu\text{m}$ (Using SMF)	32.7 cm	1.61 m	66.62 km	4.91
Ground-GEO satellite	40000 $\pm$ 5000 km	1.55	3 $\mu\text{m}$	9.42 m	14.32 m	21490 km	1.52
			3.5 $\mu\text{m}$	9.42 m	16.71 m	21490 km	1.77
Ground-GEO satellite	40000 $\pm$ 5000 km	0.8	1.5 $\mu\text{m}$	6.76 m	9.97 m	21490 km	1.47
			2 $\mu\text{m}$	6.76 m	13.29 m	21490 km	1.96

uncertainty. Once the RX terminal 'sees' this TX beam and responds back to the TX, the beam divergence can then be gradually reduced until the proper self-imaging condition has been met so that a higher power optical SNR is achieved at the RX terminal. The scenario envisioned here is that of a transceiver in the ceiling of a room functioning as a wireless internet access point for a user terminal such as a laptop computer or a personal digital assistant (PDA). An active two dimensional scanning system can also be incorporated in each transceiver in order to cater for lateral mis-pointing of the TX and RX terminals. Such a transceiver can act as an optical access switch/hub for wireless local area networks (LAN).

The total length of the TX/RX optics depends upon the focal length of the  $S_1$  and is roughly  $2f_{S_1}$ . In the indoor short-range case, this length is roughly 4 cm at  $1.55 \mu\text{m}$  wavelength. For user terminals such as some laptop computers/notebooks and PDAs, this is a relatively long device length and a much more compact device is needed. One approach to decreasing the device length is to use a shorter wavelength such as done in Table 1 using  $\lambda=0.8 \mu\text{m}$  for the same case resulting in a  $\sim 3$  cm length device, while another approach employs mirrors for path folding. The  $\sim 4$  mm diameter aperture required for the TX/RX is readily achievable with the current day LC technology although the thickness required for  $PL_1$  ( $PL_2$ ) is relatively large for a typical LC device cell for this focal length and aperture combination. An alternative to using a thick cell gap is the use of cascaded LC devices. Since these devices are very thin, they can be considered thin lenses and their optical powers can be added to obtain the desired total focal length for  $PL_1$  ( $PL_2$ ).

The link design analysis conducted in this chapter assumes that there are no atmosphere related turbulence and Gaussian beam spoiling effects in the link. This assumption is reasonable for the indoor short range and long range links as well as long-haul satellite-to-satellite links and

satellite-to-ground downlinks. On the other hand, Gaussian beam spoiling will occur for terrestrial atmospheric freespace links and ground-to-satellite uplinks, and the proposed link design must cater these effects such as via adaptive optics to prevent further beam divergence and loss of transverse coherence due to passage through the non-homogeneous atmospheric medium. Note that the link systems designs assumed transmissive (or refractive) thin lenses. The link configuration can as well be reflective using a mirror  $M_1$  instead of the thin lens  $S_1$  leading to reduced inherent chromatic dispersion associated with lenses due to the glass materials used for making them. In effect, mirror-based link designs can result in an increased communication link information carrying capacity.

In the wave optics domain, this technique might as well be called an "Inverse" adaptive optics approach as in classical adaptive optics efforts are focused on controlling the wavefront at the 'receiving' station whereas in the approach presented here the 'transmitting' wavefront is controlled in such a manner so as to prevent the unnecessary beam divergence and produce the self-imaging effect between the transmitter and receiver.

#### 9.4 Conclusion

Foundations have been laid for ultra-low loss laser communications using a self imaging technique implemented with strong and weak thin lens combination beamforming optics. The weak thin lens, designated by PL, can be either a fixed or a programmable thin lens depending upon the specific requirements of the scenario under consideration. Link design relations have been derived for such a laser communications link that relies on Gaussian beam propagation for



both symmetric and asymmetric situations. Since the laser beam is prevented from diverging unwantedly as it propagates in the communication medium, the possibility of eavesdropping is minimized. This fact by itself makes this technique suitable for use in quantum cryptographic communication systems where single photons are used to minimize eavesdropping. The technique is applicable from ultra-short to long range link scenarios including multipurpose intelligent space platforms involving optical switching and communications.<sup>31</sup>

### References

1. Paul L. Simmons, "Space communications by the use of lasers: An enumerative bibliography," IEEE Transactions on Communications Systems, Vol. 10, Issue 4, Pages 449-456, Dec. 1962.
2. John R. Barry, Joseph M. Kahn, "Link design for nondirected wireless infrared communications," Applied Optics, Vol. 34, Issue 19, Pages 3764-3776, July 1995.
3. Gary D. Wilkins, "Eye-safe free-space laser communications," Proceedings of the IEEE National Aerospace and Electronics Conference, Vol. 2, Pages 710-715, May 1996.
4. G. Stephen Mecherle, "Active pointing for terrestrial free space optics," IEEE LEOS 15<sup>th</sup> Annual Meeting, Vol. 2, Pages 451-452, Glasgow, Scotland, Nov. 2002.
5. Jeffery J. Puschell, Robert J. Giannaris, Larry B. Stotts, "The Autonomous Data Optical Relay Experiment: First two way laser communication between an aircraft and submarine," National Telesystems Conference, Pages 14/27-14/30, May 1992.

6. Larry B. Stotts, "Design considerations of a submarine laser communications system," National Telesystems Conference, Pages 14/13-14/25, May 1992.
7. Robert J. Feldmann, Robert A. Gill, "Development of laser crosslink for airborne operations," IEEE Proceedings of Military Communications Conference, Vol. 2, Pages 633-637, Oct. 1998.
8. Morio Toyoshima, Kenichi Araki, "Far-field pattern measurement of an onboard laser transmitter by use of a space-to-ground optical link," Applied Optics, Vol. 37, Issue 10, Pages 1720-1730, April 1998.
9. Marcos Reyes, Zoran Sodnik, Pablo Lopez, Angel Alonso, Teodora Viera, Gotthard Oppenhauser, "Preliminary results of the in-orbit test of ARTEMIS with the Optical Ground Station," Free-Space Laser Communication Technologies XIV, Proc. of SPIE, ed. S. Mecherle, Vol. 4635, Pages 38-49, San Jose, CA, Jan. 2002.
10. Robert J. Feldmann, "Laser communications airborne testbed: potential for an air-to-satellite laser communication link," Free-Space laser Communication Technologies, Proc. of SPIE, ed. Gerhard A. Koepf and David L. Begley, Vol. 885, Pages 10-17, Los Angeles, CA, Jan. 1988.
11. Yoshinori Arimoto, "Application of adaptive optics techniques to space-ground laser communication," Conference on Lasers and Electro-Optics/Pacific Rim, Technical Digest, Pages 16-17, July 1995.
12. Toni Tolker-Nielsen, Gotthard Oppenhauser, "In-orbit test result of an operational optical intersatellite link between ARTEMIS and SPOT4, SILEX," Free-Space Laser Communication Technologies XIV, Proc. of SPIE, ed. S. Mecherle, Vol. 4635, Pages 1-15, San Jose, CA, Jan. 2002.

13. Peter Winzer, Walter Leeb, "Space-borne optical communications - a challenging reality," The 15th Annual Meeting of the IEEE Lasers and Electro-Optics Society, Vol. 2, Pages:393-394, Nov. 2002.
14. Werner Klaus, "Development of LC optics for free-space laser communications", Intl. J. Electron. Comm., Vol. 56, Issue 4, Pages 243-253, 2002.
15. James R. Lesh, "Laser transmitter/receiver systems for NASA optical communications applications in planetary missions," IEEE Lasers and Electro-Optics Society Annual Meeting, Conference Proceedings, Pages 363-364, Nov. 1993.
16. Larry C. Andrews and Ronald L. Phillips, *Laser beam propagation through random media*, (SPIE Press, 1998, Bellingham, Washington, USA).
17. Amnon Yariv and Pochi Yeh, *Optical waves in crystals*, (John Wiley & Sons, 1984, New York, USA).
18. Charles H. Bennett, Gilles Brassard, Artur K. Ekert, "Quantum cryptography," Scientific American, Pages 50-57, Oct.1992.
19. Markus Aspelmeyer, Thomas Jennewein, Martin Pfennigbauer, Walter R. Leeb, Anton Zeilinger, "Long-distance quantum communication with entangled photons using satellites," IEEE Journal of Selected Topics in Quantum Electronics, Vol. 9, Issue 6, Pages 1541-1551, Nov.-Dec. 2003.
20. Gary Stix, "Best kept secrets," Scientific American, Pages 79-83, Jan. 2005.
21. Monte Ross, "History of space laser communications," Free-Space laser Communication Technologies, Proc. of SPIE, ed. G. Koepf and D. Begley, Vol. 885, Pages 2-9, Los Angeles, CA, Jan. 1988.

22. Martin van Buren, Nabeel A. Riza, "Foundations for Low-Loss Fiber Gradient-Index Lens Pair Coupling with the Self-Imaging Mechanism," *Applied Optics-LP*, Vol. 42, Issue 3, Pages 550-565, January 2003.
23. MATLAB is a matrix equation solving software by MathWorks Inc. of Natick, MA.  
<http://www.mathworks.com/>
24. Mikhail Y. Loktev, Valentin N. Belopukhov, Fiodor L. Vladimirov, Gleb V. Vdovin, Gordon D. Love and Alexander F. Naumov, "Wave front control systems based on modal liquid crystal lenses," *Review of Scientific Instruments*, Vol. 71, Issue 9, Pages 3290-3297, Sep. 2000.
25. Mao Ye and Susumu Sato, "Optical Properties of Liquid Crystal Lens of Any Size," *Japanese Journal of Applied Physics*, Vol. 41, Pages L 571–L 573, May 2002.
26. Hongwen Ren, Yun-Hsing Fan, Sebastian Gauza, and Shin-Tson Wu, "Tunable-focus flat liquid crystal spherical lens," *Applied Physics Letters*, Vol. 84, Issue 23, Pages 4789-4791, Jun. 2004.
27. Peter L. Wizinowich, D. Scott Acton, J. C. Shelton, Paul Stomski, John Gathright, K. Ho, William Lupton, Kevin Tsubota, Olivier Lai, Claire E. Max, James M. Brase, J. An, Kenneth Avicola, Scott S. Olivier, Donald T. Gavel, Bruce A. Macintosh, Andrea M. Ghez, and J. Larkin, "First Light Adaptive Optics Images from the Keck II Telescope: A New Era of High Angular Resolution Imagery," *Pub. Astron. Soc. Pacific*, Vol. 112, Pages 315-319, 2000.
28. *Scientific American*, March 2005, Page 7, or [www.naoj.org](http://www.naoj.org).
29. <http://www.boeing.com/defense-space/space/spacestation/flash.html>
30. <http://satobs.org/iss.html> or <http://www.hq.nasa.gov/osf/station/viewing/history.html>

31. Nabeel A. Riza, "Reconfigurable optical wireless," The 12th Annual Meeting of the IEEE Lasers and Electro-Optics Society, Vol. 1, Pages 70-71, Nov. 1999.

## **CHAPTER 10: BROADBAND RECONFIGURABLE OPTICAL ADD-DROP FILTER FOR DENSE WAVELENGTH-DIVISION-MULTIPLEXING SYSTEMS**

An optical add-drop filter (OADF) for dense wavelength-division-multiplexing (DWDM) systems is proposed using a one dimensional (1-D) Liquid Crystal (LC) deflector array. By binary control of the drive signal to the individual LC deflectors in the array, any optical channel can be selectively dropped and added. For the proof-of-concept OADF demonstration the Texas Instruments (TI) micro-electro-mechanical systems (MEMS) digital micromirror device (DMD)<sup>™</sup> is employed instead of the LC deflector array. This OADF features a polarization insensitive fault tolerant broadband operation, low loss, and the ability to selectively add/drop with high wavelength resolution multiple channels in C telecommunications band. The proof-of-concept OADF designed for the C band demonstrates low insertion loss, 0.15 dB polarization dependent loss (PDL), 3-dB wavelength resolution of 0.4 nm and an average crosstalk of better than 30 dB. With the use of a reference mirror, the OADF becomes a multi-wavelength 2 x 2 routing switch. Key systems issues such as insertion loss, polarization dependent loss, wavelength resolution and response time are analyzed in detail for comparison with the LC deflector approach.

## 10.1 Introduction

The reconfigurable optical add-drop filter (OADF) is a key component for today's optical communication networks. It provides the ability to selectively drop a channel from within a band of communication channels as well as provide the introduction of a new information carrying channel at the same wavelength without interrupting the operation of the adjoining channels. A number of approaches have been used for this purpose including on-chip planar technology that is restricted to the use of one-dimensional interconnections such as fibers or two-dimensional (2-D) interconnections such as an on-chip array of integrated-optic (IO) waveguides and switches. For example, some of these techniques include all-fiber mechanically tuned fiber Bragg grating devices,<sup>1</sup> and IO grating switch with IO directional coupler devices,<sup>2</sup> an array waveguide grating (AWG) Multiplexer with IO thermo-optic switches,<sup>3</sup> an AWG multiplexer with manually simulated 2 X 2 switches,<sup>4</sup> a phased array demultiplexer used in conjunction with 2x2 Mach-Zehnder interferometer electro-optic switches,<sup>5</sup> an IO electro-optically controlled synthesized grating-structure-based filter,<sup>6</sup> a reflective tunable resonant grating filter placed on a tiltable MEMS platform,<sup>7</sup> liquid-crystals,<sup>8-10</sup> and using dual bulk acousto-optic tunable filters.<sup>11-12</sup> MEMS micromirror based add/drop filtering has been proposed and demonstrated in linear one dimensional array in which each micromirror switches one wavelength.<sup>13-14</sup> Earlier, we proposed the use of a TI 2-D DMD™ to form a high channel-capacity DWDM add-drop filter using a 2-D micromirror array.<sup>15-17</sup> This filter features a polarization insensitive and fault-tolerant design that takes advantage of the very high space-bandwidth product (SBWP) of the DMD™ using a macro-pixel consisting of multiple micromirrors in order to switch one wavelength.

Demonstration of this filter used an un-optimized visible mode TI DMD™ that led to limitations in crosstalk, loss, resolution, and optical bandwidth. In this work, we propose the use of a one dimensional (1-D) Liquid Crystal (LC) deflector array for OADF application. By binary control of the drive signal to the individual LC deflectors in the array, any optical channel can be selectively dropped and added. For the proof-of-concept OADF demonstration, a DMD™-based OADF is implemented for DWDM operations using a DMD™ that is specifically designed for the near infra-red (NIR) band. Similarities and differences are analyzed in this chapter for the two approaches. The new DMD™ device utilizes a telecom band optimized chip with broadband anti-reflection (AR) coating on the cover glass window, while the 13.8  $\mu\text{m}$  micromirror size and 14.8  $\mu\text{m}$  pitch have been designed to concentrate maximum power ( $\sim 88\%$ ) in one of the blazed grating orders for minimum insertion loss in the telecom C band. The resulting OADF demonstrates C-band wavelength add-drop control with low loss. The rest of the chapter describes OADF design, operations, and related C-band add-drop experiments and analysis of key system parameters.

## 10.2 OADF Architecture

Figure 10.1 shows the proposed OADF. This low loss design uses freespace dispersive optics for spatially spreading and recombining the optical spectra and a spectral processing element that selects the add-drop channels. Additional interconnect optics include two fiber-optic circulators (C), two Volume Bragg Gratings (VBG) and two spherical lenses (S). Light is coupled to the freespace OADF structure using single mode fiber (SMF) Gradient Index (GRIN)



rod lenses. The distance between a GRIN lens collimator and the corresponding VBG is chosen to be the half-self imaging distance such that the Gaussian beam emerging from the GRIN lens forms a beam waist at the VBG location.<sup>18</sup> Each VBG is placed at its Bragg angle  $\theta_{\text{Bragg}}$  with respect to the input light beam so that the input spectrum spreads in the first order by an angle  $2\Delta\theta = \theta_{\text{max}} - \theta_{\text{min}}$  along the x-dimension. Here  $\theta_{\text{max}} = \sin^{-1} [(\lambda_{\text{max}}/L) - \sin \theta_{\text{Bragg}}]$  and  $\theta_{\text{min}} = \sin^{-1} [(\lambda_{\text{min}}/L) - \sin \theta_{\text{Bragg}}]$ , and  $\lambda_{\text{max}}$  and  $\lambda_{\text{min}}$  correspond to the maximum and minimum wavelengths, respectively. The spatial extent of any wavelength  $\lambda$  is defined by the VBG resolution  $\delta\lambda = \frac{L\lambda_c}{2W|m|}$ , where  $m$  is the grating order number,  $L$  is the grating period,  $\lambda_c$  is the grating center wavelength and  $2W$  is the  $1/e^2$  beam diameter incident on the grating. In the OADF, the Main-In port light after it has impinged on the VBG<sub>1</sub> and spread spatially is collimated using a spherical lens  $S_1$ .  $S_1$  transforms the input source spectrum to spread it spatially onto the DMD<sup>TM</sup> such that the spectrum size is  $X = 2F \tan(\Delta\theta)$  in the x-dimension, where  $F$  is the focal length of lens  $S_1$ . The input beam with  $1/e^2$  beam waist of  $w_1$  at the VBG<sub>1</sub> location is transformed at the DMD<sup>TM</sup> location into a waist  $w_2$  which is given by:  $w_2 = \frac{F\lambda}{\pi w_1}$ . Thus the input optical spectrum to the OADF will form a rectangular shaped beam that is  $X$  units wide and  $2w_2$  units high at the spectrum processing plane, in effect allowing control of  $N = X/2w_2$  independent wavelength channels within the  $\Delta\lambda = \lambda_{\text{max}} - \lambda_{\text{min}}$  source spectrum. Thus the OADF wavelength control resolution is  $\Delta\lambda/N$  with the VBG resolution  $\delta\lambda$  being the fundamental limiting resolution. The spectral processing element can be any optical device that allows the control of individual optical channels. Here we consider only two approaches, namely, a 1-D array of LC deflectors and the TI DMD<sup>TM</sup>. Below we describe each approach in detail.

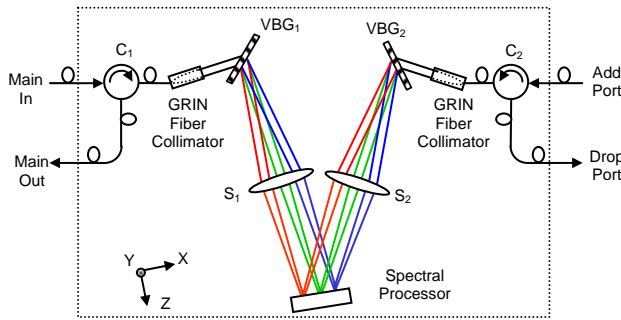


Fig. 10.1. Proposed OADF optical structure.

### 10.2.1 LC Deflector Array Approach

The spectral processing can be done by using a 1-D array of LC deflectors where each deflector controls an individual optical channel. This LC deflector array can be realized using the same underlying principle for a single LC deflector as described earlier in chapters 4-7. As shown in Fig. 10.2 this array consists a glass substrate on which a dielectric mirror is laid for the wavelength band of interest. On top of this mirror, a Quarter Wave Plate (QWP) is laid down. The high impedance electrode is laid on top of the QWP. Two linear metallic contacts are deposited for each deflector in the array. A poly-imide layer is coated on this surface and is rubbed in a direction which is at  $45^\circ$  to the QWP slow axis. A second glass substrate is coated with a uniform layer of Indium Tin Oxide (ITO) for use as the ground terminal. Again, a poly-imide layer is coated on this surface and is rubbed in a direction parallel to the first substrate. The LC is sandwiched in between these substrates. The front substrate can be AR coated to prevent un-wanted Fresnel reflections. By binary control of the drive signal to the individual LC deflectors in the array, any optical channel can be selectively dropped and added. Individual LC

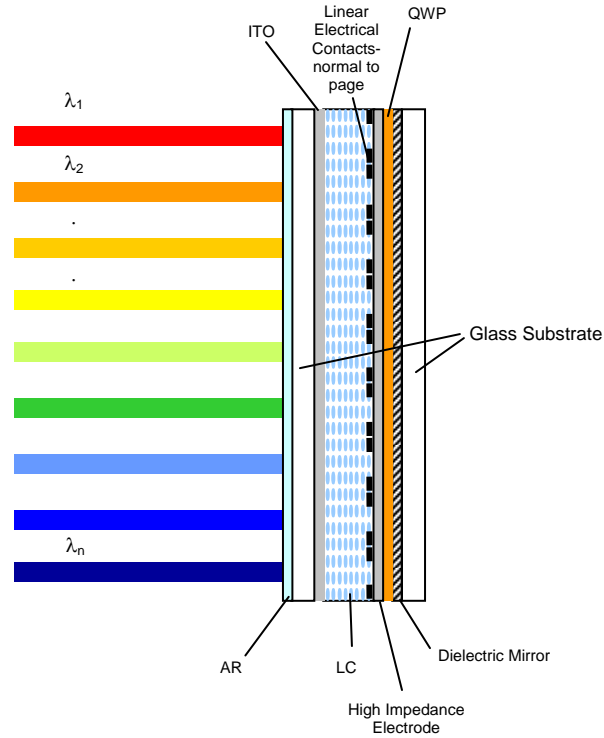


Fig. 10.2. Proposed LC Deflector array design for the OADF. QWP: Quarter Wave Plate, LC: Liquid Crystal, ITO: Indium Tin Oxide,  $\lambda$ : wavelength, AR: Anti-Reflection coating.

deflectors can be driven at different operating voltages to cater for birefringence dispersion in the LC material such that the deflection angles for all the wavelengths are the same. Since LCs are birefringent materials, hence a scheme is needed to cater for each polarization component. This is done with the use of a QWP at  $45^\circ$  and a retroreflective design using a dielectric mirror. Thus each polarization component encounters the LC in deflection state only once. The sandwiched nature of this device should help reduce the PDL in comparison with a cascade of individual LC deflector array, QWP, and mirror due to much shorter distances involved.

### 10.2.2 TI DMD™ Approach

The DMD™ is a commercially available MEMS device from TI that contains an array of square shaped micromirrors in a 2-D grid. Each micromirror is a bi-stable operation mirror having the ability to be deflected around a central (floating) position by  $+\theta$  and  $-\theta$  with the axis of rotation being the mirror diagonal. The DMD™ in the proposed OADF is oriented such that when the micromirrors are in the  $+\theta$  orientation, light from Main-In port is retro-reflected and hence is routed back to the Main-Out port through the circulator  $C_1$  (see Fig. 10.3 (a)). The DMD™ in the  $+\theta$  orientation becomes a blazed grating with the diffracted beam being in the high efficiency Littrow configuration resulting in low insertion loss for Main-In-to-Main-Out port. In the second case (see Fig. 10.3 (b)), when the micromirrors are in the  $-\theta$  orientation, light from Main-In port is routed to the Drop port through circulator  $C_2$  using a symmetrical setup of  $S_2$ , VBG<sub>2</sub> and a GRIN lens fiber collimator. Note that in this  $-\theta$  state, the DMD™ is not in the optimal high efficiency Littrow configuration. Any light present at the Add port is now routed to the Main-Out port. As shown in Fig. 10.3 (c), light from Add port can be routed to Drop port in the  $+\theta$  orientation when a fixed mirror along with a lens  $S_3$  is used in the Fig. 10.1 OADF proposed structure. Thus, the addition of the mirror to the Fig. 10.1 design forms a multi-wavelength 2 x 2 switch useful for wavelength routing. Note that the Fig. 10.3 ray traces for simplicity show single micromirror operation with the two possible mirror orientations.

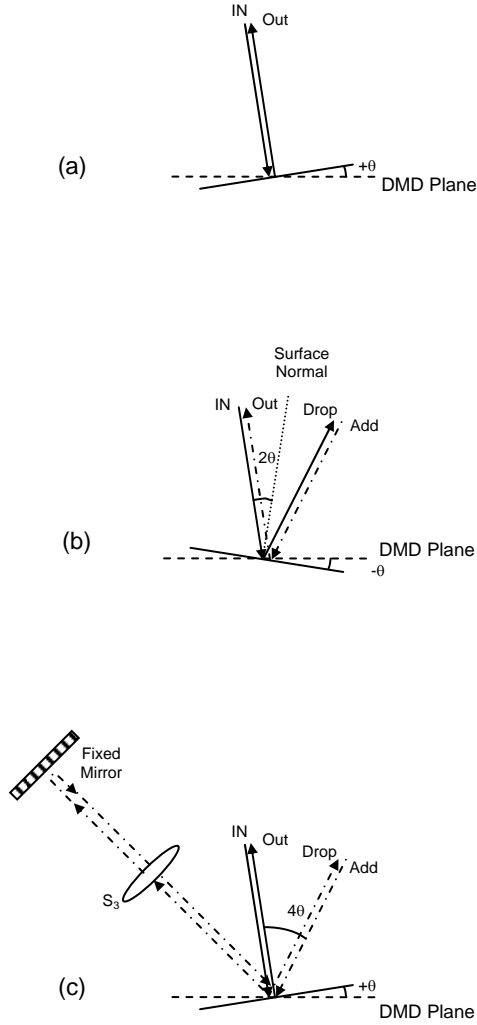


Fig. 10.3. Proposed OADF operation ray traces for (a) DMD™ set to  $+\theta$  for Main-In to Main-Out setting and (b) DMD™ set to  $-\theta$  for Add to Drop operations. (c) Modified OADF design using a fixed mirror that transforms the OADF to a multiwavelength 2 x 2 full reversible switch.

### 10.3 DMD™-based OADF Experiment

For the proof-of-concept experiment, the Fig. 10.1 design is used. Amplified spontaneous emission (ASE) from an erbium doped fiber amplifier (EDFA) is used as the broadband input

source for the test OADF. As mentioned, the VBG<sub>1</sub> is placed at the location where GRIN lens collimator forms the minimum beam waist. More importantly, the distance between the VBGs and the DMD<sup>TM</sup> is twice the focal length of the spherical lenses. Thus the minimum Gaussian beam waist at the VBG plane is also imaged on the DMD<sup>TM</sup> plane, satisfying the GRIN lens self-imaging condition required for super low loss freespace to fiber GRIN lens coupling.<sup>18</sup> Specifically, for the experimental OADF, the insertion loss due to the fiber-to-freespace-to-fiber coupling via the self-imaging mechanism is measured to be 0.1 dB. VBG<sub>1</sub> is a 940 lines/mm Dickson grating that spreads the 40 nm EDFA spectrum (1530 nm – 1570 nm) by 3.15° (2Δθ) in the first order ( $m=1$ ). This corresponds to a linear spread of 11 mm at the DMD<sup>TM</sup> plane using  $F=20$  cm for S<sub>1</sub>. The grating Bragg wavelength  $\lambda_{\text{Bragg}}$  is 1550 nm and  $\theta_{\text{Bragg}}$  is 46.76°. The DMD<sup>TM</sup> used contains an array of square shaped micromirrors in a 1024 x 768 2-D grid. This device has specifically been designed as a blazed diffraction grating in Littrow configuration for the telecommunications C-band in the +θ state. As shown in Fig. 10.5, the micromirrors have the dimensions of 13.8 μm square with the mirror pitch being 14.8 μm. This results in the total surface area of the DMD<sup>TM</sup> being 1.52 cm (=1023 x 14.8 μm + 13.8 μm) x 1.14 cm (=767 x 14.8 μm + 13.8 μm) which in-turn provides a spectral processing zone that is 1.61 cm in the x-dimension marked X' in Fig. 10.5(a). The fill factor of the DMD<sup>TM</sup> is 86.98%. The total loss due to the DMD<sup>TM</sup> is 1.9 dB which includes diffraction loss, a fill factor loss, Aluminum mirror reflectivity loss, and loss due to double pass through the AR coated glass window. Total fiber-to-fiber loss for the OADF module is measured to be 5 dB, that includes 1.4 dB loss via passage through two circulators, 0.2 dB loss for the two GRIN lens collimators, 0.8 dB two pass loss for the VBG, 0.7 dB two pass loss for the non- anti reflection (AR) coated lenses (S<sub>1</sub>/S<sub>2</sub>), and 1.9 dB

DMD<sup>TM</sup> loss. If the lenses  $S_1$  and  $S_2$  used were AR coated, the insertion loss of the OADF module can drop to 4.3 dB.

Wavelength dependence of the insertion loss was investigated and analysis shows that for the  $+0$  state corresponding to the DMD<sup>TM</sup> being in the low loss Littrow configuration, the insertion loss variation is primarily due to the Dickson grating loss as a function of wavelength (see Fig. 10.4 (a)).<sup>19</sup> Since here the DMD<sup>TM</sup> is in the low loss Littrow configuration, there is no significant angular spreading of the optical beam for this state of the filter. Fig. 10.4 (b) shows a closer look at this insertion loss profile within a narrow wavelength band while the Main-In port is routed to Main-Out port. Figure 10.4 (c) shows loss for the Add-to-Drop port configuration in a given narrow band. It is important to note that the insertion loss in this case significantly depends upon the wavelength, as the DMD<sup>TM</sup> is no longer in the low loss Littrow configuration. The DMD<sup>TM</sup> in the  $+0$  state behaves as a diffraction grating with an incident optical beam making a large  $18.4^\circ$  angle with the micromirror surface normal. This results in an angular spread of the broadband outgoing beam causing wavelength-based coupling loss.

Each micromirror in the DMD<sup>TM</sup> is deflected around a center floating position by  $\pm 9.2^\circ$  about the mirror diagonal. For the OADF demonstration, the DMD<sup>TM</sup> is oriented such that when the micromirrors are in the  $+9.2^\circ$  orientation, light from Main-In port is retro-reflected into Main-Out port. In contrast, when the micromirrors are in the  $-9.2^\circ$  orientation, light from Main-In port is routed to the Drop port and any light present at the Add port is routed to the Main-Out port.

In the first experiment, a 5 mm  $1/e^2$  beam waist diameter GRIN lens and a spherical lens  $S_1$  with  $F=20$  cm are used that result in a spot size  $2w_2$  of 79  $\mu\text{m}$  for a single wavelength at the DMD<sup>TM</sup> location. The VBG resolution  $\delta\lambda$  in this case was calculated to be 0.22 nm for  $\lambda_c=1550$  nm. With the OADF being fed with broadband ASE from an EDFA as mentioned earlier, the wavelength

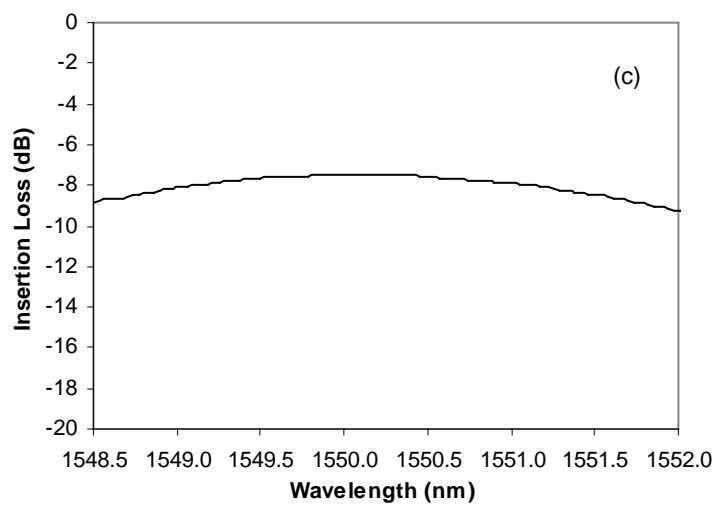
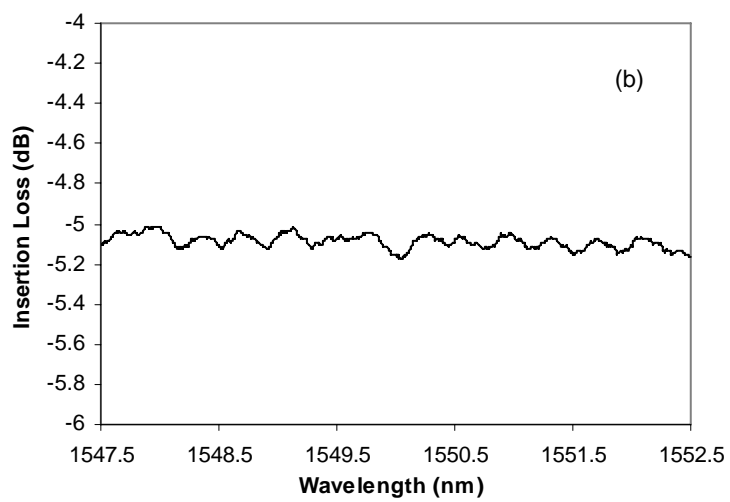
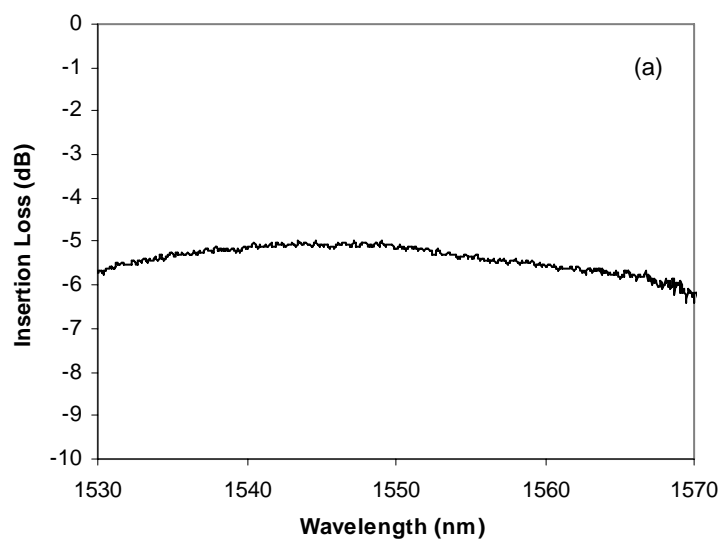




Fig. 10.4. Measured insertion loss for the OADF. (a) Insertion loss for the Main-In-to-Main-Out port configuration for the whole C-band and (b) a closer look at the insertion loss in a narrow wavelength band, and (c) Insertion loss for the Main-In-to-Drop/Add-to-Main-Out port in a narrow wavelength band.

resolution of the OADF was measured by using two independently controlled adjacent optical channels using the DMD™. Light from Main-In port is retro-reflected back to Main-Out port with the micromirrors being in +θ orientation. Next, successive columns of micromirrors are turned ON and OFF to create either a 3-dB or a 20-dB or a 30-dB notch in the EDFA source spectrum (see Fig. 10.5 for a single column's geometry). Two such notches are created in the closest possible proximity to determine the wavelength resolution of the OADF. These notches are independent of one-another such that the creation of one does not affect the shape or position of the adjacent notch. With this 5 mm GRIN lens beam diameter size, Fig. 10.6 shows the resulting 3-dB, 20-dB and 30-dB OADF resolution of 1 nm, 1.6 nm and 1.8 nm respectively. Each of the dips in the broadband EDFA input source spectrum (3-dB, 20-dB and 30-dB) was formed using 5, 22, and 28 micromirror columns which correspond to spot sizes on the DMD™ of  $61.3 \mu\text{m}$  ( $= 2a + b$ , where  $a = 20.9 \mu\text{m}$  and  $b = 19.5 \mu\text{m}$ ),  $0.24 \text{ mm}$  ( $= 11a + 0.5b$ ) and  $0.302 \text{ mm}$  ( $= 14a + 0.5b$ ), respectively (see Fig. 10.6(b)). The two dips in each case are separated by 35, 47 and 53 columns in the x-direction which corresponds to a x-dimension center-to-center linear separation of  $0.375 \text{ mm}$  ( $= 17a + b$ ),  $0.5 \text{ mm}$  ( $= 23a + b$ ) and  $0.563 \text{ mm}$  ( $= 26a + b$ ), respectively. Note that the 30-dB point wavelength resolution of 1.8 nm obtained using this GRIN lens is not sufficient for achieving WDM channel spacing (1.6 nm/200 GHz) OADF.

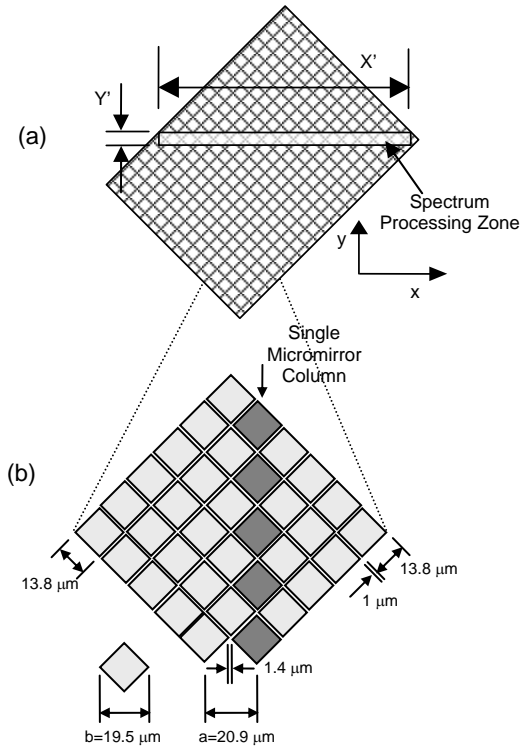


Fig. 10.5. (a) TI DMD™ geometry showing the active spectrum processing zone and (b) the micromirror pixel layout. A dark colored vertical micromirror array represents one column of micromirrors as controlled by the DMD™ software.

Hence, by using a larger input beam diameter this problem is solved. Specifically, a 1 cm  $1/e^2$  beam waist diameter input GRIN lens collimator and a spherical lens  $S_1$  with  $F=20$  cm are used that result in a spot size  $2w_2$  of  $39.5 \mu\text{m}$  at the DMD™ location. The VBG resolution  $\delta\lambda$  in this case is calculated to be  $0.11 \text{ nm}$ . Again, the 3-dB resolution of the OADF is measured using two independently controlled adjacent channels using the DMD™. Using this GRIN collimator, Figure 10.7 shows the resulting 3-dB, 20-dB and 30-dB resolution that is achieved using 2, 8 and 11 columns of the micromirrors, respectively. Specifically, these 2, 8, and 11 columns

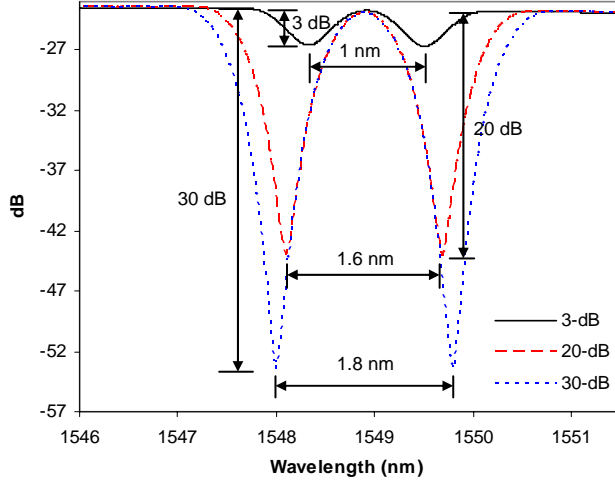


Fig. 10.6. Measured resolutions of the OADF using a 5 mm diameter GRIN collimator. These resolution values for the 3-dB, 20-dB and 30-dB points are measured to be 1 nm, 1.6 nm and 1.8 nm, respectively.

correspond to spot sizes along the x-direction on the DMD™ of  $30.7 \mu\text{m}$  ( $= a + 0.5b$ ),  $93.4 \mu\text{m}$  ( $= 4a + 0.5b$ ) and  $0.12 \text{ mm}$  ( $= 5a + b$ ) respectively. The corresponding 2, 8, 11 columns give resulting resolutions of 0.41 nm, 0.55 nm, and 0.7 nm, respectively. The two dips in each case are separated by 12, 18, and 21 columns in the x-direction which corresponds to a center-to-center linear separation of 0.135 mm ( $= 6a + 0.5b$ ), 0.198 mm ( $= 9a + 0.5b$ ), and 0.23 mm ( $= 10a + b$ ) respectively.

For the OADF demonstration for DWDM systems, the 1 cm diameter input GRIN lens mentioned is used as it has the ability to resolve wavelengths 0.7 nm apart (see Fig. 10.7). First the 40 nm broadband EDFA source spectrum is interleaved using an optical interleaver. The interleaver divides the 40 nm C-band into 100 channels with odd and even channels routed to different output ports of the interleaver. Only one set of channels, either even or odd, with a

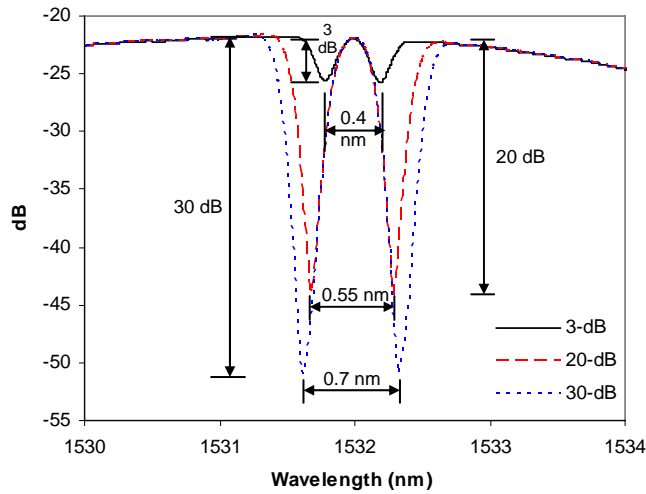


Fig. 10.7. Measured resolutions of the OADF using a 1 cm diameter GRIN collimator. These resolution values for the 3-dB, 20-dB and 30-dB points are measured to be 0.41 nm, 0.55 nm and 0.7 nm, respectively.

frequency spacing of 100 GHz between adjacent channels, is then routed to the OADF through the Main-In port. Out of the 50 channels, one channel is selectively dropped by turning 11 columns of micromirrors from  $+9.2^\circ$  to  $-9.2^\circ$  deflection state hence routing the chosen channel to the Drop port. Figure 10.8(a) shows the resulting input EDFA source spectrum along with the spectrum routed to Main-Out port showing the Drop channel operation. Figure 10.8 (b) shows this single dropped channel present at the Drop port. To demonstrate the ADD operation of the OADF, a tunable laser diode source is connected to the ADD port that is tuned to lase at the same wavelength as the dropped channel. The new channel is shown as a narrow spike in the spectrum at the Main-Out port shown in Fig. 10.8(c).

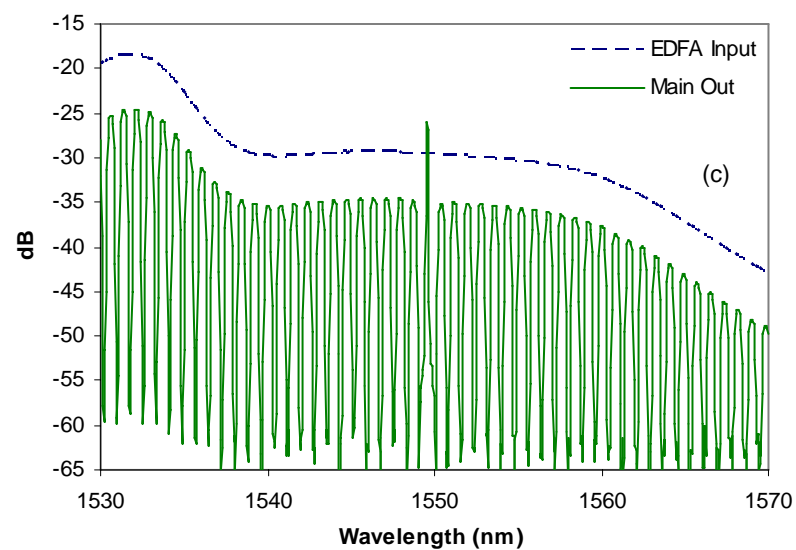
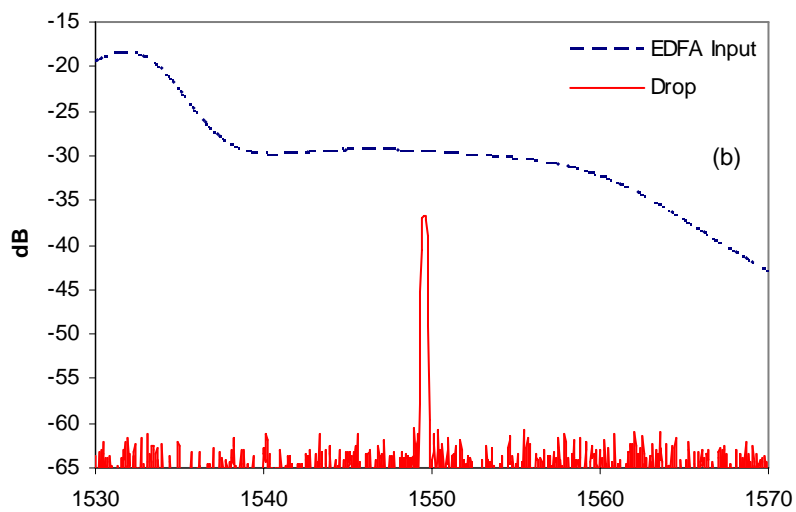
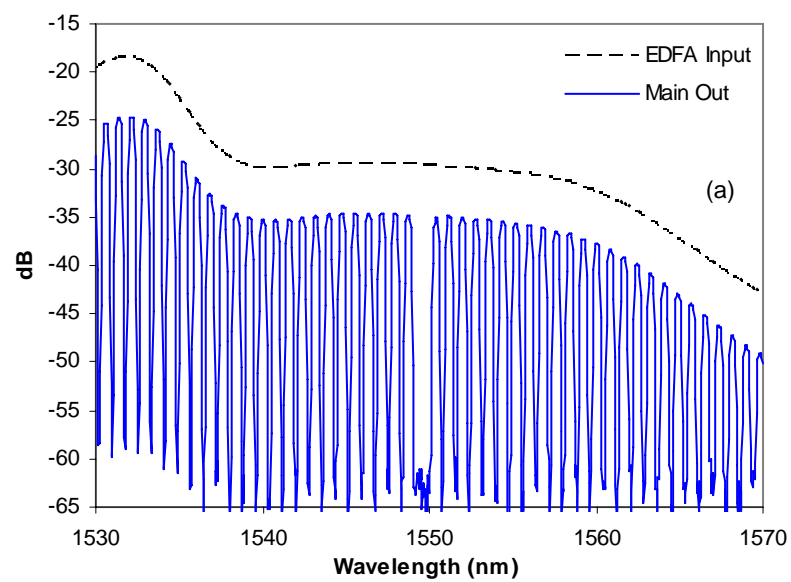


Fig. 10.8. 0.8 nm (100 GHz) DWDM spacing C-Band operation of the OADF (a) The EDFA source input to the OADF and the retro-reflected spectrum on the Main-Out port. (b) The dropped channel on the Drop port, and (c) using a tunable laser diode, a new channel is added through the Add port demonstrating the ADD operation.

Since a typical OADF is a 2 x 2 port optical module, hence crosstalk is an important issue to consider. Crosstalk is defined as the ratio of the wanted-to-unwanted light in a certain output port of the OADF. In the current freespace optics based OADF implementation, back-reflections from optical interfaces such as the fiber-to-GRIN lens interface and the circulator can be the limiting factor in defining the minimum possible crosstalk for the architecture. This is true because of the fact that these circulators consist of beam displacement prisms and surface reflections from these prisms are routed to the unwanted port resulting in crosstalk. Typical commercially available 3-port circulators have port-to-port isolation of 32 to 40 dB. Hence a 32-dB inter-port isolation circulator will limit the Main-In to Main-Out (Add to Drop, if the mirror option in Fig. 10.3 is used) crosstalk to 32-dB. In our current OADF, crosstalk was measured using a tunable wavelength source that was connected to one of the input (Main-In/Add) ports while the power was measured at one of the two output (Main-Out/Drop) ports. Ratio of the powers measured when light was routed to one particular output port and when the light was not routed to this output port gave the crosstalk measurement. As can be seen from the plot in Figure 10.8(a), the average crosstalk is measured to be 30 dB in Main-In port to Main-Out port configuration while that from Main-In Drop to Drop and Add to Main-Out port is measured to be 40 dB. In the 30 dB case, the low circulator inter-port isolation is suspected to be the prime cause of the higher crosstalk. In the 40 dB case, the lower crosstalk results due to better port isolation

as the input and output ports have separate circulators. Use of separate input output fiber collimators or dual fiber collimators for the two input and output OADF ports will allow better crosstalk performance in comparison to the circulator based OADF design. These separate input fibers would also mean that the DMD™ micromirrors will need to reflect light at a small angle along the y-axis which will be defined by the center-to-center spacing between the two fibers used to form each dual collimator. Figure 10.9 shows a visible light photograph of the DMD™ chip where the active spectrum processing zone is clearly visible.

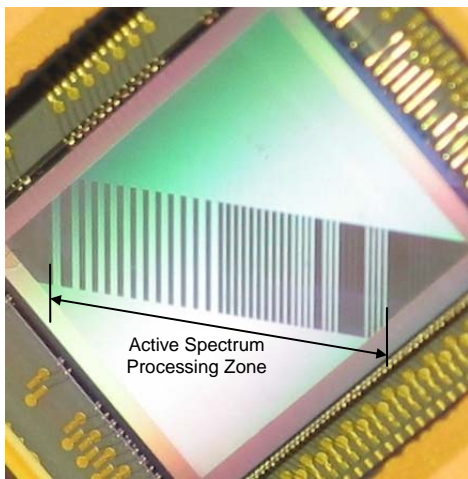


Fig. 10.9. A visible light photograph of the DMD™ chip showing the active spectrum processing zone.

An important design issue for an OADF is its wavelength control selectivity [18]. The finest wavelength selection possible can be determined by switching a single micromirror column from one state to the other and then shifting the column spatially by one micromirror through software control. Using the broadband source and the interleaver removed, the column is first turned from  $+\theta$  orientation to  $-\theta$  orientation and is then shifted by one micromirror location

to determine the shift in wavelength using the EDFA as the source. Using the 10 mm diameter GRIN lens collimator, this shift in wavelength due to a switching of adjacent micromirror column was measured to be 36 pm as shown in Fig. 10.10. Do note that the measured 36 pm wavelength selectivity of the demonstrated OADF is a key design number that should be considered in order to meet specific required system application needs. For applications requiring finer wavelength selectivity, using the full space bandwidth product of the DMD™ can result in better wavelength selectivity. Another key parameter is the clear channel bandwidth measured between the 0.5 dB points from the maxima/minima of a selectively added/dropped signal using a broadband input signal. Using the 10 mm diameter GRIN lens collimator and the EDFA as the broadband input signal, the clear channel bandwidth was measured to be 0.25 nm for the present OADF.

It is noteworthy to mention that the proposed filter does not use a single micromirror for switching; rather it uses a macro-pixel consisting of several micromirrors. In the single mirror per ITU wavelength approach,<sup>21</sup> although the mirror array has a chirped mirror width across the array that rigidly matches the spatial dispersion of the grating such that each discrete wavelength in the telecom band falls on a different micro-mirror matching its spot size and location, it nevertheless is devoid of fault-tolerance in that a single micro-mirror failure will result in the loss of one channel. Additionally, any optical spectra chirp, such as due to thermal drifts, will result in the ITU channels not perfectly matching the mirror array grid. The macro-pixel approach is attractive in this regard as the DMD™ plane is populated with multiple micromirrors for each ITU channel. Hence a single micro-mirror failure does not result in catastrophic loss of a channel, and optical spectra chirp can be countered by re-programming the macro-pixel locations corresponding to specific ITU channels.



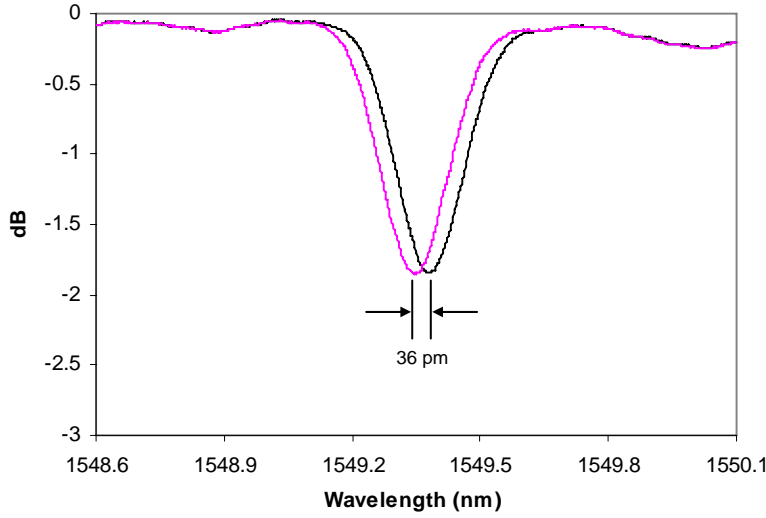


Fig. 10.10. Measured wavelength resolution of the OADF by flipping a single micromirror column from  $+\theta$  orientation to  $-\theta$  orientation and then translating it by one micromirror location.

MEMS micromirrors have also been used for wavelength selective  $1 \times N$  switches.<sup>21</sup> It is well known that multiple  $1 \times 2$  switches can be cascaded to form  $1 \times 4$ ,  $1 \times 8$  and higher port count switches. Since the proposed filter operates as a  $1 \times 2$  wavelength-selective switch, it is possible for instance to use three such switches in a two stage interconnection network to form a  $1 \times 4$  wavelength-selective switch. An important consideration for such a higher port count switch will be the increased insertion loss due to cascading of switches, in addition to cost increases. Thus, depending on the specific application system requirements, the port count of the proposed switch will be limited.

The PDL of the OADF is measured to be 0.15 dB. The PDL is measured by varying the input polarization to the OADF using a fiber-optic mechanical polarization controller. Response time is another critical issue for an OADF structure. Individual micromirror response time for the

DMD<sup>TM</sup> is 15  $\mu$ sec while total reconfiguration time for the entire DMD<sup>TM</sup> chip is approximately 1 msec using a serial computer interface.<sup>22</sup> Reset time can be improved if the DMD<sup>TM</sup> column addressing control signals are tied together in order to address all the mirrors in one column at the same time with a single control signal. This approach would reduce the number of addressing control signals required to address all the individual pixels of the DMD<sup>TM</sup> chip and would hence improve the response time significantly. This DMD<sup>TM</sup> addressing approach is a viable solution for an application like the current OADF where only column by column control of micromirrors is needed instead of individual micromirror control as required in an optical spectral equalizer.<sup>22</sup>

#### 10.4 Discussion

In Table 10.1, the two approaches have been analyzed. Key considerations are dynamic range, response time, PDL, insertion loss, and wavelength selectivity. LCs can typically obtain a switching dynamic range of about 30 dB or slightly better. This is primarily limited due to scattering in the LC material and imperfect rubbing. The DMD<sup>TM</sup> offers a dynamic range of about 35 dB or better. This is due to the digital switching nature of the micro-mirror. There is no significant scattering from the mirror surface except for any fabrication imperfection. In terms of response time, nematic LCs typically can be driven with msec speeds whereas the DMD<sup>TM</sup> has a much faster micro-second response time/micro-mirror, although the refresh rate for the whole DMD<sup>TM</sup> micro-mirror array is 1 msec. For LC devices, the response time has a square relation with the LC layer thickness. Decreasing the LC layer thickness by half will improve the response by 4 times. But in order for the LC to provide the same amount of optical phase, the

birefringence needs to be higher. Research is underway to synthesize NLC materials for larger birefringence and smaller viscosity in order to obtain faster response times.<sup>23</sup> Faster response in LCs can be obtained using the transient nematic effect<sup>24</sup> while the slower fall time can be improved by using the dual frequency effect.<sup>25</sup> The PDL for the LC device is expected to be 0.1 dB or less. This is due to the sandwiched nature of the proposed structure and is slightly better than that for the DMD<sup>TM</sup>. Insertion loss for the proposed LC device is expected to be less than 1 dB which is about half of that for the DMD<sup>TM</sup>. Wavelength selectivity will depend upon the individual pixel size of the deflector in the LC deflector array. The DMD<sup>TM</sup> with the current micro-mirror size of 13.8  $\mu\text{m}$  has a wavelength selectivity of 36 pm. Using an LC deflector with a pixel size of, say 10  $\mu\text{m}$ , this selectivity can be achieved.

An important issue to consider is the 2-D grating effect in the DMD<sup>TM</sup>. The DMD<sup>TM</sup> has been designed as a blazed diffraction grating in Littrow configuration for the telecommunications C-band in the  $+\theta$  state. Since here the DMD<sup>TM</sup> is in the low loss Littrow configuration, there is no significant angular spreading of the optical beam for this state of the filter. It is important to note that in the  $-\theta$  state the insertion loss significantly depends upon the wavelength, as the DMD<sup>TM</sup> is no longer in the low loss Littrow configuration. The DMD<sup>TM</sup> in the  $+\theta$  state behaves as a diffraction grating with an incident optical beam making a large  $18.4^\circ$  angle with the micromirror surface normal. This results in an angular spread of the broadband outgoing beam causing wavelength-based coupling loss. It is important to understand that this is due to the grating effect of the macro-pixel approach. Each wavelength incident on the DMD<sup>TM</sup> falls on multiple micro-mirrors resulting in this grating like angular dispersion at the output. This will significantly limit the broadband operation. In contrast, in the LC deflector array approach, each optical channel falls on its own LC deflector and as a result there is no grating like effect

experienced. This will prevent excess loss due to the macro-pixel approach although at the cost of fault tolerance. In the case of the one pixel/ $\lambda$  approach, a single pixel failure will result in catastrophic loss of an optical channel whereas in the macro-pixel approach a single micro-mirror failure will only attenuate the signal.

Table 10.1. Comparison of 1-D LC deflector array approach with the TI 2-D DMD<sup>TM</sup> approach.

	1-D LC Deflectors	TI 2-D DMD <sup>TM</sup>
Dynamic Range	~30dB	>35 dB
Response Time	~msec	15 $\mu$ sec
PDL	0.1 dB	0.15 dB
Insertion Loss	<1 dB	1.9 dB
Wavelength Selectivity	Geometry dependent	36 pm
Approach	1 pixel/ $\lambda$	Macro-pixel

## 10.5 Conclusion

In summary, an LC deflector array based OADF has been proposed. The approach is realized using TI DMD<sup>TM</sup> using a C-band optimized TI DMD<sup>TM</sup> device. The C-band demonstrated reconfigurable OADF module operated for DWDM (0.8 nm) channel spacing provides multiple channel add-drop routing functions. The reported OADF has a low loss, 30 dB of maximum crosstalk, and 0.15 dB PDL. The proposed OADF uses a macro-pixel approach where multiple micromirrors are used to control a single optical wavelength, hence providing fault-tolerance within the OADF structure. Key system issues have been discussed in detail.

## References

1. G. Nykolak, M. de Barros, T. Nielsen and L. Eskildsen, "All-fiber active add-drop wavelength router," IEEE Photonics Technology Letters, Vol. 9, Issue 5, Pages 605-606, May 1997.
2. Y. Shibata, S. Oku, Y. Kondo, T. Tamamura and M. Naganuma, "Semiconductor monolithic wavelength selective router using a grating switch integrated with a directional coupler," IEEE Journal of Lightwave Technology, Vol. 14, Issue 6, Pages 1027-1032, June 1996.
3. T. Saida, A. Kaneko, T. Goh, M. Okuno, A. Himeno, K. Takiguchi and K. Okamoto, "Athermal silica-based optical add/drop multiplexer consisting of arrayed waveguide gratings and double gate thermo-optical switches," IEE Electronics Letters, Vol. 36, Issue 6, Pages 528-529, 16 March 2000.
4. O. Ishida, H. Takahashi, S. Suzuki and Y. Inoue, "Multichannel frequency-selective switch employing an arrayed-waveguide grating multiplexer with fold-back optical paths," IEEE Photonics Technology Letters, Vol. 6, Issue 10, Pages 1219-1221, October 1994.
5. C. Vreeburg, T. Uitterdijk, Y. Oei, M. Smit, F. Groen, E. Metaal, P. Demeester, H. Frankena, "First InP-based reconfigurable integrated add-drop multiplexer," IEEE Photonics Technology Letters, Vol. 9, Issue 2, Pages 188-190, February 1997.

6. H. Nolting and M. Gravert, "Electro-optically controlled multiwavelength switch for WDM cross connector application," IEEE Photonics Technology Letters, Vol. 7, Issue 3, Pages 315–317, March 1995.
7. G. Niederer, M. Salt, H. Herzig, T. Overstolz, W. Noell, N. de Rooij, "Resonant grating filter for a MEMS based add-drop device at oblique incidence," IEEE/LEOS International Conference on Optical MEMS 2002, Conference Digest, Pages 99–100, 20-23 August 2002.
8. J. Patel and Y. Silberberg, "Liquid crystal and grating-based multiple-wavelength cross-connect switch," IEEE Photonics Technology Letters, Vol. 7, Issue 5, Pages 514–516, May 1995.
9. N. A. Riza, "Ferroelectric Liquid Crystal Polarization Switching-based High Speed Multi-Wavelength Add/Drop Filters using Fiber and Array Waveguide Gratings," International Optics in Computing '98 Conference, SPIE Vol.3490, P39, pp.335-338, Brugge, Belgium, June 1998.
10. S. Sumriddetchkajorn, N. A. Riza and D. K. Sengupta, "Liquid crystal-based self-aligning 2×2 wavelength routing module," Optical Engineering, Vol. 40, Issue 8, August 2001, pp.1521-1528.
11. N. A. Riza, "Low interchannel crosstalk wavelength routing switch based on bulk acousto-optic tunable filters," IEEE Lasers and Electro-Optics Society Annual Meeting, LEOS '97, Conference Proceedings, Vol. 2, Pages 341–342, 10-13 November 1997.
12. N. A. Riza and J. Chen, "Ultrahigh 47-dB optical drop rejection multiwavelength add-drop filter using spatial filtering and dual bulk acousto-optic tunable filters," Optics Letters, Vol. 23, Issue 12, Pages 945-947, June 1998.

13. J. Ford, J. Walker, V. Aksyuk, and D. Bishop, "Wavelength selectable add/drop with tilting micromirrors," IEEE Lasers and Electro-Optics Society Annual Meeting, LEOS '97, Piscataway, N.J., 1997, postdeadline paper PD2.3.
14. J. Ford, V. Aksyuk, D. Bishop, J. Walker, "Wavelength add-drop switching using tilting micromirrors," IEEE Journal of Lightwave Technology, Vol. 17, Issue 5, Pages 904–911, May 1999.
15. N. A. Riza and S. Sumriddetchkajorn, "Fault-tolerant dense multiwavelength add drop filter with a two-dimensional digital micromirror device," Applied Optics, Vol. 37, Issue 27, Pages 6355-6361, September 1998.
16. N. A. Riza and S. Sumriddetchkajorn, "Small-tilt micromirror-device-based multiwavelength three-dimensional 2 x 2 fiber optic switch structures," Optical Engineering, Vol. 39, Issue 2, Pages 379-386, February 2000.
17. N. A. Riza, "Fault-tolerant fiber-optical beam control modules," US Patent No. 6,222,954, April 24, 2001.
18. M. Buren and N. A. Riza, "Foundations for low-loss fiber gradient-index lens pair coupling with the self-imaging mechanism," Applied Optics-LP, Vol. 42, Issue 3, Pages 550-565, January 2003.
19. Z. Yaqoob and N. Riza, "Low-loss wavelength-multiplexed optical scanners using volume Bragg gratings for transmit-receive lasercom systems," Optical Engineering, Vol. 43, Issue 5, Pages 1128-1135, May 2004.
20. R. Ryf, Y. Su, L. Moller, S. Chandrasekhar, L. Xiang D. T. Neilson, C. R. Giles, "Wavelength blocking filter with flexible data rates and channel spacing," IEEE Journal of Lightwave Technology, Vol. 23, Issue 1, Pages 54-61, Jan. 2005.

21. D. M. Marom, D.T. Neilson, D.S. Greywall, P. Chien-Shing N. R. Basavanhally, V. A. Aksyuk, D. O. Lopez, F. Pardo, M. E. Simon, Y. Low, P. Kolodner, C. A. Bolle, "Wavelength-selective 1XK switches using free-space optics and MEMS micromirrors: theory, design, and implementation," IEEE Journal of Lightwave Technology, Vol. 23, Issue 4, Pages 1620-1630, April 2005.
22. N. A. Riza and M. Mughal, "Broadband optical equalizer using fault tolerant digital micromirrors," Optics Express, Vol. 11, Issue 13, Pages 1559-1565, June 2003.
23. S. Gauza, H. Wang, C. H. Wen, S. T. Wu, A. Seed, and R. Dabrowski, "High Birefringence Isothiocyanato Tolane Liquid Crystals," Japanese Journal of Applied Physics Part I, 42, 3463-3466, 2003.
24. Shin-Tson Wu and Chiung-Sheng Wu, "High-speed liquid-crystal modulators using transient nematic effect," Journal of Applied Physics, Vol. 65, Issue 2, Pages 527-532, January, 1989.
25. H. K. Bücher, R. T. Klingbiel, and J. P. VanMeter, "Frequency-addressed liquid crystal field effect," Applied Physics Letters, Vol. 25, Issue 4, Pages 186-188, August, 1974.



## **APPENDIX A: THE PARAXIAL APPROXIMATION FOR A THIN LENS**

A lens is said to be a thin lens if it causes negligible translation to a ray of light as it traverses through the lens. If the incident ray is at a distance of  $r$  away from the center of the thin lens (with  $r$  being measured orthogonal to the lens axis, see Fig. A.1) and the lens radius of curvature and the diameter being  $R$  and  $D$ , respectively, then the ray of light experiences a phase transmittance function through a plano-convex thin lens given by:<sup>32</sup>

$$U(r) = e^{jkn t_o} e^{[-jk(n-1)t(r)]}, \quad (\text{a.1})$$

where  $t_o$  is the thickness at the center of the thin lens,  $k = \frac{2\pi}{\lambda}$  is the propagation constant and  $n$  is the index of the lens material.

The thickness  $t(r)$  at a point  $r$  away from the lens axis can be obtained using the geometry shown in Fig. A.1 as:

$$t(r) = t_o - R \left( 1 - \sqrt{1 - \frac{r^2}{R^2}} \right). \quad (\text{a.2})$$

The equation (a.2) expression for the thickness function can be simplified if we restrict our attention to the portion of the lens where  $r$  is small such that the incident ray is incident at the lens surface at a position close to its axis. As a consequence of this assumption, the following approximation can be made:

$$\sqrt{1 - \frac{r^2}{R^2}} \cong 1 - \frac{r^2}{2R^2} \quad (\text{a.3})$$

The resulting approximation is sometimes called the Paraxial approximation as it holds true only for paraxial rays, i.e., rays that lie close to the thin lens axis. If we plot the left and right side expressions in equation (a.3), we see that the right side approximation is close to the left side

closed form expression in the region where  $r/R$  is less than 0.6 (see Fig. A.2). Hence, for a thin plano-convex lens,

$$t(r) \cong t_o - \frac{r^2}{2R}. \quad (\text{a.4})$$

The physical properties of the lens, i.e.,  $n$  and  $R$ , can be combined in a single number  $f$  called the *focal length*, which for a plano-convex thin lens is given by:<sup>32</sup>

$$\frac{1}{f} = \frac{(n-1)}{R} \quad (\text{a.5})$$

where  $R$  is the radius of curvature of the thin lens and  $n$  is the index of refraction of the lens material. For glass such as BK7, the index  $n$  is 1.5 at  $\lambda=1550$  nm resulting in  $f=2R$ .

The ratio of the focal length  $f$  to the beam diameter  $D$  at the thin lens surface is called the lens  $F\#$  given by:

$$F\# = \frac{f}{D}. \quad (\text{a.6})$$

Since  $f=2R$  and  $D=2r$ , hence we can rewrite the thin lens  $F\#$  as:

$$F\# = \frac{R}{r}. \quad (\text{a.7})$$

For the Paraxial approximation of equation (a.3) to hold, the plot of the exact expression and the approximate expression of equation (a.3) in Fig. A.2 should be comparable and the error between these two kept below a certain threshold maximum. Figure A.2 shows that if the ratio of  $r/R$  is equal to 0.6, an error of 2.5% between the values for the two expressions is produced. If this  $r/R=0.6$  is taken as the maximum allowed error, it implies that the lens  $F\#$  should be greater than or equal to 1.67 for the lens to be classified as a thin lens. Note that the Gaussian beam propagation analysis conducted in this chapter uses thin lenses that must obey the  $F\# \geq 1.67$

restriction. Also note that depending on the accuracy of the thin lens approximation selected (e.g., 2.5% error), the  $F\#$  restriction can be different. This means that the  $F\# \geq 1.67$  is an arbitrary criterion and it will vary depending upon what error one's system can accommodate/handle. We chose this number as this is the point where we feel that the approximation of equation (a.3) is close to the exact form of equation (a.2). This criterion is not far from real deployed systems such as the Keck and Subaru telescopes that have  $F\#$  of 1.75 and 1.8 respectively.

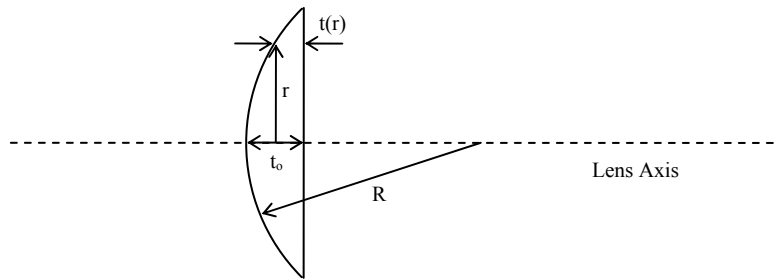


Fig. A.1: Geometry for the thin lens Paraxial approximation.

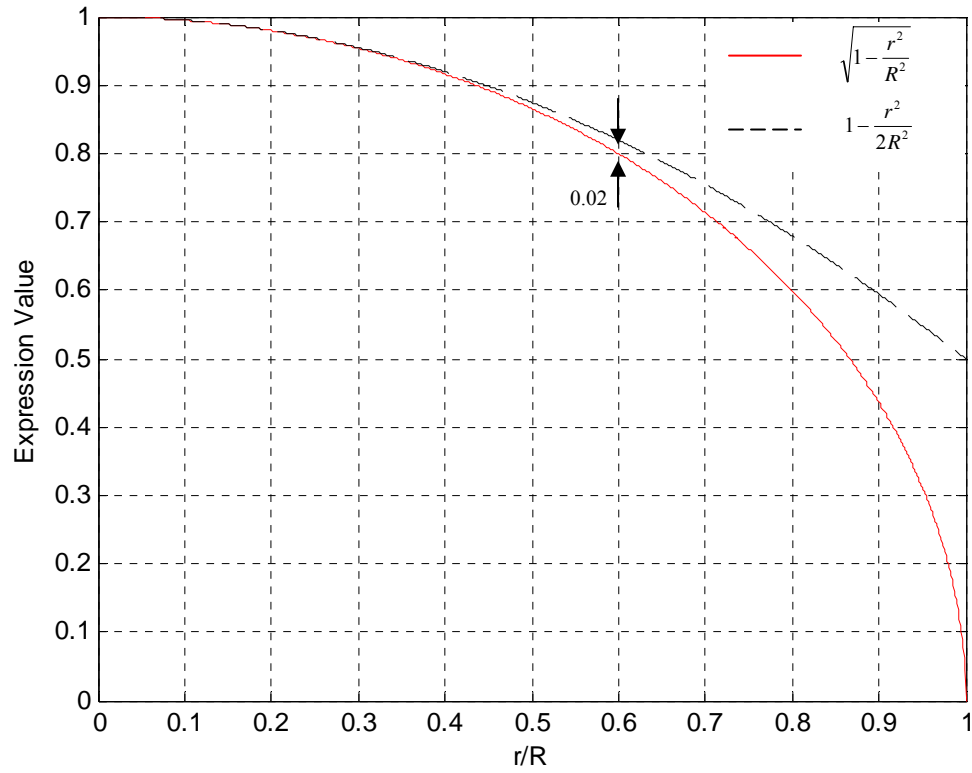


Fig. A.2: Plot of the thin lens expression obeying the Paraxial approximation and plot of the exact expression for a plano-convex lens.

### References

1. Joseph W. Goodman, *Introduction to Fourier Optics*, (McGraw-Hill Inc., 1968. New York, USA).

## **APPENDIX B: POWER CAPTURED BY A THIN LENS WITH A GAUSSIAN BEAM INPUT**

If a Gaussian beam with a beam radius of  $w(z)$  is incident on a thin lens, then the power captured by this thin lens of diameter  $D$  ( $D=2r$ ) over its surface area ( $\pi r^2$ ) is calculated by integrating the incident Gaussian beam irradiance over the lens area assuming no reflection or absorption losses are present. The power captured by the thin lens can be obtained using:<sup>33</sup>

$$P = 1 - e^{-\frac{2r^2}{w^2(z)}} \quad (\text{b.1})$$

where  $w(z)$  is the Gaussian beam radius and is related to the beam waist  $w_1$  by:

$$w^2(z) = w_1^2 \left( 1 + \frac{z^2}{z_1^2} \right), \quad (\text{b.2})$$

where  $z_1$  is the confocal beam parameter given by  $z_1 = \frac{\pi w_1^2}{\lambda}$  and  $z$  is the longitudinal distance

from the beam waist  $w_1$  location to the point where the new beam radius  $w(z)$  is being evaluated.

Since the incident beam is a Gaussian beam, therefore the power captured by the thin lens has an error function distribution as shown in Fig. B.1.<sup>22</sup> The calculated  $P$  of 2% for a  $w_1=1\text{mm}$ ,  $n=1$ ,

$z=1\text{ km}$ ,  $D=10\text{ cm}$  and  $\lambda=1550\text{ nm}$  is verified using Matlab.<sup>23</sup> Figure B.1 shows the encircled

power in a Gaussian beam as a function of the normalized radius of the thin lens. The thin lens

radius  $r$  is normalized with respect to the incident beam  $\frac{1}{e^2}$  radius  $w$ . It can be seen that 86% of

the incident power lies inside a circle of radius  $r=w$ , where  $w$  is the  $\frac{1}{e^2}$  beam radius. Also, one

can notice that to capture about 99% or more of the power in the incident beam the receiving thin

lens needs a radius  $r \geq 1.5w$ . Moreover, in case if the receiving lens radius is smaller than the  $\frac{1}{e^2}$

beam radius  $w$ , the encircled power in the beam can be calculated by the above relation.<sup>33</sup> Here we have neglected the relative angular orientation of the incident beam with respect to the thin lens surface and have also assumed that the propagation axis of the beam is collinear with the surface normal of the lens at its center. Hence in practice, the loss will also depend upon the relative shift as well as the angular tilt between the aforementioned two parameters.

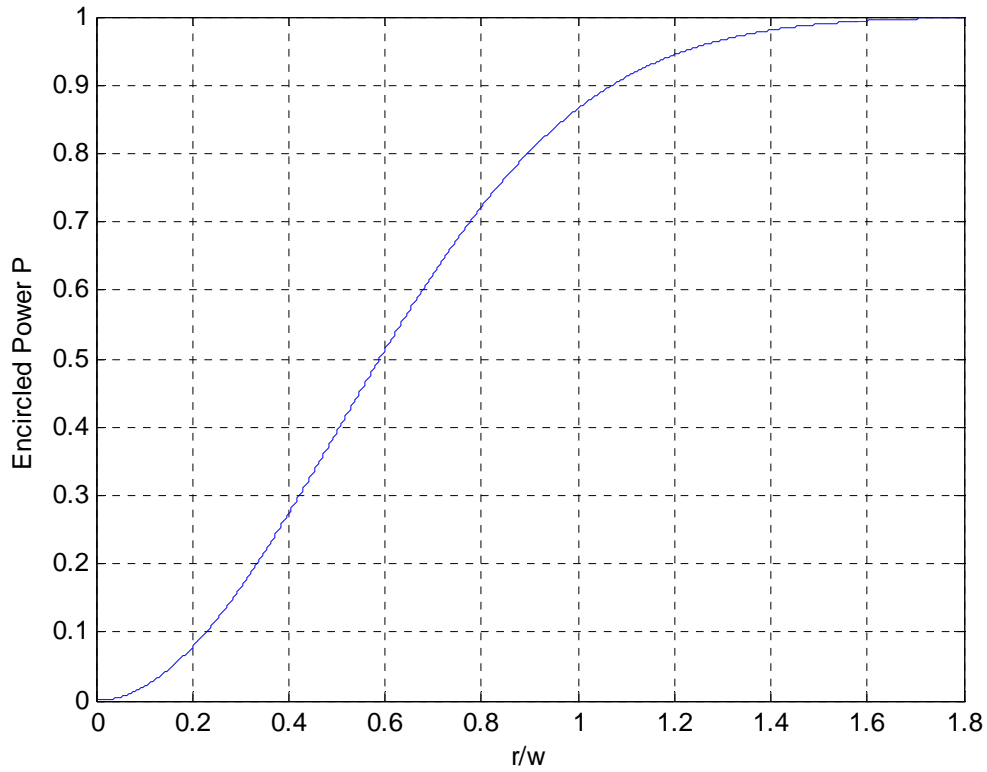


Fig. B.1. Encircled Power in a Gaussian beam as a function of the normalized radius of the thin

lens. The thin lens radius  $r$  is normalized with respect to the incident beam  $\frac{1}{e^2}$  radius  $w$ .



### References

1. Bahaa E. A. Saleh, Malvin C. Teich, Fundamentals of Photonics, (John Wiley & Sons, Inc., 1991, New York, USA).

## **APPENDIX C: CHARACTERISTICS OF MERCK BL006 NEMATIC LIQUID CRYSTAL MIXTURE**

PT            Cr <20 N 113 is <sup>1</sup>

Dielectrics     $\Delta\epsilon$  +17.3 <sup>1</sup>

Optics         $\Delta n$  +0.2860 <sup>1</sup>

use for reflective displays <sup>1</sup>

PT            Cr -15 S <-20 N 113 is <sup>2</sup>

$\eta$  71 cSt, T=20°C <sup>2</sup>

Dielectrics     $\Delta\epsilon$  +17.3 <sup>2</sup>

Dielectrics     $\epsilon_{||}$  22.8 <sup>2</sup>

Optics         $\Delta n$  +0.2860 <sup>2</sup>

Optics         $n_o$  1.5300 <sup>2</sup>

V(10.0.20) 1.77 <sup>2</sup>

V(90.0.20) 2.42 <sup>2</sup>

Elastics         $k_{11}$  17.90 E-12 N, T=20°C <sup>2</sup>

Elastics         $k_{33}$  33.50 E-12 N, T=20°C <sup>2</sup>

Elastics         $k_{33}/k_{11}$  1.87, T=20°C <sup>2</sup>

self-assembled gels, + AG1 <sup>3</sup>

non classified properties <sup>4</sup>

non classified properties <sup>5</sup>

non classified properties <sup>6</sup>

## References

1. T. Yamaguchi, H. Yamaguchi, Y. Kawata, 5th Int. Display Workshop (IDW'98), Kobe LCTp1-3, 33-36, 1998.
2. Ed.: Merck Product information: Merck Liquid Crystals Licrilite, 1995.
3. L. Guan, Y. Zhao, J. Mater. Chem. 11, 1339-1344, 2001.
4. T. Yamaguchi, H. Yamaguchi, Y. Kawata, J. Appl. Phys. 85, 7511-7516, 1999.
5. M. Okabe, S. Konishi, Hitachi Cable, Ltd., Japan JP 10.102.061 (1998/04/21), 1998.
6. T. Yamaguchi, Y. Kawata, H. Yamaguchi, Toshiba Corp., Japan JP 11.160.725 (1999/06/18), 1999.